

**Anisotropic Transfer of Resonance Photons  
in Hot Plasmas  
on Magnetized White Dwarfs**

**強磁場白色矮星に立つ高温プラズマにおける  
共鳴光子の非等方的な伝播過程**

Yukikatsu Terada

Thesis submitted to  
the University of Tokyo  
for the Degree of Doctor of Science (Physics)  
December, 2001

## Abstract

Among various astrophysical hot plasmas, those in the accretion column on magnetized white dwarfs (MWDs) are of particular interest. The plasmas are produced when a supersonic accretion flow onto magnetic poles of an MWD is thermalized through a standing shock. The plasma radiates X-ray continuum via bremsstrahlung, as well as atomic emission lines from major elements including iron in particular. In a typical accretion column of an MWD, the continuum photons are subject only to the Compton scattering with a relatively small optical depth, whereas the atomic line photons suffer in addition from resonance scattering with a very high optical depth. Therefore, the plasmas in MWDs provide an ideal laboratory to study an interplay between the optically thin and thick processes.

A subclass of MWDs, called polars, were observed extensively with the Japanese cosmic X-ray observatory *ASCA*, and several of them were found to exhibit extremely strong ionized iron-K emission lines (Terada *et al.* 1999; Ishida *et al.* 1998; Misaki *et al.* 1996). These objects are called POLE (Pole-On Line Emitter), after their geometry of the accretion column. Their iron-line equivalent widths are so large, reaching  $\sim 4000$  eV, that the implied iron abundances would become unrealistically high, e.g., 3.0 solar abundances.

In the present thesis, it is proposed that the strong iron lines of POLEs are a result of collimation of resonance line photons along the magnetic field lines, which in turn is caused by anisotropic transfer of line photons under a very high optical depth for the resonance scattering. The anisotropy occurs when the accretion column has a flat shape (geometrical collimation), and is augmented by the strong longitudinal velocity gradient in the accretion flow which invalidates the resonance condition for line photons when they propagate along the velocity gradient (physical collimation). This mechanism was quantitatively confirmed with Monte Carlo simulations; it can enhance the equivalent width of H-like and He-like iron  $K_\alpha$  resonance lines in the pole-on direction by a factor of 2 – 3 as compared to the angular average. Furthermore, with *ASCA* and *RXTE* observations of polars, the anisotropic effect was clearly detected from two objects, V834 Centauri and AM Herculis, as a rotational modulation of the equivalent width of the iron K line. The enhancement was also detected in a statistical sense from seven other polars observed with *ASCA* and *BeppoSAX*, although individual cases were insignificant.

These results provide one of the first observational confirmations of the resonance scattering in the X-ray frequency. They also quantitatively explain the very intense iron lines from POLEs: these objects are nearly co-aligned rotators, viewed almost pole-on to their accreting pole throughout their rotation. In addition, the new effects discovered here provide a novel tool with which the geometry and plasma parameters in the accretion column can be diagnosed.

# Contents

<b>1</b>	<b>INTRODUCTION</b>	<b>1</b>
<b>2</b>	<b>REVIEW</b>	<b>4</b>
2.1	White Dwarfs . . . . .	4
2.1.1	The degenerate star . . . . .	4
2.1.2	Theoretical mass versus radius relation of white dwarfs . . . . .	6
2.1.3	Observation of white dwarfs . . . . .	9
2.2	White Dwarf Binaries . . . . .	11
2.2.1	Observation of white dwarf binaries . . . . .	11
2.2.2	Cataclysmic variables . . . . .	12
2.2.3	Binary kinematics of cataclysmic variables . . . . .	13
2.3	Magnetic Field in white dwarfs . . . . .	14
2.3.1	Magnetism of white dwarfs . . . . .	14
2.3.2	Measurements of magnetic fields of white dwarfs . . . . .	16
2.4	Magnetic Cataclysmic Variables . . . . .	20
2.4.1	Polars and intermediate polars . . . . .	20
2.4.2	Mass accretion onto Magnetic Cataclysmic Variables . . . . .	23
2.4.3	Shock discontinuity of the accretion flow . . . . .	25
2.4.4	Emission from magnetic cataclysmic variables . . . . .	27
2.4.5	Hot plasma in accretion column . . . . .	29
2.4.6	Structure of accretion column: Aizu model . . . . .	31
2.5	X-ray Emission from Hot Plasmas . . . . .	34
2.5.1	Emission mechanisms . . . . .	34
2.5.2	Continuum emission . . . . .	35
2.5.3	Collisionally ionized plasma . . . . .	36
2.5.4	Atomic line emission . . . . .	37
2.5.5	Plasma diagnostics with emission lines . . . . .	40
2.6	Previous X-ray Observations of Magnetic Cataclysmic Variables . . . . .	41
2.6.1	Initial X-ray observations . . . . .	41
2.6.2	Hard X-ray continuum spectra studied with <i>Ginga</i> . . . . .	42
2.6.3	X-ray line emission with <i>Ginga</i> . . . . .	44
2.6.4	Spin modulation in X-rays: <i>Ginga</i> results . . . . .	46
2.6.5	X-ray spectroscopy of ionized line emission with <i>ASCA</i> . . . . .	48
2.6.6	The origin of fluorescent iron line . . . . .	51
2.6.7	Discovery of the strong line object POLE by <i>ASCA</i> . . . . .	52
<b>3</b>	<b>X-RAY BEAMING MECHANISM IN ACCRETION COLUMN</b>	<b>54</b>
3.1	An Overview . . . . .	54
3.2	Geometrical Beaming of Resonance Line . . . . .	55
3.3	Physical Beaming by Velocity Gradient . . . . .	56
3.4	Numerical Simulations of the Radiative Transfer . . . . .	59
3.4.1	Basic conditions of the Monte-Carlo simulation . . . . .	59
3.4.2	Algorithm for the propagation of line photons . . . . .	59
3.4.3	Confirmation of our calculation code . . . . .	62
3.4.4	Numerical results in nominal condition . . . . .	65
3.4.5	Estimation of the beaming factor . . . . .	68

<b>4</b>	<b>INSTRUMENTATION</b>	<b>70</b>
4.1	Overview of X-ray Instruments . . . . .	70
4.1.1	Our observational approach and requirements . . . . .	70
4.1.2	Current X-ray observatories . . . . .	70
4.2	The Fourth Japanese X-ray Observatory, <i>ASCA</i> . . . . .	73
4.2.1	Overview . . . . .	73
4.2.2	X-ray telescope (XRT) . . . . .	74
4.2.3	Gas Imaging Spectrometer (GIS) . . . . .	77
4.2.4	Solid-state Imaging Spectrometers (SIS) . . . . .	80
4.3	Italian X-ray Astrophysical Satellite, <i>BeppoSAX</i> . . . . .	85
4.3.1	Overview . . . . .	85
4.3.2	Concentrator Optical System (Mirror Unit) . . . . .	86
4.3.3	Medium Energy Concentrator Spectrometer (MECS) . . . . .	86
4.4	Rossi X-ray Timing Explorer (RXTE) . . . . .	88
4.4.1	Overview . . . . .	88
4.4.2	Proportional Counter Array (PCA) . . . . .	89
4.5	Method of Spectral Analysis . . . . .	91
<b>5</b>	<b>OBSERVATIONS</b>	<b>92</b>
5.1	Target Selection . . . . .	92
5.2	<i>ASCA</i> observations . . . . .	95
5.3	<i>RXTE</i> observations . . . . .	95
5.4	<i>BeppoSAX</i> observations . . . . .	96
<b>6</b>	<b>DATA ANALYSIS AND RESULTS</b>	<b>97</b>
6.1	V834 Centauri . . . . .	97
6.1.1	Average spectral continuum with <i>ASCA</i> . . . . .	97
6.1.2	Phase-averaged iron lines with <i>ASCA</i> . . . . .	100
6.1.3	Phase resolved <i>ASCA</i> spectra . . . . .	103
6.1.4	<i>RXTE</i> observations . . . . .	107
6.1.5	Phase resolved <i>RXTE</i> spectra . . . . .	110
6.2	AM Herculis . . . . .	112
6.2.1	<i>ASCA</i> observations . . . . .	112
6.2.2	Phase resolved <i>ASCA</i> spectra . . . . .	115
6.2.3	<i>BeppoSAX</i> observations . . . . .	117
6.2.4	<i>RXTE</i> observation . . . . .	121
6.2.5	Comparison of <i>ASCA</i> , <i>BeppoSAX</i> , and <i>RXTE</i> observations . . . . .	124
6.3	Other Polars . . . . .	125
<b>7</b>	<b>DISCUSSION</b>	<b>129</b>
7.1	The Origin of the Observed Line Modulation . . . . .	129
7.1.1	Essence of the observation . . . . .	129
7.1.2	Alternative possibilities of the intensity enhancement . . . . .	129
7.1.3	Quantitative examination of the enhancement . . . . .	131
7.2	Implications of the Resonance Scattering Effects . . . . .	132
7.2.1	Impact on the temperature and abundance determinations . . . . .	132
7.2.2	Solution to the mystery of POLEs . . . . .	134
7.2.3	A new plasma diagnostic method in the accretion column . . . . .	136
7.3	Prospects for the Future Studies . . . . .	138
<b>8</b>	<b>CONCLUSION</b>	<b>140</b>
<b>A</b>	<b>Analysis</b>	<b>143</b>
A.1	Energy range in <i>ASCA</i> and <i>BeppoSAX</i> analyses . . . . .	143
A.2	Fitting results for V834 Cen and AM Herculis . . . . .	143
A.3	Intermediate Polars . . . . .	146

# List of Figures

1.1	Sizes and densities of typical cosmic plasmas . . . . .	1
2.1	A Hertzsprung Russell diagram of nearby stars. . . . .	4
2.2	Optical image of M4 . . . . .	5
2.3	Mass-Radius relation of electron-degenete stars, solar-system planets . . . . .	8
2.4	A sky distribution of white dwarfs . . . . .	9
2.5	The observed mass and radius of visual of white dwarfs . . . . .	10
2.6	Gravitational potential in rotating binary system . . . . .	12
2.7	Roche lobe surfaces for four different binary-star systems . . . . .	12
2.8	The period distribution of CVs . . . . .	13
2.9	The distribution of magnetic field strength for white dwarfs . . . . .	15
2.10	An example of cyclotron humps in MCV . . . . .	16
2.11	An example of cyclotron absorption feature of neutron star binary . . . . .	17
2.12	Phase resolved optical spectra of VV Puppis . . . . .	17
2.13	An example of Zeeman observation in magnetic isolated white dwarf . . . . .	18
2.14	An optical spectrum with photospheric Zeeman and cyclotron lines . . . . .	19
2.15	Spin periods vs. orbital periods for MCVs . . . . .	20
2.16	The distribution of the estimated mass transfer rates for MCVs. . . . .	23
2.17	A schematic view of mass accretion in MCVs (1) . . . . .	24
2.18	A schematic view of mass accretion in MCVs (2) . . . . .	24
2.19	A schematic view of the accretion column on the white dwarf . . . . .	26
2.20	The cooling mechanisms of hot plasmas in a magnetic field . . . . .	27
2.21	Theoretical and observed UV – X-ray spectra of MCVs . . . . .	28
2.22	The Aizu structure for the post-shock plasma . . . . .	33
2.23	Cooling function of thin thermal plasmas . . . . .	34
2.24	Energy spectra of thermal bremsstrahlung . . . . .	35
2.25	Fractional ratios for ionized iron species in CIE . . . . .	37
2.26	Radiative transition diagram of Fe XXVI and Fe XXV . . . . .	38
2.27	Temperature dependence of the line emissivity . . . . .	39
2.28	Contribution of each line in figure 2.27 . . . . .	39
2.29	Temperature dependence of the ratio of He-like and H-like Fe line . . . . .	39
2.30	Position dependence of line emissivity in accretion column (1) . . . . .	40
2.31	Position dependence of line emissivity in accretion column (2) . . . . .	40
2.32	Radiation window for astronomical objects . . . . .	41
2.33	<i>Ginga</i> Spectrum of AM Hercuris . . . . .	42
2.34	The mass distribution of white dwarfs in MCVs by <i>Ginga</i> . . . . .	43
2.35	The definition of equivalent width . . . . .	44
2.36	The summery of line observation by <i>Ginga</i> . . . . .	45
2.37	The spin-folded light curves of AM Hercuris, obtained by <i>Ginga</i> . . . . .	46
2.38	The relation between low and high energy modulation amplitudes in MCV . . . . .	46
2.39	Schematic illustration of spin modulation in X-rays . . . . .	47
2.40	X-ray spectrum of EX Hydra obtained by <i>ASCA</i> . . . . .	48
2.41	Plasma temperatures of EX Hydra by line ratio with <i>ASCA</i> . . . . .	48
2.42	Observational constraints for shock and bottom temperatures of EX Hya . . . . .	49
2.43	Constraints on the mass versus radius ratio of EX Hya . . . . .	49
2.44	The ionization temperature and the continuum temperature for 19 MCVs . . . . .	50
2.45	The metal abundance distribution determined by <i>ASCA</i> . . . . .	50
2.46	The hydrogen column density and the equivalent width of fluorescence . . . . .	51

2.47	The X-ray spectrum of AX J1842–0423 with <i>ASCA</i> . . . . .	52
3.1	Cross section of the resonance for iron lines in the accretion column . . . . .	57
3.2	A schematic view of the physical beaming effect . . . . .	58
3.3	A schematic illustration of typical paths of resonance line photons . . . . .	60
3.4	Schematic illustration of each step in our calculation . . . . .	60
3.5	The inverse Compton spectra from a single scattering . . . . .	61
3.6	The cross section for Compton scattering by the Klein-Nishina formula . . . . .	61
3.7	Initial positions for iron photon in our calculation . . . . .	62
3.8	The free path length for resonance scattering in our calculation . . . . .	63
3.9	The distribution of Compton scattered angle in the calculation . . . . .	63
3.10	The shift energy by Compton scattering in our calculation . . . . .	63
3.11	Angular distributions of simulated line photons for simple case . . . . .	64
3.12	Angular distributions of simulated line photons for nominal case (1) . . . . .	65
3.13	The simulated line spectrum in a nominal case . . . . .	66
3.14	Phase resolved line spectra simulated in nominal case . . . . .	67
3.15	A summary of Monte-Carlo simulations (shape) . . . . .	69
3.16	A summary of Monte-Carlo simulations (density) . . . . .	69
3.17	A summary of Monte-Carlo simulations (mass) . . . . .	69
4.1	The effective area of X-ray satellites in 1990s and 2000s . . . . .	72
4.2	Overview of the <i>ASCA</i> satellite . . . . .	73
4.3	Configuration of payload instruments on board <i>ASCA</i> . . . . .	73
4.4	Schematic view of Wolter Type I optics . . . . .	74
4.5	Top view of one quadrant of <i>ASCA</i> XRT . . . . .	74
4.6	Effective area of XRT on board <i>ASCA</i> , <i>Einstein</i> and <i>ROSAT</i> . . . . .	75
4.7	The image of a point source, AM Herculis, obtained by <i>ASCA</i> . . . . .	76
4.8	Off-axis images obtained with <i>ASCA</i> XRT . . . . .	76
4.9	Examples of the XRT light path . . . . .	76
4.10	Observed stray light by Crab nebula . . . . .	76
4.11	Cross section of the GIS sensor . . . . .	78
4.12	A schematic illustration of the X-ray detection by the GIS . . . . .	78
4.13	Energy resolution of the GIS as a function of the incident energy . . . . .	78
4.14	Integrated average background spectra of GIS . . . . .	79
4.15	Long term variation of the non X-ray background of the GIS . . . . .	79
4.16	Cross section of the SIS sensor . . . . .	80
4.17	Effects of radiation damage on SIS performance . . . . .	81
4.18	Event pattern and grade definition for the SIS . . . . .	82
4.19	Background spectrum of the SIS . . . . .	84
4.20	<i>BeppoSAX</i> scientific payload accommodation . . . . .	85
4.21	A schematic view of the MECS instrument (1) . . . . .	87
4.22	Schematic view of the MECS instrument (2) . . . . .	87
4.23	MECS energy resolution . . . . .	87
4.24	A schematic view of the <i>RXTE</i> satellite . . . . .	88
4.25	The <i>RXTE</i> PCA assembly . . . . .	89
4.26	Schematic view of <i>RXTE</i> PCA unit . . . . .	89
4.27	Verification of background modeling for PCA . . . . .	90
5.1	A schematic illustration for the definition of $i$ , $\beta$ and $\theta$ . . . . .	92
5.2	Pole angle versus spin phase for known polars . . . . .	93
6.1	X-ray spectra of V834 Cen with <i>ASCA</i> . . . . .	97
6.2	X-ray continuum spectra of V834 Cen with various models . . . . .	98
6.3	Phase averaged SIS spectra in the iron K-line energy band . . . . .	100
6.4	Phase averaged spectra of V834 Cen over the Fe-K line energies . . . . .	102
6.5	Folded light curve of V834 Cen obtained with <i>ASCA</i> . . . . .	103
6.6	Phase resolved spectra of V834 . . . . .	104
6.7	Phase resolved spectra of V834 Cen over the Fe-K line energies . . . . .	105
6.8	A confidence contour of EWs in two phases, V834 Cen with <i>ASCA</i> . . . . .	106

6.9	X-ray spectra of V834 Cen with <i>RXTE</i> . . . . .	107
6.10	X-ray spectra of V834 Cen with <i>RXTE</i> (II) . . . . .	107
6.11	Phase averaged X-ray spectrum of V834 Cen . . . . .	108
6.12	Phase averaged X-ray spectrum of V834 Cen . . . . .	109
6.13	Folded light curve of V834 Cen obtained with the <i>RXTE</i> PCA . . . . .	110
6.14	Phase resolved spectra of V834 Cen with <i>RXTE</i> . . . . .	111
6.15	A confidence contour of EWs in two phases, V834 Cen with <i>RXTE</i> . . . . .	111
6.16	Comparison of $\zeta_{\text{OBS}}$ obtained with <i>ASCA</i> and <i>RXTE</i> . . . . .	111
6.17	Folded light curve of AM Her obtained with <i>ASCA</i> . . . . .	112
6.18	X-ray spectra of AM Her with <i>ASCA</i> . . . . .	113
6.19	Phase averaged spectrum of AM Herculis with <i>ASCA</i> . . . . .	113
6.20	Phase resolved spectra of AM Her over the Fe-K line energies . . . . .	116
6.21	A confidence contour of EWs in two phases, AM Her with <i>ASCA</i> . . . . .	116
6.22	Folded light curve of AM Her obtained with <i>BeppoSAX</i> . . . . .	117
6.23	Phase averaged spectrum of AM Herculis with <i>BeppoSAX</i> . . . . .	117
6.24	Phase resolved spectra of AM Herculis with <i>BeppoSAX</i> . . . . .	119
6.25	Phase resolved spectra of AM Her over the Fe-K line energies . . . . .	120
6.26	A confidence contour of EWs in two phases, AM Her with <i>BeppoSAX</i> . . . . .	120
6.27	The <i>RXTE</i> PCA spectra of AM Her . . . . .	121
6.28	Phase averaged spectra of AM Her with the <i>RXTE</i> PCA . . . . .	121
6.29	Continuum model for AM Her with the PCA . . . . .	121
6.30	Folded light curve of AM Her obtained with <i>RXTE</i> . . . . .	122
6.31	Phase resolved spectra of AM Her with the <i>RXTE</i> PCA . . . . .	123
6.32	A confidence contour of EWs in two phases, AM Her with <i>RXTE</i> . . . . .	123
6.33	Comparison of $\zeta_{\text{OBS}}$ obtained with <i>ASCA</i> and <i>RXTE</i> . . . . .	124
6.34	X-ray folded light curves of polars with <i>ASCA</i> and <i>BeppoSAX</i> . . . . .	126
6.35	Phase resolved spectra of polars with <i>ASCA</i> and <i>BeppoSAX</i> . . . . .	127
6.36	Line equivalent widths of polars in pole-on and side-on phases . . . . .	128
6.37	The line enhancement of He-like iron K line of polars vs. pole angle . . . . .	128
7.1	Estimation of the geometrical beaming on V834 Centauri . . . . .	131
7.2	Comparison of the enhancement of H-like with that of He-like line . . . . .	133
7.3	Modification of the abundance measurements with <i>ASCA</i> . . . . .	133
7.4	The phase averaged enhancement $\bar{\xi}$ on $i - \beta$ plane . . . . .	135
7.5	The probability of $\bar{\xi} > \bar{\xi}_{\text{th}}$ in $i - \beta$ plane. . . . .	135
7.6	Calculated $\zeta$ vs. post-shock density of V834 Cen and AM Her . . . . .	136
7.7	Enhancement of light elements . . . . .	138
A.1	X-ray folded light curves of intermediate polars with <i>ASCA</i> and <i>BeppoSAX</i> . . . . .	146
A.2	Phase resolved X-ray spectra of intermediate polars with <i>ASCA</i> . . . . .	150
A.3	Scatter plot of line equivalent widths of intermediate polars . . . . .	152

# List of Tables

2.1	Basic properties of currently known polars. . . . .	21
2.2	Basic properties of currently known intermediate polars. . . . .	22
2.3	Emission processes from thin thermal plasmas. . . . .	34
2.4	The mass of white dwarfs in MCVs determined by <i>Ginga</i> ( $\times M_{\odot}$ ). . . . .	43
4.1	Parameters of the <i>ASCA</i> XRT . . . . .	75
4.2	Parameters of <i>ASCA</i> GIS. . . . .	77
4.3	The basic parameters of the <i>ASCA</i> SIS. . . . .	80
4.4	The <i>BeppoSAX</i> Instruments (Boella <i>et al.</i> 1997). . . . .	86
4.5	<i>BeppoSAX</i> Mirror Unit Specifications . . . . .	86
4.6	Basic parameters of the <i>BeppoSAX</i> MECS. . . . .	87
4.7	Basic parameters of the PCA onboard <i>RXTE</i> . . . . .	90
5.1	Summary for <i>ASCA</i> observations of MCVs. . . . .	94
5.2	Summary of <i>RXTE</i> observations of AM Herculis and V834 Centauri. . . . .	95
5.3	Summary of <i>BeppoSAX</i> observations of MCVs. . . . .	96
6.1	The best fit continuum parameters for the <i>ASCA</i> GIS and SIS spectra of V834 Centauri <sup>a</sup> . . . . .	99
6.2	The best fit parameters of the iron $K_{\alpha}$ line for V834 Centauri <sup>a</sup> . . . . .	101
6.3	The best fit parameters of the iron $K_{\alpha}$ line with three narrow gaussians <sup>a</sup> . . . . .	106
6.4	The best fit parameters of the iron $K_{\alpha}$ line for V834 Centauri with the PCA <sup>a</sup> . . . . .	109
6.5	The best fit parameters of the phase-resolved V834 Cen spectra with <i>RXTE</i> PCA <sup>a</sup> . . . . .	111
6.6	The best fit continuum parameters for the <i>ASCA</i> GIS and SIS spectra of AM Herculis <sup>a</sup> . . . . .	114
6.7	The best fit parameters of the iron $K_{\alpha}$ lines of AM Her with <i>ASCA</i> <sup>a</sup> . . . . .	115
6.8	The best fit continuum parameters for the <i>BeppoSAX</i> MECS spectra of AM Herculis <sup>a</sup> . . . . .	118
6.9	The best fit parameters of the iron $K_{\alpha}$ lines of AM Her with <i>BeppoSAX</i> <sup>a</sup> . . . . .	119
6.10	The best fit parameters of the AM Herculis spectra with the <i>RXTE</i> PCA . . . . .	122
6.11	The definition of the pole-on and side-on phases of polars. . . . .	126
7.1	The plasma parameters for the accretion column of V834 Cen and AM Her <sup>a</sup> . . . . .	137
A.1	The lower energy range $E_{\min}$ for the continuum modeling of MCVs. . . . .	143
A.2	Best Fit continuum parameters for the <i>ASCA</i> GIS and SIS spectra of V834 Cen <sup>a</sup> . . . . .	144
A.3	Best Fit parameters of the iron $K_{\alpha}$ line for V834 Centauri with <i>ASCA</i> <sup>a</sup> . . . . .	145
A.4	Best Fit parameters of the iron $K_{\alpha}$ line for AM Herculis with <i>ASCA</i> <sup>a</sup> . . . . .	145
A.5	Best Fit parameters of the iron $K_{\alpha}$ line for AM Herculis with <i>BeppoSAX</i> <sup>a</sup> . . . . .	145
A.6	The phase definition of intermediate polars. . . . .	149

# Chapter 1

## INTRODUCTION

We observe hot plasmas in many astrophysical environments, whose sizes and densities are summarized in figure 1.1. The plasma diagnostics using electromagnetic waves provide one of the most important basic tools for astrophysics. The optical depth of a plasma is determined by various electromagnetic interactions, including free-free absorption and Compton (or Thomson) scattering of continuum photons, as well as resonance scattering of line photons. The electromagnetic radiation spectrum emergent from a plasma becomes very simple at the two limiting conditions. One is the optically thin limit as can be seen in solar and stellar coronae, supernova remnants, clusters of galaxies, and so on. The other is the optically thick limit, in which we can treat the emission as a black body emission, as is found in stellar interiors, atmosphere of neutron stars, accretion disks in soft-state accreting black holes, etc. Both in these extremes, we can calculate and evaluate the spectra analytically, since we do not need to consider complex radiation transfer. As a result, such plasma are relatively well understood.

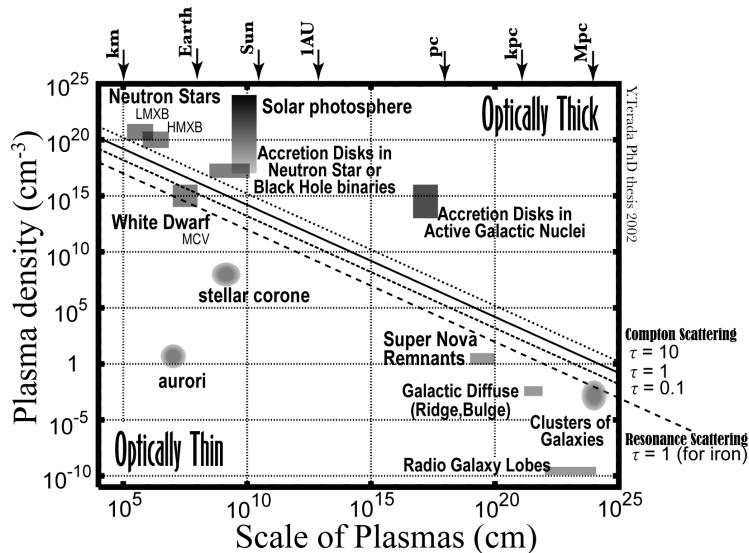


Figure 1.1: Sizes and densities of typical cosmic plasmas. The optical depth increases toward upper right. The optical depth for Compton scattering becomes 0.1, 1, and 10 along dotted line, solid line, and dashed line, respectively. On the long dashed line, optical depth for the resonance Fe  $K_{\alpha}$  line with one solar abundance become unity.

When an optical depth of a plasma is intermediate between the two extremes, i.e., gray case, the energy spectra of the emission from plasmas become very complex reflecting its physical and geometrical states; densities, temperatures, metal abundances, shapes, bulk motions, and so on. In these cases, the radiation transfer involving stochastic processes becomes important, and hence we need Monte-Carlo method to reproduce the spectra from such plasmas. However, once the radiation transfer is well understood, the energy spectra gives us a powerful information as to optically “gray” plasmas. In figure 1.1, a boundary between optically thin and thick for Compton scattering is plotted (solid line). We thus find that only hot plasmas associated with white dwarfs come in between optically thin and thick regions. Therefore, they must be an ideal laboratory to improve our knowledge of “optically gray plasma.”

White dwarfs are stars that support themselves against their gravity by the pressure of degenerate electrons. Its inner structure is determined by a rather simple equation of state, so that the mass and radius of a white dwarf can be described by a combination of fundamental physical constants, including the mass of protons which is a main source of gravity, the mass of electrons which produces degenerate pressure, and the gravitational constant. The typical mass of a white dwarf is about one solar mass ( $2 \times 10^{30}$  kg) and its radius is close to that of the earth ( $\sim 7000$  km). On its surface, the average gravitational potential per nucleon reaches a few tens keV, leading to the formation of hot plasmas.

In order to produce hot plasmas on a white dwarf, a sufficient amount of matter must be accreted onto it. Therefore, a close binary environment is needed. A magnetic cataclysmic variable (MCV) is a binary composed of a late-type low-mass main sequence star and a white dwarf with strong magnetic field ( $10^{5-8}$  G), whose emission is powered by the matter accretion. The matter spilling over the Roche lobe of the main sequence star is captured by the magnetic field of the white dwarf and accretes onto its magnetic poles, generating a shock heated plasma near the white dwarf surface. Then, the post-shock plasma is cooled down via free-free emission, forming an accretion column there. This makes an MCV a strong hard X-ray source, and this X-ray emission provides the primary diagnostic tool for the accretion-column plasma. Its diagnostics is the main subject of this thesis.

A systematic study of hard X-ray emission from MCVs was performed by Ishida (1991) using the third Japanese X-ray satellite *Ginga*, and he found that the hard X-ray emission from all the observed 12 MCVs are explained by optically thin thermal bremsstrahlung with a complex photo-electric absorption and with an iron line emission. More advanced plasma diagnostics have been developed by Fujimoto *et al.* (1996) using the fourth Japanese X-ray satellite *ASCA*, which has a higher energy resolution than *Ginga*. They measured the ratio of helium-like and hydrogenic  $K_\alpha$  lines of various elements, and found a clear evidence of multi-temperature property, which was later confirmed for a

larger sample by Ezuka and Ishida (1999). This provides direct observational evidence of free-free cooling of the plasma in accretion column. A remarkable improvement in energy resolution has been realized by the X-ray satellite *Chandra*, reaching the order of eV, allowing us to resolve the fine structure of many atomic emission lines. With *Chandra* observations of MCVs, it has been confirmed that the hot plasma is in a collisional ionization equilibrium, because of the weakness of forbidden lines compared to the resonance or intercombination lines.

In this thesis, we focus on hot plasmas on white dwarfs as representative optically “gray” plasmas among in many astrophysical sites. As can be seen in figure 1.1, these plasmas, to a first approximation, are optically thin to continuum photons, as has been assumed in all the previous studies. They are in contrast optically thick to the Fe- $K_\alpha$  line. Therefore, we can no longer treat the white-dwarf plasmas as optically-thin case, when we begin to study atomic emission lines using the improved current-day X-ray instrumentation. Furthermore, a finite Compton optical depth affects the line-photon transfer, as well. Although the resonance scattering effects were considered in plasmas in solar coronae, cluster of galaxies and so on, observational results on them were not very conspicuous because of their relatively small optical depths.

The aim of this thesis is to examine, from observations and calculations, the possibility of anisotropic radiation transfer of resonant line photons in the accretion column of MCVs, as a result of a high optical depth for resonance and the significant flow velocity gradient. Chapter 2 gives a brief review of MCVs and their fundamental properties. In chapter 3, we propose a beaming mechanism of line photons due to resonance scattering in the accretion column of MCV, and show numerical results of our Monte Carlo calculations. The X-ray instruments used in this thesis, on board *ASCA*, *BeppoSAX*, and *RXTE*, are described in Chapter 4. In Chapter 5 we describe our observational approach, and show the method of analysis and results in chapter 6. In chapter 7 we discuss the results from observation and simulation, followed by a conclusion in chapter 8.

# Chapter 2

## REVIEW

### 2.1 White Dwarfs

Before looking into thin thermal hot plasmas on white dwarfs, which form the main subject of this thesis, we review astronomical and physical backgrounds of white dwarfs.

#### 2.1.1 The degenerate star

The study of white dwarfs began with the discovery of “Sirius B” by A. G. Clark in 1862, of which the existence had already been suggested in 1832 based on the 50-year periodic proper motion of the brightest star in the sky, Sirius. As shown in figure 2.1, white dwarfs lie in the left bottom of the Hertzsprung-Russell diagram (HR diagram). This means that they are much less luminous than the main sequence stars with the same temperature, because of the extremely small size. As exemplified by figure 2.2, more than 2000 white dwarfs have been observed in visible light over the entire sky.

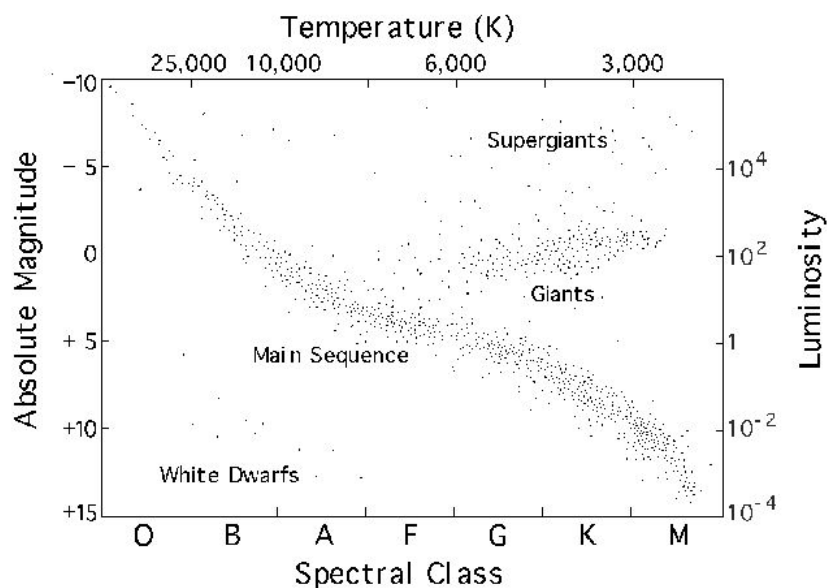


Figure 2.1: A Hertzsprung Russell diagram of nearby stars.

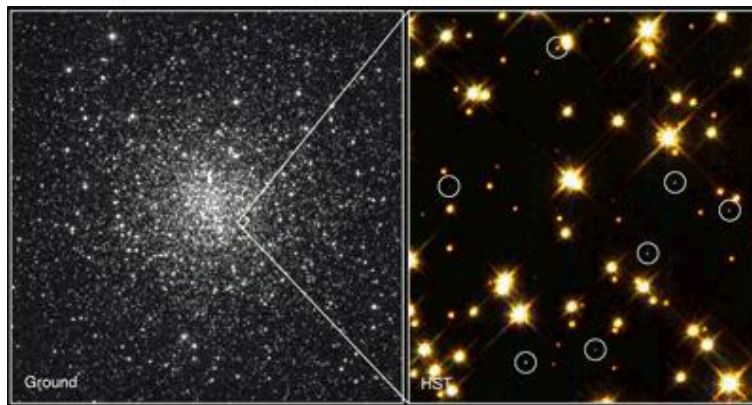


Figure 2.2: An optical image of the globular cluster M4, where white dwarfs are shown by circles.

White dwarfs are one of the end products of stars. A main sequence star is supported against its gravity by gas pressure produced via nuclear burning of hydrogen. When the hydrogen fuel is mostly consumed, the helium ash is condensed at the core region of a star. The mass of this stellar core continuously increases as hydrogen burns the core boundary, and the stellar core begins to shrink to overcome the gravity. At the same time, the outer envelope expands so that the surface temperature decreases. A star in this stage is called “red giant”, which lies in the right top of the HR diagram (figure 2.1). The core of a red giant star has a high temperature of  $\sim 10^7\text{--}10^9$  K with a high density of  $n_c \sim 10^{29}$  cm $^{-3}$ . Under the condition of such a high density, the electron degenerate pressure, rather than the gas pressure, plays an important part to support the stellar gravity. As a general characteristic of self-gravitating systems, the stellar core temperature  $T_c$  of a red giant increases as  $T_c \propto n_c^{1/3}$  as the core shrinks, and as a result, the gas pressure scales as  $P_g \propto n_c T_c \propto n_c^{4/3}$ . In contrast, the degenerate pressure increases as  $P_d \propto n_c^{5/3}$  (see the detail in equation 2.2). In the core of a red giant, the ratio  $P_d/P_g$  therefore increases as  $\propto n_c^{1/3} \propto (\text{core radius})^{-1}$ , producing a strong electron degeneracy in spite of a high temperature reaching  $\sim 10^8$  K. When the initial mass of the star is lower than  $\sim 4M_\odot$ , where  $M_\odot = 2.0 \times 10^{33}$  g is the solar mass, its outer envelope is lost as stellar winds, forming a planetary nebula, and the hot high-density core is left as a white dwarf. This is the standard scenario of the death of a relatively light star and the associated birth of a white dwarf.

Unlike a normal nuclear-burning star whose gravity is balanced with the gas pressure, white dwarfs are degenerate stars which support themselves against the gravity by the pressure of degenerate electrons.

The idea of degenerate stars was first proposed by R. H. Fowler in 1926, immediately after P. A. M. Dirac and E. Fermi formulated Fermi-Dirac statistics. White dwarfs have a typical mass of  $0.5 - 1.0 M_\odot$ , and a typical size comparable to that of the earth ( $\sim 10^9$  cm). Thus, the white-dwarf radius is only  $\sim 10^{-3}\text{--}10^{-2}$  of that of a main-sequence star of the same mass. As a result, the optical luminosity of a white dwarf is  $\sim 10^{-6}\text{--}10^{-4}$  of

that of a main sequence star. This places white dwarfs  $\sim 10 - 15$  magnitudes (see for example equation A.3 in Shapiro & Teukolsky 1983) below the main sequence in figure 2.1.

In addition to white dwarfs, there are two other types of degenerate stars; brown dwarfs and neutron stars. Brown dwarfs are those stars which are in the mass range from  $\sim 10^{-3}$  to  $0.08 M_\odot$ , i.e., heavier than planets but lighter than the critical mass for hydrogen to ignite. They cannot become a normal hydrogen-burning star, since their interior becomes too strongly degenerate in the course of initial gravitational compression. The size and mass of brown dwarfs are similar to those of white dwarfs, and they also support themselves against the gravity by electron degenerate pressure. Unlike white dwarfs, their optical emission is very faint because of low surface temperature, so they are difficult to observe. Furthermore, the chemical composition of brown dwarfs is considered to be different from those of white dwarfs; the former is made of mixed gas of hydrogen and helium, and the latter is made of pure helium. Neutron stars are also the end products of stars with masses of  $8 - 30 M_\odot$ . They have typical masses of  $1 - 3 M_\odot$  and typical sizes of  $\sim 10^{-5} R_\odot$ . Thus, they have much higher densities than white dwarfs. Their interior is devoid of electrons, and they support themselves by the degenerate pressure of neutrons.

### 2.1.2 Theoretical mass versus radius relation of white dwarfs

The electrons inside a white dwarf provide a textbook example of degenerate Fermi liquid. The Fermi energy  $\varepsilon_F$  of an ideal electron Fermi gas in three dimensional space can be described as

$$\varepsilon_F = \frac{\hbar^2}{2m_e} (3\pi^2 n_e)^{2/3}, \quad (2.1)$$

where  $\hbar$  is the Dirac constant,  $m_e$  is the electron mass, and  $n_e$  is its number density (see, for example, equation 17 in section 6 of Kittel 1996). Since the degenerate pressure  $P_d$  is approximately given as  $\sim n_e \varepsilon_F$ , we can easily understand the  $P_d \propto n_e^{5/3}$  scaling in the non-relativistic limit. According to a more exact calculation (equations 2.3.22 and 2.3.23 in Shapiro & Teukolsky 1983), we obtain

$$P_d = \frac{3^{2/3} \pi^{1/3}}{10} hc \lambda_e n_e^{5/3} \quad (\text{in Non Relativistic limit}) \quad (2.2)$$

$$\frac{3^{1/3}}{8\pi^{1/3}} hc n_e^{4/3} \quad (\text{in Extremely Relativistic limit}), \quad (2.3)$$

where  $\lambda_e \equiv \hbar/m_e c$  is the electron Compton wavelength.

The radius  $R_{WD}$  of a white dwarf of a given mass  $M_{WD}$  is determined by a balance between the gravity and the electron degenerate pressure. In the simplest treatment where the white dwarf is approximated to have a uniform density and non-relativistic, we can use the virial theorem to obtain

$$\frac{3}{5} \frac{GM_{WD}^2}{R_{WD}} = 3P_d V, \quad (2.4)$$

where  $G$  is the gravitational constant, and  $V \equiv \frac{4\pi}{3}R_{\text{WD}}^3$  is the volume of the white dwarf. Combining equation (2.2) and equation (2.4), we obtain

$$\begin{aligned} R_{\text{WD}} &= \frac{3^{4/3}}{2^{10/3}\pi^{4/3}} \frac{h^2}{Gm_e\mu^{5/3}m_p^{5/3}} M^{-1/3} \\ &= \left(\frac{3\sqrt{\pi}}{2}\right)^{4/3} \alpha_G^{-1} \lambda_e \mu^{-5/3} \left(\frac{M_{\text{WD}}}{m_p}\right)^{-1/3}, \end{aligned} \quad (2.5)$$

where  $m_p$  is the mass of nucleon, and  $\alpha_G \equiv \frac{Gm_p^2}{\hbar c} = 5.9 \times 10^{-39}$  is so-called gravitational fine structure constant defined under an analogy to electromagnetic fine structure constant. We also define the ratio  $\mu$  of the number density of nucleons (which are the main source of the gravity) and that of electrons (which supply the degenerate pressure);  $\mu = 1$  for pure hydrogen,  $\mu = 2$  for pure helium, and  $\mu = 1.2$  for the cosmic metal abundance. Thus, the mass-radius relation of white dwarfs can be described using only fundamental constants in physics. Numerically, equation (2.5) is written as

$$R_{\text{WD}} = 1.0 \times 10^{-2} R_{\odot} \left(\frac{\mu}{2}\right)^{-3/5} \left(\frac{M_{\text{WD}}}{M_{\odot}}\right)^{-1/3}. \quad (2.6)$$

The mass versus radius relation of the form  $R_{\text{WD}} \propto M_{\text{WD}}^{-1/3}$  is characteristic of degenerate stars, making a contrast to planets ( $R \propto M^{1/3}$ ) which support themselves by Coulomb force, and main sequence stars ( $R \propto M^{1/2}$ ), as shown in figure 2.3.

In the extremely relativistic case, the degenerate energy scales as  $P_{\text{D}}V \propto n_e^{3/4}V \propto R^{-1}$ , and hence the parameter  $R_{\text{WD}}$  vanishes in virial theorem to yield

$$\begin{aligned} M_{\text{WD}} &= \frac{5^{3/2}3\sqrt{\pi}}{2^4} \frac{(\hbar c)^{3/2}}{\mu^2 m_p^2 G^{3/2}} \\ &= \frac{5^{3/2}3\sqrt{\pi}}{2^4 \mu^2} \alpha_G^{-3/2} m_p. \end{aligned} \quad (2.7)$$

Numerically, the obtained radius and mass are

$$M_{\text{WD}} = 1.72 M_{\odot} \left(\frac{\mu}{2}\right)^{-2}, \quad (2.8)$$

and

$$R_{\text{WD}} = 2.8 \times 10^{-2} R_{\odot} \left(\frac{n_e}{5 \times 10^6 \text{ g cm}^{-3}}\right)^{-1/3} \left(\frac{\mu}{2}\right)^{-2/3}. \quad (2.9)$$

Thus,  $R_{\text{WD}}$  reduces to 0 as  $n_e$  increases, and  $M_{\text{WD}}$  is independent of  $n_e$  in the extremely relativistic limit.

The actual white dwarf has a non-uniform density. Taking this into account by using polytropic formalism, and considering intermediate cases between the non-relativistic and the extremely-relativistic limits, Chandrasehker (1931) for the first time constructed a realistic white dwarf model. The white dwarf mass in extremely relativistic limit, as approximated by equation (2.8), more strictly becomes  $1.457M_{\odot}$ , which is called ‘‘Chandrasehker

limit.” Neuenberg (1972) obtained an analytic approximation to the mass-radius relation of the white dwarf of zero temperature as

$$R_{\text{WD}} = 0.78 \times 10^9 \left[ \left( \frac{1.44 M_{\odot}}{M_{\text{WD}}} \right)^{2/3} - \left( \frac{M_{\text{WD}}}{1.44 M_{\odot}} \right)^{2/3} \right]^{1/2} \text{ cm}, \quad (2.10)$$

which agrees excellently with the calculation by Chandrasehker (1939). This relation is plotted in figure 2.3. Note that this reduces to equation (2.6) for  $M_{\text{WD}} \ll M_{\odot}$ .

A more comprehensive treatment of white dwarf models, including corrections to the Chandrasehker equation of state such as the effect of neutronization (or inverse  $\beta$ -decay), was given by Hamada & Salpeter (1961) and later by Wood (1990, 1995). These calculations are shown in figure 2.5. The mass-radius relation of pure iron composition deviates from those of He, C, and Mg white dwarfs due to the following two effects. First, the stable iron isotope,  $^{56}\text{Fe}$ , has  $\mu = 2.15$  instead of  $\mu = 2$  (lower dashed line in figure 2.5). In addition, the typical Fermi energy of degenerate electrons, several hundreds keV, is not sufficient to cause neutronization in light elements, but is high enough to increase the neutron fraction in heavier elements. As a result,  $\mu$  effectively increases from 2.15 upwards, in the case of pure iron composition (solid line denoting Fe in figure 2.5).

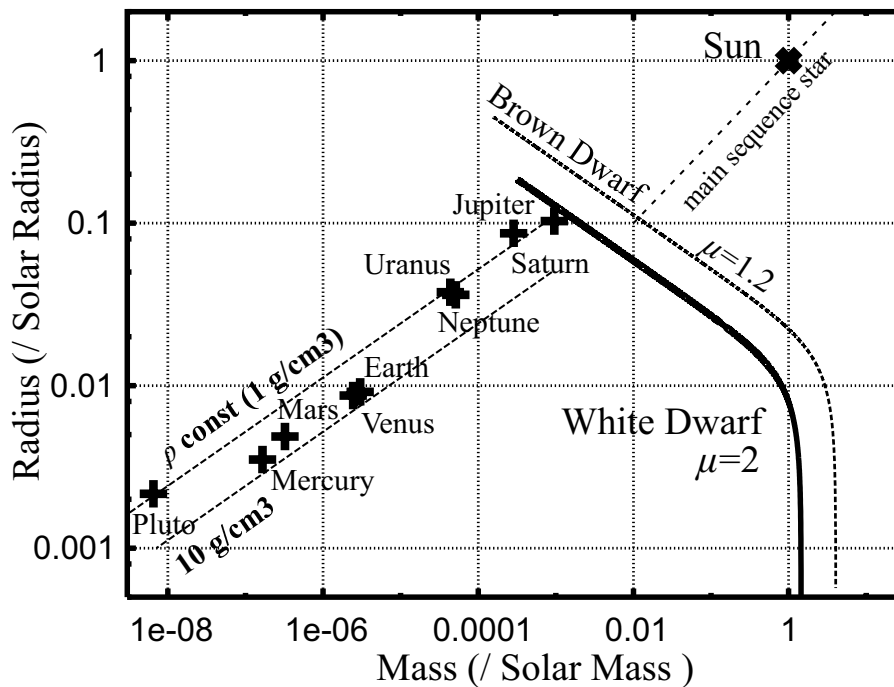


Figure 2.3: Theoretical mass-radius relations of electron-degenerate stars, represented by equation (2.10). The case of pure helium ( $\mu = 2$ ; white dwarf) and that of cosmic-abundance gas ( $\mu = 1.2$ ; brown dwarf) are plotted. The sun and solar-system planets are also plotted. Observed values of white dwarfs are given in figure 2.5.

### 2.1.3 Observation of white dwarfs

White dwarfs mainly emit blackbody radiation with a surface temperature of 5,000 – 20,000 K, exhibiting strong photo-electric absorption in the microwave to infrared band by their atmospheres of mixed hydrogen and helium. So far, a number of white dwarfs have been detected optically. For example, 2249 objects are cataloged by McCook & Sion (1999) as plotted in figure 2.4. With several systematic surveys, their local space density has been estimated to be  $0.003 \text{ stars pc}^{-3}$  (Liebert *et al.* 1988), which corresponds to  $\sim 1\%$  of the dynamical mass density in the solar neighborhood. Considering this space density and their theoretical cooling time scales, the birth rate of white dwarfs are calculated to be  $\sim 10^{-12} \text{ pc}^{-3} \text{ yr}^{-1}$ . This rate is close to the death rate of light main sequence stars (Weidemann 1977). Furthermore, about 80 % of these white dwarfs are found in the center of planetary nebulae (Drilling & Schönberner 1984); this provides the direct evidence that the progenitors of white dwarfs are light main sequence stars, such as A, F, G, and K stars (see HR diagram, figure 2.1).

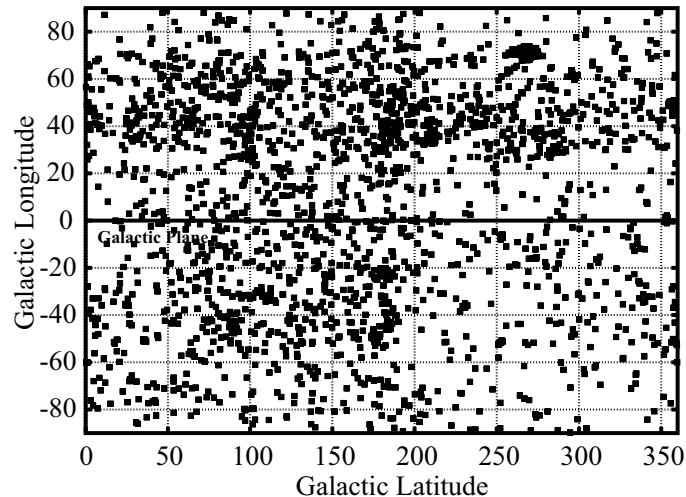


Figure 2.4: A sky distribution of white dwarfs cataloged by McCook & Sion (1999), in Galactic coordinates.

According to Stefan-Boltzmann law, a white dwarf of a surface temperature  $T_{\text{bb}}$  is expected to have a surface brightness of

$$U = \sigma_{\text{SB}} T_{\text{bb}}^4, \quad (2.11)$$

where  $\sigma_{\text{SB}}$  is the Stefan-Boltzmann constant. Since the observed flux  $F_{\text{OBS}}$  is written as

$$F_{\text{OBS}} = \frac{4\pi R_{\text{WD}}^2 U}{4\pi d^2}, \quad (2.12)$$

with  $d$  being the source distance, we can calculate the radius  $R_{\text{WD}}$  by combining equations (2.11) and (2.12), if we know  $d$ . The distance to nearby white dwarfs can be obtained by measuring trigonometric parallax, i.e., its angular shift observed at intervals of a half year, using the length from the sun to the earth as a base line. If the white dwarf forms a

binary with a main-sequence star, we can utilize various techniques in stellar astronomy to estimate the distance to the companion star (i.g. infra-red K band method, see detail in Bailey 1981; Warner 1987; Bierman *et al.* 1985).

The mass of a white dwarf,  $M_{\text{WD}}$ , can be obtained by combining the radius measurement described above and that of gravitational potential at its surface, the latter providing the ratio of mass and radius,  $M_{\text{WD}}/R_{\text{WD}}$ . There are two ways to measure the potential. One is achieved by the measurement of Einstein gravitational red shift,

$$\frac{\Delta\lambda}{\lambda} \simeq \frac{GM_{\text{WD}}}{R_{\text{WD}}c^2}, \quad (2.13)$$

where  $\lambda$  is the wave length of absorption or emission lines from a surface of white dwarf. The obtained value is usually quoted as an equivalent Doppler shift;

$$v_{\text{dop}} \equiv c \frac{\Delta\lambda}{\lambda} = 0.6362 \left( \frac{M_{\text{WD}}}{M_{\odot}} \right) \left( \frac{R_{\text{WD}}}{R_{\odot}} \right)^{-1} \text{ km s}^{-1}. \quad (2.14)$$

The second way to estimate the potential is to measure the temperature of plasmas shock-created on white dwarfs, if the matter accretion occurs onto them. Since the typical potential depth reaches hard X-ray energy, this measurement is performed in X-ray observations (Ishida 1991; Cropper *et al.* 1998; Fujimoto 1998; Ezuka and Ishida 1999; see section 2.6.2).

Through these measurements, the mean mass for isolated white dwarfs has been obtained to be a sub-solar value;  $0.6 \pm 0.1M_{\odot}$  (Koester and Weidemann 1980) and  $0.56 \pm 0.14M_{\odot}$  (Bergeron *et al.* 1992). Figure 2.5 shows the obtained masses and radii of white dwarfs (Provencal *et al.* 1998), in comparison with the theoretical mass-radius relations. Thus, the observation and calculation agree to a reasonable extent.

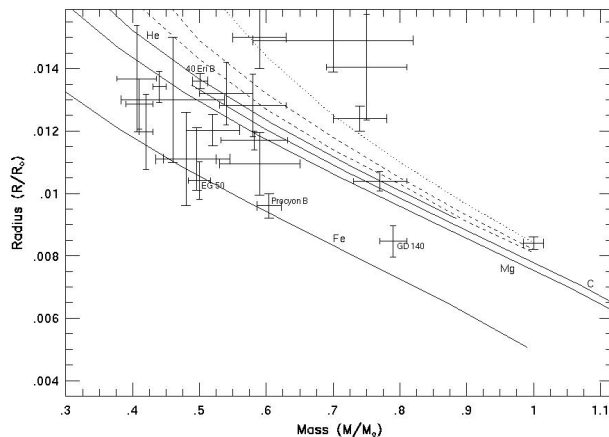


Figure 2.5: The observed mass and radius of visual white dwarf binaries and isolated white dwarfs, superposed on the theoretical mass-radius relations. Solid lines denote the zero-temperature relations by Hamada & Salpeter (1961) for different chemical compositions, and dotted lines are for a 30,000 K hydrogen atmosphere relations by Wood (1995). From Provencal *et al.* (1998).

## 2.2 White Dwarf Binaries

### 2.2.1 Observation of white dwarf binaries

Among  $\sim 2500$  white dwarfs known today, about  $2/3$  are isolated objects, while the rest are in binaries. The binaries are further divided into two subclasses; visual (or resolved) binaries, and spectroscopic and eclipsing binaries. In the former, the white dwarf can be resolved from its companion on optical images, like Sirius (Canis Major  $\alpha$ ), Procyon (Canis Minor  $\alpha$ ), Rigil (Centaurus  $\alpha$ ), Cygnus 61 etc. In the latter type, the component stars in the image are so close together that they can be identified only via spectroscopy or eclipsing light curves. Following an empirical use in astrophysics, we call the white dwarf 'primary' and the companion main-sequence star 'secondary',

The system parameters of a binary can be obtained by general motion analysis. Suppose a binary consisting of a primary (white dwarf) of mass  $M_1$  and a secondary of mass  $M_2$ . From Kepler's third law, its binary separation (the semi-major axis of the orbit)  $a$  and the orbital period  $P_{\text{orb}}$  are related as

$$\left(\frac{2\pi}{P_{\text{orb}}}\right)^2 = \frac{G(M_1 + M_2)}{a^3}, \quad (2.15)$$

which then yields

$$a = 3.5 \times 10^{10} \left(\frac{M_1 + M_2}{M_{\odot}}\right)^{1/3} \left(\frac{P_{\text{orb}}}{1\text{hr}}\right)^{2/3} \text{ cm}. \quad (2.16)$$

The radial velocity amplitude  $K$  can be written as

$$K_1 = \frac{M_2}{M_1 + M_2} a \left(\frac{2\pi}{P_{\text{orb}}}\right) \sin i \quad (2.17)$$

$$K_2 = \frac{M_1}{M_1 + M_2} a \left(\frac{2\pi}{P_{\text{orb}}}\right) \sin i, \quad (2.18)$$

where the subscripts 1 and 2 denote the primary and the secondary respectively,  $i$  is the inclination of the binary system. Using again Kepler's third law (equation 2.15), and equations (2.17) and (2.18), we can obtain a relation

$$f(M_1, M_2, i) \equiv \frac{M_1^3 \sin^3 i}{(M_1 + M_2)^2} = \frac{P_{\text{orb}} K_2}{2\pi G}, \quad (2.19)$$

where  $f(M_1, M_2, i)$  is so-called mass function of the secondary.

In the observation of white dwarfs, we can measure their orbital periods ( $P_{\text{orb}}$ ) from light curves. The observed periods of white-dwarf binaries scatter widely, over a range from an hour to a century. The values of  $K_2$  can also be measured optically by using absorption lines from photosphere of the secondary, or narrow emission lines attributed to their heated surface. Therefore, the right hand side of equation (2.19) is expressed using the observable quantities alone, and so, if  $i$  is known, we can obtain the mass ratio  $q \equiv M_2/M_1$ . We can then determine  $M_1$ , by estimating  $M_2$  from spectroscopic properties

of the secondary. In some cases,  $K_1$  can also be determined by X-ray emission lines (e.g., Cropper *et al.* 1998) or cyclotron lines (e.g., Visvanathan and Wichramasinghe 1979) from the white dwarf. In this case,  $M_1$  and  $M_2$  can be obtained separately. One of the practical problems, however, is that the inclination  $i$  can be determined precisely only for eclipsing systems, in which case we can utilize eclipsing light curves of the white dwarf by the secondary.

## 2.2.2 Cataclysmic variables

Among the white dwarf binaries, those with a very small separation, typically less than the solar radius ( $R_\odot = 7.0 \times 10^{10}$  cm), are called “close binaries.” Currently, about 300 objects are categorized in this class (Ritter and Kolb 1998).

As shown in figure 2.6, the gravitational potential of rotating two stars are connected at a point labeled  $L_1$ , called “inner Lagrangian point,” and the volumes enclosed by the two equipotential surfaces (separatrix) that just touch at  $L_1$  are called “Roche lobes.” If the separation is very close as shown in figure 2.7 case d, the secondary star fill its Roche lobe and its materials spills over via the  $L_1$  point. Thus, in close binaries, significant mass exchange often takes place. This phenomenon is called “Roche lobe overflow.”

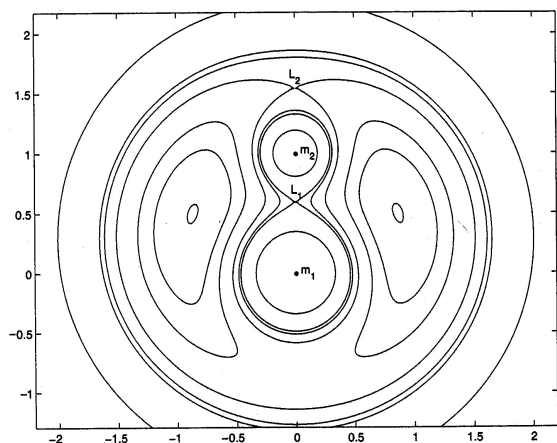


Figure 2.6: A cross section in the orbital plane of the equipotential surface for a binary system with a mass ratio  $q = 0.4$ . The two stars are fixed at  $(0, 0, 0)$  and  $(1, 0, 0)$ , so the separation is set to unity. From Hilditch (2001).

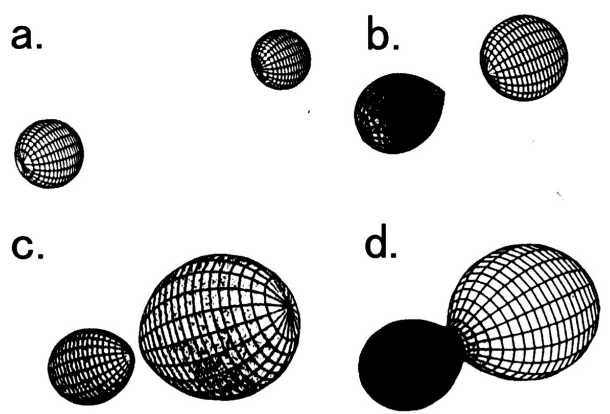


Figure 2.7: Roche lobe surfaces for four different binary-star systems. Case a shows a detached system with  $q = 0.85$ ; case b, a semidetached system with  $q = 0.3$ ; case c, a contact system with  $q = 0.4$ ; and both components are surrounded by a common envelope in case d. From Hilditch (2001).

Radiation from close binaries is mainly driven by matter accretion, i.e. by release of gravitational energies as the matter from the secondary falls onto the white-dwarf surface. Since the emission is variable in this case as the mass transfer rate changes, the mass-exchanging white-dwarf binaries are alternatively called “Cataclysmic Variables (CVs),” on which we focus from now.

### 2.2.3 Binary kinematics of cataclysmic variables

Since the accretion powered emission dominates in CVs, we cannot use the blackbody radiation to determine  $R_{WD}$ , unlike the case for isolated white dwarfs (section 2.1.3). However, the binary kinematics (section 2.2.1) instead become a powerful tool to estimate  $M_2$ , because in this case we have an additional constraint that the secondary fills its Roche lobe. The approximate formula for the radius of Roche lobe,  $R_L$ , is obtained by Paczynski (1971) as

$$\frac{R_L}{a} = \frac{2}{3^{4/3}} \left( \frac{M_2}{M_1 + M_2} \right)^{1/3}, \quad (2.20)$$

which is valid in the range of  $0 < q < 0.3$ . Combining Kepler's third law (equation 2.15) and equation (2.20), the mean density  $\bar{\rho}_2$  of a lobe-filling secondary is expressed as

$$\bar{\rho}_2 \equiv \frac{M_2}{\frac{4}{3}\pi R_L^3} = \frac{243\pi}{8G} \frac{1}{P_{\text{orb}}^2} = 1.4 \times 10^2 \left( \frac{P_{\text{orb}}}{1\text{hr}} \right)^{-2} \text{ g cm}^{-3}, \quad (2.21)$$

which lies in the range of typical low-mass main-sequence stars. From their empirical mass-radius relation (e.g., Patterson 1984),

$$\frac{R_2}{R_\odot} = \left( \frac{M_2}{M_\odot} \right)^{0.88}, \quad (2.22)$$

and equation (2.21) under the Roche-lobe filling condition of  $R_L = R_2$ , we can obtain the mass of the secondary as

$$M_2 = 0.07 M_\odot \left( \frac{P_{\text{orb}}}{1\text{hr}} \right)^{1.22}. \quad (2.23)$$

Thus, we can estimate the mass of the secondary in CV from its orbital period using equation (2.23).

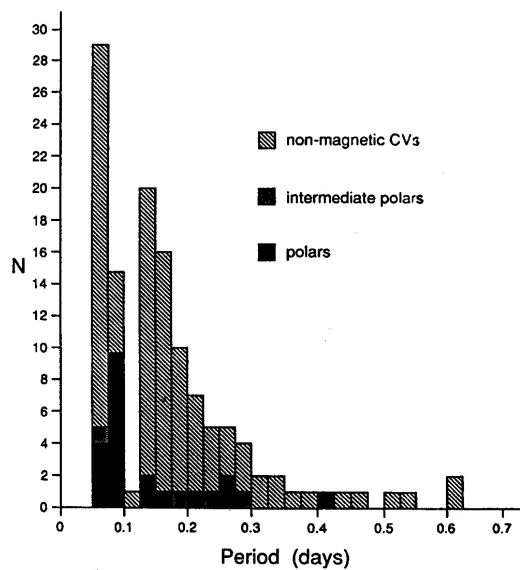


Figure 2.8: The period distribution of CVs from Cropper (1990), originally tabulated by Ritter (1987).

In the wide distribution of orbital periods for white-dwarf binaries (section 2.2.1), those for CVs are naturally clustered in the shortest end, ranging from 8 hr down to  $\sim 79$  minutes as shown in figure 2.8. The period gap, lying on  $\sim 2\text{--}3$  hr in this figure, may be related to binary evolution of CVs (Rappaport *et al.* 1983; Spruit *et al.* 1983; Hameury *et al.* 1988; Howell *et al.* 2001). This distribution, in combination with equation (2.23), indicates the secondary mass in the range of  $0.1 M_{\odot} - 0.5 M_{\odot}$ . Since they are above the lower mass limit ( $0.08 M_{\odot}$ ) of the hydrogen-burning main-sequence star (see section 2.1.1), the secondaries are thought to be main sequence stars, probably not degenerate brown dwarfs.

We cannot use this method to determine the mass of the white dwarf,  $M_1$ , principally because of no volume constraint. Instead of this, we can obtain  $M_1$  from equation (2.19). However,  $i$  has a large uncertainty for non-eclipsing systems, and the measurement of  $K_2$  in CV is difficult because the accretion powered emission overwhelms the emission from the secondary. As a result,  $M_1$  has been measured for only a few CVs;  $0.66 M_{\odot}$  for MR Ser,  $0.38 M_{\odot}$  for ST LMi,  $0.99 M_{\odot}$  for AM Her, and  $0.58 M_{\odot}$  for QQ Vul (Mukai and Charles 1987). These values are consistent with masses derived from the another method of mass determination by the gravitational measurement with X-ray observation (section 2.1.3 and section 2.6.2), and are also consistent with the mass distribution for isolated objects (section 2.1.3). Thus,  $M_1$  and  $M_2$  have typically sub-solar values. Consequently, the binary separation,  $a$ , of a CV is comparable to the solar radius (equation 2.16), and the secondary radius is close to  $\sim 0.4a$  (equation 2.20).

## 2.3 Magnetic Field in white dwarfs

### 2.3.1 Magnetism of white dwarfs

Among over 2000 white dwarfs, about 5.1% (McCook & Sion 1999) or 4.3% (Schmidt & Smith 1995) of objects have observable strong magnetic fields of  $3 \times 10^4 - 10^9$  G (Wickramasinghe & Ferrario 2000, and references therein). They are called magnetic white dwarfs. Very strong fields have also been recognized in CVs, after Tapia (1977) found a strongly circularly-polarized optical emission from a CV named AM Herculis. These CVs with fields of  $10^{5-8}$  G are categorized as ‘‘Magnetic Cataclysmic Variables (MCVs).’’ About 25 % of 300 CVs are classified as MCVs, and the rests are called non-magnetic cataclysmic variables, or ‘‘dwarf nova.’’ This percentage of MCVs is higher than that for isolated magnetic white dwarfs, possibly because of observational selection effects (e.g., Chanmugam 1992). We show in figure 2.9 the distribution of observed magnetic fields for isolated white dwarfs and MCVs (Wickramasinghe & Ferrario 2000), although both distributions are subject to selection biases, particularly toward lower fields below  $\sim 10^6$  G, where the field determination becomes difficult. The obtained mean value is 16 MG for the former, and 38 MG for the latter.

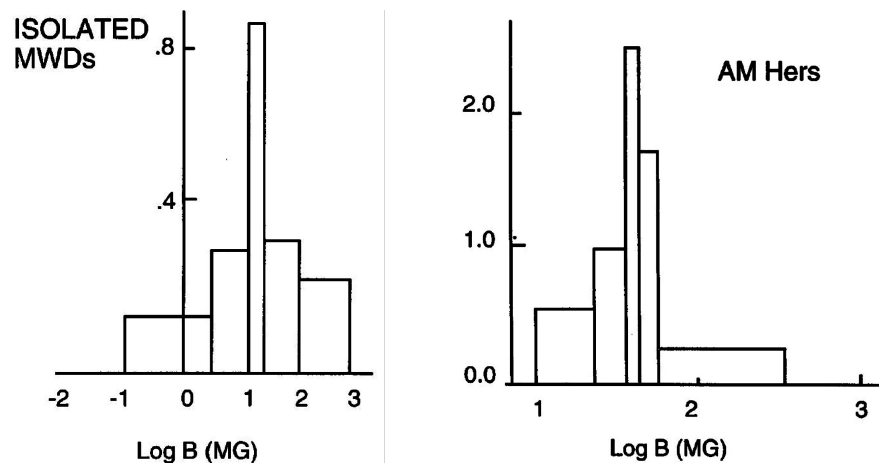


Figure 2.9: The distribution of magnetic field strength for isolated magnetic white dwarfs (*left*), and magnetic cataclysmic variables (*right*). They are not corrected for selection effects. From Wickramasinghe & Ferrario (2000).

The origin of strong magnetic field observed in white dwarfs is still poorly understood. One possibility is that their strong fields are inherited from their progenitors, and decay of the magnetic flux causes the large scatter in field strength. The most likely candidate for the progenitor of magnetic white dwarfs is the early-type “magnetic” main-sequence stars, called Ap and Bp stars. In fact, the surface magnetic fluxes of magnetic white dwarfs,  $\sim R_{\text{WD}}^2 B \sim 10^{24-26}$  G cm<sup>2</sup>, are similar to those of Ap/Bp stars. In support of this, the space density of the former can be estimated, by their percentage ( $\sim 5\%$ ) in number and that for the entire white dwarfs (section 2.1.3), as  $\sim 1.5 \times 10^{-4}$  pc<sup>-3</sup>; this is consistent with those of the latter (e.g., Angel *et al.* 1981). Furthermore, the magnetic white dwarfs have slightly higher masses than non-magnetic objects (Libert 1988; Sion *et al.* 1988; Vennes 1999). This suggests that they have massive and younger progenitors, i.e. A or B stars, as compared to the average white dwarfs. These pieces of observational evidence support the fossil origin for the field of white dwarfs. Presumably, the magnetic field is sustained by persistent ring current in the white-dwarf interior. However, the spread of their field distribution (figure 2.9) is two order of magnitude larger than those for the progenitors,  $\sim 10^2 - 10^4$  G. Furthermore, if the magnetic decay is due to Ohmic loss, its time scale amounts to  $\sim 10^9-10^{10}$  years (Mastel 1965; Chanmugam & Gabriel 1972; Fontaine *et al.* 1973; Wendell *et al.* 1987), which is longer than their cooling time scale. Thus, the concept of fossile magnetic field cannot explain all the aspects of the magnetic fields of white dwarfs.

Another possibility is that the magnetic fields of white dwarfs originate from spin-aligned ferromagnetism of hydrogen near the surface of white dwarfs (Ichimaru 1997). This mechanism may be able to produce a field strength of  $10^{5.5-7.5}$  G. Yet, a third alternative is thermal origin, as has first been constructed to explain magnetic fields of neutron stars (Mestel 1961; Blanford *et al.* 1983), although this is probably insufficient for white dwarfs (Blanford *et al.* 1983; Moss 1986).

## 2.3.2 Measurements of magnetic fields of white dwarfs

There are three methods to measure the magnetic field strength of white dwarfs; cyclotron harmonics, Zeeman splitting spectroscopy, and halo Zeeman lines. These measurements are all achieved in the infrared to optical band. The former two methods are used for both isolated white dwarfs and MCVs, although the cyclotron technique is mainly used for MCVs and the Zeeman spectroscopy for isolated objects. The halo Zeeman method is applicable only to a limited subset of MCVs.

### 1) cyclotron harmonics

The cyclotron harmonics appear when free electrons are placed in a magnetic field. The kinetic energy of electrons perpendicular to the field is quantized into Landau levels;

$$E_{\text{cyc}} = \hbar\omega_c \left( n + \frac{1}{2} \right) \quad (2.24)$$

$$= 0.12 \left( \frac{B}{10^7 \text{G}} \right) \left( n + \frac{1}{2} \right) \text{eV}, \quad (2.25)$$

where  $\omega_c \equiv \frac{eB}{m_{ec}}$  is the cyclotron frequency,  $\hbar$  is the Dirac constant (section 2.1.2), and  $n$  is the principal quantum number. For white dwarfs, this can be observed as line emissions, emergent from optically-thin hot atmospheres near their magnetic poles. For MCVs with typical field of  $\sim 30$  MG (figure 2.9), the fundamental harmonic corresponds to 0.3 eV, and higher harmonics come into the optical band as shown in figure 2.10. For reference, neutron stars exhibit cyclotron harmonics in the hard X-ray band, since they have field strength of about  $10^{12}$  G. As shown in figure 2.11, the resonance in neutron stars appears in absorption rather than emission, because plasmas on the neutron-star surface are optically thick.

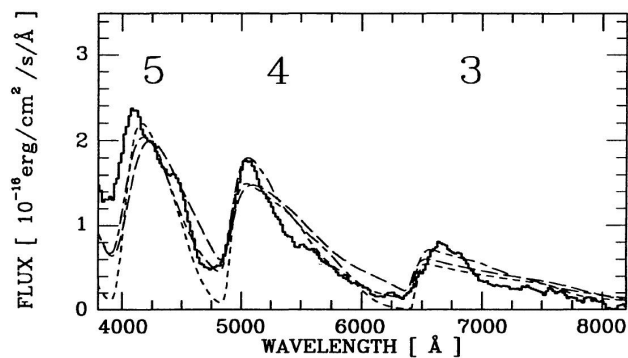


Figure 2.10: An example of cyclotron humps in MCV. The average spectrum of UZ For (heavy line), with model calculations for a fixed viewing angle of  $70^\circ$  to the field (short dash for temperature of 5 keV and  $B = 53.5$  MG; long dash for temperature of 10 keV and  $B = 53$  MG). The third, fourth, and fifth cyclotron harmonics can be seen (Schwope *et al.* 1990).

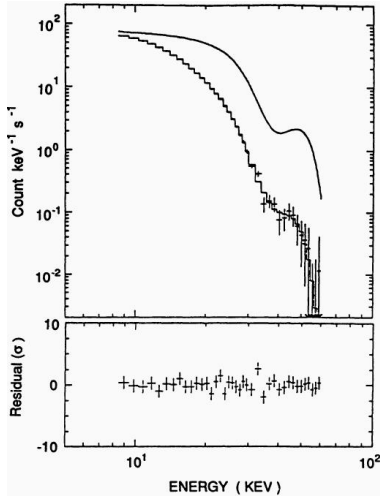


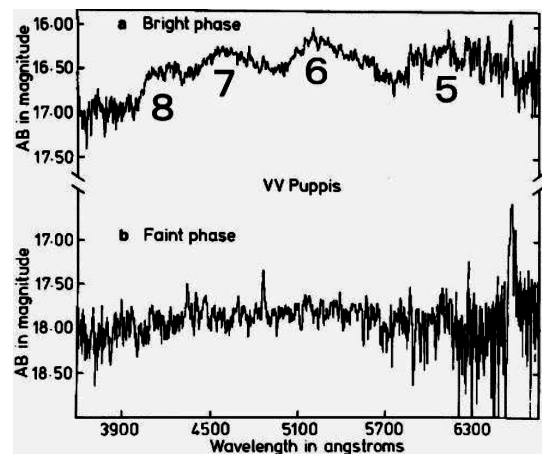
Figure 2.11: An example of cyclotron absorption feature in the hard X-ray energy spectrum of neutron star binary, Her X-1, obtained by *Ginga* (Mihara *et al.* 1990). The solid curve is the best-fit incident spectrum corrected for the detector response.

When bulk doppler effect in the hot plasma is taken into account, the cyclotron harmonic energies become (Bekefei 1966)

$$\omega_n (\equiv E_{\text{cyc}}/\hbar) = \frac{n}{(1 - \beta_{\parallel} \cos \theta)} \frac{\omega_c}{\gamma}, \quad (2.26)$$

where  $\beta$  is the electron bulk velocity in light units, the subscript  $\parallel$  means the parallel component to the field,  $\theta$  is the viewing angle to the field line,  $\gamma = \sqrt{1 - \beta^2}$ , and  $\omega_c/\gamma$  is the fundamental cyclotron frequency for relativistic electrons of masses  $\gamma m_e$ . Since  $\beta_{\parallel}$  changes significantly along the hard X-ray emission region on the magnetic poles of an MCV, the cyclotron lines are generally broadened, although this effect vanishes if the accretion column is viewed nearly side-on ( $\theta \sim 90^\circ$ ). As a result, the cyclotron lines are often smeared out when the magnetic poles of an MCV is viewed pole-on, as shown in figure 2.12. Even when the poles are viewed nearly side-on ( $\theta \sim 90^\circ$ ), the cyclotron lines are broadened by thermal Doppler effects (expressed by  $\gamma$  in equation 2.26) in the hot plasmas of temperature 10 – 30 keV. This broadening reaches  $\sim 1000 \text{ \AA}$  in optical band.

Figure 2.12: Side-on (denoted as *a* Bright phase) and pole-on (denoted as *b* Faint phase) spectra of VV Puppis in its 1979 low state (Visvanathan and Wickramasinghe 1979). The pole-on spectrum shows broad cyclotron emission features centered at 6200, 5300, 4500, and 4100  $\text{\AA}$ , corresponding to harmonic numbers 5, 6, 7, and 8 respectively, for a field intensity of 32 MG. The lines are smeared out in the pole-on spectrum.



## 2) Zeeman splitting

The Zeeman effect is caused by electrostatic interactions between magnetic momenta of bound electrons and the external magnetic field. The splitting energy is described as

$$\Delta E_{\text{Zeeman}} = \frac{e\hbar}{2m_e c} B = 5.8 \times 10^{-2} \left( \frac{B}{10^7 \text{G}} \right) \text{eV}. \quad (2.27)$$

Since we can resolve a splitting of some hundreds  $\text{\AA}$  ( $\sim 10^{-2}$  eV) in the optical band, the Zeeman spectroscopy becomes a powerful method for investigating the field structure of white dwarfs. Usually, the Zeeman technique is applied to absorption lines, produced by hydrogen or helium in the atmosphere of white dwarfs. An example for isolated white dwarfs is shown in figure 2.13. For MCVs, this method is usable during low states, when the photospheric emissions from the white dwarf dominate over the accretion-powered radiation. Some MCVs show photospheric Zeeman lines and cyclotron lines simultaneously as in figure 2.14. This usually occurs when the system is in a state of intermediate activity so that the cyclotron component is strong but does not overwhelm the contribution from the photosphere of white dwarf.

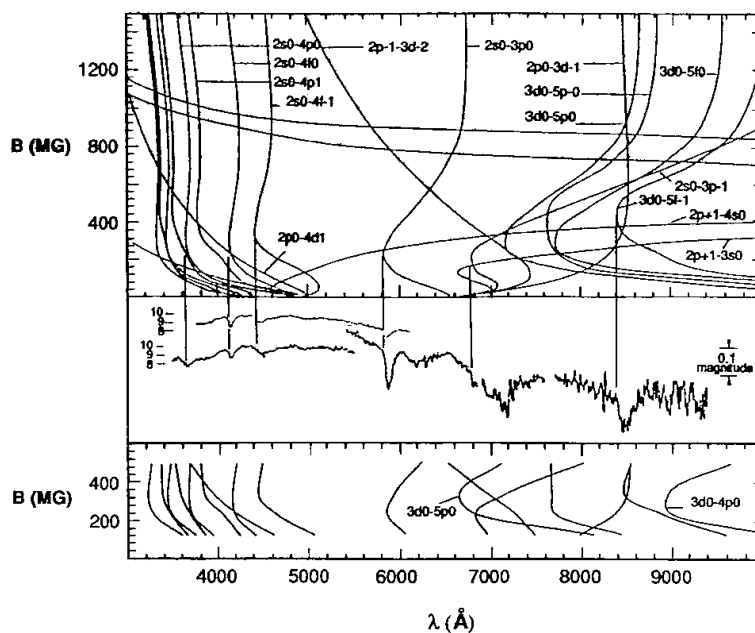


Figure 2.13: Observation of a magnetic isolated white dwarf, Gew+70°8247, by Angel *et al.* (1985) compared with the calculated field dependence of Zeeman components of hydrogen. The obtained magnetic field strength is about 320 MG.

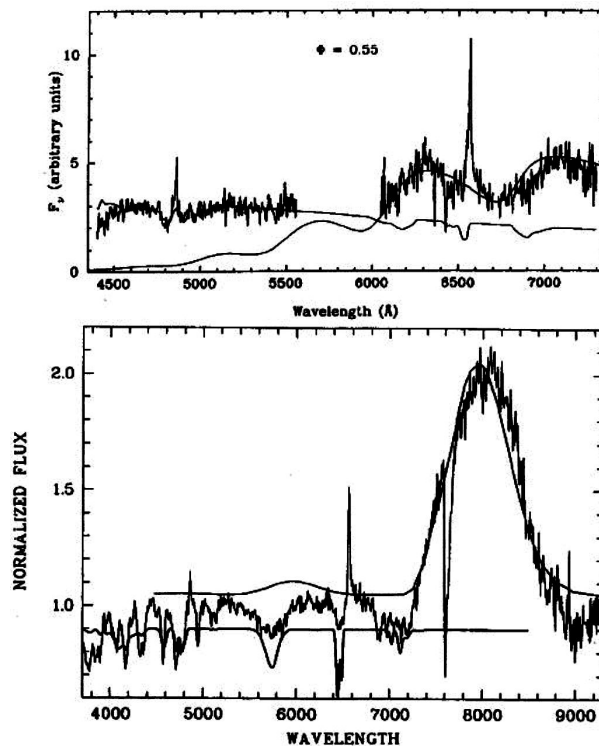


Figure 2.14: (*top*) An optical spectrum observed from an MCV, V834 Centauri, showing both photospheric Zeeman ( $B = 31$  MG) and cyclotron lines ( $B = 23 \pm 1$  MG), compared with models (Ferrario *et al.* 1992). (*bottom*) That of 1RXS J012851.9-233931 showing a strong cyclotron line ( $B = 45 \pm 1$  MG) in the red, and a photospheric Zeeman split in  $H\beta$  and  $H\alpha$  lines with  $\langle B \rangle = 36 \pm 1$  MG (Schwope *et al.* 1999).

### 3) Halo Zeeman lines

For MCVs, another method by “halo” Zeeman lines is available to estimate the magnetic field strength. This method utilizes the fact that accretion-powered hard X-ray from an MCV surface (see section 2.4.4) are reprocessed by the accreting material, and produce optical emission lines. Thus, this method employs optical emission lines, unlike the photospheric Zeeman technique which utilizes absorption lines as shown above. This can be seen only when the emission region is viewed nearly perpendicular to the field direction. There is generally very close agreement between fields determined using the cyclotron lines and the halo Zeeman features. For example, the field strength of V834 Centauri deduced by the halo Zeeman method,  $B = 23$  MG, is very close to that determined by cyclotron measurements,  $B = 23$  MG (Wichramasinghe *et al.* 1987).

## 2.4 Magnetic Cataclysmic Variables

### 2.4.1 Polars and intermediate polars

MCVs are further divided into two subgroups, polars (or “AM Her type objects”) and intermediate polars (or “DQ Her type objects”). The former show strong circular and linear polarizations (after which the name of “polar” is given) in the optical band, and the rotation period,  $P_{\text{spin}}$ , is synchronized with  $P_{\text{orb}}$  as shown in figure 2.15. On the other hand, the latter show no optical polarization, and their  $P_{\text{spin}}$  is shorter than  $P_{\text{orb}}$ . With many optical to X-ray observations, 50 polars and 23 intermediate polars have been known today among more than 300 CVs (Ritter & Kolb 1998). Table 2.1 and 2.2 summarize basic parameters of the known polars and intermediate polars, respectively. The most important *intrinsic* difference between the two subclasses is the magnetic field strength; polars have field strength exceeding  $10^7$  G, while intermediate polars have  $10^{5-6}$  G. The polarized optical emission from polars is undoubtedly due to their stronger magnetic fields. In addition, the phase-locked rotation of polars is thought to be a result of magnetic braking; the magnetic fields of intermediate polars are probably too weak to realize the phase-locking.

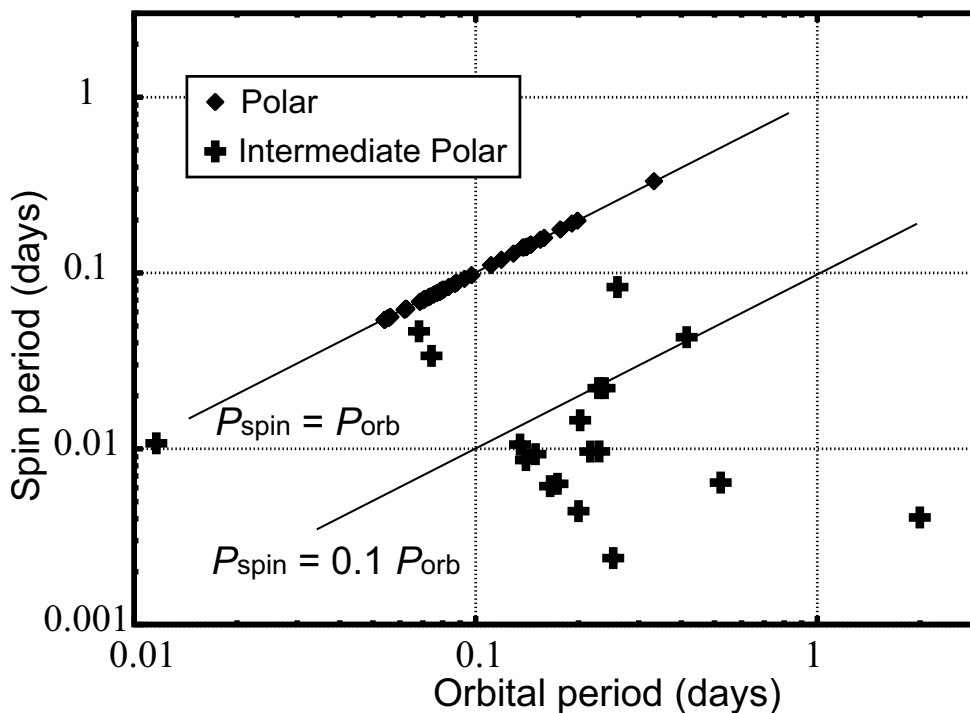


Figure 2.15: Spin periods vs. orbital periods for polars and intermediate polars. From tables 2.1 and 2.2.

Table 2.1: Basic properties of currently known polars.

Object <sup>a</sup> name	Other <sup>a</sup> designation	$P_{\text{orb}}$ (days)	$B$ (MG)	$i$ ( $^{\circ}$ )	$\beta$ ( $^{\circ}$ )	$d$ (pc)	Ref <sup>b</sup>
V1309 Ori	J0515+0104	0.332613		$\sim 80$	$\sim 30$	$> 500$	28,40
V895 Cen	J1429-3804	0.198553					
J0203+2959		0.1913					
J1313-32		0.1770					
VY For	For 1, EXO 0329-2607	0.1586		$9 \pm 3$	$\sim 9$		7
<b>QQ Vul</b>	1E 2003+225	0.154520		$60 \pm 14$	$19 \pm 9$	$\geq 400$	14,16,33,35,45
J2316-05		0.1451					
J1007-20		0.1444					
MN Hya	J0929-2404	0.1412				300–700	40
<b>V1432 Aql</b>	J1940-1025	0.140235,0.140626				180–250	40
<b>BY Cam</b>	H 0538+608	0.13979,0.138434	$40.8 \pm 1.5$	$50 \pm 10$	$38 \pm 8$		12,17
V1500 Cyg	N Cyg 1975	0.139613,0.137171	14, 14.5			$1200 \pm 200$	30,36
<b>AM Her</b>	J1816+4952	0.128927		$52 \pm 5$	$66 \pm 5$	75	3,16,29,38,49,54
J0501-03		0.1188					
V349 Pav	DR V211b	0.1109					
<b>QS Tel</b>	J1938-4612	0.097187	60				24
UW Pic	J0531-4624	0.09268					
<b>UZ For</b>	EXO 0333-255	0.087865	53, 56, 75	$\sim 88$	$\sim 14$	250	6,20,21,27,41
EU Cnc	CV in M 67	0.0871					
<b>HU Aqr</b>	J2107-0517	0.086820	37				43
J1724+41		0.0833					
AR UMa	1ES1112+4314	0.08052		$50 \pm 10$	$23 \pm 13$		48
<b>WW Hor</b>	EXO 0234-523	0.080199		$\sim 74$	$\sim 48$	500	2,5
AN UMa	PG 1101+453	0.079753	$35.8 \pm 1.0$	$65 \pm 20$	$20 \pm 5$	$\geq 270$	16,17,34
<b>EK UMa</b>	1E 1048+542	0.07948	$47 \pm 3$	$56 \pm 19$	$56 \pm 19$		16,18,32
<b>ST LMi</b>	CW 1103+254	0.079089	19, 12	$64 \pm 5$	$141 \pm 4$	128	16,23,39,47
<b>BL Hyi</b>	H 0139-68	0.078915	30, 23	$70 \pm 10$	$153 \pm 10$	128	15,16,26,53
MR Ser	PG 1550+191	0.078798	$26, 24.6 \pm 0.6$	$43 \pm 5$	$38 \pm 5$	112	16,17,44,46,56
<b>V884 Her</b>	J1802+1804	0.07850					
<b>V2301 Oph</b>	1H 1752+081	0.078450	7	77		$150 \pm 27$	25,40
J2115-5840		0.07691					
CE Gru	Gru V1	0.0754					50
J1002-19		0.0736					
EP Dra	H 1907+690	0.072656					
RS Cae	J0453-4213	0.0708					
J0953+14		0.0708					
<b>V834 Cen</b>	1E 1405-451	0.070498	$31, 22 \pm 2$	$45 \pm 9$	$25 \pm 5$	86	8,16,22,31,42
<b>VV Pup</b>	J0815-1903	0.069747	31.7, 55	$76 \pm 6$	$152 \pm 6$	145	4,16,51,52,55
<b>J1957-5738</b>		0.068625					
EU UMa	RE J1149+28	0.06260					
V347 Pav	J1844-7418	0.062553					
<b>DP Leo</b>	1E 1114+182	0.062363	$31, 59, 44.0 \pm 1.4$	$76 \pm 10$	$103 \pm 5$	$\geq 380$	9,10,16,17,19
<b>CP Tuc</b>	J2315-5910	0.061834					
<b>EF Eri</b>	2A 0311-227	0.056266	16.5, 21	$58 \pm 12$	$27 \pm 18$	$\geq 89$	1,11,16,26
J0153-59		0.0556					
FH UMa	J1047+6335	0.0556					
<b>J1015+0904</b>		0.055471		$55 \pm 5$	$43 \pm 7$		13
EV UMa	RE J1307+53	0.055338					
J2022-3954		0.054179					
J0132-6554		0.054049					

<sup>a</sup> From [37] Ritter and Kolb (1998); <sup>b</sup> References. See the foot of the next page.

**Footnote for table 2.1**

**References:** [1] Achilleos et al (1992); [2] Bailey et al (1988); [3] Bailey et al (1991); [4] Barrett and Chanmugam (1985); [5] Beuermann et al (1986); [6] Beuermann et al (1988); [7] Beuermann et al (1989a); [8] Beuermann et al (1989b); [9] Biermann et al (1982); [10] Biermann et al (1985); [11] Boley, private communication in Griffiths et al (1979); [12] Bradt et al (1988); [13] Burwitz et al (1998); [14] Catalan et al (1999); [15] Cropper (1982); [16] Cropper (1988b); [17] Cropper et al (1988); [18] Cropper et al (1989); [19] Cropper and Wickramasinghe (1993); [20] Ferrario et al (1988); [21] Ferrario et al (1989); [22] Ferrario et al (1992); [23] Ferrario et al (1993); [24] Ferrario et al (1994); [25] Ferrario et al (1995a); [26] Ferrario et al (1995b); [27] Giommi et al (1987); [28] Harrop-Allin et al (1997); [29] Latham et al (1981); [30] Lance et al (1988); [31] Mason et al (1982); [32] Morris et al (1987); [33] Mukai et al (1988); [34] Mumford (1976); [35] Nousek et al (1982); [36] Patterson (1979); [37] Ritter and Kolb (1998); [38] Schmidt et al (1981); [39] Schmidt et al (1983); [40] Schmidt and Stockman, ApJ 548, 410, 2001 [41] Schwobe et al (1990); [42] Schwobe and Beuermann (1990); [43] Schwobe et al (1993a); [44] Schwobe et al (1993b); [45] Schwobe et al (2000); [46] Stockman et al (1981); [47] Stockman et al (1982); [48] Szkody et al (1999); [49] Tapia (1976); [50] Tuohy et al (1987); [51] van Gent (1931); [52] Wickramasinghe and Meggitt (1982); [53] Wickramasinghe et al (1984); [54] Wickramasinghe and Martin (1985); [55] Wickramasinghe et al (1989); [56] Wichramasinghe et al (1991a);

Table 2.2: Basic properties of currently known intermediate polars.

Object name	Other designation	$P_{\text{spin}}$ (days)	$P_{\text{orb}}$ (days)	$d$ (pc)	Ref.
<b>AE Aqr</b>	1ES 2037-0102	0.0003828326	0.411655	90	15
V533 Her		0.0044189605	$\sim 0.2$	1000	15
<b>DQ Her</b>		0.0008225162	0.1936212	420	15
H0253+193		0.0023877315	0.2527	200	15
<b>GK Per</b>		0.00406645	1.99680	490	15
YY Dra	2A 1150+72	0.00612532	0.165	155	15
V471 Tau		0.00641939	0.52118321	45	15
<b>V1223 Sgr</b>	4U 1849-31	0.00862854	0.140244	400, 600	2,12,15,18,27
<b>AO Psc</b>	H2252-935	0.00931948	0.149627	250, 88	15,19,20,28
<b>PQ Gem</b>	RE 0751+144	0.0096459939	0.216459	400	9,15,16,22,23
<b>BG CMi</b>	3A 0729+103	0.0105729	0.134749	500	15
<b>J1712-2414</b>	Oph 3	0.010737	0.01161		6,7,15,25
<b>FO Aqr</b>	H2215-086	0.01451911	0.20206	300	14,15,21,24,26,29
<b>TV Col</b>	2A 0526-328	0.02211	0.228600	400, 160	3,10,15
<b>TX Col</b>	H0542-407	0.02212	0.23825	500, 180	5,13,15
VZ Pyx	H0857-242	0.03377	0.0742	250	15
<b>V1062 Tau</b>	H0459+246	0.04313	0.41458	1100	15
<b>EX Hya</b>		0.0465465	0.06823383	100, 130	4,11,15
TW Pic	H0534-581	0.08319	$\sim 0.26$	500	15
<b>V405 Aur</b>	J0558+535	0.006313154	0.173455		1,8,15,17
<b>J1914+2456</b>					
<b>XY Ari</b>		0.00238773	0.2526505		30,31

**References:** [1] Allan et al. MNRAS,279,1345 (1996); [2] S.van Amerongen et al. MNRAS 228, p377 (1987); [3] T.Augusteijn et al. A&AS 107 p219 (1994); [4] I. A. Bond and R. V. Freeth, (1988); [5] Buckley et al., A&A 344,376 (1989); [6] D.A.H.Buckley et al. MNRAS 275 1028 (1995); [7] D.A.H.Buckley et al. MNRAS 287,117 (1997); [8] Haberl et al. A&A,291,171 (1994); [9] C.Hellier, MNRAS 288 p817 (1997); [10] C.Hellier et al. MNRAS, 248,p5 (1991); [11] Hellier and Spoats (1992); [12] F.Jablonsky et al. ApJ 323,p672 (1987); [13] A.J.Norton et al.MNRAS 289,362 (1997); [14] J.Patterson, IBVS 3264 (1988); [15] Patterson 1994, and references therein; [16] S.B.Potter, MNRAS, 285, p82 (1997); [17] Skillman.D. et al, PASP,108,130 (1996); [18] J.E.Steiner et al. ApJ 249, L21 (1981); [19] J.Kaluzny et al. IBVS 3145 (1988); [20] M.Kubiak, AcA, 34, p397 (1984); [21] A.Kruszewski et al. AcA, 43, p127 (1993); [22] Mason, K. O., MNRAS,285, p493 (1997); [23] S.B.Potter, MNRAS, 285, p82 (1997); [24] I.Semeniuk et al. AcA,38,p49 (1988); [25] H.Vath, A&A, 317, 476 (1997); [26] A.W.Shafter et al. MNRAS,228,p193 (1987); [27] B.Warner et al. MNRAS 206, p261 (1984); [28] H.Woerd et al. A&A, 131, p137 (1984); [29] E.Zhang et al. IBSconf, 358 (1994); [30] Kamata Y. et al. ApJ 379, L65 (1991); [31] Takano et al. IAU C., 4745, 1 (1989).

## 2.4.2 Mass accretion onto Magnetic Cataclysmic Variables

In an MCV, the mass accretion from the secondary onto the white dwarf occurs via Roche lobe overflow. As shown in figure 2.16, the mass transfer rate in MCVs is typically  $\dot{M} \sim 10^{16} \text{ g s}^{-1}$ , or  $10^{-10} M_{\odot} \text{ yr}^{-1}$ .

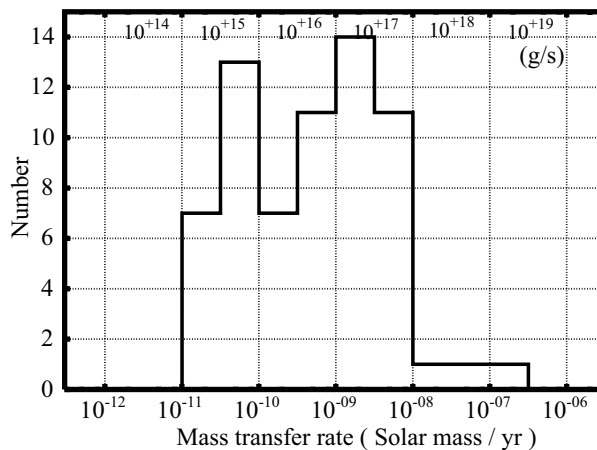


Figure 2.16: The distribution of the estimated mass transfer rates for MCVs. Originally tabulated by Patterson (1984).

The falling gas has too much angular momentum to accrete directly, so that an accretion disk is formed around the white dwarf. As the gas falls inward, it reaches the point  $R_A$ , called “Alfvén radius”, where the kinetic energy density of the gas  $P_{\text{ram}} \equiv \rho u^2$  (where  $\rho$  and  $u$  are the local gas density and the velocity) is equal to the magnetic energy density  $P_{\text{mag}} \equiv B^2/8\pi$ . The dipole-like magnetic field of white dwarf can be described as

$$B(r) \simeq \frac{\mu_m}{r^3}, \quad (2.28)$$

where  $r$  is the distance from the center of the white dwarf, and  $\mu_m$  is its magnetic moment, related to the surface magnetic field  $B_s$ , as

$$\mu_m \simeq 10^{33} \left( \frac{B_s}{10^6 \text{ G}} \right) \left( \frac{R_{\text{WD}}}{10^9 \text{ cm}} \right)^3 \text{ G cm}^3. \quad (2.29)$$

Since the gas velocity  $v(r)$  becomes simply the free-fall velocity  $\sim (2GM_{\text{WD}}/r)^{1/2}$ , the Alfvén radius can be calculated as

$$R_A = 2.7 \times 10^{10} \left( \frac{\mu_m}{10^{33} \text{ G cm}^3} \right)^{4/7} \left( \frac{M_{\text{WD}}}{M_{\odot}} \right)^{-1/7} \left( \frac{\dot{M}}{10^{16} \text{ g s}^{-1}} \right)^{-2/7} \text{ cm}. \quad (2.30)$$

For  $r \lesssim R_A$ , the accretion stream is strongly affected by the magnetic pressure, and the accretion disk becomes disrupted at  $\sim 0.5R_A$  (Lamb 1988). Since this becomes comparable to the binary separation in the case of polars (equation 2.16), a polar system generally lacks an accretion disk. In contrast, intermediate polars are thought to have accretion disks, because their Alfvén radii are much smaller than their binary separations. The schematic view of mass accretion in polars and intermediate polars is shown in figure 2.17.

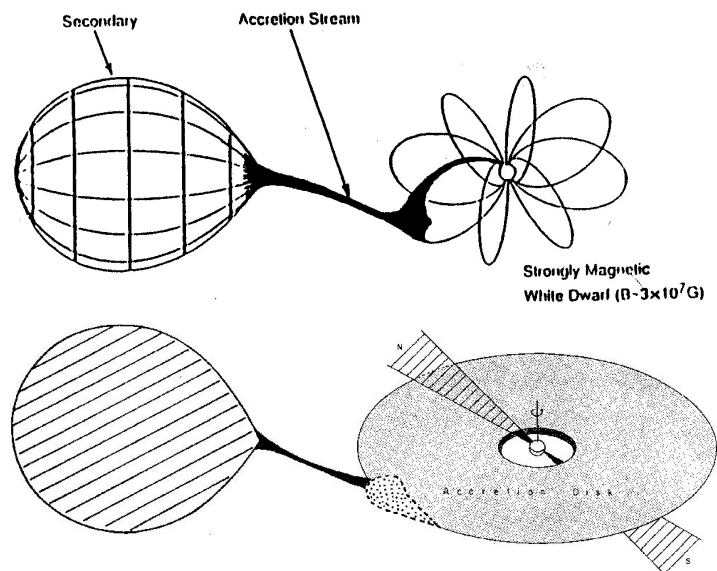


Figure 2.17: A schematic view of mass accretion in a polar system (top; Patterson 1994) and an intermediate polar system (bottom; Cropper 1990).

Inside the Alfvén radius, the infalling gas is guided along field lines to accrete radially onto the magnetic poles of white dwarf as shown in figure 2.18. It is considered that the mass accretion tends to occur onto both magnetic poles in the case of intermediate polars, whereas one-pole accretion is thought to occur sometimes in polars. The accreting flow becomes super-sonic near the white dwarf, having a free-fall velocity as

$$\begin{aligned}
 u_{\text{ff}} &= \sqrt{\frac{2GM_{\text{WD}}}{R_{\text{WD}}}} \\
 &= 3.6 \times 10^8 \left(\frac{M_{\text{WD}}}{0.5M_{\odot}}\right)^{1/2} \left(\frac{R_{\text{WD}}}{10^9\text{cm}}\right)^{-1/2} \text{ cm/s}.
 \end{aligned}
 \tag{2.31}$$

Therefore, we expect a standing shock to be produced near the white dwarf surface.

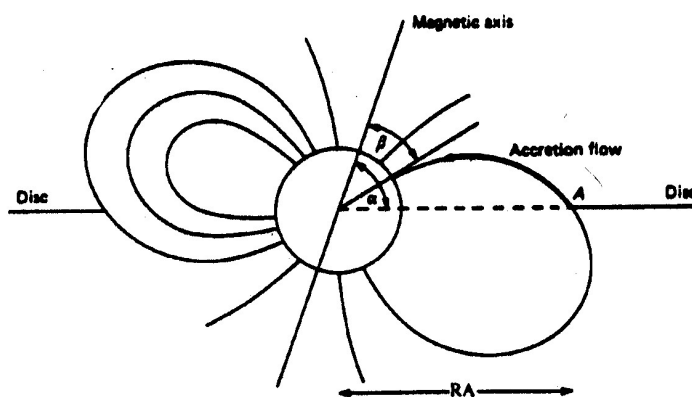


Figure 2.18: A schematic view of the mass accretion from a disk to a magnetic pole of a white dwarf. From Frank, King, and Raine (1985).

### 2.4.3 Shock discontinuity of the accretion flow

In crossing the shock front, the well-aligned bulk flow of pre-shock matter is randomized, so that its motion energy is converted into thermal energies to heat up the gas. Thus, the temperature  $T$ , the density  $\rho$ , and the bulk velocity  $u$  change discontinuously there. Let us consider an ideal gas with specific heat ratio (or adiabatic index) of  $\gamma$ . In the limit of strong shock, the Rankine-Hugoniot relations that describe the discontinuity conditions gives

$$\begin{aligned} u^{\text{fs}} &= \frac{\gamma + 1}{4} (u^{\text{fs}} - u^{\text{sh}}) + \sqrt{\left\{ \frac{\gamma + 1}{4} (u^{\text{fs}} - u^{\text{sh}}) \right\}^2 + (c_s)^2} \\ &\sim \frac{\gamma + 1}{2} (u^{\text{fs}} - u^{\text{sh}}), \end{aligned} \quad (2.32)$$

where superscript “fs” and “sh” denote front and back side of the shock, respectively, and  $c_s$  is the pre-shock sound velocity ( $\sqrt{\gamma kT}$ ). Thus, we obtain

$$u^{\text{sh}} = \frac{\gamma - 1}{\gamma + 1} u^{\text{fs}}. \quad (2.33)$$

In the same way, the jumps in  $\rho$  and  $kT$  are given by

$$\rho^{\text{sh}} = \frac{\gamma + 1}{\gamma - 1} \rho^{\text{fs}} \quad (2.34)$$

$$kT^{\text{sh}} = \frac{2\gamma(\gamma - 1)}{(\gamma + 1)^2} \left( \frac{u^{\text{fs}}}{c_s^{\text{fs}}} \right)^2 kT^{\text{fs}}, \quad (2.35)$$

where  $k$  is the Boltzmann constant.

In the mass accretion onto MCVs, we assume the gas to be an ideal one with  $\gamma = 3/5$ . Because the pre-shock temperature (typically  $\sim 50$  eV) is much lower than the kinetic energy of its bulk motion ( $\sim$  a few tens keV), the pre-shock stream is highly supersonic, and the shock must be a strong one. Since the pre-shock velocity reaches  $u_{\text{ff}}$  which is described by equation (2.31), the matter is shock-heated to a temperature of

$$kT^{\text{sh}} = \frac{4(\gamma - 1)}{(\gamma + 1)^2} \frac{GM_{\text{WD}}\mu m_{\text{H}}}{R_{\text{WD}}} = \frac{3}{8} \frac{GM_{\text{WD}}\mu m_{\text{H}}}{R_{\text{WD}}} \quad (2.36)$$

$$= 16 \left( \frac{\mu}{0.615} \right) \left( \frac{M_{\text{WD}}}{0.5M_{\odot}} \right) \left( \frac{R_{\text{WD}}}{10^9 \text{cm}} \right)^{-1} \text{keV}, \quad (2.37)$$

$$= 16 \left( \frac{\mu}{0.615} \right) \left\{ 1.23 \left( \frac{M_{\text{WD}}}{0.5M_{\odot}} \right)^{-8/3} - 0.30 \left( \frac{M_{\text{WD}}}{0.5M_{\odot}} \right)^{-4/3} \right\}^{-1/2} \text{keV}. \quad (2.38)$$

Here, equation (2.38) utilizes the mass-radius relation of white dwarfs (equation 2.10). Thus, the plasma has a typical temperature of hard X-ray emitter, forming an accretion column illustrated in figure 2.19.

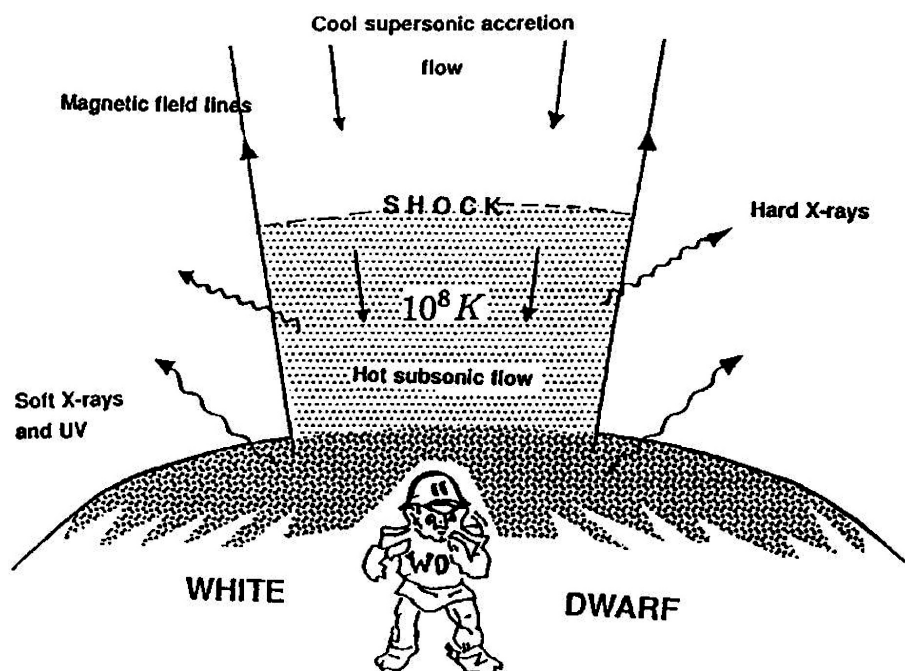


Figure 2.19: A schematic view of the accretion column on the white dwarf of an MCV (Patterson 1994).

### 2.4.4 Emission from magnetic cataclysmic variables

The main cooling mechanisms of the post-shock hot plasmas on MCVs are cyclotron emission and bremsstrahlung (or free-free) emission. The cyclotron emissivity scales as  $\propto n_e B^3 T$ , while that of bremsstrahlung as  $\propto n_e^2 T^{1/2}$  (see equation 2.41). As a result, the cyclotron resonance dominates the other when the magnetic field is strong and the electron density is low. This is illustrated in figure 2.20, where three characteristic regimes are identified on the  $B - L$  plane, where  $L$  is the accretion luminosity. In regime I, the temperatures of ions and electrons are comparable so that the post-shock plasma can be treated as a single fluid. The cooling via bremsstrahlung dominates the cyclotron cooling. In regime II, electrons are cooled to a temperature below that of ions by cyclotron emission, so the plasma acts as a two temperature fluid. In regime III, the magnetic field is so strong that the velocity distribution of ions becomes non-Maxwellian, and the shock structure collapses entirely. Both polars and intermediate polars lie in regime I. The former, having stronger magnetic fields and lower mass accretion rates than the latter, lie closer to regime II where the cyclotron cooling becomes relatively more important.

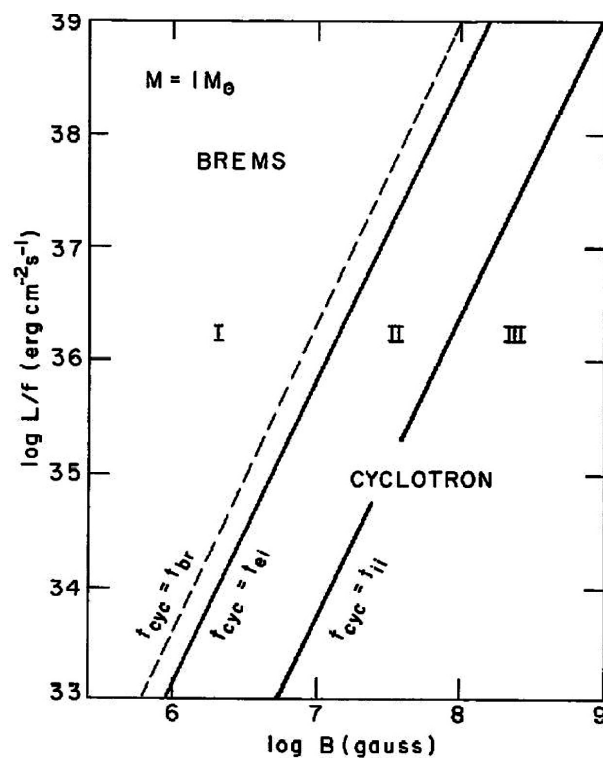


Figure 2.20: The cooling mechanisms of hot plasmas in a magnetic field of strength  $B$ , with a local luminosity of  $L$ . Note that  $f$  in the vertical axis is the fraction of the accretion region to the entire white-dwarf surface. Bremsstrahlung cooling dominates toward top left, and cyclotron cooling dominates toward right bottom (Lamb and Master 1979).

Based on this diagram, three radiation components are expected from a magnetic pole, as illustrated in figure 2.19:

- The bremsstrahlung emission from the post-shock hot plasma, which appears in the hard X-ray range.
- The cyclotron emission from the hot plasma, which appears in the infrared and optical band. The plasma is optically thick to the fundamental cyclotron frequency (far-infrared band), but optically thin to high harmonics (near-infrared to optical band).
- Ultraviolet to soft X-ray blackbody emission, as a reprocessed radiation from the white dwarf surface which is heated by the above two emissions.

In the left panel of figure 2.21, the theoretically expected spectra calculated by Lamb & Master (1979) are shown. Examples for regime I (upper) and II (lower) are plotted in this figure. The spectrum from AM Herculis observed with the X-ray satellite *HEAO-1* is shown in the right panel of figure 2.21. There, we can see the bremsstrahlung emission with iron line, and the reprocessed blackbody radiation.

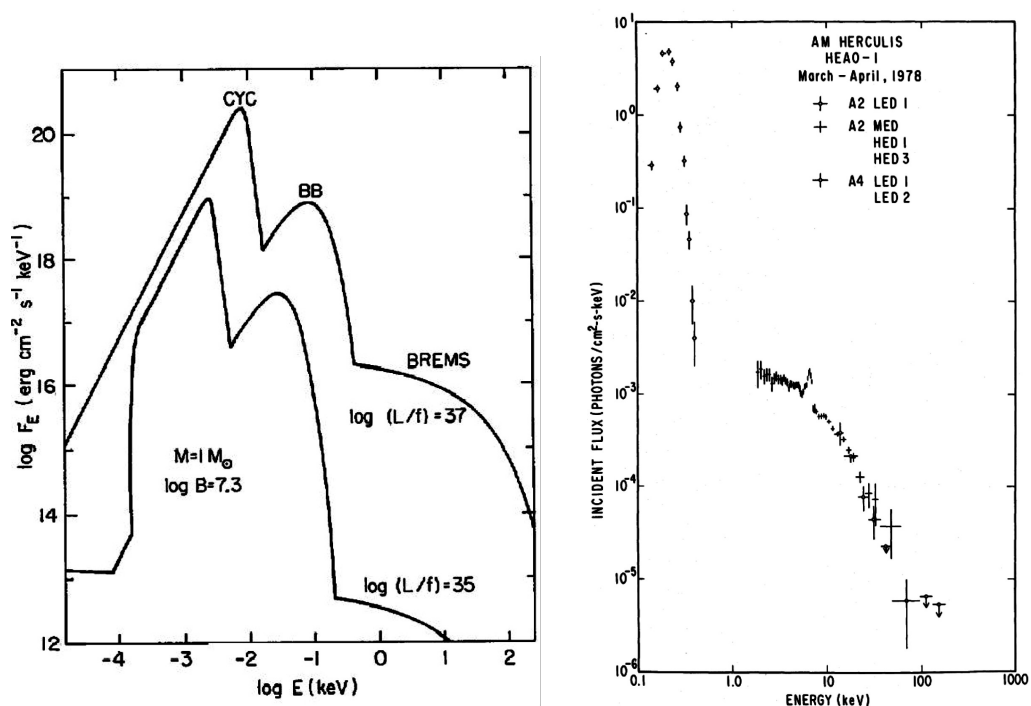


Figure 2.21: (*left*) The calculated UV – X-ray spectra from accretion regions of MCVs with two different accretion rates. The spectrum consists of three components; cyclotron emission (denoted as CYC), blackbody emission (BB), and bremsstrahlung (BREMS). (*right*) The spectrum of AM Herculis, observed by *HEAO-1* (Rothschild *et al.* 1981).

### 2.4.5 Hot plasma in accretion column

In the accretion column of an MCV, the temperature beneath the shock front is  $kT^{\text{sh}} \sim 16$  keV (equation 2.37), and the velocity there,  $u^{\text{sh}}$ , is described by shock discontinuity (equation 2.33) and  $u_{\text{ff}}$  (equation 2.31) as

$$\begin{aligned} u^{\text{sh}} &= \frac{u_{\text{ff}}}{4} \\ &= 0.9 \times 10^8 \left( \frac{M_{\text{WD}}}{0.5M_{\odot}} \right)^{1/2} \left( \frac{R_{\text{WD}}}{10^9 \text{cm}} \right)^{-1/2} \text{cm/s}. \end{aligned} \quad (2.39)$$

Assuming that the plasma is a single fluid (regime I, in figure 2.20) and that the abundance is one solar, the electron density of the post-shock plasma is then given as

$$\begin{aligned} n_e^{\text{sh}} &\simeq \left( \frac{\dot{M}}{\pi r^2 u^{\text{sh}} \mu m_{\text{H}}} \right) \times \left( 1 + \frac{1}{\mu} \right)^{-1} \\ &= 7.7 \times 10^{15} \left( \frac{\mu}{1.2} \right) \left( \frac{\dot{M}}{10^{16} \text{g s}^{-1}} \right) \\ &\quad \times \left( \frac{M_{\text{WD}}}{0.5M_{\odot}} \right)^{-1/2} \left( \frac{R_{\text{WD}}}{10^9 \text{cm}} \right)^{1/2} \left( \frac{r}{5 \times 10^7 \text{cm}} \right)^{-2} \text{cm}^{-3}, \end{aligned} \quad (2.40)$$

in the case of the solar abundances ( $\mu = 1.2$ ; see section 2.1.2).

The post-shock plasma cools mainly by radiating the bremsstrahlung hard X-rays. Their volume emissivity,  $\varepsilon_{\text{ff}}$ , is given by

$$\varepsilon_{\text{ff}} = \left( \frac{2\pi kT}{3m_e} \right)^{1/2} \frac{2^5 \pi e^6}{3hmc^3} Z^2 n_e n_i \bar{g}_{\text{B}} \quad (2.41)$$

$$\simeq 1.7 \times 10^9 \left( \frac{kT^{\text{sh}}}{16 \text{keV}} \right)^{1/2} \left( \frac{n_e^{\text{sh}}}{7.7 \times 10^{15} \text{cm}^{-3}} \right)^2 \text{erg s}^{-1} \text{cm}^{-3}. \quad (2.42)$$

where  $Z$  is the mean atomic number,  $n_i$  is the ion density, and  $\bar{g}_{\text{B}}$  is the average Gaunt factor which takes a value of order unit (see figure 5.2 and equation 5.15 in Rybicki & Lightman 1979). Thus, the free-free cooling time scale  $t_{\text{ff-cool}}$  becomes

$$\begin{aligned} t_{\text{ff-cool}} &\equiv \frac{3n_e kT}{2\varepsilon_{\text{ff}}} \\ &= 0.35 \left( \frac{kT^{\text{sh}}}{16 \text{keV}} \right)^{\frac{1}{2}} \left( \frac{n_e^{\text{sh}}}{7.7 \times 10^{15} \text{cm}^{-3}} \right)^{-1} \text{s}. \end{aligned} \quad (2.43)$$

Since the shock front is sustained by the pressure of the post-shock plasma against the gravity, the height  $h$  of the accretion column is described by  $h \sim u^{\text{sh}} t_{\text{ff-cool}}$  (Hōshi 1973). According to detailed estimation by Aizu (1973),  $h$  is given more specifically as

$$\begin{aligned} h &= 0.605 u^{\text{sh}} t_{\text{ff-cool}} \\ &= 1.9 \times 10^7 \left( \frac{kT^{\text{sh}}}{16 \text{keV}} \right)^{\frac{1}{2}} \left( \frac{n_e^{\text{sh}}}{7.7 \times 10^{15} \text{cm}^{-3}} \right)^{-1} \text{cm}, \end{aligned} \quad (2.44)$$

In comparison to equation (2.43), the ion to electron energy transfer time scale,

$$t_{\text{eq}} = 5.6 \times 10^{-3} \left( \frac{kT^{\text{sh}}}{16\text{keV}} \right)^{\frac{3}{2}} \left( \frac{n_e^{\text{sh}}}{7.7 \times 10^{15} \text{cm}^{-3}} \right)^{-1} \text{ s} \quad (2.45)$$

[see eq (5.31) in Spitzer 1962], is much shorter, so we expect the ions and electrons to share the same temperature. Thus, the assumption of a single fluid must be valid.

It is difficult to know the cross-sectional shape of the hot plasma, since there are large uncertainties in the fractional area  $f$  of the accretion region relative to the entire white dwarf surface. We assume for simplicity a cylinder shape, and use an effective radius  $r$  of the cross-section, defined as  $r \equiv \sqrt{4f}R_{\text{WD}}$ . Since  $f$  is estimated to be  $\sim 10^{-3}$  (Rosen 1992) or smaller for polars,  $r$  is typically  $5 \times 10^7$  cm, which is the same order as  $h$ . Then, the optical depth of the accretion column with typical path length  $l \sim 5 \times 10^7$  cm for Thomson scattering is given by

$$\tau_{\text{T}} = 0.24 \left( \frac{l}{5 \times 10^7 \text{cm}} \right) \left( \frac{n_e^{\text{sh}}}{7.7 \times 10^{15} \text{cm}^{-3}} \right), \quad (2.46)$$

implying that the post-shock plasma is optically thin for electron scattering. Since that for free-free absorption,  $\tau_{\text{ff}}$ , is much smaller,

$$\tau_{\text{ff}} = 0.88 \times 10^{-10} \tau_{\text{T}} \left( \frac{E}{6\text{keV}} \right)^{-2} \left( \frac{kT}{16\text{keV}} \right)^{-\frac{3}{2}} \left( \frac{n_e^{\text{sh}}}{7.7 \times 10^{15} \text{cm}^{-3}} \right) \quad (2.47)$$

[see equation (5.18) in Rybicki & Lightman 1979], it is negligible compared to the electron scattering.

### 2.4.6 Structure of accretion column: Aizu model

We review hydrodynamic modeling of the structure of the post-shock emission region of an MCV, which was first proposed by Hōshi (1973) and formulated by Aizu (1973). The model assumes that the temperatures of electrons and ions are the same, so the plasma act as a single fluid, that the plasma is cooled down via only free-free emission, and that it is optically thin. We further assume that the shock height  $h$  is much smaller than  $R_{\text{WD}}$ ; i.e., the gravity is almost constant over the emission region. We denote this constant gravitational acceleration  $g$ . For simplicity, the flow is assumed to be one-dimensional; we take a vertical coordinate  $z$ , which has the origin at the foot of the emission region on the white dwarf surface, and increases in the direction opposite to the gravity.

The gas mass density  $\rho$ , velocity  $u$ , temperature  $T$ , and pressure  $p$  are functions of  $z$ . According to standard hydrodynamics, the basic equations of continuity, momentum transfer, and energy conservation are described respectively as

$$\frac{d}{dz}(\rho u) = 0 \Leftrightarrow \rho u = \rho^{\text{sh}} u^{\text{sh}}, \quad (2.48)$$

$$\rho u \frac{du}{dz} = -\frac{dp}{dz} - \rho g, \quad (2.49)$$

$$\rho T u \frac{dS}{dz} = -\varepsilon_{\text{ff}}, \quad (2.50)$$

where  $S$  is the entropy defined by

$$S \equiv \frac{3k}{2\mu m_{\text{H}}} \log(T \rho^{-2/3}). \quad (2.51)$$

Equation (2.50) assumes that the plasma is in thermal equilibrium, and neglects the heat conductivity. The vertical structure of the pre-shock flow is obtained by solving these equations.

First, equation (2.48) immediately yields

$$\frac{u}{u^{\text{sh}}} = \left( \frac{\rho}{\rho^{\text{sh}}} \right)^{-1}. \quad (2.52)$$

Because of the boundary condition on the surface of white dwarf ( $u = 0$  at  $z = 0$ ), the velocity  $u$  decreases and the density  $\rho$  increases, as gas falls down ( $z$  decreases).

In the next, to see the macroscopic momentum balance, we integrate the motion equation (2.49) by  $z$ , to obtain

$$\begin{aligned} [\rho u^2 + p]_0^h &= -\int_0^h \rho g dz \\ \Leftrightarrow P_{\text{ram}} + P_{\text{gas}} &= -m_{\text{ac}} g, \end{aligned} \quad (2.53)$$

where  $P_{\text{ram}}$  and  $P_{\text{gas}}$  are the ram and gas pressure respectively, and  $m_{\text{ac}}$  is the total weight of emission region. After the randomization at the shock,  $P_{\text{gas}}$  dominates in the left hand side of equation (2.53). Furthermore, the self gravity  $m_{\text{ac}} g$  can be negligible, since

it contributes only a factor of  $\sim h/R (\ll 1)$  compared to  $P_{\text{ram}}$ . Thus, the thermal gas pressure  $p$  in the post-shock region becomes

$$p(z) \simeq P_{\text{gas}} + \int_z^h \rho(z') g dz' \sim P_{\text{gas}}, \quad (2.54)$$

so it is almost constant everywhere in the emission region. Since we have  $p = \rho k T$  from the equation of state for ideal gas,  $\rho T$  must also be constant from equation (2.54). Thus, the relation between  $T$  and  $u$  is given as

$$\frac{T}{T^{\text{sh}}} = \left( \frac{\rho}{\rho^{\text{sh}}} \right)^{-1}. \quad (2.55)$$

Finally, we look into the equation of energy conservation. Since the volume emissivity for free-free emission,  $\varepsilon_{\text{ff}}$ , scales as  $n^2 T^{1/2}$  (equation 2.43), we can take

$$\varepsilon_{\text{ff}} = \epsilon_0 \rho^2 T^{1/2}. \quad (2.56)$$

Thus, equation (2.50) rewrites as

$$\begin{aligned} & \left( \frac{T}{T^{\text{sh}}} \right)^{5/2} \frac{d}{dz} \left[ \log \left\{ T^{\text{sh}} (\rho^{\text{sh}})^{-2/3} \left( \frac{T}{T^{\text{sh}}} \right)^{5/3} \right\} \right] = \frac{2\epsilon_0 \rho^{\text{sh}} \mu m_{\text{H}}}{3k (T^{\text{sh}})^{1/2} u^{\text{sh}}} \\ \Leftrightarrow & \left( \frac{T}{T^{\text{sh}}} \right)^{3/2} \frac{d}{dz} \left( \frac{T}{T^{\text{sh}}} \right) = \frac{2\epsilon_0 \rho^{\text{sh}} \mu m_{\text{H}}}{5k (T^{\text{sh}})^{1/2} u^{\text{sh}}} \\ \Rightarrow & \left( \frac{T}{T^{\text{sh}}} \right) = \left\{ z / \left( \frac{k (T^{\text{sh}})^{1/2} u^{\text{sh}}}{\epsilon_0 \rho^{\text{sh}} \mu m_{\text{H}}} \right) \right\}^{2/5}, \end{aligned} \quad (2.57)$$

from  $S$  (equation 2.51),  $\varepsilon_{\text{ff}}$  (equation 2.56), and the relations between  $\rho, k, T$  (equations 2.52, 2.55). Because of the boundary condition for  $T$  on the shock front ( $T = T^{\text{sh}}$  at  $z = h$ ), equation (2.57) becomes

$$\left( \frac{T}{T^{\text{sh}}} \right) = \left( \frac{z}{h} \right)^{2/5}, \quad (2.58)$$

$$h = \frac{k (T^{\text{sh}})^{1/2} u^{\text{sh}}}{\epsilon_0 \rho^{\text{sh}} \mu m_{\text{H}}}. \quad (2.59)$$

The latter equation simply means

$$h \sim t_{\text{ff-cool}} u^{\text{sh}}, \quad (2.60)$$

as mentioned in equation (2.44), since  $t_{\text{ff-cool}}$  is given as

$$t_{\text{ff-cool}} = \frac{3}{2} \frac{k T^{1/2}}{\epsilon_0 \rho \mu m_{\text{H}}} \simeq \frac{15}{16} \frac{k (T^{\text{sh}})^{1/2}}{\epsilon_0 \rho^{\text{sh}} \mu m_{\text{H}}} \sim \frac{k (T^{\text{sh}})^{1/2}}{\epsilon_0 \rho^{\text{sh}} \mu m_{\text{H}}}, \quad (2.61)$$

using equations (2.43) and (2.56).

As a result, from three basic equations [(2.48), (2.49), and (2.50)], we can obtain the relations between  $T, u, \rho$ , as described by equations (2.52), (2.55), and (2.58), respectively.

We hence obtain

$$\frac{kT}{kT^{\text{sh}}} = \frac{u}{u^{\text{sh}}} = \left( \frac{n}{n^{\text{sh}}} \right)^{-1} \simeq \left( \frac{z}{h} \right)^{\frac{2}{5}}. \quad (2.62)$$

Figure 2.22 shows the profiles of  $kT$ ,  $u$ , and  $\rho$  as a function of  $z/h$  of this approximate solution (equation 2.62), compared to the exact solutions obtained by Aizu (1973). The latter is obtained by expanding basic three relations (equations 2.48, 2.49, and 2.50) using a small parameter  $\alpha \equiv h/R$ , without the approximation in equation (2.54); i.e., this solution includes the gravitational force. Since the approximate solution is thus sufficiently close to the exact one, we can use equation (2.62) for the structure of accretion column instead of the exact solution.

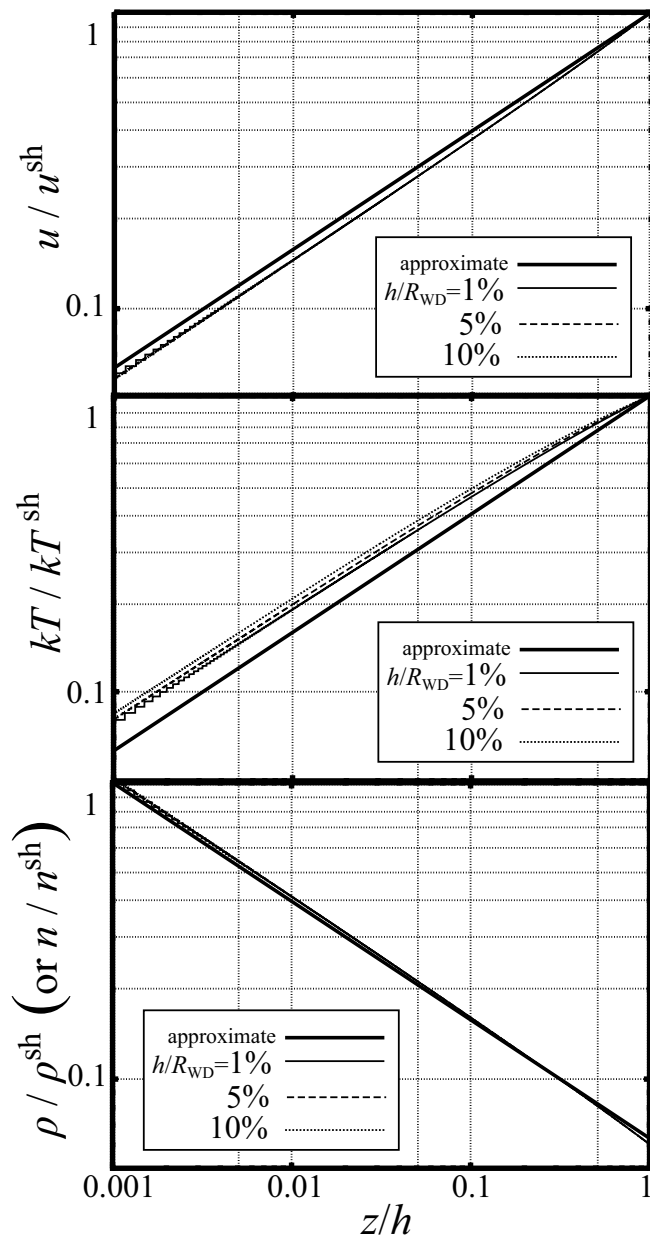


Figure 2.22: The Aizu (1973) solution for the post-shock velocity, temperature, and density, as a function of the normalized height from white dwarf surface. Thin solid, dashed, and dotted curves represent the case for  $h/R_{\text{WD}}$  of 1%, 5%, and 10% respectively. The thick curve presents the approximate solution described by equation (2.62).

## 2.5 X-ray Emission from Hot Plasmas

### 2.5.1 Emission mechanisms

In the case of an optically thick plasma, features of interactions in the plasma between the gas and photons are lost in its emission, which approaches blackbody radiation. On the other hand, in the case of an optically thin plasma as seen on magnetic poles of MCVs, features of individual processes creating photons are visible in the emergent spectra. The expected emission processes in optically-thin hot plasmas are listed in table 2.3. Some processes produce continuum spectra, while others form line spectra. Each of these processes is a result of electron impact upon relevant ions. Therefore, like in equation (2.41), the emissivity of each process is written as

$$\varepsilon = \Lambda(T)n_en_i, \quad (2.63)$$

where  $n_i$  is the density of relevant ions, and  $\Lambda(T)$  is a quantity called cooling function. Figure 2.23 shows overall cooling function, together with the constituent components (Gehrels & Williams 1993). Thus, under a temperature of a few tens keV typical for accretion columns, the main cooling mechanism is free-free emission, as mentioned in section 2.4.4. In addition, line emission must also be seen from the accretion column.

Table 2.3: Emission processes from thin thermal plasmas.

Transition Type	Atomic process
<b>Continuum:</b>	
free-free	thermal bremsstrahlung
free-bound	radiative recombination
bound-bound	two-photon decay
<b>Line:</b>	
bound-bound	innershell ionization – fluorescent excitation line
	innershell excitation – satellite line
	radiative recombination – cascade line
	dielectric recombination – satellite line

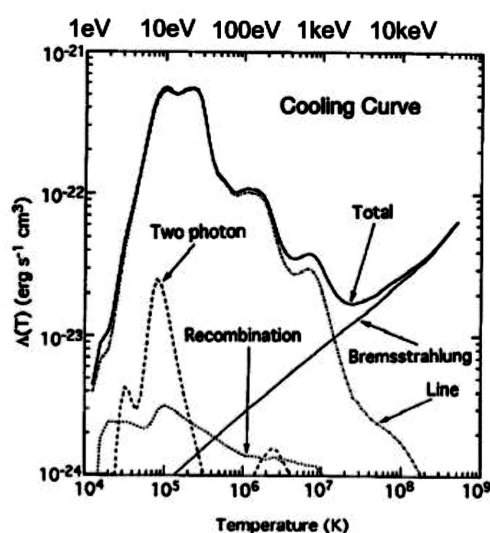


Figure 2.23: Cooling function of thin thermal plasmas (Gehrels & Williams 1993).

## 2.5.2 Continuum emission

The main emission mechanism in the accretion column is thermal bremsstrahlung (or free-free) radiation. This emission is caused when an electron with charge  $e$  is accelerated in the Coulomb field of an ion with charge  $Ze$ . An electron with a given velocity emits photons of various energies, depending on the impact parameter of the collision, with the maximum photon energy equal to the electron kinetic energy. The spectrum from a single electron is then convolved with the Maxwellian electron distribution. As a result, the overall spectrum has an exponential form close to the Maxwellian distribution for the emitting electrons. Specifically, the spectral emissivity per photon frequency  $\nu$  for thermal bremsstrahlung is given by

$$\begin{aligned}\varepsilon_{\nu,\text{ff}} &= \frac{2^5 \pi e^6}{3m_e c^3} \left( \frac{2\pi}{3km_e} \right)^{1/2} Z^2 T^{-1/2} n_e n_i \exp \left\{ -\frac{h\nu}{kT} \right\} \bar{g}_{\text{ff}} \\ &= 6.8 \times 10^{-38} Z^2 T^{-1/2} n_e n_i \exp \left\{ -\frac{h\nu}{kT} \right\} \text{erg s}^{-1} \text{cm}^{-3} \text{Hz}^{-1}.\end{aligned}\quad (2.64)$$

As a result, the total photon flux from a thin thermal plasma with a volume  $V$  is given by

$$Br(E, kT, EM) = \frac{3.02 \times 10^{-15}}{4\pi d^2} EM \times (kT)^{-1/2} \exp \left\{ -\frac{E}{kT} \right\} \text{ph s}^{-1} \text{cm}^{-2} \text{keV}^{-1}, \quad (2.65)$$

where  $EM$  is the emission measure of plasma defined as  $\int n_e n_i dV$  in unit of  $\text{cm}^{-3}$ , and  $d$  is the distance to the object in cm. Figure 2.24 shows examples of bremsstrahlung spectra for several plasma temperatures.

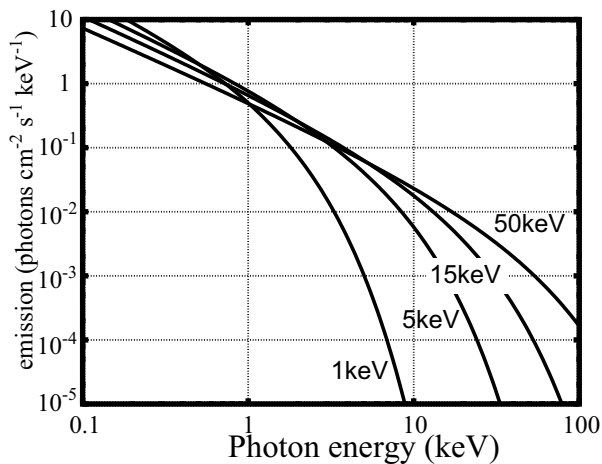


Figure 2.24: Energy spectra of thermal bremsstrahlung for emission measure of  $4 \times 10^{56} (d/100\text{pc})^2 \text{cm}^{-3}$  with a temperature of 1, 5, 15, and 50 keV.

As listed in table 2.3, free-bound transition can be also seen in the continuum spectra, which occurs when an ion captures a free electron and emits a photon of a surplus energy between the kinetic energy of the captured electron and its bounding energy. Since the final states are discrete, the resultant spectra have edge-like structures, which correspond to the onset of electron capture into different levels. The bound-bound emission via two photon decay (table 2.3) also appears as a continuum spectrum (see section 2.5.4). This emission is important in ultraviolet band.

### 2.5.3 Collisionally ionized plasma

In a hot plasmas with a temperature of  $\gtrsim 1$  keV, atoms are ionized due to collisional impact by electrons. Ionization structure of a plasma for ion  $Z^{+q}$ , where  $Z$  is the atomic number and  $q$  is its charge, is determined by the balance between ionization and recombination processes as follows.

- **Direct ionization** ( $Z^q \rightarrow Z^{q+1}$ )

An ion  $Z^q$  is directly ionized to  $Z^{q+1}$  by electron impact.

- **Autoionization** ( $Z^q \rightarrow Z^{q*} \rightarrow Z^{q+1}$ )

An inner electron of an ion  $Z^q$  is first excited by an electron impact to  $Z^{q*}$ . Subsequently, if the excitation energy exceeds the ionization energy of any other electrons, the excited ion eject an electron, to be ionized to  $Z^{q+1}$ .

- **Radiative recombination** ( $Z^{q+1} \rightarrow Z^q$ )

A free electron is captured by an ion  $Z^{q+1}$ , and the excess energy is emitted as a photon. The inverse process is called photo ionization.

- **Dielectronic recombination** ( $Z^{q+1} \rightarrow Z^{q*} \rightarrow Z^q$ )

First, an electron excites an ion  $Z^{q+1}$ , and captured by the same ion to a high energy state. This produces a doubly excited state  $Z^{q*}$ . Second, the ion is rearranged to  $Z^{q+1}$  (autoionization) by emitting one of the excited electrons, or de-excited to  $Z^q$  by emitting a photon. The latter is called dielectronic recombination.

The rate equation for the number density  $N_{Z,q}$  of ion  $Z^q$  is described by

$$\frac{1}{n_e} \frac{dN_{Z,q}}{dt} = N_{Z,q-1} C_{Z,q-1} - N_{Z,q} (C_{Z,q} + \alpha_{Z,q}) + N_{Z,q+1} \alpha_{Z,q+1}, \quad (2.66)$$

where  $C_{Z,q}$  is the electron collisional ionization rate coefficient for  $Z^q \rightarrow Z^{q+1}$  described by the former two processes, and  $\alpha_{Z,q}$  is the recombination rate coefficient for  $Z^q \rightarrow Z^{q-1}$  by the latter two.

The ionized plasma will reach an equilibrium state, called collisional ionization equilibrium (CIE). According to Masai (1984), it takes about  $\gtrsim 10^{12} \times (n_e \text{ cm}^{-3})^{-1}$  s. Since the typical density in an accretion column is  $\sim 10^{15-16} \text{ cm}^{-3}$  (equation 2.40), this time scale is very short compared to that for the free-free cooling (equation 2.43). The plasma must therefore be in a CIE. Thus, equation (2.66) becomes

$$C_{Z,q-1} \eta_{Z,q-1} = \alpha_{Z,q} \eta_{Z,q}, \quad (2.67)$$

where  $\eta_{Z,q}$  is a fractional abundance for ion  $Z^q$  (i.e.,  $\sum_q Z^q = 1$ ). By simultaneously solving these  $q+1$  equations with different values of  $q$ , we can determine the ionization structure  $\eta_{Z,q}$  for each element in a plasma. The detailed calculations of ionization balance are made by Shull & Steenberg (1982), Arnaud & Rothenflug (1985), Arnaud & Raymond

(1992) and so on. An example of the solution for Fe ions are shown in figure 2.25. Thus, at the temperature typical for the accretion column, namely a few tens keV (equation 2.38), almost all iron ions are ionized to He-like, H-like or naked. Lighter elements such as Mg, Si, S, and Ar, are completely ionized at lower temperature of  $0.1 \sim 5$  keV because of lower binding energies.

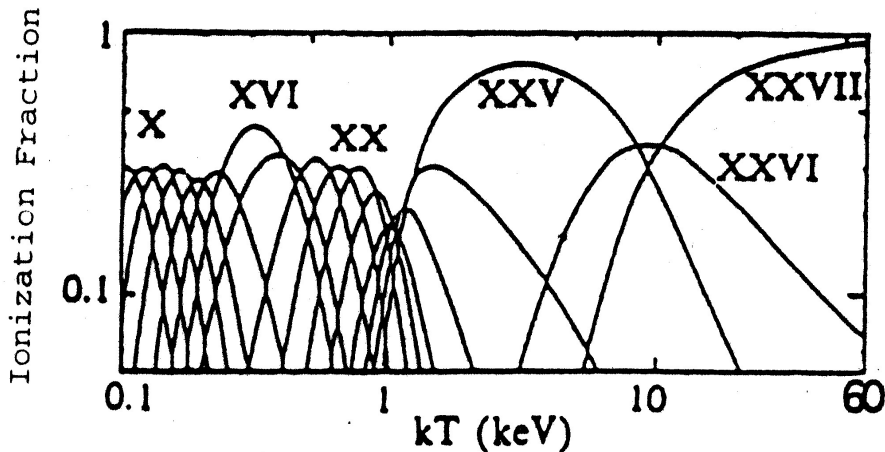


Figure 2.25: Fractional ratios for ionized iron species in the ionization equilibrium (Makishima 1986).

#### 2.5.4 Atomic line emission

Line photons are emitted by transitions of an electron between two bound status (bound-bound transition) in an ion. Emission lines are classified into two groups by selection rule; permitted lines produced by electric-dipole (E1) transition, and forbidden lines by higher multipole transitions such as magnetic-dipole (M1) and electric-quadrupole (E2) transitions. Although the latter is not allowed by the selection rule, it can work in an ion with multi electrons, by spin-orbit interactions between them. Since collisions rarely occurs in a thin gases as seen in astrophysical sites, an electron can stay in a metastable excited state, without collisionally de-excited, until it returns to the ground state by emitting a forbidden-line photon.

Here, we look into the transitions for  $K_{\alpha}$  lines from hydrogenic or helium-like iron ions, because these ionization states dominate in accretion columns (figure 2.25). Due to spin-orbit interaction, the energy level of principal quantum number  $n = 2$  for hydrogenic ion is split into three levels;  $^2S_{1/2}$ ,  $^2P_{3/2}$ , and  $^2P_{1/2}$ . An example of transition diagram for hydrogenic Fe ion is shown in figure 2.26 left. The transition from  $^2P$  to ground state  $^2S_{1/2}$  is permitted within electric dipole approximation, so the resultant emission is called “resonance line.” This is so-called Lyman  $\alpha$  line. In helium-like ion, in contrast, the  $n = 2$  state is split into  $^3P_2$ ,  $^3P_1$ ,  $^3P_0$ ,  $^3S_1$ ,  $^1P_1$ , and  $^1S_0$ , due to Coulomb interaction, exchange interaction, and spin-orbit interaction, as exemplified for the case of iron in figure 2.26 right. Among these levels, only the transition from  $^1P_1$  to the ground state is electric

dipole transition, so it is resonant. The others are not permitted by selection rule. The transition from  ${}^3P_2$  and  ${}^3P_1$  to ground state is the magnetic quadrupole transition over the different spin multiplicity (triplet to singlet), and is called “intercombination line.” For heavier ions, this transition, although not “resonant”, has a relatively large probability amplitude, since the spin triplet and singlet states are mixed by spin-orbit interaction of electrons. The transition from  ${}^3S_1$  to ground state is simply called “forbidden line,” which can be seen only in thin plasmas.

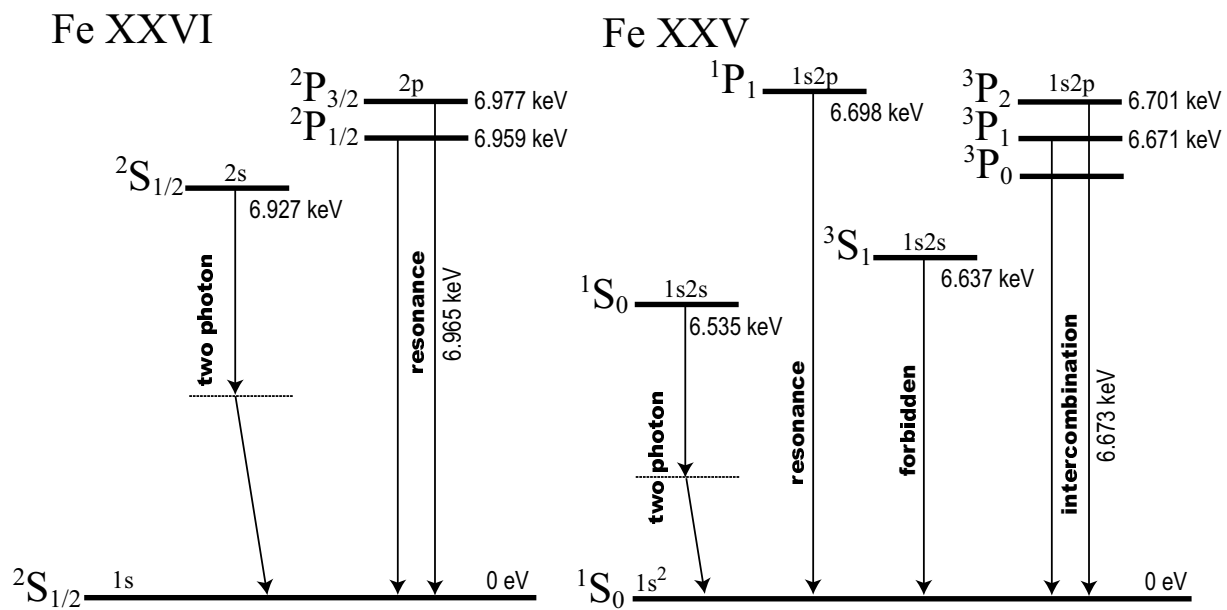


Figure 2.26: Radiative transition diagram of  $n = 2 \rightarrow 1$  for hydrogen-like Fe ions (Fe XXVI; *left*), and helium-like Fe ions (Fe XXV; *right*).

Using the relative population of various ionization species as shown in figure 2.25, temperature dependence of the iron line emissivity in optically thin plasmas has been calculated by many authors; e.g. Mewe, Gronenschild and Oord (1985). Figure 2.27 shows the corresponding  $\Lambda(kT)$  (equation 2.63) for Fe  $K_\alpha$  lines is calculated assuming one solar abundance. Using these results for helium-like iron  $K_\alpha$  lines, the ratios of the resonance, intercombination, and forbidden lines to the total are obtained as in figure 2.28. Thus, the resonance line is dominant at higher temperatures; this originates from the temperature dependence of dielectric recombination coefficients. As shown in figure 2.29, the ratio of the hydrogenic line emissivity to the helium-like one also depends significantly on the temperature, serving as a good indicator of the plasma temperature.

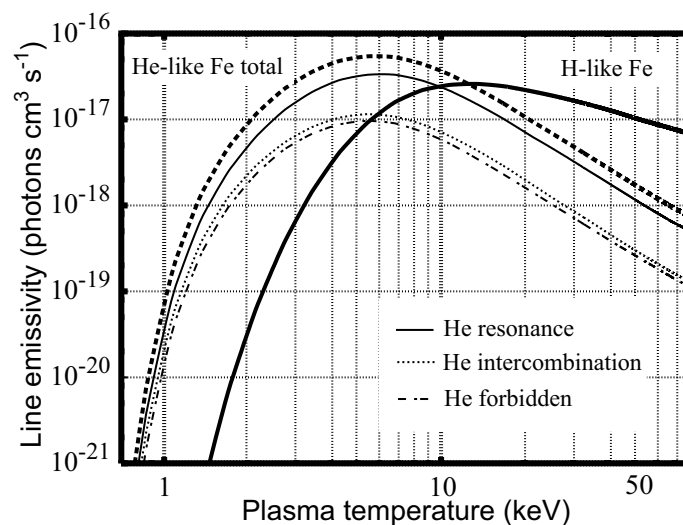


Figure 2.27: Temperature dependence of the emissivity for the Fe XXVI  $K_\alpha$  and Fe XXV  $K_\alpha$  lines (Mewe *et al.* 1985).

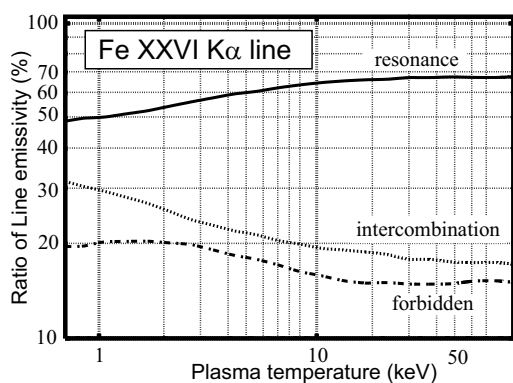


Figure 2.28: Contribution of the resonance line, intercombination line, and forbidden line to the total emissivity of the Fe XXVI  $K_\alpha$  line.

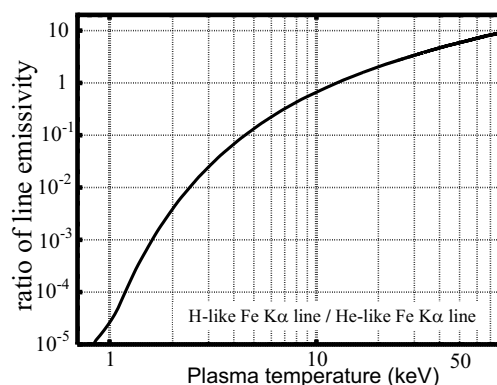


Figure 2.29: The ratio of the emissivity for hydrogenic and helium-like Fe  $K_\alpha$  lines as a function of the plasma temperature.

### 2.5.5 Plasma diagnostics with emission lines

The temperature and density in the accretion column of white dwarfs exhibit a strong vertical gradient (section 2.4.6). The line emissivity hence become a function of the vertical position as well, because it is determined by there two quantities (equation 2.63). Figure 2.30 shows the calculated position dependence of the Fe  $K_\alpha$  line emissivity for a temperature of 16 keV and 60 keV, adopting Aizu solution (equation 2.62) and the line emissivities by Mewe *et al.* (figure 2.27). The hydrogenic iron line photons are produced predominantly in the top regions of the accretion column, while the helium-like lines are mostly produced near the bottom. For lighter elements, such as Mg, Si, S, and Ar, K-lines are produced in narrow regions at the bottom as shown in figure 2.31, where the cooling approximation by the Aizu formalism becomes incomplete. Therefore, among many line emissions seen in MCV spectra, the Fe  $K_\alpha$  lines provide one of the most suitable diagnostic tools for plasma diagnostic of the accretion column within the Aizu formalism.

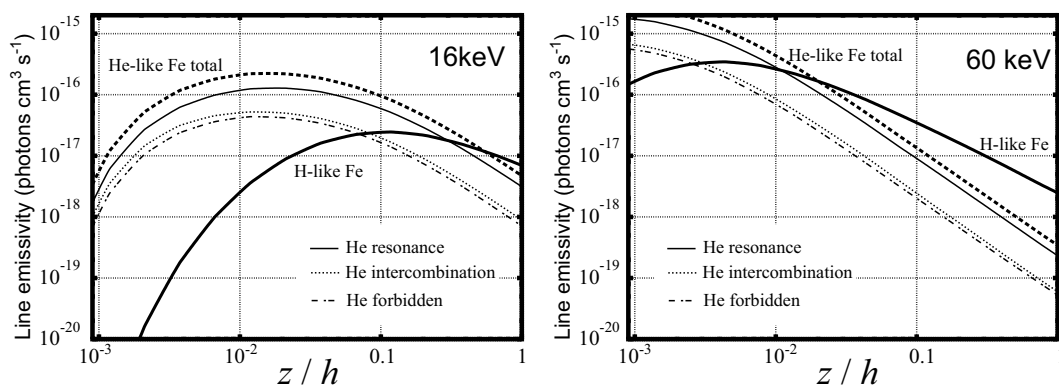


Figure 2.30: The volume emissivity of Fe–K line photons in the accretion column, calculated assuming the Aizu model, shown as a function of  $z/h$ . The assumed plasma temperature beneath the shock is  $kT^{\text{sh}} = 16$  keV (*left*), and 60 keV (*right*).

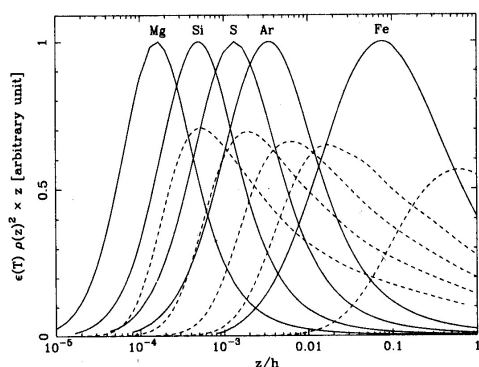


Figure 2.31: Emissivity distributions of atomic K-emission lines of Mg, Si, S, Ar, and Fe, calculated for a shock temperature of 15 keV, and shown as a function of normalized distance from the white dwarf,  $z/h$ . The solid and dashed lines represent the helium-like and hydrogenic  $K_\alpha$  lines of each element, respectively. The ordinate is the local emission measure normalized to the maximum emissivity for each element (Fujimoto 1998).

## 2.6 Previous X-ray Observations of Magnetic Cataclysmic Variables

### 2.6.1 Initial X-ray observations

Any X-ray astrophysical objects can not be seen from the ground, because of strong absorption by the atmosphere of the earth, as shown in figure 2.32. Thus, they must be observed only by balloons, rockets, or satellites. The X-ray observation began with the first accidental discovery of the brightest X-ray source in the sky, Scorpion X-1, with the rocket observation by Giacconi *et al.* in 1962. Many theoretical models were proposed and improved, for example those by Hōshi and Aizu, to account for the observed energy spectra of Sco X-1. Following rocket and balloon experiments during the 1960s, the first Earth-orbiting X-ray explorers were launched in the 1970s (*Uhuru*, *SAS 3*, *Ariel 5*), followed in late 1970s by larger missions (*HEAO-1*, *Einstein*). With these satellites, a large number of X-ray objects have been discovered inside and outside our Galaxy. Among them, most sources in the Galaxy are close binaries, each consisting of a main sequence star and a compact object, i.e. black hole, neutron star, or white dwarf. In this section, we review X-ray observations of white-dwarf close binaries, with a particular emphasis on MCVs.

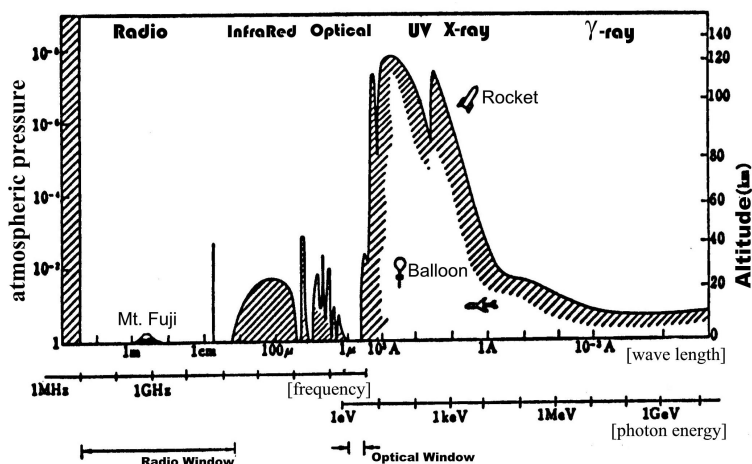


Figure 2.32: The altitude above the ground where radiation from astronomical objects is absorbed by atmosphere (Oda 1972).

The first-generation satellites described above, in particular *HEAO-1*, successfully detected the hard X-ray component from two MCVs, AM Her (Rothschild *et al.* 1981) and EF Eri (White 1981), as already shown in figure 2.21 right. Although the obtained spectra were generally consistent with thermal bremsstrahlung models, more detailed spectral evaluation was difficult because of the lack of energy resolution for detectors (Rothschild *et al.* 1981). Subsequently, the *Einstein* Observatory drastically increased the number of X-ray detected MCVs, utilizing the superb sensitivity in soft X-rays. However, the hard bremsstrahlung continuum of these MCVs remained poorly studied, because *Einstein* did not have a sensitivity above  $\sim 3$  keV.

## 2.6.2 Hard X-ray continuum spectra studied with *Ginga*

The hard X-ray observations of MCVs have made a big progress thanks to the third Japanese X-ray satellite *Ginga*, which has a large effective area up to 4000 cm<sup>2</sup> and a wide energy range of 2 – 37 keV. This energy range is very suitable to a typical plasma temperature of accreting matter onto the white dwarf. Figure 2.33 shows a typical X-ray pulse-height spectrum of an MCV obtained by *Ginga*; here and hereafter, we present the spectra without removing the detector response, so that they differ from their incident forms.

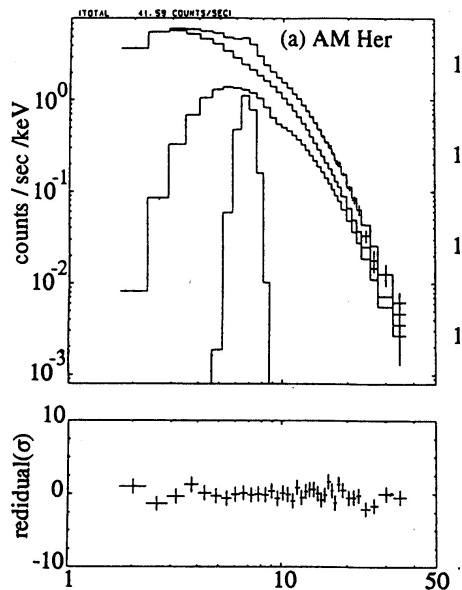


Figure 2.33: The X-ray spectrum for a representative MCV, AM Hercuris, obtained by *Ginga* (Ishida 1991).

A systematic study of the hard X-ray emission from MCVs was performed by Ishida (1991) using *Ginga*. He found that the hard X-ray emission from all the observed 12 MCVs are explained by optically thin thermal bremsstrahlung with a photo-electric absorption, as

$$M(E) = Br(E, EM, kT) \times Ab(E), \quad (2.68)$$

where  $M(E)$  is the incident photon flux at energy  $E$ ,  $Br(E, EM, kT)$  is the bremsstrahlung energy distribution (equation 2.65), and  $Ab(E)$  is the absorption at  $E$  which is attributed to the pre-shock matter. Since the observed temperature of  $Br(E, EM, kT)$  is related to the gravitational potential like equation (2.36), the mass to radius ratio,  $M_{WD}/R_{WD}$ , of white dwarf have been estimated for many MCVs. These measurements were then combined with the theoretical mass-radius relation (i.g., equation 2.10), to yield estimates on the white dwarf mass (section 2.1.3) as listed in table 2.4 and figure 2.34. This is one of the important results obtained by *Ginga*.

When the absorbing matter is represented by a single equivalent hydrogen column density,  $N_{\text{H}}$ , the spectral absorption can be expressed as

$$Ab(E, N_{\text{H}}) = \exp \{-N_{\text{H}}\sigma(E)\}, \quad (2.69)$$

where  $\sigma(E)$  means the cross section of photoelectric absorption (e.g., Morrison & McCammon 1977). The *Ginga* spectra from some MCVs have been accounted for by a single absorption, while some needed “leaky absorber model”, as exemplified in figure 2.33 solid lines. In this case, the absorption is expressed by two column densities,  $N_{\text{H1}}$  and  $N_{\text{H2}}$ , as

$$Ab(E, N_{\text{H1}}, N_{\text{H2}}, CF) = CF \times \exp \{-N_{\text{H1}}\sigma(E)\} + (1 - CF) \times \exp \{-N_{\text{H2}}\sigma(E)\}, \quad (2.70)$$

where  $CF$  is the covering fraction.

Table 2.4: The mass of white dwarfs in MCVs determined by *Ginga* ( $\times M_{\odot}$ ).

Target	Ishida <i>et al.</i> <sup>a</sup>	Wu <i>et al.</i> <sup>b</sup>	Cropper <i>et al.</i> <sup>c</sup>	others
AM Her	0.44	0.69	1.22	0.75 <sup>d</sup>
EF Eri	0.39	0.57	0.88	
BY Cam	0.63	1.10	1.08	
V834 Cen	0.33	0.51	0.51	
QQ Vul	0.66	1.20	1.12	0.58 <sup>d</sup>
EX Hya	0.24	0.35	0.52	0.48 <sup>e</sup>
AO Psc	0.32	0.50	0.40	0.40 <sup>f</sup>
FO Aqr	0.49	0.80	1.22	
TV Col	0.52	0.88	1.20	
BG CMi	0.50	0.85	1.25	
TX Col			0.55	
PQ Gem	0.31	0.65	1.35	
AE Aqr			0.3	0.89 <sup>g</sup>
mean	0.44	0.74	0.89	

Data taken from, (a) Ishida 1991; (b) Wu *et al.* 1995; (c) Cropper *et al.* 1998; (d) Mulai and Charles 1987; (e) Fujimoto and Ishida 1996 (Note that this is the *ASCA* result); (f) Hellier *et al.* 1996; (g) Welsh *et al.* 1994.

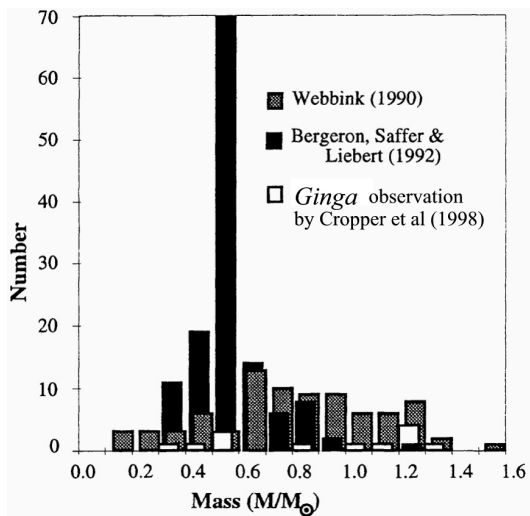


Figure 2.34: The mass distribution of white dwarfs in MCVs from *Ginga* observations (Cropper *et al.* 1998), compared with those of field white dwarfs (Bergeron *et al.* 1992), and white dwarfs in CVs (Webbink 1990).

### 2.6.3 X-ray line emission with *Ginga*

As shown in figure 2.33, the hard X-ray spectra of MCVs obtained by *Ginga* exhibits a strong iron emission line. Although this line had been already known in previous observation, the large effective area of *Ginga* allowed the line intensity and its center energy to be measured with a high accuracy; the former with 30% accuracy, and the latter within 0.1 keV, under a typical observing condition. The observed iron line feature is accounted for by single narrow component within the energy resolution of *Ginga* ( $\sim 20\%$  FWHM at 6 keV), which is insufficient to resolve the line components.

In an X-ray spectrum, the line intensity is usually described by a quantity called equivalent width (EW); as illustrated in figure 2.35, this is defined as

$$EW = \frac{L}{F_c(E_{\text{line}})}, \quad (2.71)$$

where  $L$  is the total line flux (photons), and  $F_c$  is the continuum flux (photons / keV) at the line energy  $E_{\text{line}}$ . Thus, it has a dimension of energy.

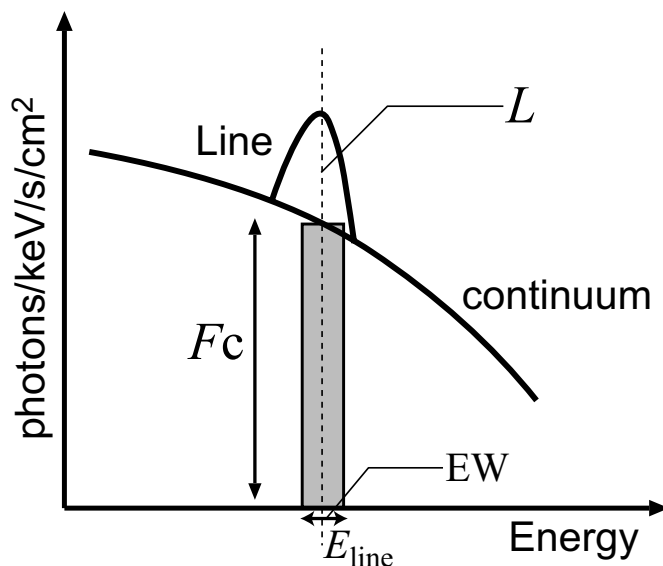


Figure 2.35: The definition of equivalent width (EW) for a line with line center energy  $E_{\text{line}}$ .

As clearly seen in the top panel of figure 2.36, the observed line EW of MCVs tends to decrease with increasing continuum temperature. This suggests that the observed line emission mainly comes from optically thin thermal plasma. This inference is more directly supported by the measured values of  $E_{\text{line}}$ , which is significantly higher than that of cold fluorescence line (6.4 keV) as shown in the bottom of figure 2.36.

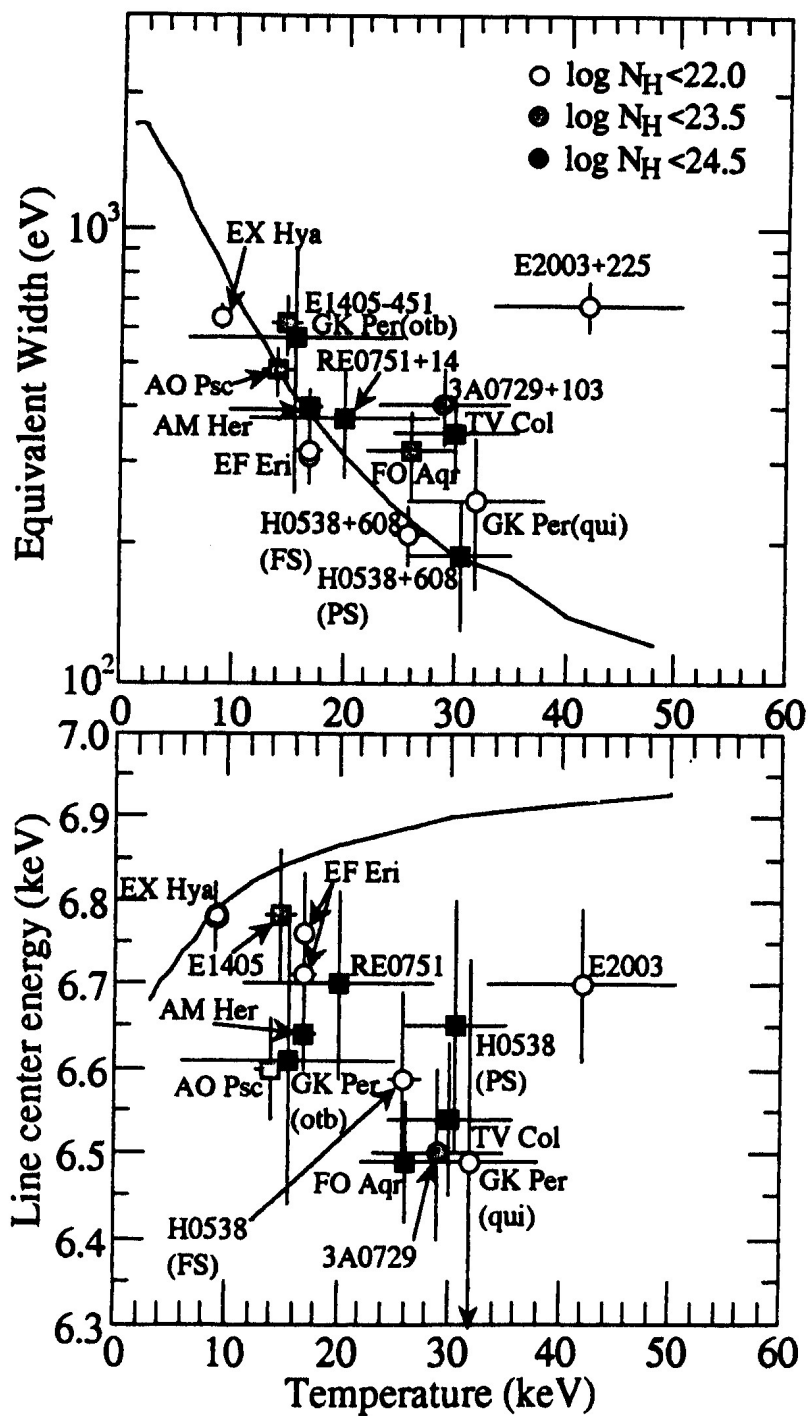


Figure 2.36: The iron line equivalent width (*top*) and line center energy (*bottom*) derived from the model fitting of the spin-phase average spectra of MCVs observed by *Ginga* (Ishida 1991). The solid lines show those calculated for plasmas in an collisional ionization equilibrium.

### 2.6.4 Spin modulation in X-rays: *Ginga* results

As had been already known previously, periodic X-ray modulations have also been seen in the light curves of MCVs obtained by *Ginga*, as exemplified in figure 2.37 (Ishida 1991). In most cases, the period of X-ray modulation agrees with the spin period of the white dwarf, which is measured in the optical band. With *Ginga* observations, a clear difference in the modulation pattern between polars and intermediate polars have been discovered as shown in figure 2.38. Thus, the modulation in harder X-rays is deeper than that in softer ones for polars, and the relation is reversed for intermediate polars.

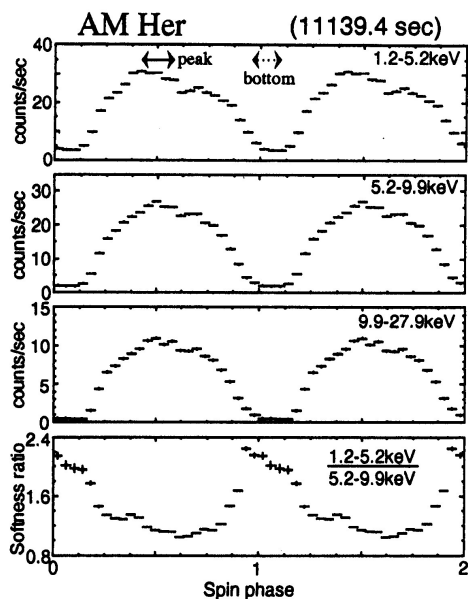


Figure 2.37: The spin-folded light curves of AM Hercuris, obtained by *Ginga* (Ishida 1991).

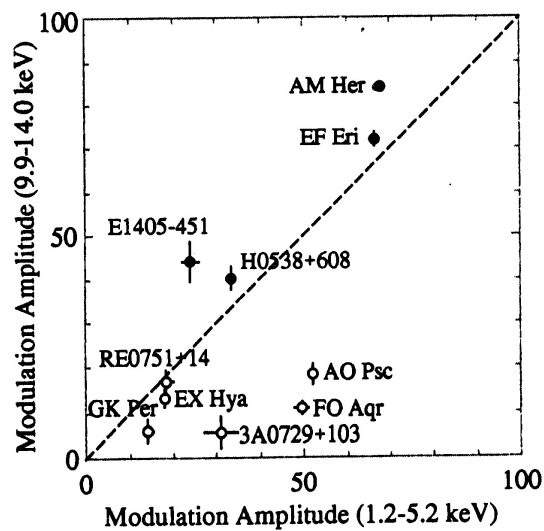


Figure 2.38: The relation between low-energy and high energy modulation amplitudes for polars (filled circle) and intermediate polars (open circles). From Ishida (1991).

Through phase-resolved spectroscopy with *Ginga*, the behavior of intermediate polars in figure 2.38 has been simply understood as a result of spin-phase dependent changes in photoelectric absorption; the absorption becomes deepest at the pulse-bottom phase, with the intrinsic flux remaining nearly constant. Since the accretion in intermediate polars is considered to occur onto two magnetic poles of the white dwarf, their spin modulation in X-rays must be mainly caused by the photoelectric absorption due to pre-shock matter, as schematically illustrated in figure 2.39 top. This idea of self-absorption is supported by the Doppler measurement of He II emission lines from the pre-shock matter (Hellier *et al.* 1987; 1990).

In contrast, the spin modulation of the X-ray intensity of polars in figure 2.38 is characterized by the large energy-independent modulation amplitude. If this modulation were caused by photo-electric absorption, the inferred hydrogen column density would be very high ( $\gtrsim 10^{24}$  cm<sup>2</sup>). Thus, their almost energy-independent modulations are mainly attributed to changes in the X-ray flux itself. The absorption in polars slightly increases at

the pulse-peak phase, as evidenced by shallower modulations in lower energies (figures 2.37 and 2.38); therefore the pulse-peak phase corresponds to nearly pole-on phase. As a result, the X-ray modulation in polars must be caused by an eclipse of the emission region by the limb of white dwarf, as schematically illustrated in figure 2.39 bottom. Furthermore, according to the detailed observations of AM Herculis with *Ginga* (Beardmore *et al.* 1995), some fraction of the emission from the accretion column, scattered and/or reflected from the WD surface, is thought to cause the X-ray modulation even while the column is fully visible [phase (a) in figure 2.39 bottom]. This picture is consistent with the fact that the rise and decline of X-ray light curves occur simultaneously with the linear polarization pulses in the optical band (Stockman and Liebert 1985; Mason 1985), which can be observed when the magnetic field line is perpendicular to us. This idea is valid for polars with single pole accretion, whereas the behavior of intermediate polars with two pole accretion cannot be explained by this idea since the other pole must be visible when one pole is eclipsed [phase (b) in figure 2.39 bottom].

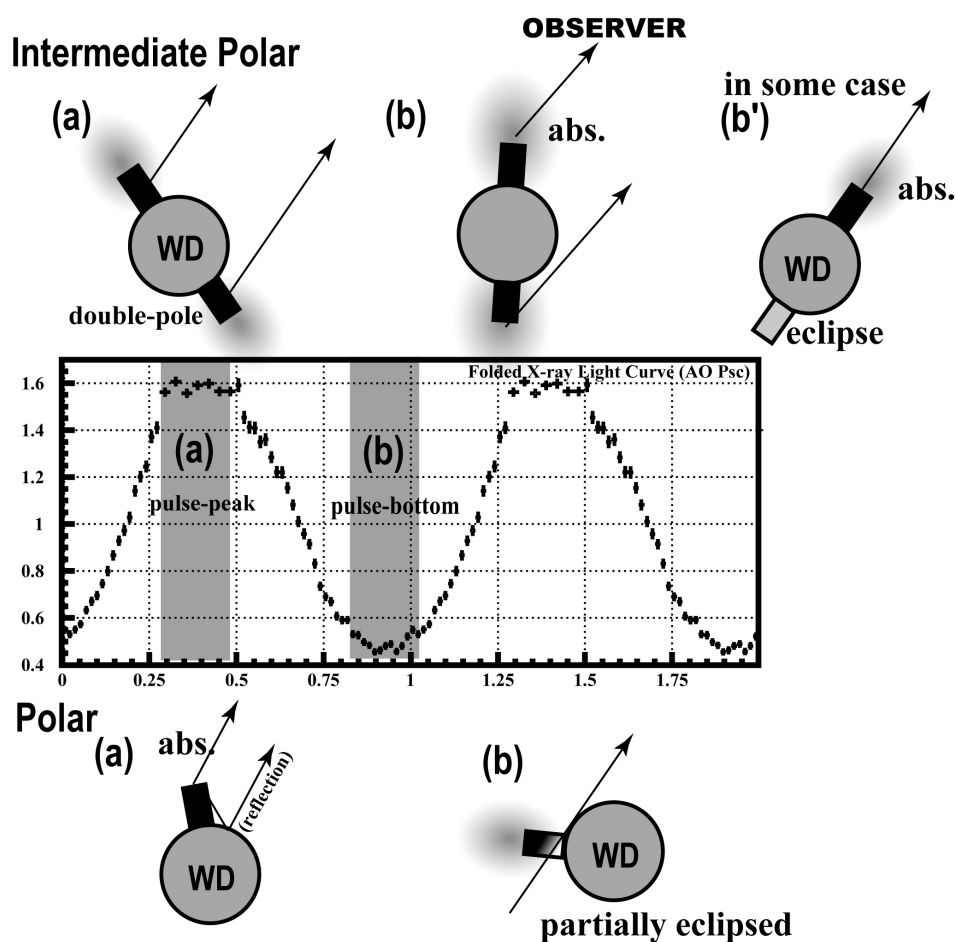
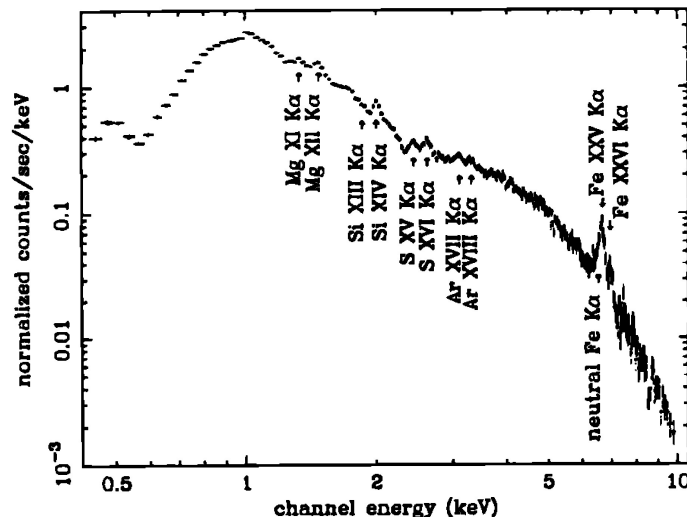
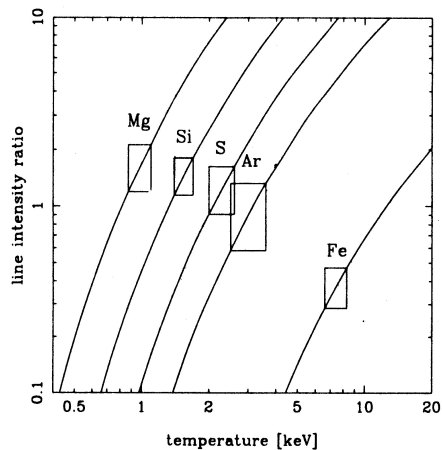


Figure 2.39: Schematic illustration of spin modulation in X-rays.

2.6.5 X-ray spectroscopy of ionized line emission with *ASCA*Figure 2.40: X-ray spectrum of EX Hydra obtained by *ASCA* (Fujimoto and Ishida 1997).

More detailed plasma diagnostics in accretion column of MCVs has been performed by Fujimoto (1998) using the fourth Japanese X-ray satellite *ASCA*, which has the energy resolution of an order of magnitude higher than *Ginga*. A typical X-ray spectrum of MCV acquired with the *ASCA* CCD camera (SIS; see section 4.2.4) is shown in figure 2.40, which again includes the response of the detector. In addition to the bremsstrahlung continuum, the spectrum bears many emission lines from major elements, such as Mg, Si, S, Ar, and Fe. Since the intensity ratio between He-like and H-like  $K_{\alpha}$  lines of an element is strongly dependent on the plasma temperature (figure 2.29), we can convert the measured line ratio of each element into a characteristic “ionization temperature”. Figure 2.41 shows the ionization temperatures thus measured in reference to various elements, seen in the *ASCA* spectrum of an MCV, EX Hya (Fujimoto and Ishida 1997). Thus, different elements indicate different temperatures. This is easily understood as a result of the vertical temperature gradient in the accretion column (section 2.4.6), which produces a multi-temperature spectrum. Lines with lower energies are mainly emitted from cooler regions closer to the white dwarf surface.

Figure 2.41: Temperatures of the emission region of EX Hydra, determined from the line intensity ratios with *ASCA* (Fujimoto 1998). Solid curves represent the expected He-like to H-like  $K_{\alpha}$  line ratios for Mg, Si, S, Ar, and Fe, calculated against the plasma temperature. Boxes show the observed values with 90% confidence uncertainties.

Adopting the Aizu distribution (equation 2.62), the shock temperature  $kT^{\text{sh}}$  and the bottom one  $kT_{\text{b}}$  are restricted by the observed line ratios of major elements, as exemplified for the case of EX Hya in figure 2.42. As shown in figure 2.43, the obtained shock temperature agrees well with the depth of the gravitational potential of the white dwarf in this system (equation 2.37), calculated from an optically estimated mass (section 2.1.3) and the theoretical mass-radius relation (section 2.1.2).

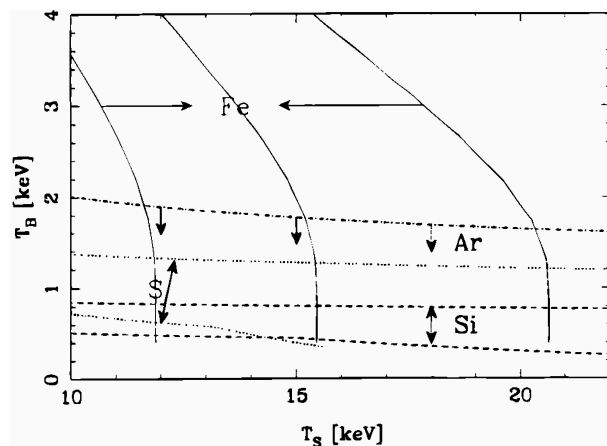


Figure 2.42: The 90% confidence regions for shock temperature  $kT_{\text{s}}$  and the bottom temperature  $kT_{\text{B}}$  of EX Hya (Fujimoto and Ishida 1997). The dash, dot, dash-dot, and solid curves represent constraints derived with silicon, sulfur, argon, and iron, respectively. The center line for the Fe region corresponds to the best fit value. The obtained  $kT^{\text{sh}}$  is  $15.4^{+5.3}_{-2.6}$  keV.

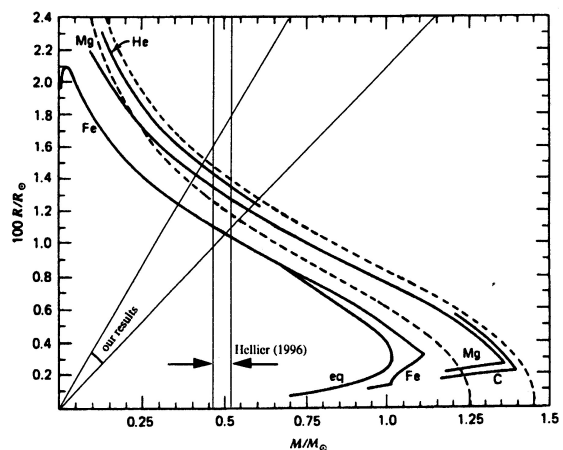


Figure 2.43: Constraints on the mass versus radius ratio of EX Hya obtained with *ASCA*, presented in the mass-radius plane (Fujimoto 1998). The mass determination by Hellier (1996) and the theoretical mass-radius relations (section 2.1.2) obtained by Hamada & Salpeter (1961) are also shown.

Systematic studies with *ASCA* using this method have been made by Ezuka and Ishida (1999). They found that the temperature gradient is a common feature in MCVs, and the continuum temperature is slightly higher than the ionization temperature, as shown in figure 2.44. This fact is another evidence of multi-temperature plasma. Hence, the temperature structure in the accretion column has been observationally confirmed by *ASCA*, the metal abundances can be calculated by the absolute value of the observed line intensities. The obtained abundances for 19 MCVs are distributed in sub-solar range, as shown in figure 2.45.

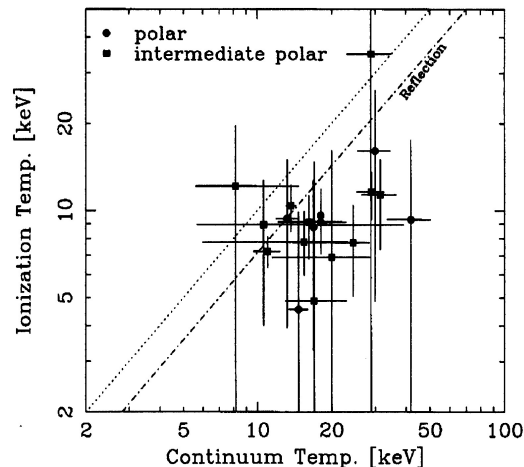


Figure 2.44: A scatter plot between the ionization temperature and the continuum temperature obtained by systematic data analysis of *ASCA* for 19 MCVs (Ezuka & Ishida 1999). The dotted line indicates an agreement between the two temperatures, and the dot-dashed line indicates a 40% correction to the continuum temperature.

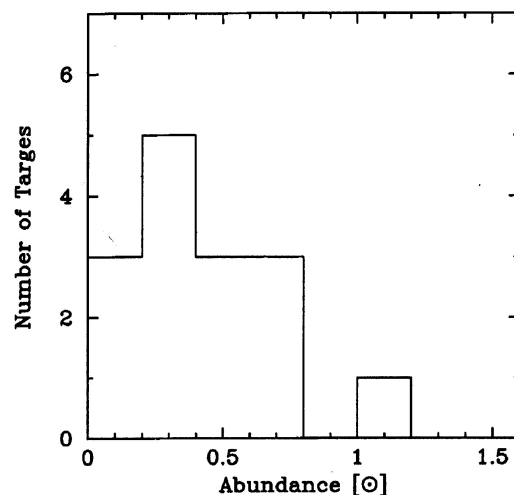


Figure 2.45: The metal abundance distribution determined by *ASCA* measurements of emission lines for 19 MCVs (Ezuka & Ishida 1999).

### 2.6.6 The origin of fluorescent iron line

With the energy resolution of *ASCA*, the cold iron fluorescence  $K_\alpha$  line has been separated from the ionized lines, and detected from many MCVs at  $EW \sim 100$  eV. The fluorescent line is considered to be produced in surrounding cold matter or atmosphere on the white dwarf surface, which are irradiated by hard X-rays from the accretion column. Figure 2.46 shows the scatter plot of equivalent width of iron  $K_\alpha$  fluorescent lines and the column density of absorption measured by *ASCA*. Thus, the obtained EWs far exceed those expected from the X-ray irradiated pre-shock matter. This difference can be accounted for by an additional reprocessing on the white dwarf surface. Therefore, the fluorescent  $K_\alpha$  emission is thought to be emitted mainly from the white dwarf surface.

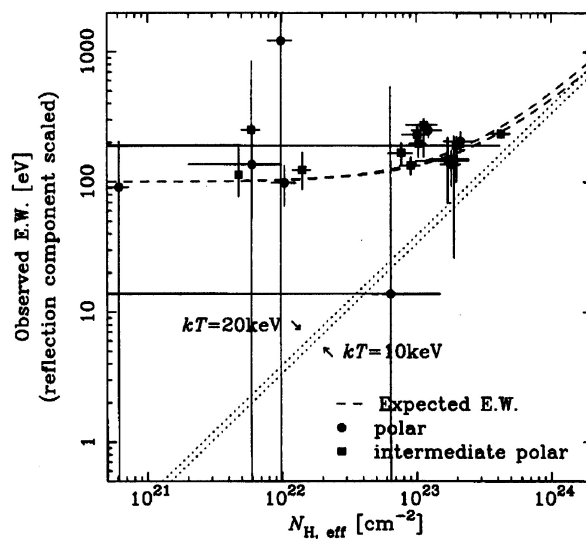


Figure 2.46: A scatter plot between the hydrogen column density and the equivalent width of the fluorescent iron  $K_\alpha$  emission line measured by *ASCA* (Ezuka & Ishida 1999). Dotted lines show expected relation when a point-like thermal bremsstrahlung source is surrounded by a uniform absorber over the  $4\pi$  solid angle. Dashed curves represent the equivalent widths expected from the sum of contributions from the white dwarf surface and the line-of-sight absorber.

### 2.6.7 Discovery of the strong line object POLE by *ASCA*

Extremely strong ionized iron emission lines have been discovered from a few polars with *ASCA*. For example, AX J2315–0592 exhibits a strong ionized Fe-K $_{\alpha}$  line centered at  $6.84^{+0.13}_{-0.09}$  keV, whose equivalent width reaches  $900^{+300}_{-200}$  eV (Misaki et al. 1996). This object has been serendipitously discovered by *ASCA* in 1995, and identified as a polar by the follow up optical spectroscopy (Thomas and Reinsch 1995). Similarly, RX J1802.1+1804, which has been discovered by *ROSAT* All-Sky-Survey in 1990 and categorized as a polar (Greiner et al. 1998), exhibits a strong Fe-K $_{\alpha}$  line with EW  $\sim 4000$  eV in an *ASCA* spectrum (Ishida et al. 1998). In order to interpret these strong lines simply as thermal plasma emission, the plasma metallicity would have to much exceed one solar abundance;  $\sim 2$  solar for the former, and  $3.04 \pm 1.47$  solar for the latter. Although MCVs often exhibit highly ionized Fe-K lines, the implied abundances are usually sub-solar (figure 2.45), so these value are unusually high.

There is another example of extremely strong iron K line emitter; an X-ray transient source AX J1842–0423, which is discovered with *ASCA* on the Galactic plane (Terada et al. 1999). Since its X-ray spectrum is accounted for as that from a thin-thermal plasma, and the allowed source size is  $10^{8.5-17.7}$  cm, this object may be a polar with a strong intrinsic absorption. Its spectrum shows a very conspicuous iron emission line at  $6.78^{+0.10}_{-0.13}$  keV, whose EW is extremely large at  $4000^{+1000}_{-500}$  eV as shown in figure 2.47. To explain this line equivalent width, a plasma metallicity as high as  $3.0^{+4.3}_{-0.9}$  solar abundance would be required.

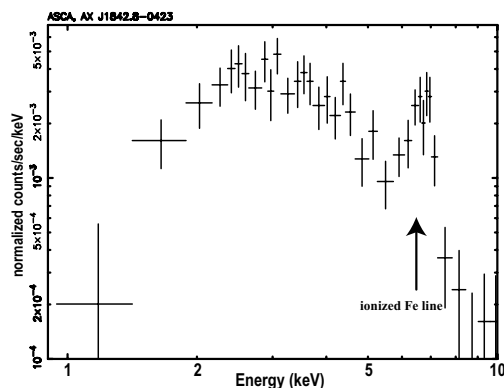


Figure 2.47: The X-ray spectrum of AX J1842–0423 with *ASCA*.

There is a common feature among these object, which may provide a clue to the strong iron K line. AX J2315–0592 exhibits a large ( $87 \pm 2\%$ ,  $57 \pm 2\%$ ) orbital modulation in the 0.7 – 2.3 keV and 2.3 – 6.0 keV light curves, but almost no modulation in the 6.0 – 10.0 keV band. Similarly, RX J1802.1+1804 exhibits a large ( $\sim 100\%$ ) orbital modulation amplitude below 0.5 keV according to a *ROSAT* observation (Greiner et al. 1998), but the *ASCA* light curves are extremely flat (Ishida et al. 1998). In AX J1842–0423, there is no periodicity over the period range of 62.5 ms to a few hours. The lack of hard-

band modulation implies that a constant fractional volume of the accretion columns is observed throughout the rotational phase, and hence the inclination of the orbital plane  $i$  is rather small. Then, the soft-band modulation must be due to changes in absorption by the pre-shock accretion flow, indicating that we observe nearly right down onto a single pole at the absorption maximum. This in turn requires the magnetic co-latitude  $\beta$  to be close to  $i$ . In short, these systems are inferred to have  $\beta \sim i \sim 0$ . We hence name these polars “POLE (Pole-On Line Emitter)” (Terada *et al.* 2001). Although POLEs have these common features, the emission mechanism of the surprisingly strong line have not been solved yet.

# Chapter 3

## X-RAY BEAMING MECHANISM IN ACCRETION COLUMN

### 3.1 An Overview

The aim of this chapter is to find out a new idea to solve the mystery of unrealistically strong iron line emission from POLE (section 2.6.7). We think the line equivalent widths in POLEs are unphysical, because they are 2 – 3 times higher than those of other polars (figure 2.45). In other words, we consider that the iron line equivalent widths of POLEs are somehow enhanced by an unknown yet universal mechanism, rather than indicating a truly high metallicity of those systems.

The only difference between POLEs and “normal” polars is that the former objects are always observed from pole-on direction to their accretion columns. Therefore, if there is a mechanism which can enhance line photons along the magnetic field lines, we can explain the mystery of POLE. This mechanism must produce an enhancement by a factor of  $\gtrsim 2$  to explain the large line equivalent widths observed from POLEs. Since the mechanism must enhance the line equivalent width, which is defined as a ratio of line flux to continuum flux (see section 2.6.3), we have to find a physical process that distinguishes line photons from continuum photons. Thomson scattering and free-free absorption work on both photons, whereas resonance scattering, which is intrinsic to atomic radiative transitions (section 2.5.4), acts only on line photons. Furthermore, plasma in accretion column, that is optically thin for the former processes (section 2.4.5), is at the same time optically thick for the latter as detailed in section 3.2. Thus, we focus on the resonance scattering process.

Since the optically-thick resonance line photons can escape only from the surface of an accretion column, their equivalent width must be enhanced into the pole-on direction, if the column has a flat coin-like shape and hence its surface area appears larger when viewed pole-on. This effect, called “geometrical beaming”, is discussed further in later section 3.2. However, its enhancement is insufficient to solve the mystery of POLEs. In section 3.3, we introduce an additional new mechanism, called as “physical beaming”, based

on a consideration of stochastic transfer of resonance photons in an accretion column, where physical parameters, such as temperature, density, and bulk velocity, have vertical gradient (section 2.4.6). In order to quantitatively examine our novel idea, we carry out extensive Monte-Carlo simulations in section 3.4.

### 3.2 Geometrical Beaming of Resonance Line

Assuming that the scattering medium has neither bulk flow nor local turbulence, the cross section of resonance scattering,  $\sigma_R$ , for a photon with energy,  $E_0$ , can be described generally as

$$\sigma_R = \frac{\pi e^2}{m_i c} f_{12} \frac{h}{\sqrt{2\pi} \Delta E} \exp \left\{ -\frac{(E_0 - E_{RS})^2}{2\Delta E^2} \right\} \text{cm}^2 \quad (3.1)$$

where  $f_{12}$  is the oscillator strength for Lyman- $\alpha$  transition ( $n = 1$  to  $2$ ),  $E_{RS}$  is the resonance energy in the rest frame, and  $\Delta E$  is an energy width for resonance (equations 10.68 and 10.70 in Rybicki & Lightman 1979). Numerically, the first factor is  $\frac{\pi e^2}{m_{Fe} c} f_{12} = 1.2 \times 10^{-17} \text{cm}^2$ . The energy width,  $\Delta E$ , is determined by the natural broadening, which is approximately described by a width of  $\Delta E^{na}$ , and thermal Doppler broadening effect with a width of  $\Delta E^{th}$ , as detailed below.

The natural broadening originates from uncertainty principle; namely, the spread in energy  $\Delta E^{na}$  and the duration  $\Delta t$  in the relevant energy state must satisfy

$$\Delta E^{na} \Delta t \sim \hbar. \quad (3.2)$$

In optically thin CIE plasmas (section 2.5.3),  $\Delta t$  is determined by the spontaneous decay time, which has the same order as the inverse of spontaneous transition rate. The energy distribution of  $\Delta E^{na}$  is described by Lorentzian shape. Typically, the natural width in approximate description by Gaussian becomes

$$\Delta E^{na} \sim 1\text{eV}. \quad (3.3)$$

The Doppler broadening is caused by thermal motion of ions. Since the plasma has a typical temperature of few tens keV (equation 2.38), the thermal velocity of ion of mass  $m_i$  reaches

$$\begin{aligned} v_i &= \sqrt{\frac{kT}{m_i}} \\ &= 2.4 \times 10^7 \left(\frac{z}{h}\right)^{\frac{1}{5}} \left(\frac{m_i}{56m_H}\right)^{-\frac{1}{2}} \left(\frac{kT}{16\text{keV}}\right)^{\frac{1}{2}} \text{cm s}^{-1}, \end{aligned} \quad (3.4)$$

with  $m_H$  the mass of a hydrogen atom. Thus, the thermal Doppler width of the resonance becomes

$$\begin{aligned} \Delta E^{th}(z) &= E_0 \frac{v_i}{c} \\ &= 3.7 \left(\frac{z}{h}\right)^{\frac{1}{5}} \left(\frac{m_i}{56m_H}\right)^{-\frac{1}{2}} \left(\frac{E_0}{6.695\text{keV}}\right) \left(\frac{kT}{16\text{keV}}\right)^{\frac{1}{2}} \text{eV}. \end{aligned} \quad (3.5)$$

Comparing equations (3.3) and (3.5), indicates  $\Delta E$  of a few eV, which is mainly due to  $\Delta E^{\text{th}}$ . From equation (3.1), the cross section of resonance scattering at the line-center energy,  $E_0 = E_{\text{RS}}$ , is therefore given as

$$\sigma_{\text{R}} \simeq 2.0 \times 10^{-18} \left(\frac{z}{h}\right)^{-\frac{1}{5}} \left(\frac{m_i}{56m_{\text{H}}}\right)^{\frac{1}{2}} \left(\frac{E_0}{6.695\text{keV}}\right)^{-1} \left(\frac{kT}{16\text{keV}}\right)^{-1/2} \text{cm}^2. \quad (3.6)$$

Since the typical scale of an accretion column is  $\sim 10^7$  cm and the typical number density is  $\sim 10^{15}$   $\text{cm}^{-3}$  (section 2.4.5), the optical depth for the resonance scattering along a path length  $l$  is calculated to be

$$\tau_{\text{R}} = 36 \left(\frac{n_e}{7.7 \times 10^{15} \text{cm}^{-3}}\right) \left(\frac{A_{\text{Fe}}}{4.68 \times 10^{-5}}\right) \left(\frac{l}{5 \times 10^7 \text{cm}}\right), \quad (3.7)$$

at the energy of hydrogenic iron  $\text{K}_{\alpha}$  line, where  $A_{\text{Fe}}$  is the abundance for iron by number, which is normalized to the value for one solar. Thus, in an accretion column, the plasma that is optically thin for both electron scattering and free-free absorption (equations 2.46 and 2.47) is at the same time optically thick for resonance lines. As a result, the resonance line photons can escape only from locations close to the surface of accretion column. If the accretion column has a flat coin-shaped geometry, and our line-of-sight is nearly pole-on to it, we will observe the enhanced Fe-K lines simply because a larger surface area can be viewed. We call this effect “geometrical beaming” of resonance line.

In the extremely optically thick case when the resonance photons can only escape from the surface of the column, the directional photon flux emerging from the column is given as

$$f(\theta) d\cos\theta \propto \pi r^2 \cos\theta + 2rh \sin\theta, \quad (3.8)$$

where  $\theta$  is the angle measured from the column axis. Therefore, the flux along  $\theta \simeq 0$  is enhanced by a factor of

$$\frac{f(\theta)}{\langle f \rangle} = \frac{\pi r^2}{\frac{1}{2}\pi r^2 + \frac{\pi}{2}rh} = \frac{2}{1 + \frac{2}{\pi} \left(\frac{h}{r}\right)}, \quad (3.9)$$

where  $\langle f \rangle$  is the average of  $f(\theta)$  over  $\theta$ . Since, at the coin-shaped limit ( $h/r \rightarrow 0$ ), this approaches 2, the resonance-line emission can be enhanced by a factor of 2.0 to the angular average. However, this enhancement is still insufficient to explain the behavior of POLEs. Furthermore, in the extremely optically thick limit, resonance photons can not escape as line emission; i.e., line structure is destroyed as photons transfer in the plasma by energy shifts via Compton scattering. Therefore, additional mechanism to cause anisotropical radiative transfer of line photons is required, although geometrical beaming effect must be operating in accretion column of MCVs.

### 3.3 Physical Beaming by Velocity Gradient

In this section, we show the additional beaming mechanism of resonance line by the vertical gradient of  $kT$ ,  $u$ , and  $n_e$  in the accretion column (section 2.4.6).

Let us imagine, for example, that a line photon of rest-frame energy,  $E_0$ , is produced at a position near the bottom of accretion column,  $z \simeq 0.1h$ , where the emissivity of helium-like iron line photon becomes maximum (figure 2.30), and that this photon moves vertically by its mean free path of resonance scattering  $l_R$ , which is given as

$$\begin{aligned} l_R &= (\sigma_R A_{\text{Fe}} n_e)^{-1} \\ &= 1.3 \times 10^6 \left(\frac{z}{h}\right)^{\frac{3}{5}} \left(\frac{n_e^{\text{sh}}}{7.7 \times 10^{15} \text{cm}^{-3}}\right)^{-1} \left(\frac{A_{\text{Fe}}}{4.68 \times 10^{-5}}\right) \text{cm}. \end{aligned} \quad (3.10)$$

This roughly equals to  $0.07h(\frac{z}{h})^{3/5}$ , because  $h$  is  $\sim 10^7$  cm as described in equation (2.44). Adopting the Aizu solution of the bulk flow velocity  $u$  (equation 2.62), will change by  $\Delta u = 4.0 \times 10^6$  cm s $^{-1}$  at  $z \simeq 0.1h$  over a distance  $l_R$ . So, over the same distance  $\sim l_R$ , the resonance energy for the line photon shifts due to Doppler effect by

$$\begin{aligned} \Delta E^{\text{bk}} &= E_0 \frac{\Delta u}{c} \\ &\sim 0.9 \left(\frac{E_0}{6.695 \text{keV}}\right) \left(\frac{u^{\text{sh}}}{0.9 \times 10^8 \text{cm}^{-3}}\right) \text{eV}. \end{aligned} \quad (3.11)$$

As the photon moves upward over a significant fraction of the column height, the local resonance center energy thus changes by  $\sim 10$  eV in the rest frame, as shown in the left panel of figure 3.1. On the other hand, the resonance profile becomes broader as photon moves upwards (figure 3.1 left panel), since the energy width  $\Delta E^{\text{th}}$  for resonance has a temperature dependence as described in equation (3.5). Numerically, the accumulated shifts of  $\Delta E^{\text{bk}}$  for upward-moving photons, produced at various depths of the accretion column, are shown in right panel of figure 3.1. The energy width  $\Delta E^{\text{th}}$  is also plotted in dashed curve.

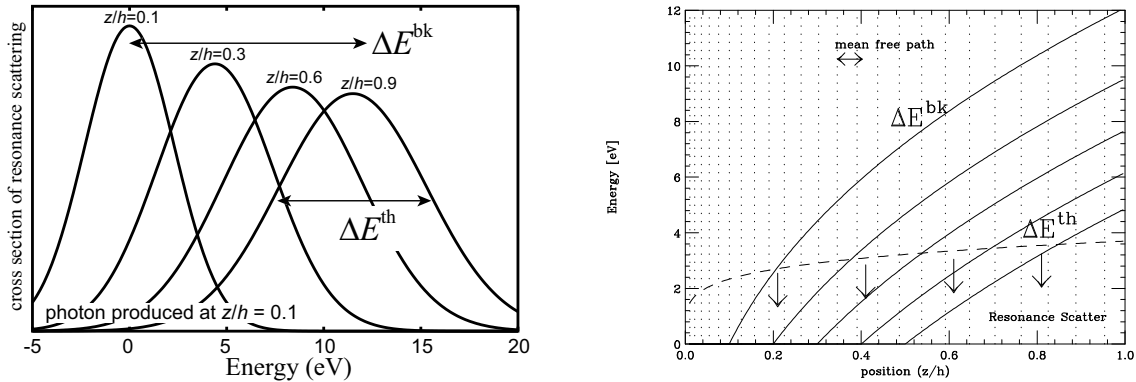


Figure 3.1: (*left*) Cross section of resonance scattering for an iron  $K_\alpha$  line photon, which is produced at  $z/h = 0.10$  and moves vertically. The resonance centroid energy shifts by  $\Delta E^{\text{bk}}$  as a function of the vertical position (specified by  $z/h$ ). (*right*) The cumulative shift of the resonance energy (solid line) for upward-moving Fe-K line photons, which are produced at  $z = 0.1h, 0.2h, 0.3h, 0.4h$ , and  $0.5h$ . The thermal width of the resonant Fe-K line is given by the dashed curve. The dotted vertical lines are separated from adjacent ones by the mean free path  $l_R$  of resonant photons.

Figure 3.1 clearly shows that, if a line photon gradually moves upward through repeated scattering, its energy becomes different from the local resonance energy, by an amount  $\Delta E^{\text{bk}}$  (equation 3.11) which eventually becomes larger than the thermal width  $\Delta E^{\text{th}}$  (equation 3.5). Numerically, this ratio for a photon produced at  $z = z_0$  can be described as

$$\begin{aligned} \frac{\Delta E^{\text{bk}}(z)}{\Delta E^{\text{th}}(z)} &= \frac{\Delta u}{v_i} = \frac{u^{\text{sh}} \left\{ (z/h)^{\frac{2}{5}} - (z_0/h)^{\frac{2}{5}} \right\}}{\sqrt{3 \frac{\mu m_{\text{H}}}{m_i}} u^{\text{sh}} \left( \frac{z}{h} \right)^{\frac{1}{5}}} \\ &= 5.5 \left( \frac{m_i}{56 m_{\text{H}}} \right)^{\frac{1}{2}} \left( \frac{\mu}{0.615} \right) \left\{ \left( \frac{z}{h} \right)^{\frac{1}{5}} - \left( \frac{z_0}{h} \right)^{\frac{2}{5}} \left( \frac{z}{h} \right)^{-\frac{1}{5}} \right\} \end{aligned} \quad (3.12)$$

$$\simeq 2.2 \left( \frac{m_i}{56 m_{\text{H}}} \right)^{\frac{1}{2}} \left( \frac{\mu}{0.615} \right) \left( \frac{\delta z}{h} \right) \left( \frac{z}{h} \right)^{-\frac{4}{5}} [\delta z \ll h], \quad (3.13)$$

with  $\delta z = z - z_0$ , and we used the relation of  $kT^{\text{sh}} = 3\mu m_{\text{H}}(u^{\text{sh}})^2$  from equations (2.38) and (2.39). Then, the photon is no longer scattered efficiently, and can escape out. This effect does not occur in the horizontal direction because of little velocity gradient. As a result, a resonant line photon produced near the bottom of accretion column escapes with a higher probability when its net displacement due to random walk is directed upward, rather than horizontal. In other words, iron K line photons are collimated to the vertical direction. The schematic view of this beaming effect is illustrated in figure 3.2. We call this effect “physical beaming”. The essence of this effect is that the mass of iron,  $m_i$  in equation (3.12), is high enough for the bulk velocity gradient to overcome the thermal line broadening.

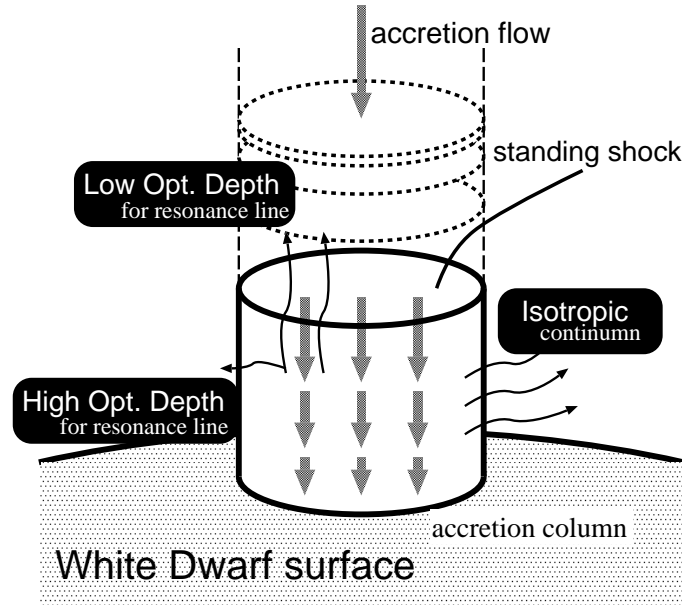


Figure 3.2: A schematic view of the physical beaming effect due to resonance scattering in the accretion column on white dwarfs.

### 3.4 Numerical Simulations of the Radiative Transfer

The beaming effects described in sections 3.2 and 3.3 involve significant scattering processes, which make analytic calculation difficult. In this section, we accordingly examine the proposed effects using Monte-Carlo simulations.

#### 3.4.1 Basic conditions of the Monte-Carlo simulation

Consider a simple cylinder of height  $h$  and radius  $r$ , filled with X-ray emitting plasma. In our simulation, we adopt Aizu solution for  $kT$ ,  $n_e$ , and  $u$  as described by equation (2.62). We first produce a number of Monte-Carlo iron line photons. The location of photon production is made proportional to its emissivity, which in turn is determined by  $kT$  and  $n_e$  there, using the calculations by Mewe *et al.* (1985) as shown in figure 2.27. We isotropically randomize their initial direction of propagation in the rest frame of iron nuclei. The line energy of each iron photon is also randomized; i.e. the average value of the energy is Doppler shifted in the observer frame according to the bulk velocity law shown in equation (3.11), and its dispersion is determined by the local thermal motion of equation (3.4). We then trace the propagation of each line photon with a constant step length, which is taken to be 1/100 of the mean free path of resonance scattering at the bottom of the cylinder, where the temperature falls below 1 keV. At each step, the behavior of photon is determined by calculating the probabilities of resonance scattering and Compton scattering. We trace its propagation until it moves outside the cylinder. Typical trajectories of line photons are schematically illustrated in figure 3.3. We can thus tabulate the final energies, final moving directions, and escaping positions for the simulated line photons.

#### 3.4.2 Algorithm for the propagation of line photons

Treatment of the resonance scattering process, taking into account both the bulk flow and the thermal motion of ions, is a key point of the present simulation. As seen from the observer, a representative ion located at the  $i$ -th position of photon propagation has a velocity  $\vec{w}_i$ , which is expressed as a sum of the bulk flow velocity,  $\vec{u}(\vec{r}_i)$ , and a random thermal velocity,  $v$ ; i.e.,  $\vec{w}_i = \vec{u}(\vec{r}_i) + \vec{v}$ . The energy,  $E_i^{\text{in}}$ , of an incoming photon relative to this representative ion is given as

$$E_i^{\text{in}} = E_{i-1}^{\text{out}} \left\{ 1 + (\vec{w}_{i-1} - \vec{w}_i) \cdot \frac{\vec{e}_{i-1,i}}{c} \right\}, \quad (3.14)$$

where  $E_{i-1}^{\text{out}}$  is the outgoing photon energy as expressed in the rest frame of the previous scatterer, and  $\vec{e}_{i-1,i}$  is the unit vector along the photon propagation direction from the  $(i-1)$ -th to the  $i$ -th scattering sites as shown in figure 3.4. Thus the scattering probability  $P_R(\vec{r}_i)$  is calculated as

$$P_R(\vec{r}_i) \propto \sigma_R(E_i^{\text{in}}, kT) \times n_i(\vec{r}_i), \quad (3.15)$$

where  $n_i(\vec{r}_i)$  is the local ion density there (equations 2.40), and  $\sigma_R(E_i^{\text{in}}, kT)$  is given by equation (3.6). If the scattering occurs at  $\vec{r}_i$ , we randomize the line photon energy from  $E_i^{\text{in}}$  to  $E_i^{\text{out}}$  according to the natural width, and isotropically randomize the direction of the outgoing photon in the rest frame of the present scatterer. If, instead, the scattering does not occur at  $\vec{r}_i$ , we proceed to the next step without changing either the direction or energy of the photon. Thus, our calculation automatically includes both the bulk-flow Doppler effect and the thermal broadening. However, we do not consider energy shifts by the ion recoil, which is completely negligible. We do not consider higher-order Doppler effects (of order  $(w/c)^2$  or higher) either, since we typically have  $|w/c| \sim 10^{-2} - 10^{-3}$ . The scattering probability for a non-resonant photon is set to 0.

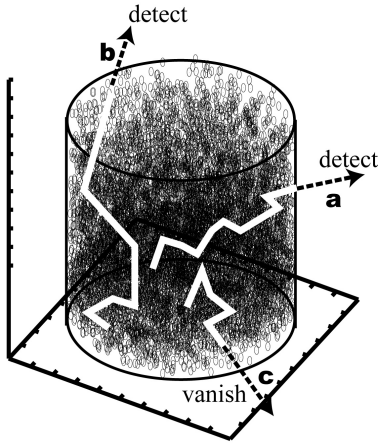


Figure 3.3: A schematic illustration of typical paths of resonance line photons. (a) horizontal path with thick optical depth; (b) vertical path where optical depth is reduced as photon moves upwards; (c) photon goes out from the bottom of cylinder.

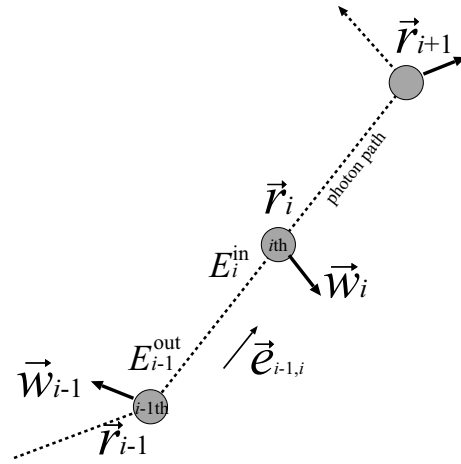


Figure 3.4: Schematic illustration of each step in our calculation;  $\vec{r}_i$  is the calculation site at the  $i$ -th step,  $\vec{w}_i$  is the ion motion there in the observer's frame, which is a sum of bulk flow motion and random thermal motion, and  $E_i$  is the photon energy in the rest frame of the  $i$ -th ion (see the text).

In addition to the resonance scattering, we must consider the Compton scattering process by a thermal electron. Since the electron temperature,  $kT_e$ , is equal to that of ions (equation 2.45) in the accretion column, it is as high as a few tens keV (equation 2.38). Accordingly, the electron velocity reaches

$$v_e = \sqrt{\frac{kT}{m_e}} = 0.18c \left( \frac{z}{h} \right)^{\frac{1}{5}} \left( \frac{kT}{16\text{keV}} \right)^{\frac{1}{2}}, \quad (3.16)$$

where  $c$  is the light velocity. Thus, a single Compton or inverse Compton scattering will change the photon energy by more than  $\sim 1$  keV, as shown in figure 3.5, far beyond the resonance energy width of a few eV. Therefore, the resonance scattering can no longer occur after a Compton scattering.

When a Compton scattering occurs at  $\vec{r}_i$  in our calculation code, we first convert physical quantities from the observer's frame into the rest frame of the scattering electron, which has a random thermal velocity and the bulk flow velocity. We then calculate the scattering angle,  $\theta_{\text{CMP}}$ , following the Klein-Nishina formula, which is almost identical to the classical formula in the iron line energy region as shown in figure 3.6. We also calculate the photon energy after the scattering as

$$E_i^{\text{out}} = \frac{E_i^{\text{in}}}{1 + \frac{E_i^{\text{in}}}{m_e c^2} (1 - \cos \theta'_{\text{CMP}})}, \quad (3.17)$$

where the notation  $'$  means the value in the electron frame. Finally, we convert these values back into those in the observer's frame. In this way, both the Compton and the inverse Compton process are described in our calculation, and the anisotropic angular distribution of Compton scattering caused by the bulk motion of electron is also be taken into account. In our calculation, we neglect the process that the energy of a Compton-scattered continuum photon comes accidentally into the resonance energy range, since we do not generate continuum photons in the Monte-Carlo code. Under the condition appropriate for our study, this process is expected to affect the iron-line equivalent width only by  $\sim 3$  eV, and it hence negligible.

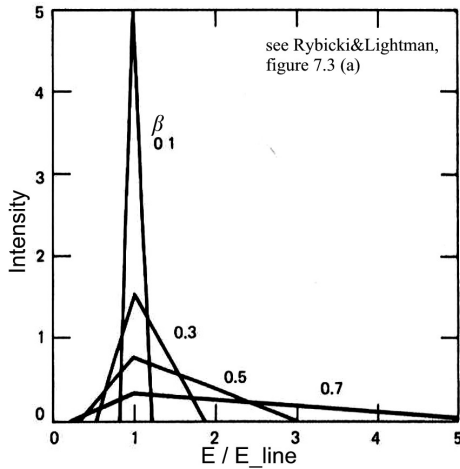


Figure 3.5: The inverse Compton spectra from a single scattering by electrons with various velocities (figure 7.3 in Rybicki and Lightman, 1979).

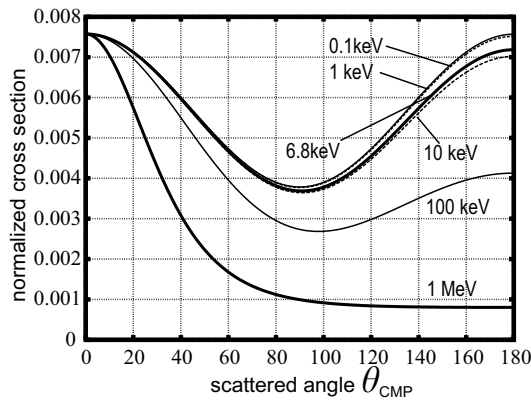


Figure 3.6: The cross section for Compton scattering by the Klein-Nishina formula.

### 3.4.3 Confirmation of our calculation code

We constructed the Monte-Carlo simulation code, consisting of more than 2300 lines, by ourselves (not using any ready-made calculation code). First, we confirmed individual functions in our code. We paid a particular attention to the process of randomization, which is used in setting the initial conditions in generating photons, in the calculation of scattering probabilities, and in the generation of scattered angles after the resonance and Compton processes. In our calculation, the most accurate expression must be needed for randomizing probability of Compton scattering, which is typically of order  $\sim 10^{-5}$  (the cross section of  $\sim 10^{-25}$  cm<sup>2</sup>, typical electron density of  $10^{15}$  cm, and a step length of  $\sim 10^5$  cm; see equation 3.15); thus, an accuracy exceeding  $10^6$  is required for randomization. We used the randomization function `aste_rnd()` in `aste_tool` package, which has been developed for analysis tools of the next generation Japanese X-ray satellite *ASTRO-E*. We have confirmed that this function can generate randomized number completely to the order of  $10^{17}$ -th place, whose accuracy is enough for our calculation, whereas the standard pseudo-random function `rand()` reaches only  $10^7$ -th place.

For the initial step of photon generation in our code, we confirmed the position distribution of the generated line photons to follow their emissivity, as exemplified in figure 3.7. In the next propagation step, as demonstrated in figure 3.8, we confirmed the distribution of free path length for resonance scattering to follow the probability specified by the surrounding temperature and ion density (equation 3.10). Similarly, we examined our treatment of Compton scattering, and confirmed that the scattering angle in the electron frame is distributed as predicted by the Kline-Nishina formula, as shown in figure 3.9. The energy shift with Compton scattering produced by our code is also distributed in accordance with the analytic solution, as shown in figure 3.10. Slight mismatch to the expected curve in figure 3.10 is negligible in calculating an angular distribution of resonance photons, since the energy of Comptonized photons are completely out of the resonance condition, in either way.

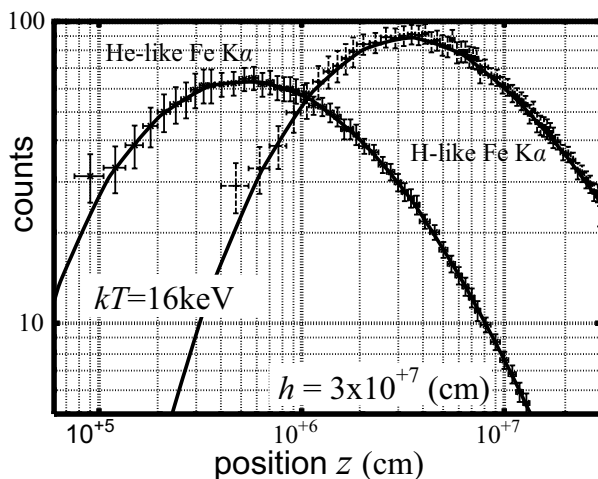


Figure 3.7: The distribution of initial positions where iron line  $K_\alpha$  photons are produced, assuming that the plasma temperature is 16 keV, the column height is  $3 \times 10^7$  cm, and the column radius is  $10^8$  cm. Solid curves represents the analytic distribution, as already shown in figure 2.30 left, calculated by adopting the emissivity table by Mewe *et al.* (1985), and Aizu solution of post-shock flow (section 2.4.6).

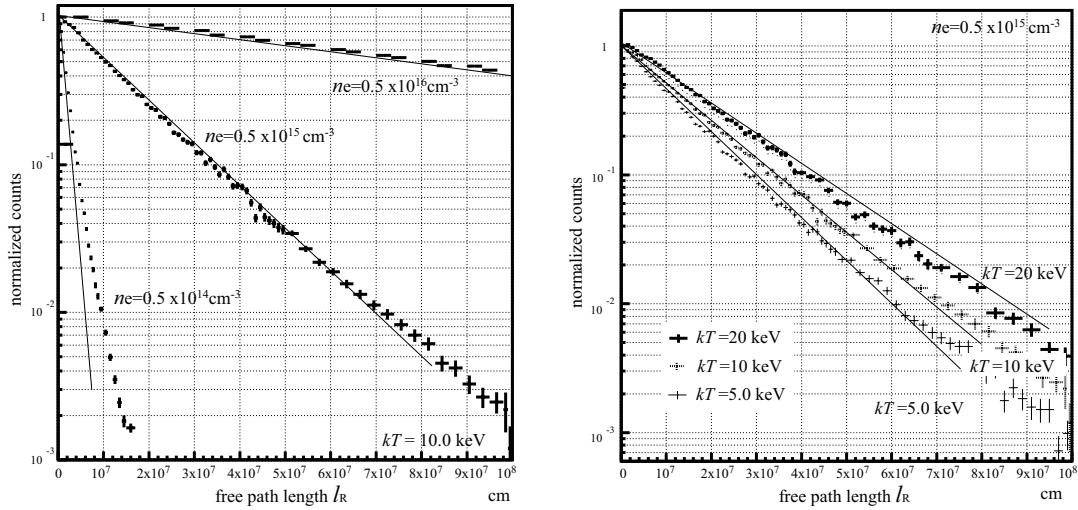


Figure 3.8: The distribution of the free path length for resonance scattering in our Monte Carlo simulation with various densities (*left*) and temperatures (*right*). Analytic solutions by equation (3.10) for each condition are shown in solid curve.

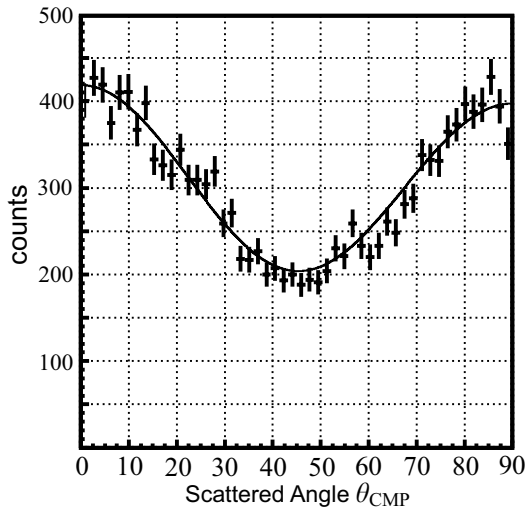


Figure 3.9: The distribution of scattered angle  $\theta_{\text{CMP}}$  by Compton scattering, produced by our Monte Carlo code. The photon energy is set to helium-like iron  $K_{\alpha}$  value (6.95keV). The solid curve represents the Kline-Nishina distribution for 6.95 keV photons.

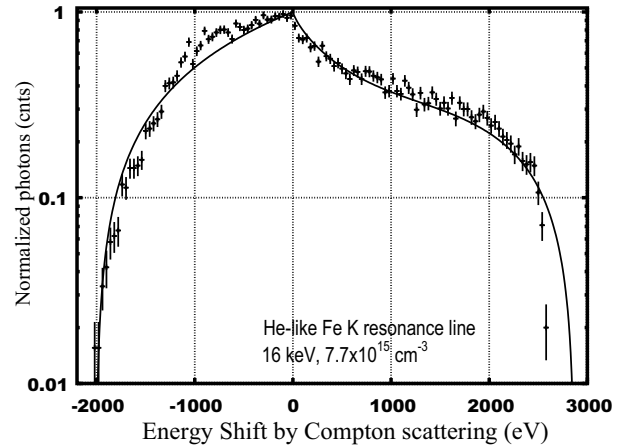


Figure 3.10: The distribution of the shift energies by Compton scattering in our Monte Carlo code. The photon energy is set to hydrogenic iron  $K_{\alpha}$  value (6.68keV), the electron temperature is 16 keV, and the density is  $7.7 \times 10^{15} \text{ cm}^{-3}$ . The solid line represents the analytic distribution by Blumenthal and Gold (1970).

Second, we simulated the simplest case wherein the plasma is hydrostatic with a single temperature and a single density: i.e.  $u$  is set to 0 and there is no vertical gradient in  $kT$  or  $n_e$ . The angular distributions of the emergent line photon flux, calculated under this simple condition for various densities, are shown in figure 3.11. The results confirm that the photons are emitted isotropically when the plasma density is low, and as the density increases, the geometrical beaming becomes progressively prominent. At  $n_e = 10^{16-17} \text{ cm}^{-3}$ , the Monte-Carlo result agrees nicely with the limiting analytic solution which assumes a completely optically-thick condition; i.e. line photons are emitted only from the surface of the accretion column (equation 3.8). This verifies proper performance of our Monte-Carlo simulation.

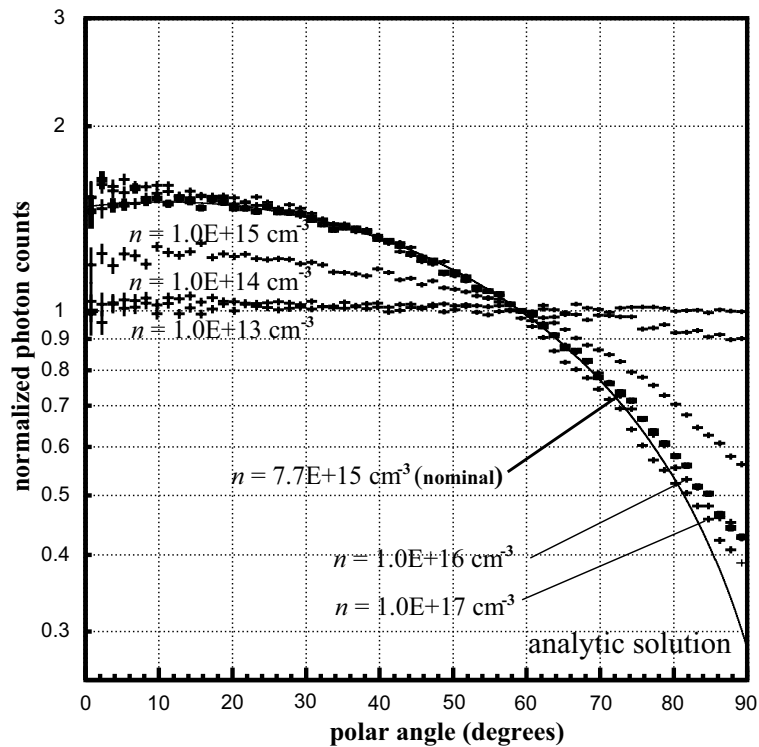


Figure 3.11: Angular distributions of resonant line photons emergent from a simple thin thermal plasma, simulated by neglecting the vertical motion ( $u = 0$ ) and neglecting the vertical gradient in  $n$  and  $kT$ . Abscissa is the angle  $\theta$  from the vertical axis of the column, and ordinate is the photon flux per unit steradian normalized to the value of an isotropic emission. The plasma parameters are set to the nominal values (section 2.4.5);  $kT = 16 \text{ keV}$ ,  $r = 5 \times 10^7 \text{ cm}$ , and  $h = 1.9 \times 10^7 \text{ cm}$ . The solid line represents the analytic solution when only the column surface shines as described by equation (3.8). The crosses show the results calculated for various densities as specified in the figure.

### 3.4.4 Numerical results in nominal condition

In this section, we performed the simulation by fully considering the vertical gradient in  $kT$ ,  $u$ , and  $n_e$  (equation 2.62). Figure 3.12 shows the calculated angular distribution of He-like iron line when the relevant parameters are set to the nominal values described in section 2.4.5. The resonance line flux is thus enhanced in the vertical direction (i.e.,  $\theta = 0^\circ$ ) more strongly than in figure 3.11 (thin solid crosses  $\rightarrow$  thick solid ones). This reconfirms the physical beaming mechanism described in section 3.3. For comparison, the intercombination photons, which are free from the resonance scattering, exhibit a nearly isotropic distribution.

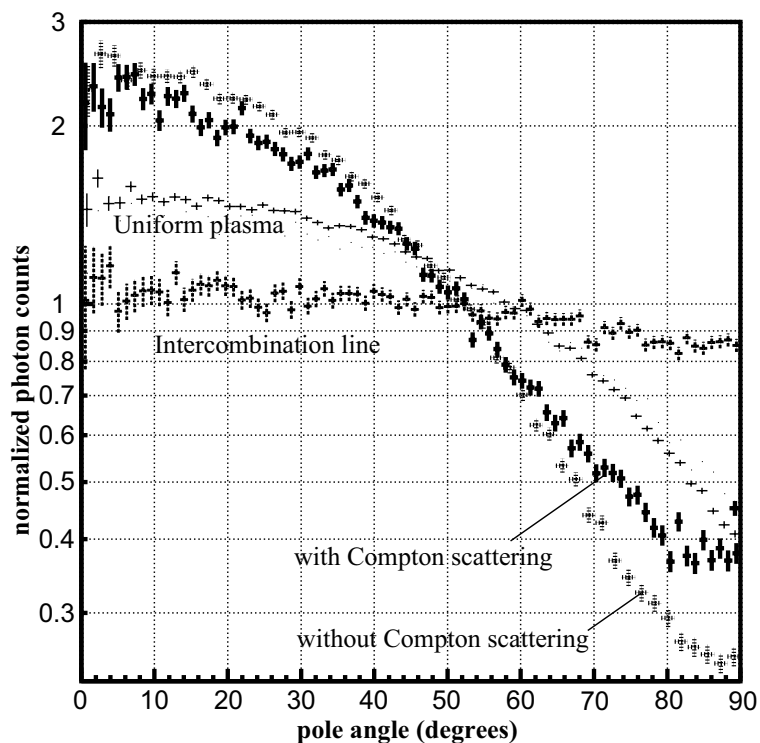


Figure 3.12: The same as figure 3.11, but calculated with the vertical structure of the accretion column by Aizu (1973), for the He-like iron  $K_\alpha$  lines. The plasma parameters are set to the nominal values shown in section 2.4.5:  $kT^{\text{sh}} = 16$  keV,  $u^{\text{sh}} = 0.9 \times 10^8$  cm s $^{-1}$ ,  $n_e^{\text{sh}} = 7.7 \times 10^{15}$  cm $^{-3}$ ,  $r = 5 \times 10^7$  cm, and  $h = 1.9 \times 10^7$  cm. The thin crosses show the same profile as presented in figure 3.11 (nominal case). Thick solid crosses represent the results considering the Compton scattering, while dashed crosses represent those neglecting the Compton process. The dotted crosses show the profile of the intercombination line.

As demonstrated in figure 3.12, the Compton scattering is confirmed to slightly reduce the enhancement, because of large energy shifts that invalidate the resonance condition (section 3.4.2). This energy shift can be recognized in the calculated energy spectrum, presented in figure 3.13, as a broad quasi-continuum. (Note that we do not produce bremsstrahlung continuum photons in the calculation.) About 15 % of the generated photons are Comptonized in number; 14 % photons are singly scattered, 1 % are doubly

scattered, and 0.2 % are scattered more than three times. This percentage is consistent with the optical depth for Compton scattering,  $\tau_T = 0.24$ , at the center of the plasma (equation 2.46).

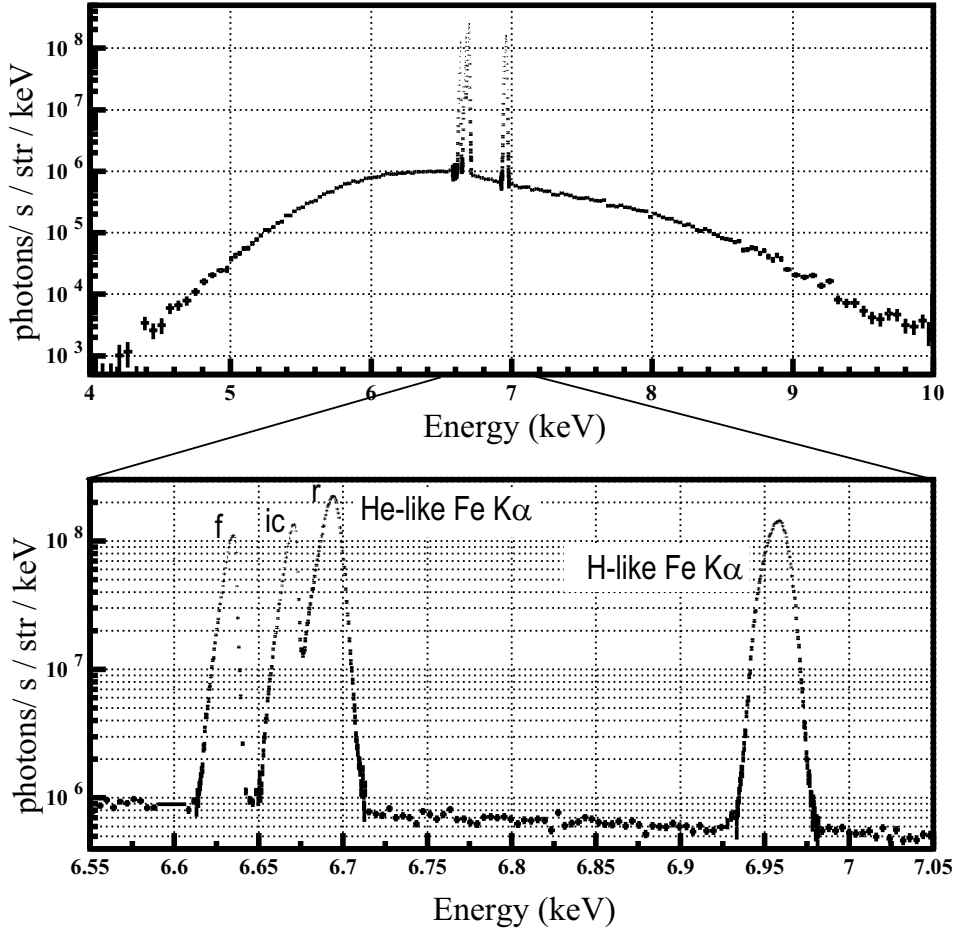


Figure 3.13: A simulated spectrum of hydrogenic and helium-like iron  $K_\alpha$  lines. The lower panel is an expanded view of the upper panel. The plasma parameters are set to the nominal values as described in section 2.4.5 (see text). In the calculation, the continuum photons are not included, so this spectrum presents only line photons.

In the angle-averaged energy spectrum (figure 3.13), we can see that the line cores are broadened by about 20 – 30 eV. This broadening is clearly larger than that caused by thermal Doppler effect, about 4 eV (equation 3.5). The additional contribution to the line width comes from the bulk-motion Doppler effect associated with the post-shock flow. It causes only redshift but not blueshift, because the flow is directed away from the observer. Furthermore, since the flow is just vertical, the shift must have an angular dependence; it becomes maximum at the pole-on phase ( $\theta = 0$ ), and it vanishes in the side-on phase ( $\theta = 90$ ). To confirm this, the angle-resolved energy spectra of iron  $K_\alpha$  lines are plotted in figure 3.14; the shift becomes maximum in the pole-on phase, as expected. The line broadening in the side-on spectrum is purely caused by thermal Doppler effect of  $\Delta E^{\text{th}}$  (described in section 3.3), while the effect of  $\Delta E^{\text{bk}}$  is seen as the energy shift relative to the

side-on spectrum. This figure also visualizes the rotational modulation in the resonance lines, which results from the condition of  $\Delta E^{\text{th}} \ll \Delta E^{\text{bk}}$ . This phenomenon provides the demonstration of the physical beaming mechanism we propose. On the other hand, the intercombination and forbidden lines from He-like iron are not modulated, although their line widths are reduced in side-on phase ( $\theta \sim 90^\circ$ ) because of vanishing the Doppler effect by bulk motion. In this figure, the Comptonized photons are almost isotropically distributed.

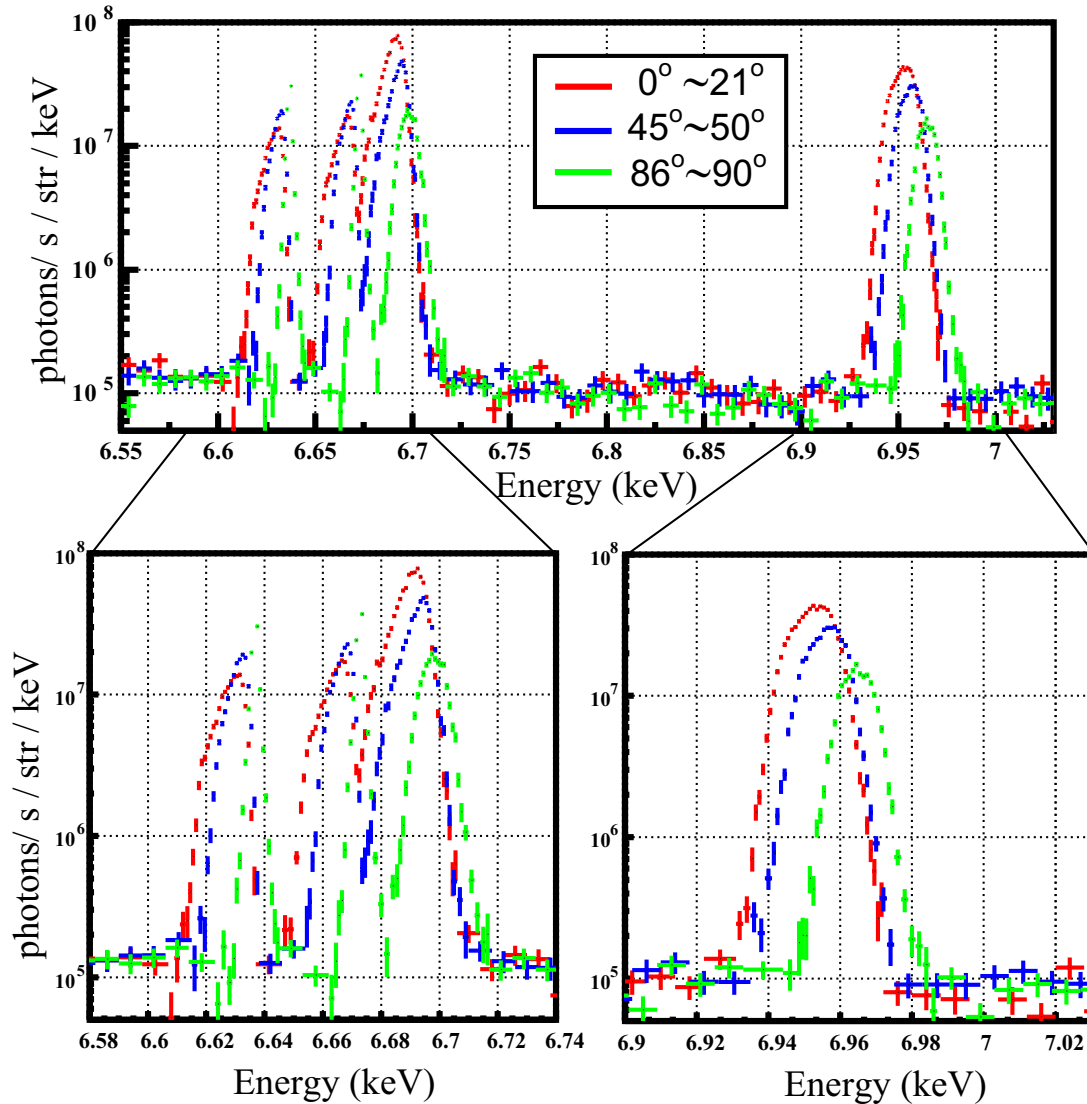


Figure 3.14: Phase resolved energy spectra for iron  $K_\alpha$  lines calculated by our Monte Carlo simulation in the nominal case (see text). The pole-on spectra with angle  $0 \sim 21$  degrees is shown in black, that with medium angle ( $45 \sim 50$  degrees) in red, and side-on ( $86 \sim 90$  degrees) in green. The upper panel covers the energy range of  $6.4 - 7.0$  keV, and the lower panels give expanded view of the helium-like iron  $K_\alpha$  lines (*bottom left*) and the hydrogenic iron  $K_\alpha$  line (*bottom right*).

### 3.4.5 Estimation of the beaming factor

We repeated the Monte-Carlo simulations by changing  $h/r$ ,  $n^{\text{sh}}$ ,  $kT$ , and  $u^{\text{sh}}$ , around their baseline values of  $kT = 16.0$  keV,  $u^{\text{sh}} = 0.9 \times 10^8$  cm s $^{-1}$ ,  $n_e^{\text{sh}} = 7.7 \times 10^{15}$  cm $^{-3}$ ,  $r = 5 \times 10^7$  cm, and  $h = 1.9 \times 10^7$  cm (section 2.4.5), and obtained various angular distributions of line photon flux  $f(\theta)$ . We summarize the results in terms of the enhancement factor at pole-on,

$$\xi_m \equiv \xi(\theta = 0), \quad (3.18)$$

where  $\xi(\theta)$  is the angular-photon distribution normalized to the average (for example, figures 3.11 or 3.12); i.e.,

$$\xi(\theta) = \frac{f(\theta)}{\int_0^{\pi/2} f(\theta) d \cos \theta}, \quad (3.19)$$

in which photons are accumulated without discarding Comptonized ones.

As shown in figure 3.15, the beaming factor  $\xi_m$  increases as  $h/r$  decreases (cylinder to coin shaped column); this can be mainly explained by geometrical beaming (section 3.2). In the coin-shaped limit ( $h/r \lesssim 0.1$ ),  $\xi_m$  decreases because  $h$  becomes geometrically too thin for the column to be optically thick for the resonance photons. Actually, this effect becomes less clearly visible as the density increases (figure 3.15 right). Figure 3.16 shows the density dependence of  $\xi_m$ . The enhancement increases as density increases, but when the density exceeds  $\sim 10^{16}$  cm $^{-3}$ , it diminishes again because of Compton scattering. This inference is achieved by comparing results with and without Compton process. In other words, the anisotropic effect becomes maximum when the plasma has moderate optical depth (thin for Compton scattering and thick for resonance). As shown in figure 3.17, the WD mass dependence of  $\xi_m$  is small: it increases slightly as the mass increases, because the shock velocity increases (i.e., steeper velocity gradient) with deeper gravity potential, and it starts decreasing mainly because density decreases.

Figures 3.15, 3.16 and 3.17 also compare the He-like and H-like resonance lines. We can thus expect the former to be intrinsically more collimated than the latter, because the former photons are produced predominantly in the bottom regions of the accretion column (figure 2.30), where the electron density is higher, thermal Doppler effect is smaller, and the path of escape from the column is longer, as compared to the top region where the latter photons are mostly emitted.

We can expect a strong collimation with a density of  $n_e \sim 10^{16}$  cm $^{-3}$  (figure 3.16) and a shape of  $h/r \sim 0.1$ – $0.5$  (figure 3.15) with typical radius  $\sim 10^7$  cm. For example, strong enhancement of  $\xi_m \sim 3$  for helium-like iron resonance line is achieved under the condition of  $kT^{\text{sh}} = 10$  keV,  $r = 5 \times 10^7$  cm,  $n_e = 7.9 \times 10^{15}$  cm $^{-3}$  and  $EM = 10^{55}$  cm $^{-3}$ , which yield an X-ray luminosity of  $1.0 \times 10^{32}$  erg s $^{-1}$  (2 – 10 keV). This is a reasonable condition for MCVs. Hereafter, we call this condition “strong case”. Thus, the beaming mechanism proposed in section 3.2 and 3.3 can quantitatively explain the strong iron line emission observed from POLEs.

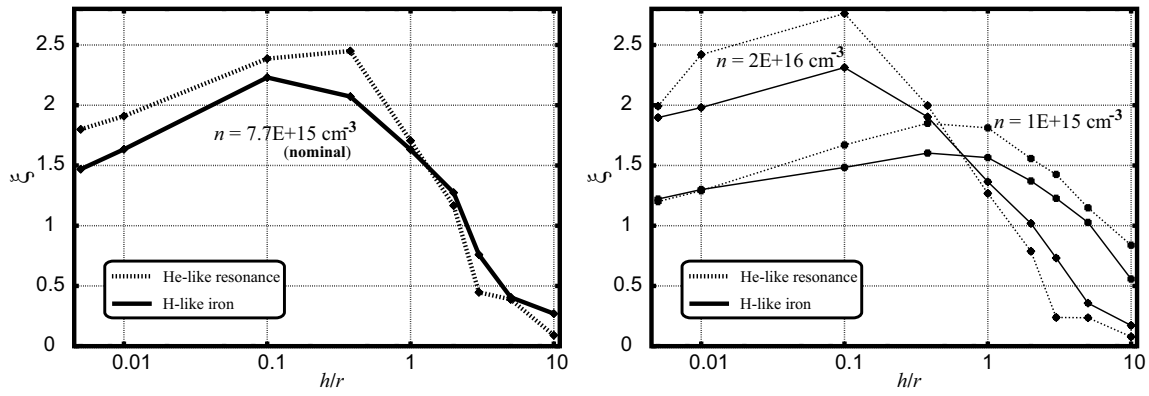


Figure 3.15: The beaming factor  $\xi_m$  for various column shapes, where the volume  $r^2h$  is fixed. Solid and dashed lines show the H-like and He-like resonance Fe K lines, respectively. The baseline condition of the calculation is given in the text. Calculation is performed for three densities as specified in the figure.

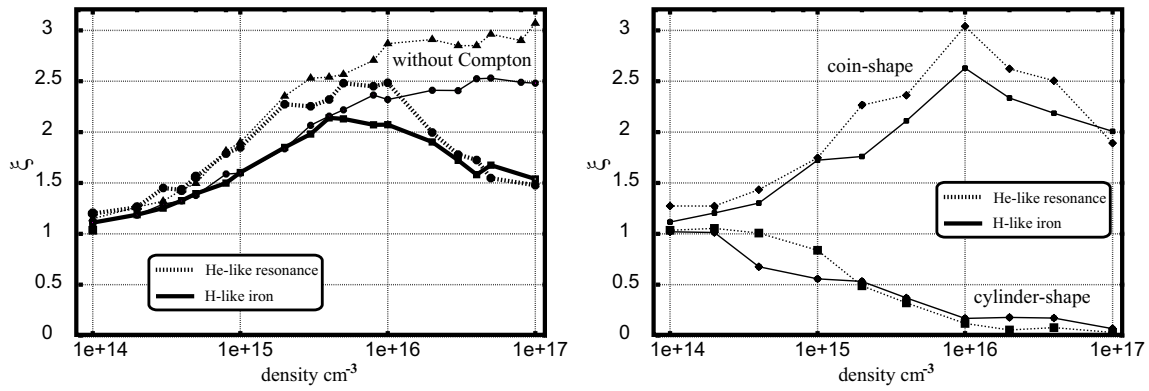


Figure 3.16:  $\xi_m$  for various densities with three different column shapes; coin, nominal, and cylinder shape. The coin shaped column has  $r = 1 \times 10^8$  cm and  $h = 1 \times 10^7$  cm, while the cylinder column has  $r = 1 \times 10^7$  cm and  $h = 1 \times 10^8$  cm. The conditions of calculation are otherwise the same as those in figure 3.15. Calculations without Compton scattering are also shown (thin curves in the *left* panel).

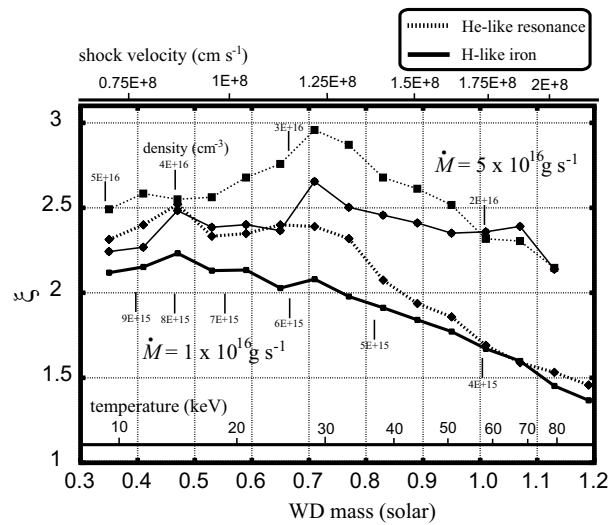


Figure 3.17:  $\xi_m$  calculated for various WD masses. The conditions of calculation are otherwise the same as those in figure 3.15. The temperature and density depend on the WD mass through equations (2.38) and (2.39), respectively. The mass transfer rate is set to  $\dot{M} = 1 \times 10^{16}$  g s $^{-1}$  and  $5 \times 10^{16}$  g s $^{-1}$ .

# Chapter 4

## INSTRUMENTATION

### 4.1 Overview of X-ray Instruments

As a beginning of our observational study, we present our approach to verify the anisotropic transfer of resonance photons as proposed in Chapter 3. Then, based on its requirements, we select suitable instruments to be utilized in this thesis.

#### 4.1.1 Our observational approach and requirements

In order to experimentally verify the anisotropic mechanism (chapter 3), it is necessary to measure a modulation of line equivalent width as a function of viewing angle,  $\theta$ , to the axis of accretion column. The essence of the enhancement effect is that the mass of ion is high enough for bulk-motion Doppler shift to overcome the thermal broadening, thus iron line must be the best tool for our confirmation of mechanism. Radiation from ionized iron ion is intrinsically strong for cosmic X-ray emitting plasmas, and furthermore iron  $K_\alpha$  lines are produced at the hot part of the accretion column (section 2.5.5) within the Aizu formalism. In this thesis, we thus mainly attend to iron  $K_\alpha$  lines.

The basic requirements for X-ray instruments to fulfill our purpose are to have high sensitivity around the iron line band ( $\sim 6$  keV), and have high energy resolution to separate ionized iron line from fluorescent line, since the latter is not radiated from the hot plasma of accretion column. Since MCVs are point sources (section 2.2.2) and their rotational periods are a few hours (section 2.2.3), we do need neither a high angular resolution nor a high timing resolution.

#### 4.1.2 Current X-ray observatories

X-ray observatories currently working (or worked in recent years) are summarized below. For a reference, the effective area of these satellites are plotted in figure 4.1.

- *ROSAT* (June 1990 – February 1999; 0.2 – 2 keV)

An X-ray observatory in the 1990s, which have been developed through collaboration

among Germany, the United States, and the United Kingdom. The most important feature of this satellite is a high spacial resolution up to  $\sim 5''$  in the soft X-ray band.

- *ASCA* (February 1993 – March 2000; 0.5 – 10 keV)

The fourth Japanese X-ray satellite, worked in the same period as *ROSAT*. Complementing the insufficient X-ray spectroscopic properties of *ROSAT*, *ASCA* had a high sensitivity in a harder X-ray band covering the iron line band, with a high energy resolution of  $\sim 2\%$  at 6 keV.

- *RXTE* (November 1995 – present; 2 – 250 keV)

A hard X-ray mission developed by National Aeronautics and Space Administration (NASA). The key character is its huge effective area of  $\sim 6500 \text{ cm}^2$  in the medium X-ray band of 3 – 30 keV.

- *BeppoSAX* (April 1996 – present; 0.5 – 200 keV)

An Italian X-ray observatory, in collaboration with Netherlands and European Space Agency (ESA). The main feature of this satellite is a very wide energy coverage incorporating two imaging instruments for softer X-rays and two non-imaging ones for harder photons.

- *Chandra* (July 1999 – present; 0.5 – 10 keV)

One of the new-generation X-ray satellites in the first decade of this century, developed by NASA. The most outstanding feature of *Chandra* is its X-ray imaging optics with a very high spacial resolution of  $\sim 0.5''$ . In addition, by employing X-ray diffraction gratings, high-resolution spectroscopy with an energy resolution of  $\sim \text{eV}$  is available. However, its performance in the iron-K band is rather limited in sensitivity.

- *XMM-Newton* (December 1999 – present; 0.5 – 10 keV)

Another new generation satellite developed by ESA. The principal sales point of *XMM-Newton* is its large effective area exceeding  $1000 \text{ cm}^2$  in 0.5-10 keV. However, because of a high elongated orbit beyond the Earth's magnetosphere, the background is much higher and more unstable compared with *ASCA*.

- *ASTRO-E* (February 2000, LOST; 0.5 - 600 keV)

The fifth Japanese X-ray satellites, developed as another new generation instrument in this decade. Compared with *Chandra* and *XMM-Newton*, this satellite has two important features; a high-resolution ( $\sim 10 \text{ eV}$ ) spectroscopy with a high efficiency covering the iron-K band, and an unprecedented sensitivity in the hard (10 – 600 keV) energy band. Unfortunately, *ASTRO-E* have been lost by a failure in the first stage of the launching rocket, M-V-4, in February 10, 2000.

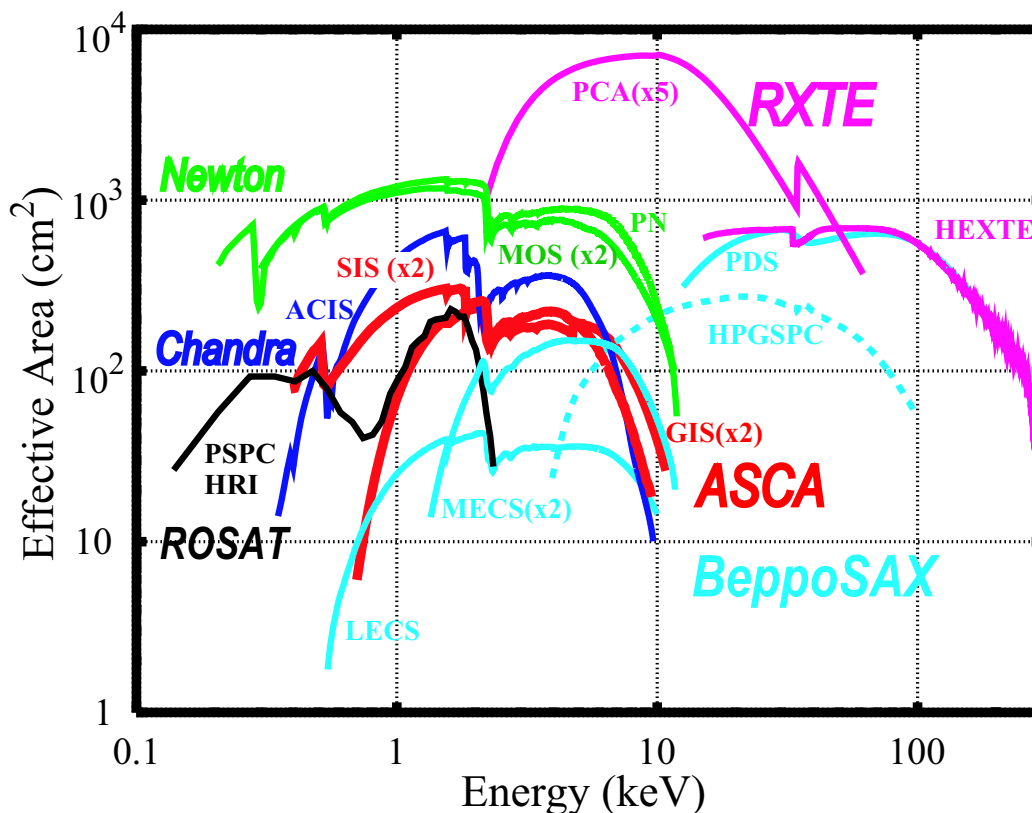


Figure 4.1: The effective area of *ROSAT*, *ASCA*, *RXTE*, *BeppoSAX*, *XMM-Newton*, and *Chandra*, in black, red, magenta, cyan, green, and blue, respectively. For X-ray imaging instruments, both the effective area of the optics and the detector efficiency are included.

For our plasma diagnostics using iron  $K_{\alpha}$  line emission, the best mission is undoubtedly *ASTRO-E*, which has however been lost. The other new generation satellites, *XMM-Newton* and *Chandra*, have currently little observational data on MCVs, and these observations mostly lack sufficient exposure for our purpose. Therefore, we do not use these data in this thesis. Thus, we mainly rely on *ASCA* for our study of MCVs, including both our own observations and the archived data. We additionally analyze archived data obtained by *BeppoSAX* and *RXTE*. In the remainder of this Chapter, we describe properties of X-ray instruments onboard *ASCA*, *BeppoSAX* and *RXTE*.

## 4.2 The Fourth Japanese X-ray Observatory, *ASCA*

### 4.2.1 Overview

*ASCA* (Advanced Satellite for Cosmology and Astrophysics) is the fourth Japanese X-ray satellite developed by Institute of Space and Astronautical Science (ISAS), following *Hakucho*, *Tenma*, and *Ginga*. The satellite was successfully launched by the M-3SII-7 rocket from Kagoshima Space Flight Center on February 20, 1993, and was put into an approximately circular orbit with a perigee of 520 km, an apogee of 620 km, and inclination angle of  $\sim 31.1^\circ$ , revolving the Earth in about 96 minutes. On July 14, 2000, its attitude control was lost during a geomagnetic storm caused by an intense solar flare, after which no scientific observations could not be performed. *ASCA* reentered the atmosphere on March 2, 2001 after more than 8 years in orbit.

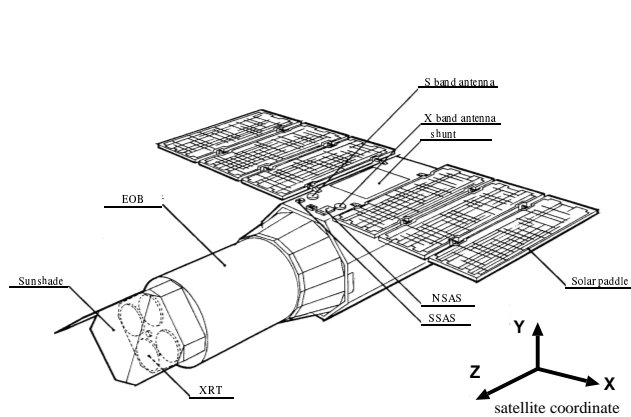


Figure 4.2: Overview of the *ASCA* satellite.

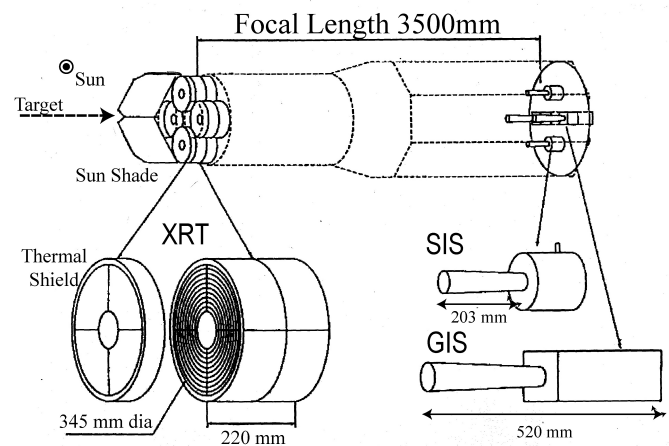


Figure 4.3: Configuration of payload instruments onboard *ASCA*.

Figure 4.2 shows the in-orbit configuration of *ASCA* (Tanaka *et al.* 1994). As shown in figure 4.3, *ASCA* is equipped with four identical grazing-incidence X-ray telescopes (XRT; Serlemitsos *et al.* 1995; Tsusaka *et al.* 1995) on top of the satellite, and two types of detectors on the focal plane, two sets of imaging gas scintillation proportional counter (Gas Imaging Spectrometer – GIS; Ohashi *et al.* 1996; Makishima *et al.* 1996), and two X-ray sensitive CCD cameras (Solid-state Imaging Spectrometer – SIS; Burke *et al.* 1991; Yamashita *et al.* 1997).

### 4.2.2 X-ray telescope (XRT)

It is difficult to design X-ray imaging optics because X-rays impinging at normal incidence on any material are largely absorbed rather than reflected. Since the index of refraction is near unity at X-ray band for all materials, any refracting system, such as lenses sufficiently thin to transmit X-rays, must possess a long focal length, which would be highly impractical for use in space experiments. On the other hand, the index of refraction in most materials is slightly less than unity for X-rays, so that “total internal reflection” does occur for X-rays under a very small angle of incidence ( $\lesssim 1^\circ$ ). This phenomenon can be applied to X-ray reflecting optics. The shape of an X-ray mirror may be basically a paraboloid, as in optical reflecting telescopes, but its mirror surface must be almost edge-on to the incoming photons, because of the required grazing incidence for X-rays. As a result, an “imaging” X-ray telescope needs at least two reflectors in series. Most X-ray telescopes adopt the reflecting optics called “Wolter Type I” as illustrated in figure 4.4, which employs a paraboloid and a hyperboloid with a common focus. Furthermore, to increase the geometrical area for X-ray reflection, several pairs of paraboloid and hyperboloid, with a common focus, are coaxially nested like figure 4.5.

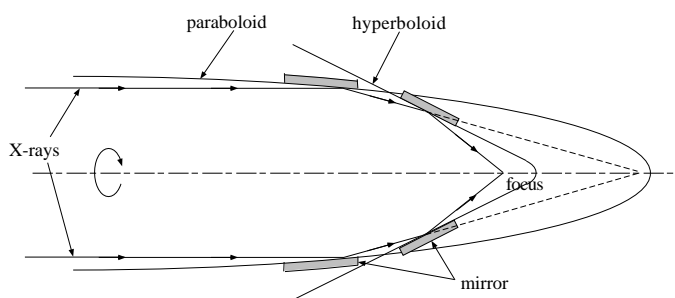


Figure 4.4: Schematic view of the X-ray reflecting mirror adopting Wolter Type I optics.

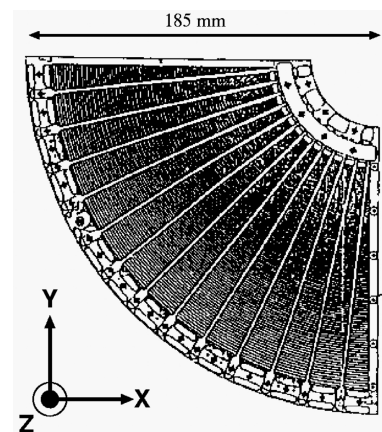


Figure 4.5: Top view of one quadrant of the *ASCA* XRT, adjusting 120 foils by alignment bars running radially.

It becomes more difficult to obtain a large effective area, as incident X-ray energy increases, because of smaller critical reflection angle. For example, the band pass of Wolter Type I telescopes on board *Einstein* and *ROSAT* is limited to  $2 \sim 3$  keV, as shown in figure 4.6, although their angular resolution and imaging quality are excellent. The *ASCA* XRT is designed to have a larger effective area in harder energy bandpass covering iron  $K_\alpha$  line energies (6.4 – 6.9 keV). This has been realized by adopting multi-nested (120 layers) thin-foil conical optics, as shown in figure 4.5, to allow maximum use of the aperture for X-ray reflection (Serlemitsos *et al.* 1995). Each reflector is an aluminum foil of 0.127 mm thickness coated with  $\sim 10 \mu\text{m}$  acrylic lacquer and  $500 \text{ \AA}$  gold. The inner and outer diameters are 120 mm and 345 mm, respectively, and the focal length is

350 cm. The basic parameters of *ASCA* XRT is summarized in table 4.1.

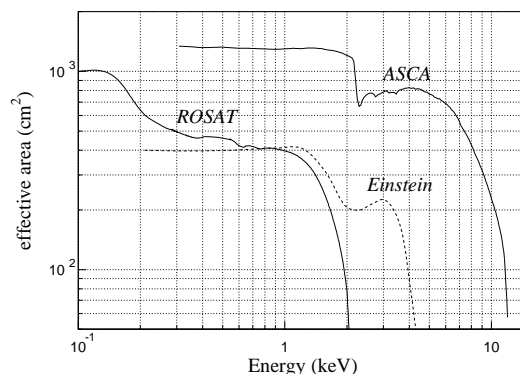


Figure 4.6: Effective area of the XRT on board *ASCA* in comparison with that of *Einstein* and *ROSAT*.

Table 4.1: Parameters of the *ASCA* XRT

Energy bandpass	$\lesssim 10$ keV
Effective area	$\sim 1300$ cm <sup>2</sup> @ 1keV, $\sim 600$ cm <sup>2</sup> @ 7keV (4 XRTs total)
Geometrical area	558 cm <sup>2</sup> / telescope
Field of view	24' (FWHM) at 1 keV, 16' (FWHM) at 7 keV
Half Power diameter	$\sim 3'$
Focal length	3500 mm
Mirror height	100 mm
Nesting number	120 foils
Outer/Inner diameter	345 mm / 120 mm
Mirror substrate thickness	127 $\mu$ m
Incident angle	0.24° $\sim$ 0.7°
Total mirror weight	39340 g (4 XRTs total)

The image of a point X-ray source obtained with the *ASCA* XRT has a shape like a clover leaf or a butterfly, as shown in figure 4.7, because it is synthesized by four quadrants (figure 4.5). The off-axis image is compressed towards the radial direction and elongated towards the azimuthal direction, as shown in figure 4.8. The point-source image is further dependent on the X-ray energy. Since several anomalous light passes may occur as exemplified in figure 4.9, stray light becomes significant in the case that a strong X-ray source exists near a field of view, as shown in figure 4.10.

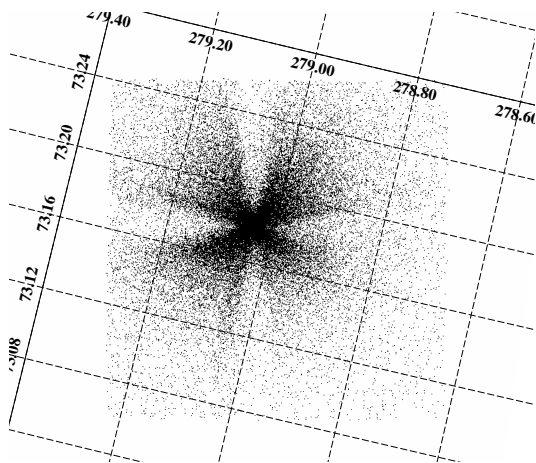


Figure 4.7: The image of a point source, AM Herculis, obtained by ASCA.

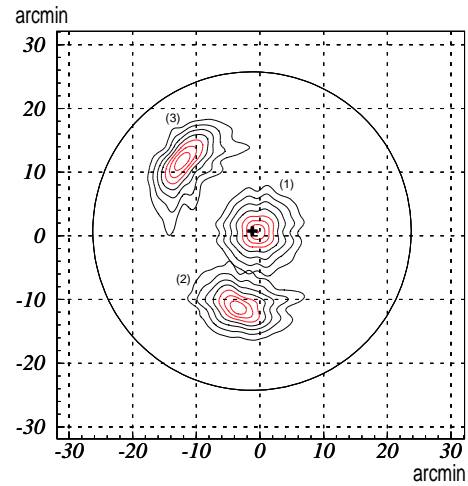


Figure 4.8: The 0.5 – 10 keV image of Cyg X-1 smoothed with  $\sim 0'.5$ , observed at off-axis angle of  $1'.9$  (a),  $12'.9$  (b), and  $17'.0$  (c). Contours are logarithmically spaced by a factor 2.

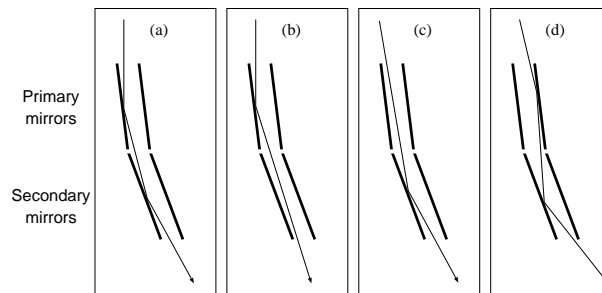


Figure 4.9: Examples of the XRT light path; (a) nominal, (b) reflection only by the primary mirror, (c) reflection only by the secondary mirror, and (d) multiple reflection.

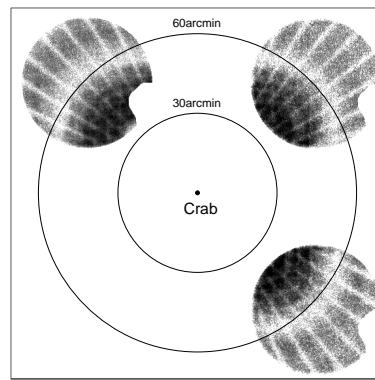


Figure 4.10: Observed stray light produced by the Crab nebula (Ishisaki 1996).

### 4.2.3 Gas Imaging Spectrometer (GIS)

The Gas Imaging Spectrometer (GIS) is an imaging gas scintillation proportional counter (GSPC), developed by the University of Tokyo, Tokyo Metropolitan University, Meisei Electric Co. Ltd. and Japan Radio Corporation Co. Ltd. (Ohashi *et al.* 1996; Makishima *et al.* 1996). It has been based on the GSPC experiment (Koyama *et al.* 1984) on board the *Tenma* satellite (Tanaka *et al.* 1984), improved by adopting a position sensitive imaging photo-multiplier tube (IPMT) to have an imaging feature. It is characterized by a wide field-of-view, a good timing resolution, a low detector background level, and moderate energy and spatial resolutions. The design parameters and performance of the GIS are summarized in table 4.2.

Table 4.2: Parameters of *ASCA* GIS.

Energy bandpass	0.7 – 15 keV
Energy resolution	8% at 5.9 keV (FWHM)
Effective area	50 mm diameter
Filed of view	50' diameter
Positional resolution	0.5 mm (FWHM)
Timing resolution	~ 61 $\mu$ sec (minimum in PH Mode) 1.95msec (minimum in MPC Mode)
Entrance Window	10 $\mu$ m beryllium
Absorption Material	Xe (96%) + He (4%), 10mm depth, 1.2 atm at 0 °C

As shown in figure 4.11, GIS consists of a gas cell, IPMT, a high voltage unit, and electronics (GIS-E). Figure 4.12 shows a schematic view of its detector operation. The gas cell is made of a ceramic cylinder with a beryllium entrance window and a quartz exit window, filled with 96 % of xenon and 4 % of helium gas with a pressure of 1.2 atm. It is further divided into two regions; a drift region and a scintillation region. X-rays are absorbed in the former region through photo-electric absorption, to generate primary electrons, of which the number is proportional to the incident X-ray energy. Since the electric field there is not so strong ( $< 1 \text{ keV cm}^{-1}$ ), the primary electrons undergo no electron avalanche nor excitation of xenon gas; thus they simply drift with keeping their number. Then, in the scintillation region, the electron cloud is accelerated due to a strong electric field by the high voltage of  $\sim 5 \text{ keV}$ , and excites xenon atoms, which produce a large number of scintillation ultraviolet photons. The electric field here is optimized to prevent electron avalanche ( $< 6 \text{ keV cm}^{-1}$ ) to keep the information of primary electron number. The UV lights are emitted along the path of the electron cloud and are distributed on the quartz exit window centered around the position of incident X-ray photon. Finally, the UV lights are absorbed in a bialkali photo-electrode of the IPMT attached beneath the gas cell, and converted into electric charge. The IPMT has 16 multi-anodes in the  $x$ -direction, and 16 multi-anodes in the  $y$ -direction. The summation of their output charge, i.e., the pulse height (PH) of the last dynode, gives the incident

X-ray energy. As shown in figure 4.13, the energy resolution of the GIS is about 7.8 % at 6 keV and inversely proportional to the square root of the incident X-ray energy, The incident X-ray positions are calculated by fitting the PH distribution of signals from 16 anodes with a Lorentz function. Since the rise time (RT) of the signal waveform represents the time for generation of UV photons in the scintillation region, it is used to separate photon signals from background particle-originated events. The information of the spread of the event (SP) is also used for background rejection.

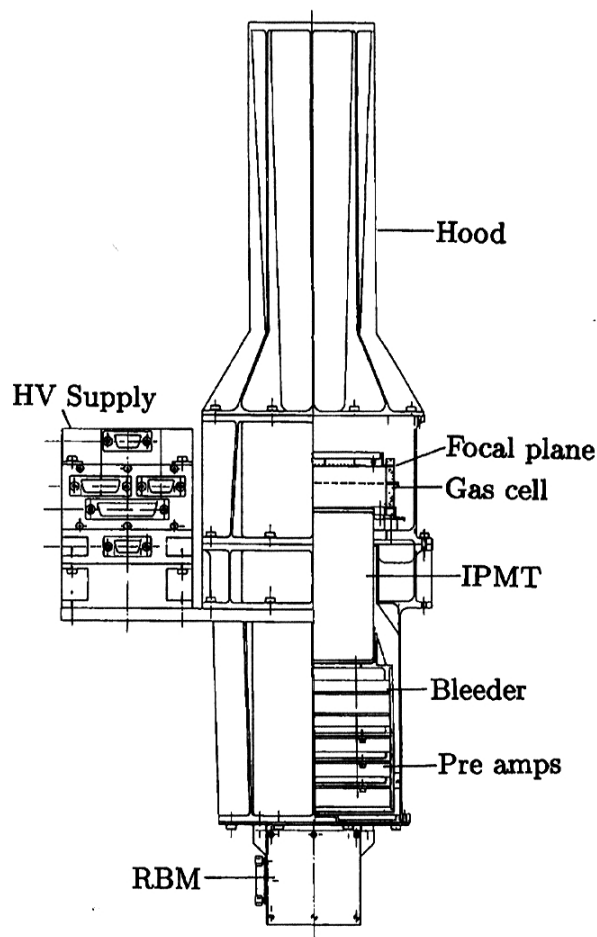


Figure 4.11: Cross section of the GIS sensor (Ohashi *et al.* 1996). The radiation belt monitor (RBM) is not attached to GIS3.

Figure 4.13: Energy resolution of the GIS as a function of the incident energy.

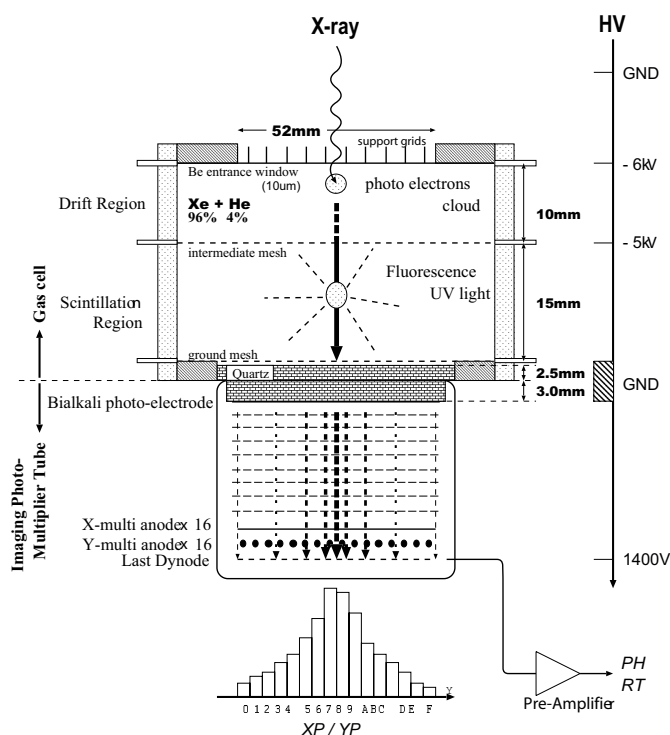
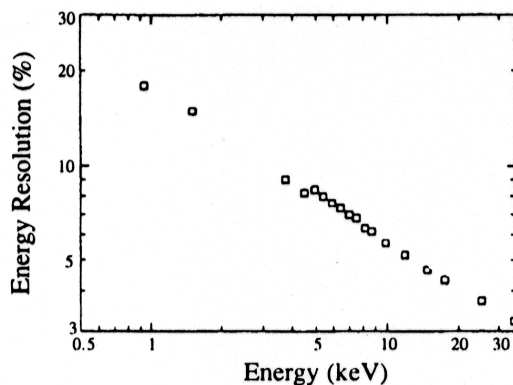


Figure 4.12: A schematic illustration of the X-ray detection by the GIS.



The gain of the GIS depends both on the incident X-ray position and on the temperature of the gas cell and IPMT. The former dependence originates from the positional variation in the gain of IPMT, which can be corrected by a 2-dimensional position-dependent gain table, so-called *gain-maps*, measured in pre-flight calibrations on the ground (Makishima *et al.* 1996), and the analysis of spectral lines from the bright earth in orbit. The latter dependence originates mainly from chemical properties of dynodes in the IPMT. This variation can be followed by the temperature measured in orbit, because there is a good correlation between the temperature and PH of the calibration source (radioactive isotope  $^{55}\text{Fe}$ ) which is attached to the rim of the detector aperture. There also exists a secular gain variation due possibly to a degradation of the sensor (Tashiro *et al.* 1995; Makishima *et al.* 1996), which is also monitored by the calibration source. Thus, the gain variations within the observation can be corrected with gain maps, the instantaneous temperature, and the long-term gain history.

One of the notable properties with the GIS is the very low background level. In addition to the onboard background rejection, more sophisticated reduction using PH – RT cuts achieve an intrinsic background rate as low as  $(5\text{--}9) \times 10^{-4}$  cnt s $^{-1}$  keV $^{-1}$  cm $^{-2}$ . Figure 4.14 shows background spectra of the GIS, obtained by observations of night earth, blank sky, and day earth, which correspond to the non X-ray background (NXB), NXB plus cosmic X-ray background (CXB), and NXB plus scattered solar X-rays, respectively. For monitoring such sporadic changes in the background, the number of events which exceed the lower-level discriminator is useful. The NXB intensity is primarily determined by geomagnetic cutoff rigidity at the spacecraft location, because this quantity control the incoming cosmic-ray flux. However, the NXB intensity also exhibits unpredictable, rather stochastic changes. With extensive studies by Ishisaki (1996) and Ishisaki *et al.* (2000), the modeling of time-variable GIS background is confirmed within a systematic error of  $\sim 7\%$  at a 10 ksec exposure, as demonstrated in figure 4.15.

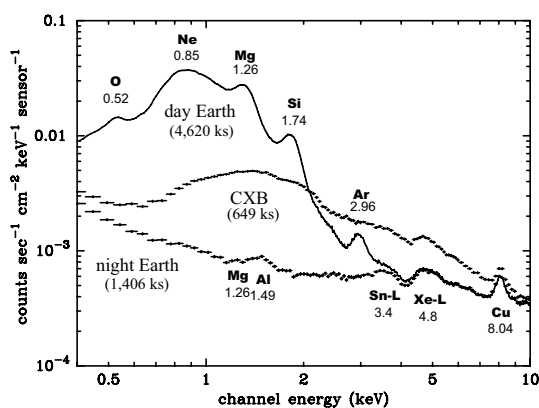


Figure 4.14: Integrated average background spectra of the day-earth (smooth line), the blank sky including the cosmic X-ray background (crosses), and the night-earth (filled circle). These spectra have been accumulated within  $17'$  from the detector center (Ishisaki 1996).

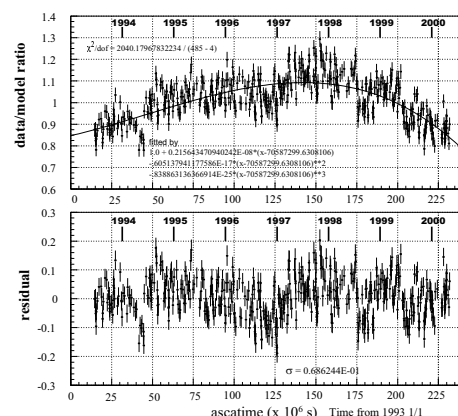


Figure 4.15: Long term variation of the non X-ray background of the GIS from the launch to July 2000 (Ishisaki *et al.* 2000). The vertical axis shows a event rate accumulated in night-earth epoch, normalized to the model rate estimated by the standard method.

### 4.2.4 Solid-state Imaging Spectrometers (SIS)

The Solid-state Imaging Spectrometers (SIS), shown in figure 4.16, is the first CCD camera for photon counting usage in orbit (Burke *et al.* 1991; 1994). It has been developed by ISAS, Osaka University, and the Massachusetts Institute of Technology (MIT). It utilizes so-called *frontside-illuminated frame-transfer* CCD; i.e., the electrodes are on the surface of the silicon substrate, and the electronic charge, produced by X-rays incident on the imaging region, is first temporarily stored in the accumulation region and is then read out line by line. There are two identical detectors, SIS0 and SIS1, at the focal plane of the XRT, each of which consists of four CCD chips and achieves square field-of-view of  $22' \times 22'$ . Each chip consists of  $422 \times 420$  pixels of  $27 \mu\text{m} \times 27 \mu\text{m}$  size. Although there are four chips, we can select by commands the chips to be read out. Typical choice is 4-CCD, 2-CCD, or 1-CCD mode, with an accumulation time per exposure of 16 sec, 8 sec, and 4 sec, respectively. In table 4.3, we summarize the basic parameters of the SIS.

Table 4.3: The basic parameters of the *ASCA* SIS.

Energy bandpass	0.4 – 12 keV
Energy resolution <sup>a</sup>	2% at 5.9 keV (FWHM)
Geometrical area	11 mm $\times$ 11 mm per chip
Filed of view	$22' \times 22'$ per sensor
Pixel size	$27 \mu\text{m} \times 27 \mu\text{m}$
Pixel number	420 pixels $\times$ 422 lines per chip (image region)
Depletion layer thickness	25 ~ 30 $\mu\text{m}$
Quantum efficiency	80% at 6 keV
Drive temperature	~ -62 °C

<sup>a</sup> Value in the first year, 1993. It is gradually degraded by radiation damage (see also figure 4.17).

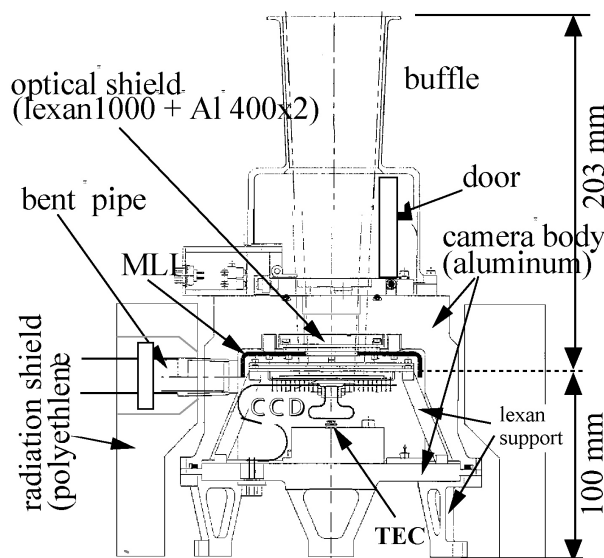


Figure 4.16: Cross section of the SIS sensor.

An incident X-ray photon is photo-absorbed by a silicon depletion layer. Its energy  $E_x$  is first given into photo-electrons and Auger electrons, and then converted into electron-hole pairs of which the number of  $E_x/w$ , where  $w \sim 3.65$  eV is the average energy of electron-hole pair creation. Because the X-ray energy is also lost into phonon excitation,  $w$  is slightly larger than the band-gap energy. Thus, few hundreds to thousands of electron-hole pairs are created so that the contribution of their statistical error is negligible to the energy resolution of the SIS. Their dispersion  $\sigma_{\text{pair}}$  is slightly narrower than Poissonian, and is given by

$$\sigma_{\text{pair}}^2 = F \frac{E_x}{w}, \quad (4.1)$$

where  $F$  is the Fano factor, which is  $\sim 0.12$  for silicon. Therefore, the SIS can achieve high energy resolution in principle, but in reality, electronic read-out noise and thermal noise (or dark current) become dominant. The electronic noise is suppressed by using low-noise amplifiers together with tight electrical shielding. In order to reduce the dark current, CCD chips are cooled down to  $-60$  °C by combining a Peltier element called Thermal Electric Cooler (TEC) and a radiation system with a heat pipe. The achieved energy resolution, in pre-flight calibration, reaches  $\sim 2\%$  at 6 keV. This performance has gradually been reduced by radiation damage in orbit, as shown in figure 4.17. For example, the FWHM resolution of Fe K line has degraded from 130 eV at launch to 220 – 250 eV in 1995 for 1-CCD mode data.

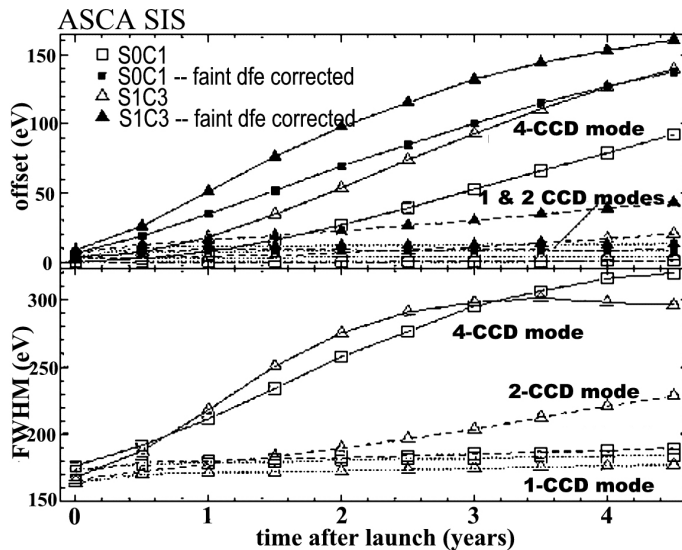


Figure 4.17: (*Upper panel*) Systematic offsets of the line center energy at 6.6 keV due to the RDD are shown for various clocking modes and analysis methods. Solid, dashed, and dotted lines correspond to 4-CCD, 2-CCD and 1-CCD mode data, respectively. (*Lower panel*) Degradation of the energy resolution at 6.6 keV due to the RDD. From ASCA news by Dotani *et al.* (1995).

When using a CCD in the photon counting mode as in the SIS, we process individual electric pulses, each caused by a single X-ray photon. Since the charge originating from one X-ray photon sometimes split into more than two pixels, we cannot determine an X-ray event by a simple comparison of the pixel charge with a fixed discrimination level. Accordingly, we use a hit-pattern, called “grade”, illustrated in figure 4.18, to recognize an X-ray event. Because the secondary electron cloud is only  $\lesssim 5 \mu\text{m}$  in size, we only have to consider  $3 \times 3$  pixels for the grade specification. Single events (grade 0), in which all the charge falls into one pixel, and single-sided split events (grade 2, 3, 4), in which some of the charge is split into one of the four horizontally or vertically adjacent pixels, are considered X-ray events. The incident X-ray energy are determined by summing up pulse heights of the split pixels.

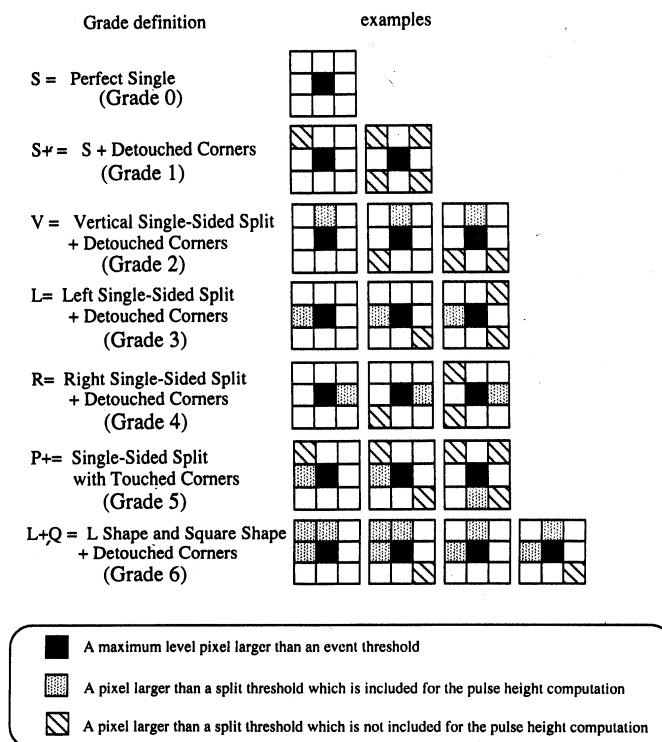


Figure 4.18: Event pattern and grade definition for the SIS.

Off-line processing of the charge reconstruction are available only for Faint mode data, which is one of the three observational modes for SIS, as listed below.

- **Faint mode** Operation mode for an observation of comparatively faint sources. The pulse height of all the any pixel reporting an event is telemetered, together with those of the adjacent eight pixels.
  - **Bright mode** Operation mode for comparatively bright sources. The grade determined by onboard software and the summation of all the pixel levels above the split threshold are telemetered.
  - **Fast mode** Another mode for fast reading, which is not used in this thesis.
- In actual observations, we choose one of these modes, considering X-ray flux of the target against available at a transmission capacity of *ASCA*, together with scientific requirements for the data quality.

The off-line data reduction for the SIS is usually performed in several steps, in the following order.

1. **Zero level**

Zero level means the CCD output analog signal level with no input signal charge. In ground experiments using CCDs, this may be available by covering the CCD to shut out the input signal. However, for space experiments, it is difficult to get this information continuously, because payload is designed to avoid mechanically movable components, and the bandpass for data transmission is limited. In the *ASCA* SIS, a correction factor of zero level, called “dark frame (or dark level)”, is continuously monitored by calculating outputs from pixels without signal detection.

2. **Residual Dark Distribution (RDD) correction**

Radiation damage increases not only the average dark current level, but also its fluctuations among pixels on the chip. These give false offsets to the energy zero point, and degrade energy resolution. Even after the standard other corrections (see below), there remains significant pixel-by-pixel fluctuations in the dark level. This is called residual dark distribution (RDD). In order to get information necessary to correct RDD, the SIS is sometimes operated in “frame mode”, in which all pixel levels are telemetered.

3. **Grade determination**

Determination of the grade, as schematically shown in figure 4.18.

4. **Echo correction**

The pixel level suffers from an artificial increase by “echo” phenomenon, in which some charge at a certain pixel appears to be added to the next pixel. This probably originates in a delay line used in SIS analog electronics (Otani & Dotani 1994). A fractional increase in the charge at one pixel from the right-hand pixel is almost uniform in a chip ( $\sim 1 - 2\%$ ), but it varies individually for each sensor, as a function of time. For Faint mode data, the echo can be corrected using the  $3 \times 3$  pixel matrix, while for Bright mode data it cannot. Thus, this effect should be taken into account by the detector response (see section 4.5) for Bright mode data.

5. **Dark Frame Error (DFE) correction**

A dark frame error (DFE) is a residual dark level due to a problem in the onboard software algorithm (Otani & Dotani 1994). A pixel level is shifted by a constant amount, depending on the accumulation time (thus, on clocking mode). This mainly arises from asymmetric distribution of zero levels, which is affected by X-ray events, particle events, and also optical light leakage.

6. **Charge Transfer Inefficiency (CTI) correction**

The efficiency of the transfer and read-out of charges from CCDs is reduced by

charge traps. This problem is called Charge transfer inefficiency (CTI). These traps are made by lattice defects has in channels of electrons, which are in turn caused by radiation damage in orbit, CTI gradually increased as time passed (Yamashita 1995; Dotani *et al.* 1995). In order to evaluate this effect, several known X-ray objects with many lines (such as Cassiopeia A) have been observed repeatedly at various positions of the same chip.

## 7. Gain adjustment

The correction of gain dispersion on the amplifiers on each chips.

## 8. Removing Hot and Flickering pixel

A hot or flickering pixel is a pixel reporting fake events without incident signal photons. The former almost always exceeds the event threshold, while the latter is more moderate, and sometimes reports a spurious event. Since these pixels exhibits a large charge with high statistical significance compared to the surrounding pixels, they can be removed by Poisson tests.

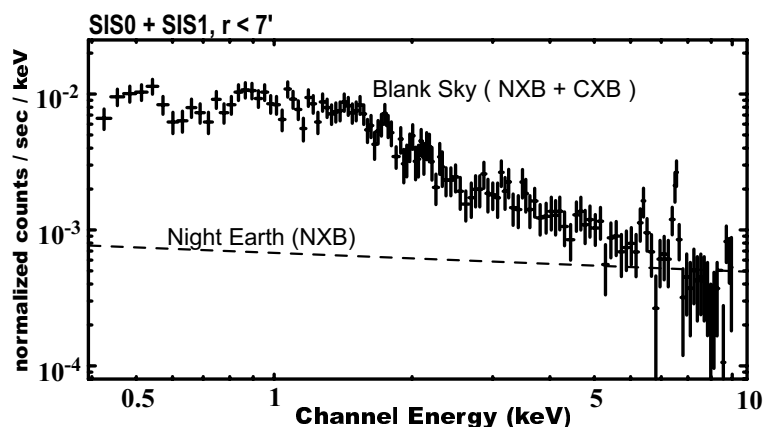


Figure 4.19: Background spectrum of the SIS from black sky survey data, accumulated within  $7'$  from the nominal position.

Figure 4.19 shows the SIS background spectrum, accumulated in blank sky observation, which corresponds to the non X-ray background plus the cosmic X-ray background. The NXB spectrum measured with the SIS is flat. Its level is much less than  $10^{-3}$   $\text{cnt s}^{-1} \text{cm}^{-2} \text{keV}^{-1}$ , and exceeds the CXB level at  $\sim 7$  keV (Gendreau 1994; Gendreau *et al.* 1995). In the NXB spectrum, there are some prominent fluorescent lines of instrumental origin, such as Al  $K_{\alpha}$  line at 1.49 keV from the camera body, Si  $K_{\alpha}$  line at 1.74 keV in the CCD chip, and Fe  $K_{\alpha}$  and  $K_{\beta}$  lines at 6.40 keV and 7.06 keV, respectively, Ni  $K_{\alpha}$  and  $K_{\beta}$  lines at 7.48 keV and 8.27 keV, respectively, and Au  $L_{\alpha 1}$  line at 9.71 keV from CCD package.

## 4.3 Italian X-ray Astrophysical Satellite, *BeppoSAX*

### 4.3.1 Overview

*BeppoSAX* (Satellite italiano per Astronomia X, "Beppo" in honor of Giuseppe Occhialini), is the Italian X-ray mission with a sensitivity in a wide energy bandpass of 0.1 – 300 keV. This satellite has been developed by the Italian Space Agency (ASI) with participation by the Netherlands Agency for Aerospace Programs (NIVR). It has been launched in April 1996 into an almost circular orbit with a height of 600 km and inclination angle of 3 ° to the equator. Figure 4.20 shows a schematic view of its scientific payload. The wide band capability is provided by a set of four instruments, as listed below, which are co-aligned with the  $z$  axis of the satellite.

- **Low Energy Concentrator Spectrometer (LECS)** X-ray telescope with position sensitive GSPC at the focal plane, designed for a low energy bandpass of 0.1-10 keV (Parmar *et al.* 1997 and references therein).
- **Medium Energy Concentrator Spectrometers (MECS)** A medium energy (1.3-10 keV) set of X-ray telescopes (Citterio *et al.* 1985, Conti *et al.* 1994), with two position sensitive GSPCs at their focal planes (Boella *et al.* 1996 and references therein).
- **High Pressure Gas Scintillation Proportional Counter (HPGSPC)** A High Pressure GSPC designed for higher energy bandpass of 4 – 120 keV, filled with a high purity gas mixture of Xenon (90 %) and Helium (10 %) at 5 atmospheres. To maximize its operational life time, it is used only for brighter sources than 10 mCrab (i.e.,  $10 \times 10^{-3}$  times of X-ray flux from Crab Nebula).
- **Phoswich Detector System (PDS)** Collimated phoswich scintillators using NaI and CsI crystals, for 15-300 keV (Frontera *et al.* 1996 and references therein).

The basic parameters of these detectors are summarized in table 4.4. Their sensitivities are already shown in figure 4.1. In this thesis, we only use the MECS instrument, because the others do not cover the iron-line energy region, or lack the sensitivity there. In addition to these instruments, *BeppoSAX* carries onboard Wide-Field Instrument (WFI) for transients and gamma-ray bursts, but we skip the description.

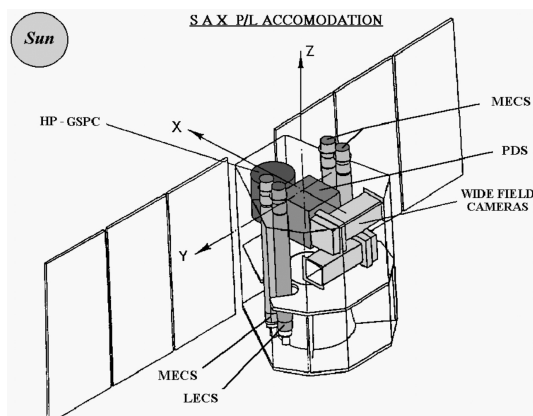


Figure 4.20: *BeppoSAX* scientific payload accommodation.

Table 4.4: The *BeppoSAX* Instruments (Boella *et al.* 1997).

Instrument	Energy range (keV)	FOV <sup>a</sup> °	Ang. Res. <sup>b</sup> arcmin	Effective Area cm <sup>2</sup>	E. reso <sup>c</sup> %
1 LECS	0.1 – 10	0.5	3.5 @0.25 keV	22 @0.25 keV	8 % @6 keV
3 MECS	1.3 – 10	0.5	1.2 @6 keV	150 @6 keV	8 % @6 keV
1 HPGSPC	4 – 120	1.1	collimated	240 @30 keV	4 % @60 keV
1 PDS	15 – 300	1.3	collimated	600 @80 keV	15 % @60 keV
2 WFC <sup>d</sup>	2 – 30	20° × 20°	5	140 @10 keV	18 % @6 keV

<sup>a</sup> Field of view. Radius containing 50% of the power; <sup>b</sup> Angular resolution;

<sup>c</sup> Energy resolution (FWHM); <sup>d</sup> Values per unit through mask.

### 4.3.2 Concentrator Optical System (Mirror Unit)

The mirror units for the LECS and MECS have a similar optical design as the *ASCA* XRT. Each mirror unit is composed of thirty nested coaxial and confocal mirrors having thickness from 0.2 to 0.4 mm. The mirrors have a double cone geometry to approximate the Wolter Type I configuration, with diameters ranging from 162 to 68 mm, and focal length of 1850 mm. The basic parameters are summarized in table 4.5.

Table 4.5: *BeppoSAX* Mirror Unit Specifications

Energy bandpass	$\lesssim 10$ keV
Effective area	$\sim 80$ cm <sup>2</sup> @ 1keV, $\sim 39$ cm <sup>2</sup> @ 7keV (per MU)
Geometrical area	123.964 cm <sup>2</sup> / MU
Field of view	40' for LECS, 30' for MECS
Half Power diameter	$\sim 40''$
Focal length	1850 mm
Nesting number	30 foils
Outer/Inner diameter	300 mm / 150 mm
Total mirror weight	8702 g / MU

### 4.3.3 Medium Energy Concentrator Spectrometer (MECS)

The MECS consists of three units, each composed of a grazing incidence mirror unit (section 4.3.2), and of a position sensitive GSPC located at the focal plane. The basic parameters for MECS are listed in table 4.6. As schematically shown in figure 4.21, the gas cell of a detector unit is composed by a cylindrical ceramic body with 96 mm internal diameter, closed by a 50  $\mu$ m-thick entrance Beryllium window with 30 mm diameter (at the top), and an UV exit window (at the bottom) which is made of Suprasil quartz with 80 mm diameter and 5 mm thickness. The entrance window is externally supported by a Beryllium strongback structure, and two <sup>55</sup>Fe collimated calibration sources are mounted there, as shown in figure 4.22. Thus, MECS detector is very similar to the *ASCA* GIS, although the field of view is slightly smaller than the GIS. The energy resolution to incident X-ray energy is shown in figure 4.23. Since the orbit of *BeppoSAX* has a very small inclination angle, the particle background is intrinsically lower than that of *ASCA*.

Table 4.6: Basic parameters of the *BeppoSAX* MECS.

Energy bandpass	1.3 – 10 keV
Energy resolution	8% at 6.0 keV (FWHM)
Effective area	30 mm diameter
Filed of view	30' diameter
Positional resolution	0.4 mm (FWHM)
Timing resolution	~ 15 $\mu$ sec
Entrance Window	55 $\mu$ m beryllium
Absorption Material	Xe, 20 mm depth, 1.0 atm at 25 °C

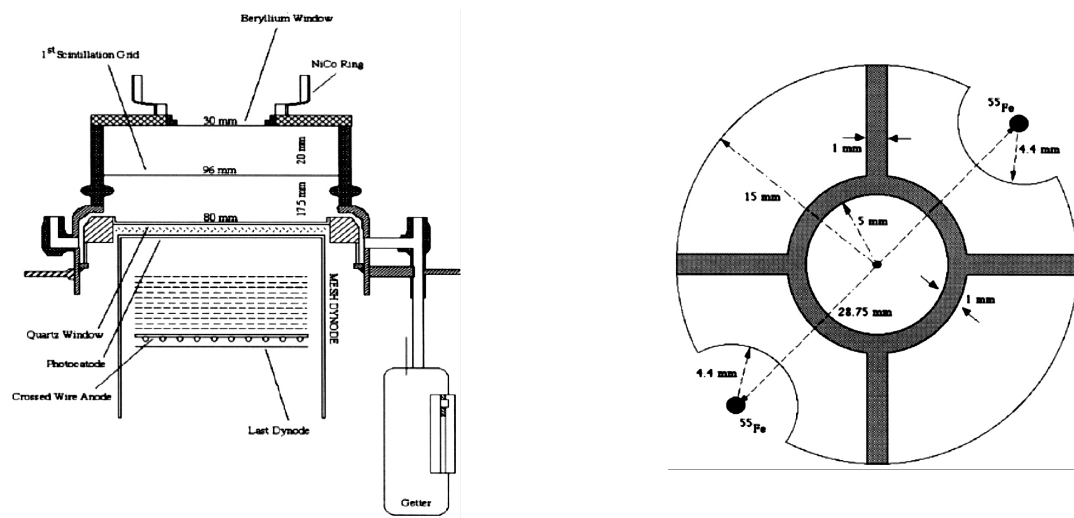


Figure 4.21: A schematic view of the MECS instrument; gas cell and position sensitive GSPC.

Figure 4.22: The structure of Beryllium strongback on the entrance window of the MECS.

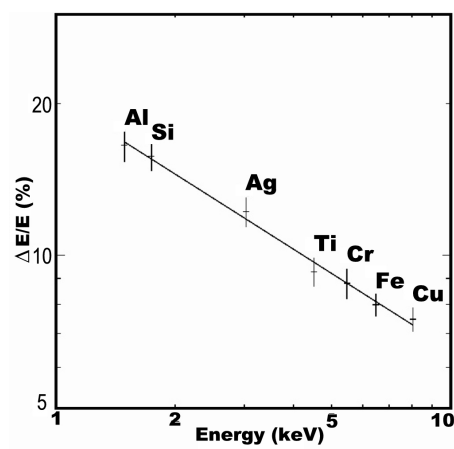


Figure 4.23: Energy resolution of the MECS.

## 4.4 Rossi X-ray Timing Explorer (RXTE)

### 4.4.1 Overview

The *Rossi X-ray Timing Explorer (RXTE)*, named after Bruno Rossi, a cosmic-ray physicist and one of those who first discovered cosmic X-rays (see also section 2.2.2), have been developed by NASA Goddard Space Flight Center, the University of California at San Diego (UCSD), and MIT. A schematic view of this satellite is shown in figure 4.24. *RXTE* carries three scientific instruments as listed below.

- **Proportional Counter Array (PCA)** Five xenon-gas proportional counter detectors, that are sensitive to X-rays with energies from 2 to 60 keV with a large collecting area of  $6250 \text{ cm}^2$  in total.
- **High-Energy X-ray Timing Experiment (HEXTE)** Phoswich-type scintillation counter consisting of NaI(Tl) and of CsI(Na). It is sensitive in the 15 – 250 keV energy range, and has a large collecting area of  $1600 \text{ cm}^2$ .
- **All-Sky Monitor (ASM)** Three scanning shadow cameras on a rotating assembly, to monitor the long-term behavior of a number of the brightest X-ray sources, and to give observers an opportunity to spot any new phenomenon quickly.

The PCA and HEXTE are co-aligned, while the ASM scans the sky over every hour. Since many calibration uncertainties remain in the HEXTE, and its sensitivity is not high enough for our purpose, we only use the PCA data in this thesis.

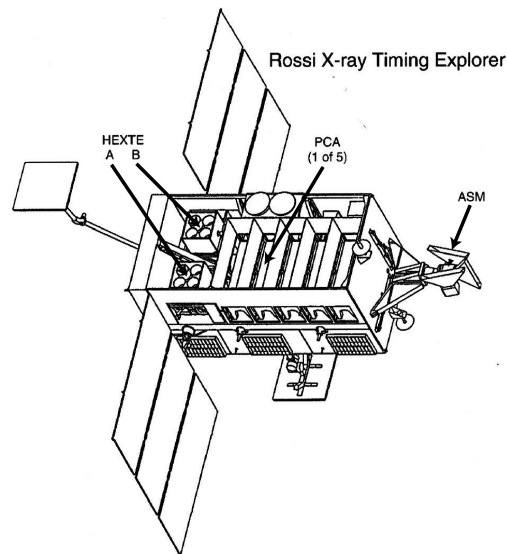


Figure 4.24: A schematic view of the *RXTE* satellite.

### 4.4.2 Proportional Counter Array (PCA)

The PCA, which is based on the *HEAO-1* A2 experiment, is sensitive to hard X-rays in the 2 – 60 keV band. Its design parameters and performance are summarized in table 4.7. As schematically illustrated in figure 4.25, PCA comprise five identical co-aligned Proportional Counter Units (PCUs) with unabsorbed collecting area of  $\sim 1400 \text{ cm}^2$  each. They are mechanically collimated Xenon-Methane proportional counters, and a schematic view of one unit is shown in figure 4.26. The collimator module contains a large number of hexagonal tubes which restrict the field-of-view to  $\sim 1^\circ$ . Each PCU is co-aligned to one another within  $6'$ . The gas unit is attached at the bottom of an equipped collimator, and it is covered with a thin window of aluminized mylar, which curtail the lower energy boundary of the pass band at around 2 keV. It is split into two volumes; the upper propane veto volume and the main xenon volume. Through these volumes, five layers of anode-wire grids are running; two veto layers at the top and bottom (in propane and xenon volume, respectively), and three signal xenon layers, each of which consists of two wires. Among three signal layers, the top one is the most sensitive; approximately 90 % of low energy photons of  $\lesssim 10 \text{ keV}$  are absorbed there. The effective area of five PCUs (in total) with three signal layers is plotted in figure 4.1.

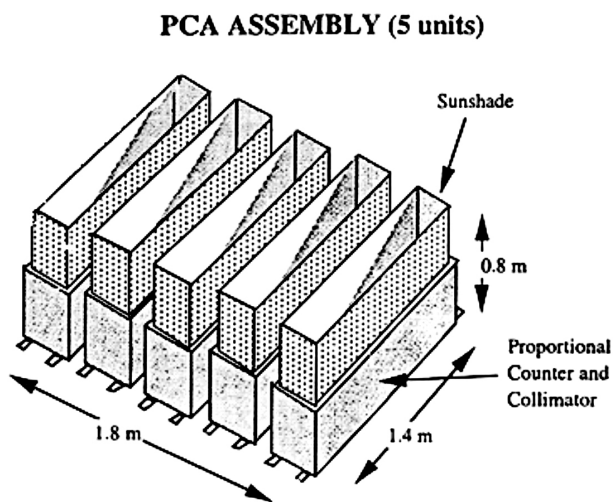


Figure 4.25: Assembly of the PCA, consisting of five proportional counter units.

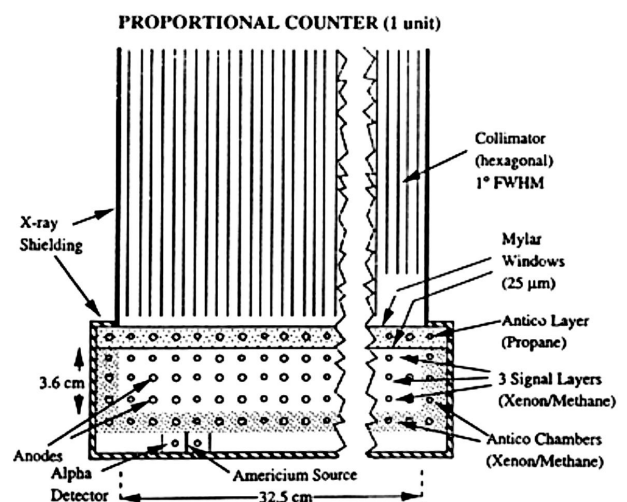


Figure 4.26: A schematic view of one proportional counter unit of the PCA.

The PCA achieves a low background level through efficient anti-coincidence schemes, including side and rear veto chambers and top propane layer. The overall background after rejecting all coincident events varies between 100 and 250 counts per sec according to the orbital coordinate of the spacecraft. Since the PCA has no imaging capability, the background is subtracted by modeling rather than by direct measurement. From the detailed study in observations of blank skies (Jahoda *et al.* 1999), its time-variant background is accounted for mainly by radiation from radio-activated components on the

Table 4.7: Basic parameters of the PCA onboard *RXTE*.

Energy bandpass	2.0 – 60 keV
Energy resolution	$\lesssim 18\%$ at 6.0 keV (FWHM)
Effective area	3000 cm <sup>2</sup> @ 3keV and 6000 cm <sup>2</sup> @ 10keV (5 PCU)
Filed of view	1 degree (FWHM), hexagonal
Timing resolution	1 $\mu$ sec
Layers	1 Propane (for anti-coincidence) + 3 Xe + 1 Xe
Sensitivity	$\sim 0.1$ m Crab
Background	$\sim 2$ m Crab

payload, due to irradiation by high-energy particles, particularly when the spacecraft is passing through the South Atlantic Anomaly (SAA). This is the same effect as was found previously with *Ginga* (Hayashida *et al.* 1989). The modeled background spectrum is estimated by data-based activation model, observational conditions, such as position of the spacecraft, monitor counts for activation (rejected counts for very large event; VLE), that by HEXTE particle monitor (Rothschild *et al.* 1998), and so on. As exemplified in figure 4.27, the background model works well in reproducing variations in non-SAA orbits.

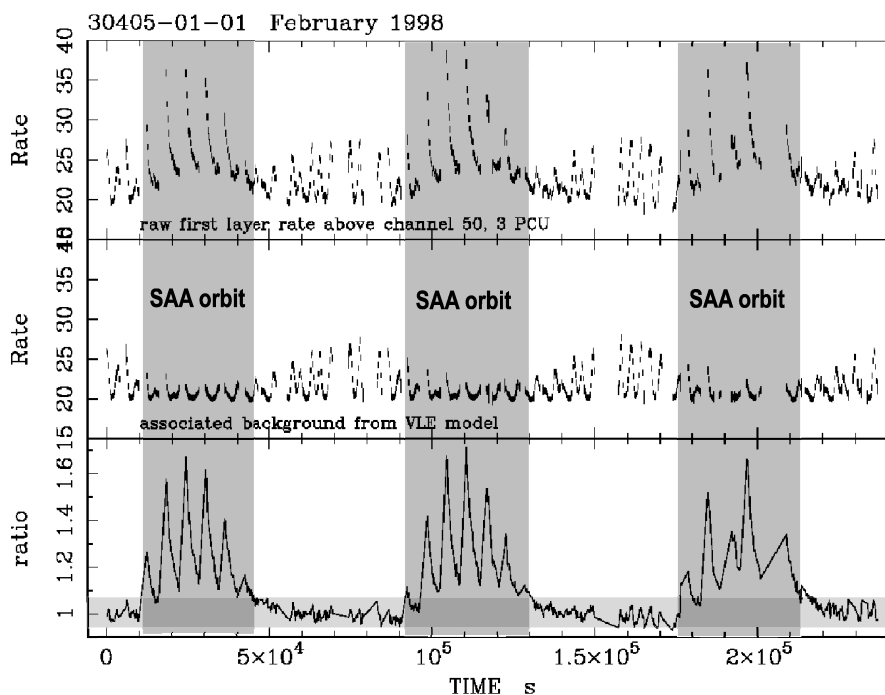


Figure 4.27: The count rate of the PCA in the observation of a faint source, IRAS 18325-5926, and that of the expected background model. (*top*) Observed raw rate from the first layer of PCU 0, 1, and 2 in channels 51 – 249; (*middle*) Very Large Event (VLE) background model corresponding to this data; and (*bottom*) the ratio of data / model. From *RXTE* PCA report by Jahoda *et al.* (1998).

## 4.5 Method of Spectral Analysis

By observing an X-ray source with incident spectrum  $S(E)$ , we obtain a pulse-height (PH) distribution  $D_{\text{det}}(PH)$ . These two quantities are related as

$$D_{\text{det}}(PH) = \sum_E R(E, PH) \cdot S(E), \quad (4.2)$$

where  $R(E, PH)$  is the detector response.

To estimate  $S(E)$  from  $D_{\text{det}}(PH)$  is so-called inverse problem. Usually, it is very difficult to deconvolve directly as

$$S(E) = \sum_{PH} R^{-1}(E, PH) \cdot D_{\text{det}}(PH), \quad (4.3)$$

since the inverse matrix  $R^{-1}$  is subject to large errors due to limited performances of the actual detector responses, such as energy resolution, spatial resolution, and energy bandpass. To avoid this difficulty, we usually employ “forward” method. We restrict the solution to a family of physical models  $M(E; a, b, \dots)$  as

$$S(E) = M(E; a, b, \dots), \quad (4.4)$$

where  $a, b, \dots$  are parameters describing the model. We then simulate PH distribution as

$$D_{\text{sim}}(PH) = \sum_E R(E, PH) \cdot M(E; a, b, \dots), \quad (4.5)$$

and compare it with  $D_{\text{det}}(PH)$ . We search for a set of parameters ( $a, b, \dots$ ) that minimize the difference between  $D_{\text{det}}(PH)$  and  $D_{\text{sim}}(PH)$  in terms of the standard  $\chi^2$  evaluation. The essence of the employed forward method is to reduce the freedom by limiting possible solutions to a particular family. Thus, a physically realistic selection of the model becomes important in the data analysis. In this thesis, we utilize thermal bremsstrahlung model (equation 2.65), Gaussian model, and photo-electric absorption model (equation 2.69).

# Chapter 5

## OBSERVATIONS

### 5.1 Target Selection

The best objects for our observational approach (section 4.1.1) to experimentally confirm the anisotropic mechanism are those MCVs of which our viewing angle to their accretion column swings from pole-on to side-on as they rotate.

With polarimetric observations in the optical to ultraviolet band, inclination  $i$  and pole colatitude  $\beta$  have been measured with a reasonable accuracy from many polars, as listed in table 2.1. The definition of these values are schematically illustrated in figure 5.1. The viewing angle  $\theta$  of accretion column to its vertical axis changes from  $|i - \beta|$  to  $(i + \beta)$  as the spin phase  $\phi$  changes, like

$$\cos \theta = \cos i \cos \beta - \sin i \sin \beta \cos \phi. \quad (5.1)$$

Figure 5.2 shows  $\theta$  of polars with known geometry, as a function of  $\phi$ . Among them, BY Cam, AM Her, EK UMa, V834 Cen, DP Leo, EF Eri and J1015+0904 sweep from  $\theta \sim 10^\circ$  to  $\sim 80^\circ$ .

As for intermediate polars, there is no information on  $\beta$ , since their optical emission is unpolarized. Thus, we can not select objects based on the geometrical criteria.

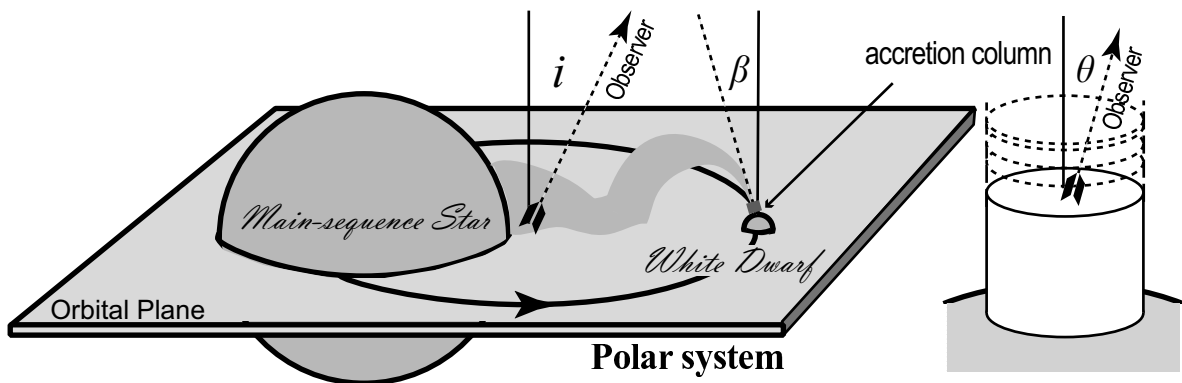


Figure 5.1: A schematic illustration for the definition of inclination  $i$ , pole co-latitude  $\beta$ , and pole angle  $\theta$ .

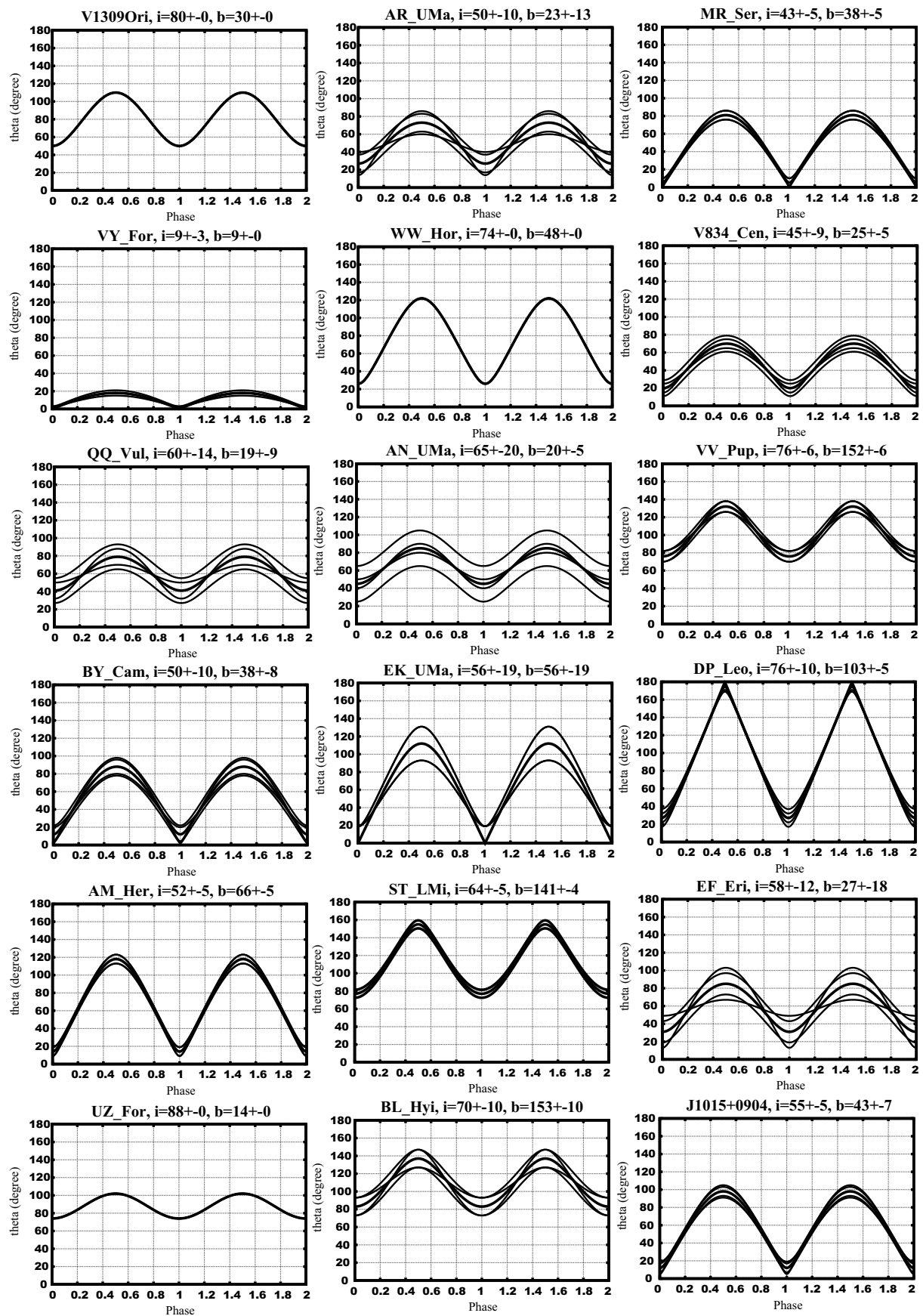


Figure 5.2: Variation of the pole angle  $\theta$  for polars with known geometries, shown as a function of the spin phase.

Table 5.1: Summary for *ASCA* observations of MCVs.

Target name	Date of observation (UT)	Exp. (k sec) <sup>a</sup>		Obs. Mode <sup>b</sup>	Cnt Rate		PI <sup>c</sup>
		SIS	GIS		SIS	GIS	
***** <b>Polar</b> *****							
QQ Vul	1994/10/23.79–24.46	18.3	27.7	Faint	0.07	0.05	Mukai
BY Cam	1994/03/11.49–12.16	29.5	34.7	Faint	0.98	0.68	Kallman
AM Her	(1) 1993/09/27.22–28.27	30.9	43.5	Faint/Bright	0.61	0.43	Gotthelf
	(2) 1995/03/06.84–07.22	18.3	16.8	Faint	0.92	0.66	Ishida
	(3) 1995/03/09.03–10.03	45.5	41.1	Faint	0.89	0.65	Ishida
QS Tel	1996/09/28.93–29.57	15.4	18.1	Faint	0.062	0.040	Rosen
HU Aqr	1994/11/03.77–04.29	21.8	23.3	Faint/Bright	0.048	0.040	Schlegel
EK UMa	1999/05/06.54–07.78	53.0	34.7	Faint	0.017	0.013	Terada
BL Hyi	1994/10/11.47–12.59	41.4	43.5	Faint	0.21	0.16	Fujimoto
V884 Her	<sup>d</sup> 1996/09/30.72– <sup>10</sup> /02.96	84.6	69.0	Faint/Bright	0.023	0.011	Ishida
V2301 Oph	1998/09/28.49–30.21	70.6	73.0	Faint	0.21	0.15	Ishida
V834 Cen	(1) 1994/03/03.64–04.13	21.7	23.2	Faint	0.26	0.18	Mukai
	(2) 1999/02/09.93–11.72	62.3	53.5	Faint	0.25	0.19	Ishida
VV Pup	1993/11/14.92–16.11	40.7	31.5	Faint	0.029	0.022	Ishida
CP Tuc	<sup>e</sup> 1995/11/02.55–03.86	off-axis	35.2	Faint	off-axis	0.34	Misaki
EF Eri	1993/07/23.90–24.77	35.9	39.0	Faint	0.93	0.61	Ishida
RX J1015.5+0904	1999/05/04.08–05.41	54.0	54.0	Faint	0.092	0.073	Terada
***** <b>Intermediate Polar</b> *****							
AE Aqr	1995/10/14.01–14.96	41.6	43.5	Faint/Bright	0.31	0.15	Bookbinder
GK Per	(qu.) 1995/02/04.40–05.47	41.6	41.6	Faint/Bright	0.37	0.36	Mauche
	(o.b.) 1996/03/04.27–04.87	24.0	23.7	Faint	1.21	1.24	Ishida <sup>f</sup>
V1223 Sgr	1994/04/24.18–25.96	57.0	59.2	Faint	1.23	1.00	Osborne
AO Psc	1994/06/22.29–24.56	81.0	84.3	Faint/Bright	0.57	0.48	Hellier
PQ Gem	(1) 1994/11/04.91–07.10	76.2	80.2	Faint	0.37	0.30	Fujimoto
	(2) 1999/10/19.71–20.31	35.0	42.9	Faint/Bright	0.37	0.28	Mukai
BG CMi	(1) 1996/04/14.76–15.97	42.0	43.4	Faint/Bright	0.16	0.17	Mukai
	(2) 1996/04/17.44–18.53	40.9	41.5	Faint/Bright	0.15	0.16	Mukai
RX J1712-2414	1996/03/18.85–21.24	81.4	84.2	Faint/Bright	0.79	0.65	Hellier
FO Aqr	1993/05/20.93–02.04	37.8	38.0	Faint/Bright	0.27	0.32	Mukai
TV Col	1995/02/28.25–01.44	36.7	39.9	Faint/Bright	0.65	0.54	Mauche
TX Col	1994/10/03.29–04.42	39.9	45.1	Faint	0.22	0.16	Wheatley
V1062 Tau	1998/02/16.89–18.48	57.5	14.7	Faint	0.23	0.24	Hellier
EX Hya	1993/07/16.45–17.64	36.0	38.8	Faint	2.79	1.50	Ishida
V405 Aur	(1) 1996/10/05.56–07.47	47.5	41.1	Faint/Bright	0.34	0.23	Mukai
	(2) 1999/03/21.40–22.44	39.0	43.3	Faint/Bright	0.38	0.26	Mukai
J1914+2456	1998/04/09.28–10.24	39.0	23.3	Faint/Bright	0.01	0.006	Mason
XY Ari	(1) 1995/08/07.00–07.91	34.6	34.9	Faint	0.14	0.15	Schlegel
	(2) 1996/01/28.21–29.73	58.5	61.0	Faint	0.16	0.16	Ishida
	(3) 1996/02/18.97–19.56	24.4	25.6	Faint	0.13	0.14	Ishida

<sup>a</sup> Averaged exposure of two sets (SIS0 and SIS1, GIS2 and GIS3) for SIS and GIS.<sup>b</sup> Observation mode. For GIS, all observations have been performed in PH nominal mode.<sup>c</sup> Principal Investigator. <sup>d</sup> V884 Her = RX J1802+1804, POLE.<sup>e</sup> CP Tuc = AX J2315-5910, POLE. This has been serendipitously discovered in the observation for IRAS 23128-5919.<sup>f</sup> TOO (Target of opportunity) observation.

## 5.2 *ASCA* observations

*ASCA* observations of MCVs are summarized in table 5.1. Some objects (V834 Cen, EK UMa, and RX J1015+0904) are the approved targets of our proposal for this purpose, and others are achieved (or published) observations. Among seven polars selected by the geometrical criteria (section 5.1), AM Her and V834 Cen are the best suited for our purpose from a viewpoint of X-ray flux and the exposure actually realized in *ASCA* observations.

For extracting the source photons, we accumulated the GIS and SIS events within a circle of radius 4'.5 centered on the object, employing the following data-selection criteria. We discarded the data during the *ASCA* passing through the South Atlantic Anomaly, and rejected the events acquired when the field of view of *ASCA* was within 5° of the Earth's rim. Furthermore, we discarded the GIS data during occasional errors in the onboard CPU, as well as the SIS data acquired when the FOV is within 10° of the bright Earth rim and those acquired near the day-night-transition of the spacecraft.

## 5.3 *RXTE* observations

In this thesis, we mainly use *ASCA* to study the geometrically selected objects, and additionally analyze their archived *RXTE* data utilizing its large effective area in the phase resolved spectroscopy. Table 5.2 shows the summary of *RXTE* observations of AM Her and V834 Cen.

Table 5.2: Summary of *RXTE* observations of AM Hercuris and V834 Centauri.

Target	Date of observation	Exp. (k sec)	div. number <sup>a</sup>	PI
AM Her	(1) 1998/08/04.40 – 05.72	55.7	2	Christian
	(2) 1998/08/24.40 – 28.55	113.4	8	Beardmore
V834 Cen	(1) 1996/03/19.20 – 20.23	4.2	2	Barrett
	(2) 1996/05/17.10 – 18.19	37.7	5	Imamura
	(3) 1996/08/02.67 – 02.97	25.3	1	Barrett
	(4) 1998/06/23.39 – 25.53	30.0	3	Barrett

<sup>a</sup> Number of division in one series of observation.

We accumulated events with following standard data-selection criteria. We have discarded the data during and within 30 second after the passage of SAA, and those while background caused by the activation (section 4.4.2) is significant as indicated by the monitor count, ELECTRON, exceeding the standard threshold, 0.1. We also rejected events when the field of view (FOV) of PCA was within 10 degrees from the rim of the earth, and when the aiming point (or optical axis) of PCA is departed from the object by more than 0.02 degrees. We estimated time-dependent background events as described in section 4.4.2, using standard software package, *pcabackest*, with the background models supported by the *RXTE* instrument team.

## 5.4 *BeppoSAX* observations

In order to reinforce our scenario as to the anisotropic mechanism, we also search the data of other MCVs for possible evidence of the enhancement of line equivalent width. For this purpose, we use the *BeppoSAX* archived data, in addition to those from *ASCA*. In table 5.3, we summarize *BeppoSAX* observations of MCVs.

Table 5.3: Summary of *BeppoSAX* observations of MCVs.

Target	Date of observation	Exp. (k sec)	div. number <sup>a</sup>	PI
V1309 Ori	1996/10/05.64 – 06.93	56.6	1	Matt Giorgio
V1432 Aql	1997/04/02.28 – 21.06	12.3	4	Luciano Burderi
AM Her	1998/05/08.47 – 09.20	33.5	2	Matt Giorgio
UW Pic	1999/02/14.24 – 15.35	46.7	1	Matt Giorgio
BL Hyi	1996/09/27.42 – 27.62	11.3	1	Matt Giorgio
EU UMa	1998/12/30.49 – 31.29	10.3	1	Matt Giorgio
CP Tuc	1996/11/06.84 – 07.82	50.3	1	James Wheatley
EF Eri	1997/01/07.52 – 08.88	59.1	1	James Wheatley
PQ Gem	1996/11/09.68 – 12.27	115.0	1	Belloni Tomaso
V405 Aur	1996/10/07.17 – 08.13	44.9	1	Osborne Julian

<sup>a</sup> Number of division in one series of observation.

Among polars observed with *ASCA* and *BeppoSAX* (tables 5.1 and 5.3, respectively), we selected the objects with a simple criteria; X-ray flux is  $> 0.05$  counts/s for the GIS or the MECS, and the exposure is  $> 20$  k sec to have enough photon statistics for the phase-resolved analyses.

# Chapter 6

## DATA ANALYSIS AND RESULTS

### 6.1 V834 Centauri

#### 6.1.1 Average spectral continuum with *ASCA*

As summarized in table 5.1, the *ASCA* observations of V834 Centauri were carried out for about 20 ksec on March 1994 and for 60 ksec on February 1999. Before examining the *ASCA* data for the expected phase modulation of the equivalent width of iron K lines, we have analyzed the phase averaged X-ray spectra to construct a proper spectral model (section 4.5). Figure 6.1 shows the background-subtracted *ASCA* SIS and GIS spectra of V834 Cen. We can recognize the continuum X-ray emission from 0.8 to 10.0 keV, and iron line emission around 6.0 – 7.0 keV band.

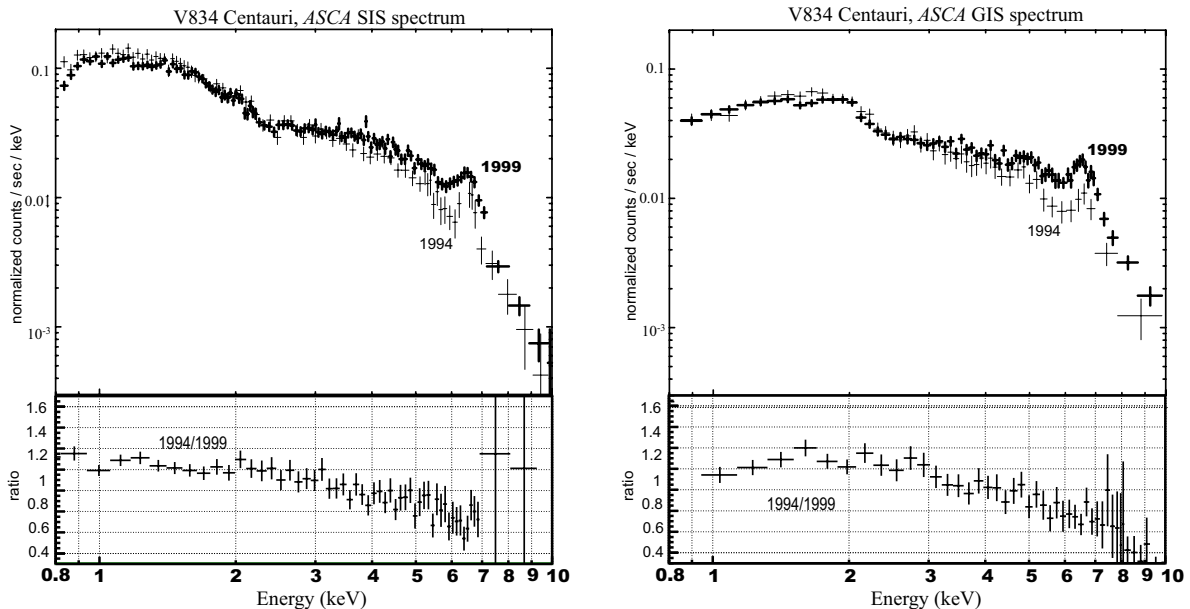


Figure 6.1: X-ray spectra of V834 Cen taken in 1994 and 1999 with the *ASCA* SIS (*left*) and GIS (*right*), shown without removing the instrumental responses. The ratios between the two observations are shown in the bottom panel.

We attempted to quantify the 1.0 – 10.0 keV continua, neglecting the line energy band of 6.0–7.5 keV. In constructing a continuum model, we used the 1999 data, which

has higher statistics than the 1994 data. However, the simplest model for polars, namely a single temperature bremsstrahlung continuum absorbed by a single column density, failed to reproduce the observed spectrum (figure 6.2 *left*; Model 1 in table 6.1). This failure is not surprising, considering that polars generally exhibit multi-temperature X-ray emission with complex absorption by the pre-shock absorber (section 2.6). The extremely high temperature,  $> 200$  keV, obtained by Model 1, is presumably an artifact, compared with the *Ginga* measurement,  $14.7 \pm 1.3$  keV (Ishida 1991).

To accurately estimate the hottest component of the continuum, avoiding complex absorption in soft energies, we then restricted the fit energy band to a narrower hard range of 4.5 – 10.0 keV (Model 2 in table 6.1). This lower limit (4.5 keV) was determined by changing the energy bandpass to optimize the determination of model parameters, as described in §3.2 of Ezuka and Ishida 1994 (appendix A.1). In this case,  $N_{\text{H}}$  is determined solely by the depth of the iron K-edge absorption at  $\sim 7.1$  keV. This model has successfully yielded a temperature consistent with the *Ginga* value. Considering that the K-edge absorption in the observed spectra are relatively shallow, the value of  $N_{\text{H}}$  obtained in this way is thought to approximate the covering-fraction-weighted mean value of multi absorption, which is hence inferred to be  $\sim 10^{23}$  cm $^{-2}$ .

Based on the result by Model 2, we next fitted the original 1.0 – 10.0 keV continuum spectra by adding another bremsstrahlung component to Model 1, and obtained acceptable results (figure 6.2 center; Model 3 in table 6.1). However, the first temperature  $kT_1$  is still too high, and the fit became unacceptable when we fixed  $kT_1$  to the *Ginga* value. Furthermore, the obtained  $N_{\text{H}}$  of  $\sim 10^{22}$  cm $^{-2}$  is not consistent with the inference from Model 2. Thus, we regard Model 3 as inappropriate. As a fourth spectral model, we alternatively added another absorption to Model 1, adopting the concept of partially covered absorption (section 2.6.2). This fitting has been fully acceptable (figure 6.2 right; Model 4 in table 6.1). The obtained  $N_{\text{H}2}$  is consistent with that suggested by Model 2, and the fit remained good even when we fix the temperature to the *Ginga* value. We therefore utilize Model 4 or Model 2 as the best representation of the continuum spectra in 1.0 – 10.0 keV or 4.5 – 10.0 keV, respectively. We also applied the same models to the 1994 data (table 6.1), to find that all the models are acceptable because of poor photon statistics.

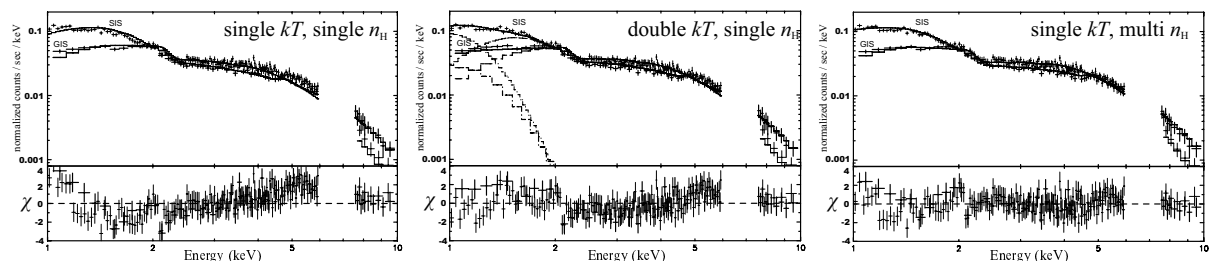


Figure 6.2: Phase averaged GIS and SIS spectra of V834 Cen in 1999, fitted simultaneously with various models; single temperature bremsstrahlung absorbed by a single column density (*left*), double bremsstrahlung with single absorption (*center*), and single bremsstrahlung with leaky absorption (*right*). The best fit parameters are summarized in table 6.1 below an entry of “In 1999”.

Table 6.1: The best fit continuum parameters for the *ASCA* GIS and SIS spectra of V834 Centauri<sup>a</sup>.

model	band <sup>b</sup>	$kT_1$ keV	$kT_2$ keV	$N_{\text{H1}}$ $\times 10^{22} \text{ cm}^{-2}$	$N_{\text{H2}}$ $\times 10^{22} \text{ cm}^{-2}$	cov. frac <sup>c</sup> %	bol. lum. <sup>d</sup> ( $10^{31} \text{ erg s}^{-1}$ )	$\chi^2$ (dof)
<b>In 1994</b>								
Model 1	(single $N_{\text{H}}$ , single $kT$ )	W	—	$< 0.06$	—	—	4.6	0.68 (101)
Model 2	(single $N_{\text{H}}$ , single $kT$ )	N	—	$< 20.9$	—	—	2.1	0.78 (12)
Model 3	(single $N_{\text{H}}$ , double $kT$ )	W	$28.0^{+10.3}_{-7.3}$	$0.15^{+0.05}_{-0.04}$	—	—	2.9	0.65 (99)
Model 3			$14.7^e$	$0.17^{+0.25}_{-0.03}$	—	—	1.9	0.79 (100)
Model 4	(multi $N_{\text{H}}$ , single $kT$ )	W	$17.9^{+39.1}_{-8.8}$	$< 0.04$	$2.7^{+2.5}_{-2.0}$	$21.8^{+15.9}_{-10.9}$	2.3	0.66 (99)
Model 4			$14.7^e$	$< 0.05$	$2.8^{+2.3}_{-1.0}$	$25.7^{+3.8}_{-3.1}$	2.2	0.66 (100)
<b>In 1999</b>								
Model 1	(single $N_{\text{H}}$ , single $kT$ )	W	$> 192$	$0.13^{+0.02}_{-0.03}$	—	—	(13)	2.19 (210)
Model 2	(single $N_{\text{H}}$ , single $kT$ )	N	$12.8^{+20.6}_{-5.2}$	$12.8^{+6.0}_{-3.7}$	—	—	4.6	0.55 (54)
Model 3	(single $N_{\text{H}}$ , double $kT$ )	W	$> 66$	$0.74^{+0.05}_{-0.01}$	—	—	(7.1)	1.29 (208)
Model 3			$14.7^e$	$1.2^{+0.1}_{-0.2}$	—	—	2.8	1.97 (209)
Model 4	(multi $N_{\text{H}}$ , single $kT$ )	W	$> 37$	$< 0.01$	$8.3^{+3.1}_{-1.5}$	$42.4^{+4.1}_{-7.1}$	(6.9)	0.98 (208)
Model 4			$14.7^e$	$< 0.07$	$9.7^{+1.9}_{-1.6}$	$56.4^{+2.1}_{-2.1}$	3.7	1.10 (209)

<sup>a</sup> Excluding the Fe  $K_{\alpha}$  line band (6.0 – 7.5 keV).<sup>b</sup> Energy bandpass for fitting; “W” means 1.0 – 10.0 keV, and “N” 4.5 – 10.0 keV.<sup>c</sup> The covering fraction (%) of  $N_{\text{H1}}$ .<sup>d</sup> Bolometric luminosity. The distance is assumed to be 100 pc.<sup>e</sup> Continuum temperature fixed at the value measured with Ginga (Ishida 1991).

### 6.1.2 Phase-averaged iron lines with *ASCA*

Having quantified the continuum spectra, we proceed to the study of the iron K-line. For this purpose, we used the SIS spectrum (in 1999) because of higher energy resolution than the GIS, and again limited the energy range to the 4.5 – 10.0 keV band to avoid the complex absorption structure in lower energies.

We modeled the iron line with various Gaussian(s), while represented the continuum with Model 2, and obtained the results as in figure 6.3 and table 6.2. A single narrow ( $\sigma = 0.0001$  keV fixed) Gaussian model failed to reproduce the line profile, while a broad Gaussian model with  $\sigma \sim 0.24$  keV has been found to be successful. However, the obtained line centroid energy is too low for ionized Fe-K species from a  $\sim 10$  keV plasma. We can alternatively fit the data successfully with two narrow Gaussians, where the centroid energy of the first Gaussian turns out to be consistent with that of the fluorescent iron  $K_{\alpha}$  line (6.40 keV), and that of the second Gaussian comes in between those of He-like (6.65 – 6.70 keV) and H-like (6.97 keV) iron  $K_{\alpha}$  lines; this implies that the second component is in reality a composite of them. We therefore employed a line model consisting of three narrow Gaussians, each having a free centroid energy and a free normalization. We have then obtained an acceptable fit, with the three centroid energies consistent with the Fe-K line energies of the neutral, He-like, and hydrogen-like species. These three lines have been observed in X-ray spectra of many MCVs with *ASCA* (Ezuka and Ishida 1999, section 6.3, and appendix A.3). Hereafter, we adopt the three narrow Gaussian model in quantifying the iron K lines.

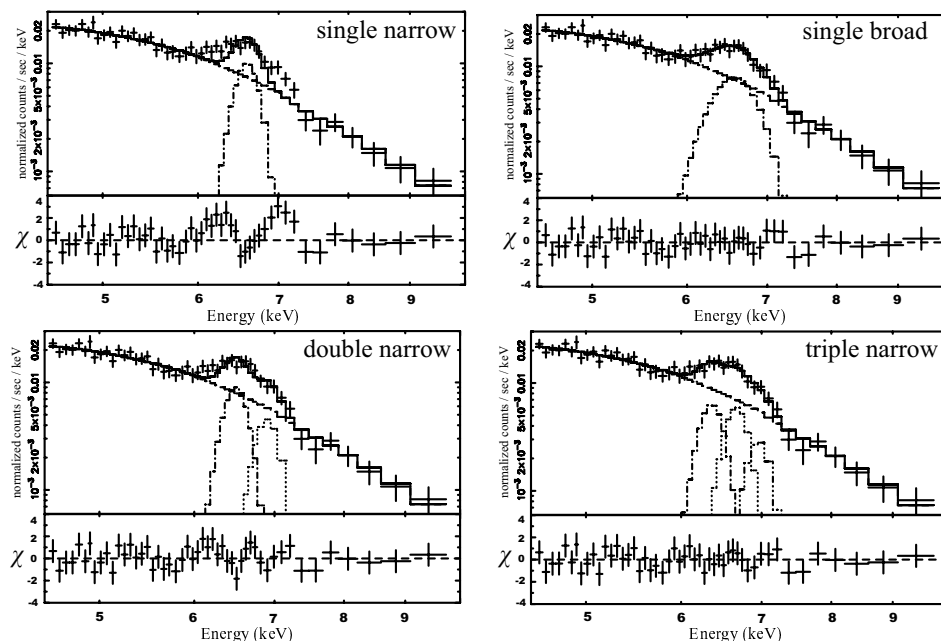


Figure 6.3: An expanded view of the iron- $K_{\alpha}$  line region of the phase averaged SIS spectrum of V834 Cen, obtained in 1999. The line feature is fitted with a single narrow Gaussian (*left top*), a single broad Gaussian (*right top*), a double narrow Gaussian (*left bottom*), and a triple narrow Gaussian model (*right bottom*). The continuum spectrum is represented by Model 2 in table 6.1. The best-fit parameters are shown in table 6.2.

In order to reduce couplings among the three components, we fixed the centroid energy of the first Gaussian (identified with a fluorescent line) at 6.40 keV. This is justifiable, because the 6.40 keV fluorescent Fe-K line is frequently observed from polars. The result is of course successful (table 6.2). Since the theoretical line-energy ratio of the hydrogenic  $K_\alpha$  line to that of helium-like  $K_\alpha$  line is fairly constant in the temperature range of interest (see figure 2.28; Mewe *et al.* 1985), we further fixed the ratio of the second to the third Gaussians to the theoretical value of 1.042, and obtained an acceptable result (table 6.2). Therefore, we employ these conditions in the line modeling.

Table 6.2: The best fit parameters of the iron  $K_\alpha$  line for V834 Centauri<sup>a</sup>.

line model	iron $K_\alpha$ line						statistics
	l.c. 1 <sup>b</sup> (keV)	$\sigma_1$ (keV)	l.c. 2 <sup>b</sup> (keV)	$\sigma_2$ (keV)	l.c. 3 <sup>b</sup> (keV)	$\sigma_1$ (keV)	$\chi^2_\nu$ (dof)
single narrow	$6.59^{+0.03}_{-0.05}$	0.0001 <sup>c</sup>	–	–	–	–	1.44 (48)
single broad	$6.61^{+0.05}_{-0.05}$	$0.24^{+0.07}_{-0.03}$	–	–	–	–	0.63 (47)
double narrow	$6.49^{+0.07}_{-0.37}$	0.0001 <sup>c</sup>	$6.89^{+0.11}_{-0.25}$	0.0001 <sup>c</sup>	–	–	0.88 (46)
triple narrow	$6.35^{+0.19}_{-0.21}$	0.0001 <sup>c</sup>	$6.66^{+0.03}_{-0.07}$	0.0001 <sup>c</sup>	$6.96^{+0.15}_{-0.06}$	0.0001 <sup>c</sup>	0.66 (44)
	6.40 <sup>c</sup>	0.0001 <sup>c</sup>	$6.66^{+0.07}_{-0.06}$	0.0001 <sup>c</sup>	$7.01^{+0.09}_{-0.09}$	0.0001 <sup>c</sup>	0.63 (45)
	6.40 <sup>c</sup>	0.0001 <sup>c</sup>	$6.67^{+0.06}_{-0.06}$	0.0001 <sup>c</sup>	6.95 <sup>d</sup>	0.0001 <sup>c</sup>	0.66 (46)

<sup>a</sup> The phase averaged spectrum. Only SIS data are used for the fitting. Fitted with a single temperature and single column density model in 4.5–10.0 keV. Fixed the continuum temperature and  $N_{\text{H}}$  to the Model 2 in table 6.1.

<sup>b</sup> Line center energies (keV).

<sup>c</sup> Fixed.

<sup>d</sup> The line energy ratio of the second Gaussian to the third is fixed to 1.042.

Having constructed the spectral model, we finally fitted the phase-averaged spectra in 1994 and 1999, separately. The GIS and SIS spectra are simultaneously fitted with Model 2 continuum and three narrow Gaussians. The results are shown in figure 6.4 and table 6.3 (in the row of “Average”). As already displayed in section 6.1.1, the continuum temperature and  $N_{\text{H}}$  are consistent between the two epochs. The equivalent width of H-like iron line is comparatively smaller than that of He-like iron line. The equivalent widths of He-like and H-like lines are consistent with being constant between the two epochs within 90% error. On the other hand, that of fluorescent line increased in 1999 with > 90% significance. This variation is not surprising, since this emission is thought to be a reprocessed radiation by a surrounding cold material (such as white dwarf surface, or pre-shock matter) of the accretion column.

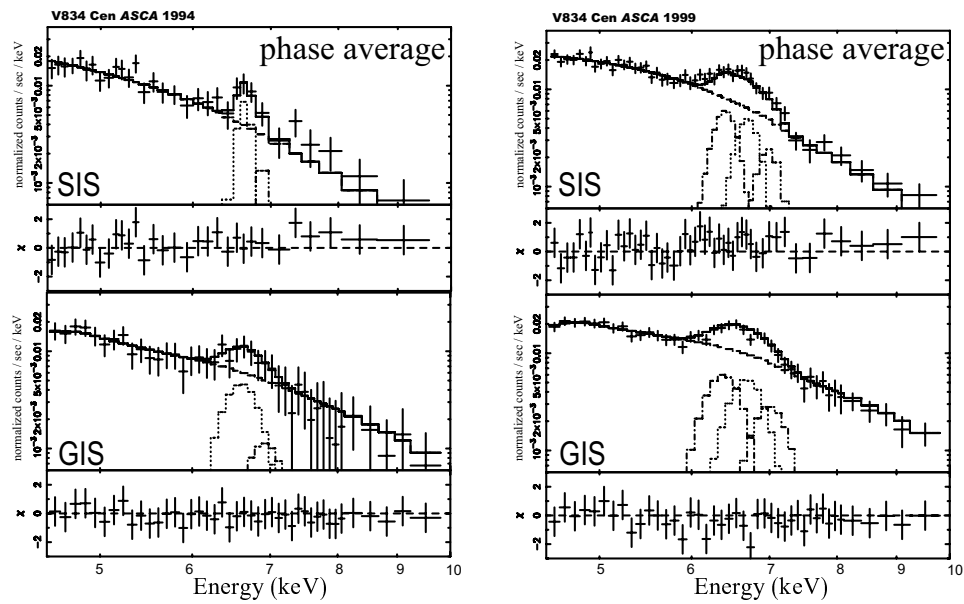


Figure 6.4: Phase-averaged spectra in 1994 (*left*) and 1999 (*right*) over the Fe-K line energies, fitted with the continuum Model 2 and three narrow Gaussians. The data of the SIS and GIS are simultaneously fitted. The central energy of the first Gaussian is fixed at 6.4 keV, and the line center ratio of the second Gaussian to the third is fixed at 1.042. The best-fit parameters are shown in table 6.3.

### 6.1.3 Phase resolved *ASCA* spectra

To perform the phase resolved analysis with *ASCA*, we folded the X-ray light curve of V834 Cen by its rotational period, 1.69194 hr (table 2.1; Schwope *et al.* 1993), as shown in figure 6.5. We can recognize small dips in the softer two energy bands at phase  $\phi \sim 0.65$  in 1994 and  $\sim 0.86$  in 1999. These dips are thought to arise from photoelectric absorption by a pre-shock matter on the accretion column. The pole-on phase is determined by the optical photometry and polarimetry (see table 1 of Bailey *et al.* 1983), which corresponds to a phase  $\phi \sim 0.65$ – $0.85$  in this figure. Therefore, the pole-on phase is consistent between the optical and X-ray datasets, and we defined pole-on phase as  $\phi = 0.73 \pm 0.25$  and side-on phase as  $\phi = 0.23 \pm 0.25$ . The folded light curve in the iron line energy band (6.2 – 7.2 keV) exhibits a slight hump at or near the pole-on phase, suggesting that the proposed line enhancement is indeed taking place in this system.

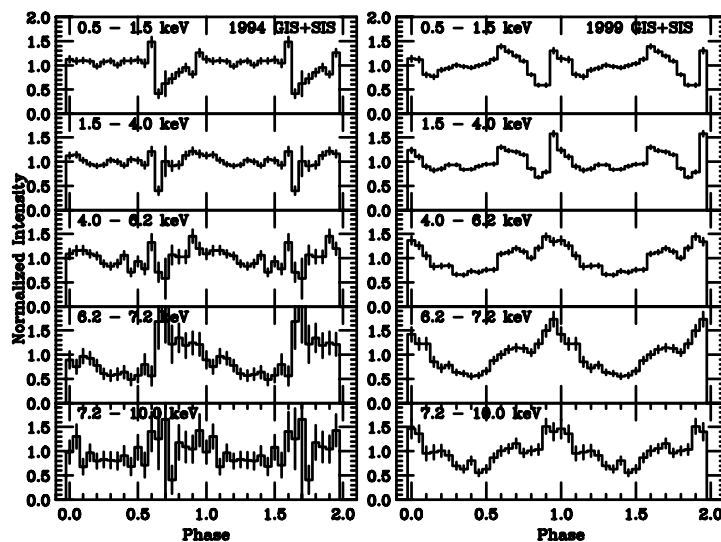


Figure 6.5: Energy resolved light curves of V834 Cen obtained with *ASCA*, folded at its spin period, 1.69194 hr. The X-ray arrival times are corrected to the solar barycentric values. Phase  $\phi = 0$  corresponds to HJD 2445048.9500 (Schwope *et al.* 1993), which is common to the 1994 (*left*) and 1999 (*right*) light curves. Each curve is shown for two cycles.

To examine the enhancement in detail, we have accumulated the GIS and SIS data over the two phases separately, and plotted the phase-resolved X-ray spectra as shown in figure 6.6. We can see the intensity of iron line relative to the continuum emission, i.e., the line equivalent width, becomes slightly stronger in pole-on phase, as expected.

In order to quantify the equivalent widths of the iron lines, we fitted simultaneously the 0.4 – 10 keV GIS and SIS spectra, using Model 2 continuum (established in section 6.1.1) and three narrow Gaussians with some of the parameters fixed or constrained (section 6.1.2). The results are summarized in figure 6.7 and table 6.3. The temperature and  $N_{\text{H}}$  are the same between the two phases within 90% errors, and the equivalent widths of fluorescent and H-like iron lines are also consistent with being unmodulated. This

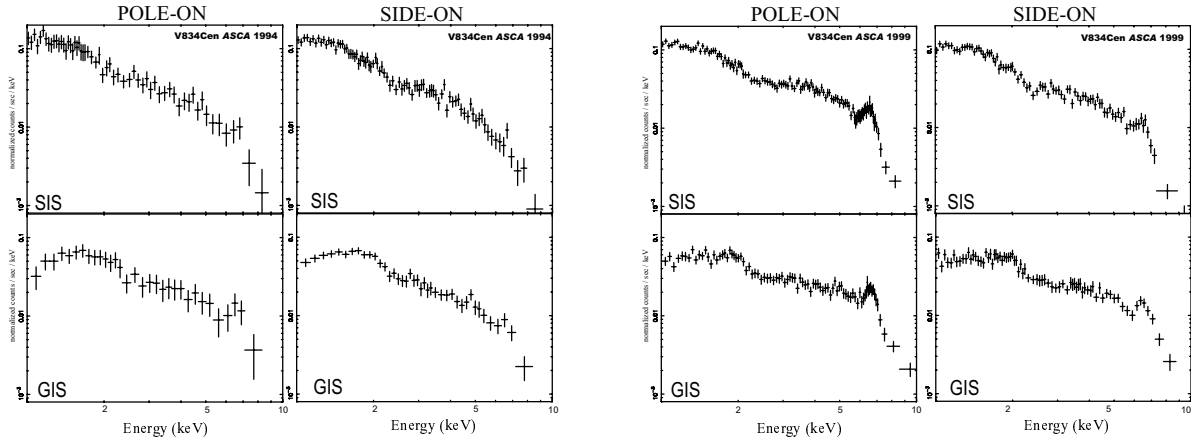


Figure 6.6: Phase resolved *ASCA* SIS (*top*) and GIS (*bottom*) spectra obtained in 1994 (*left*) and 1999 (*right*).

statement applies both to the 1994 and 1999 data sets. In contrast, the equivalent width of the He-like line is clearly enhanced at pole-on phase by  $\zeta_{\text{obs}}(\text{He}) = 1.9^{+1.0}_{-0.7}$  times in 1999 with  $> 90\%$  statistical significance. This factor is defined by the ratio of the equivalent width of pole-on phase to that of side-on phase as

$$\zeta \equiv \frac{EW(\text{pole})}{EW(\text{side})}, \quad (6.1)$$

which corresponds to

$$\zeta = \frac{\langle \xi(\theta) \rangle_{\text{pole}}}{\langle \xi(\theta) \rangle_{\text{side}}}, \quad (6.2)$$

where  $\xi(\theta)$  is defined by equation (3.19). The results do not change significantly [ $\zeta_{\text{obs}}(\text{He}) = 1.9^{+0.9}_{-0.6}$ ; table A.3] even if we employ the entire energy band together with the continuum Model 4 (appendix A.2). The 1994 datasets exhibit the same tendency, although in this case we cannot exclude the hypothesis of constant equivalent width due to the poorer statistics.

To demonstrate the enhancement more clearly, we simultaneously fitted the pole-on and side-on spectra, by constraining the continuum temperature and all the line energies to be common (but free) between the two phases. This is justifiable, because these quantities are consistent with being unmodulated (table 6.3), and there is no reason for them to depend on the spin phase with the energy resolution of *ASCA*. We allow  $N_{\text{H}}$  and the line equivalent widths to be different between the two phases. Figure 6.8 shows the confidence contours of the equivalent widths between the two phases. Thus, the equivalent widths of the fluorescent and H-like iron lines are consistent with being unmodulated, whereas that of the He-like line is enhanced in the pole-on phase by a factor of  $\zeta_{\text{OBS}}(\text{He}) = 1.9^{+1.0}_{-0.7}$  in 1999 with  $>90\%$  significance. Similarly, the He-like iron line is enhanced by a factor of  $\zeta_{\text{OBS}}(\text{He}) = 1.8^{+1.6}_{-1.0}$  in 1994, though statistically insignificant. This clear spin modulation of He-like iron K line supports our scenario, and hence V834 Centauri is the first object to observationally demonstrate the resonance scattering effect.

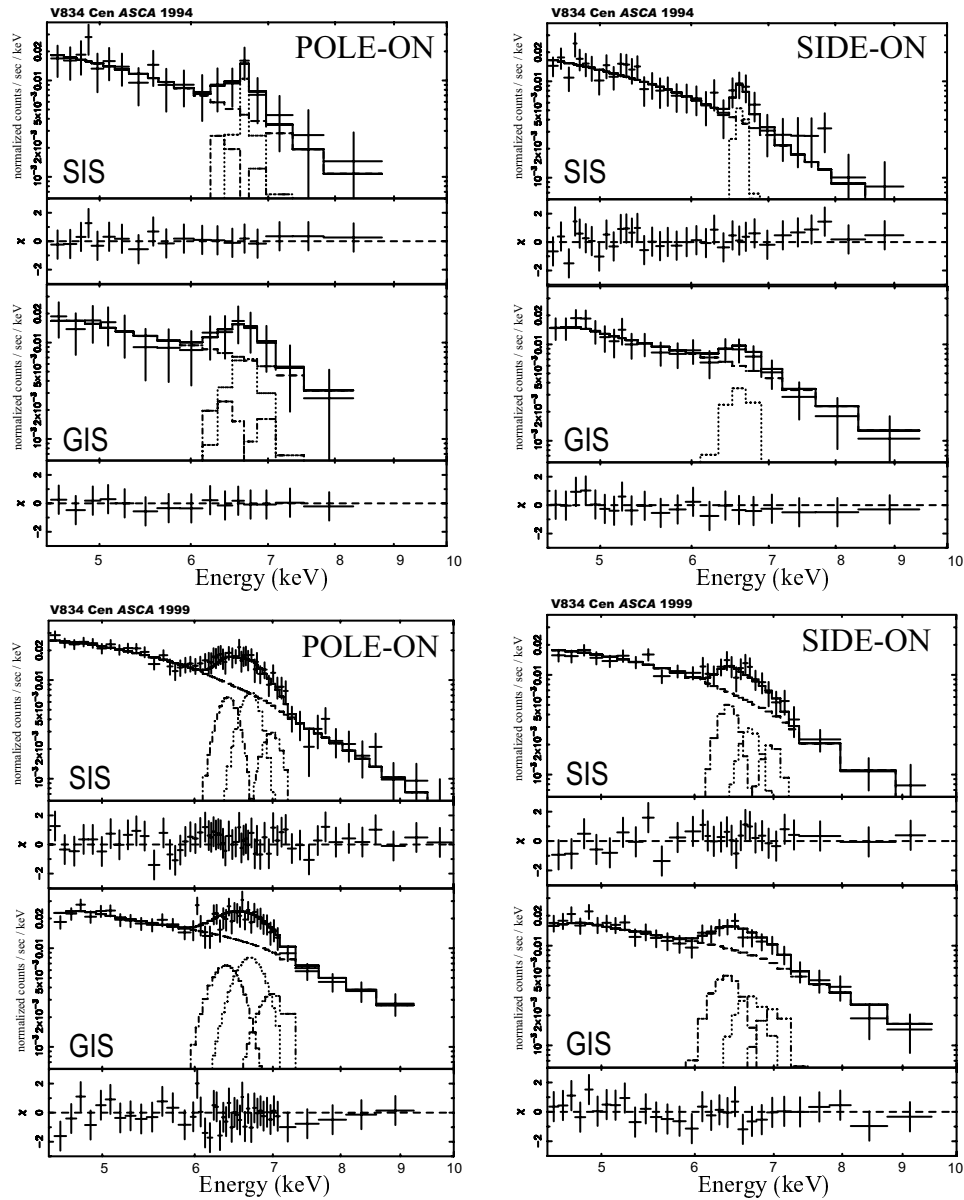


Figure 6.7: The same plot as figure 6.4, but shown separately for the pole-on ( $\phi = 0.73 \pm 0.25$ ) and the side-on ( $\phi = 0.23 \pm 0.25$ ) phases. The best-fit parameters are given in table 6.3.

Table 6.3: The best fit parameters of the iron  $K_\alpha$  line with three narrow gaussians<sup>a</sup>.

phase <sup>b</sup>	continuum		fluo.	He-like $K_\alpha$		H-like $K_\alpha$		$\chi^2_\nu$ (dof)
	$kT$	$N_H$	$EW$	l. c. <sup>c</sup>	$EW$	l. c. <sup>c</sup>	$EW$	
	(keV)	$\times 10^{22} \text{ cm}^{-2}$	(eV)	(keV)	(eV)	(keV)	(eV)	
<b>In 1994</b>								
Average	$11.3^{+112}_{-7.1}$	$3.5^{+12.9}_{-3.53}$	< 108	$6.64^{+0.07}_{-0.08}$	$400^{+127}_{-127}$	6.92	$119^{+135}_{-118}$	0.41 (68)
Pole-on	$15.5^{+103}_{-7.4}$	< 40.4	< 443	$6.68^{+0.12}_{-0.11}$	$562^{+359}_{-343}$	6.96	$162^{+451}_{-161}$	0.16 (27)
Side-on	> 3.1	< 23.3	< 98	$6.62^{+0.10}_{-0.32}$	$319^{+154}_{-157}$	6.89	$74^{+161}_{-74}$	0.41 (49)
<b>In 1999</b>								
Average	$10.6^{+11.3}_{-3.6}$	$14.5^{+5.5}_{-4.3}$	$272^{+49}_{-45}$	$6.69^{+0.06}_{-0.04}$	$288^{+52}_{-57}$	6.97	$183^{+64}_{-55}$	0.67 (86)
Pole-on	$11.3^{+11.6}_{-2.6}$	$13.7^{+23.5}_{-7.8}$	$264^{+61}_{-66}$	$6.70^{+0.07}_{-0.05}$	$378^{+86}_{-86}$	6.98	$197^{+80}_{-86}$	0.56 (97)
Side-on	$10.5^{+11.7}_{-3.8}$	$14.9^{+4.4}_{-4.1}$	$274^{+91}_{-81}$	$6.69^{+0.70}_{-0.13}$	$201^{+92}_{-97}$	6.97	$184^{+102}_{-118}$	0.50 (53)

<sup>a</sup> The determination of continuum spectrum is performed in 4.5 keV – 10.0 keV with Model 2 in table 6.1.  
<sup>b</sup> Pole-on corresponds to  $\phi = 0.73 \pm 0.25$  and Side-on to  $\phi = 0.23 \pm 0.25$ .  
<sup>c</sup> The line center energy (keV). That of the fluorescent component is fixed at 6.40 keV, and the ratio of H-like and He-like line is fixed to 1.042.

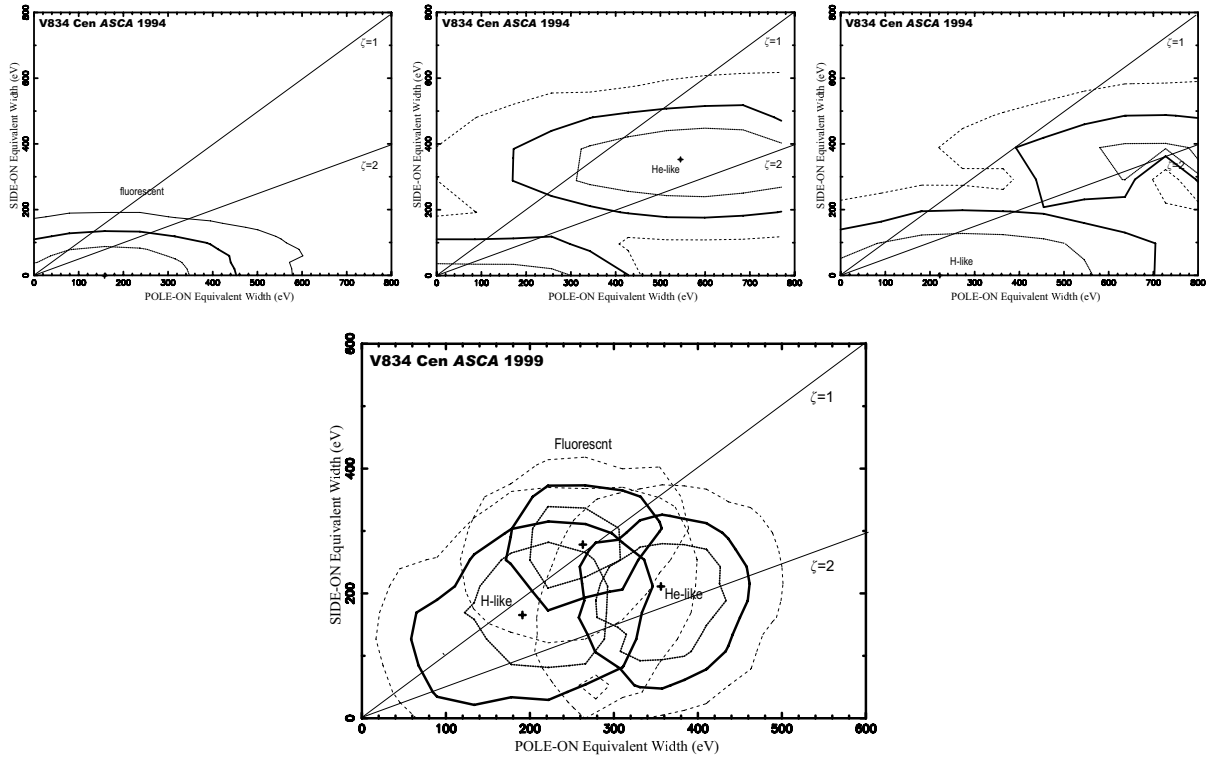


Figure 6.8: A confidence contour of the equivalent width between pole-on and side-on phases, derived by simultaneously fitting the GIS/SIS spectra of the two phases. Details are described in the text. The contour is plotted for 68.3% (thin dotted line), 90% (thick solid line) and 99% (dashed line) confidence levels. The straight lines indicate  $\zeta = 1$  (no modulation) and  $\zeta = 2$  (a factor 2 enhancement in the pole-on phase).

### 6.1.4 *RXTE* observations

We have analyzed the *RXTE* data of V834 Centauri to examine consistency with the *ASCA* results. The observations were performed in 1996, 1997, and 1998, as summarized in table 5.2. Figures 6.9 and 6.10 show the phase-averaged spectra of the three observations. We can see bremsstrahlung-like continuum and an iron line hump near 7 keV.

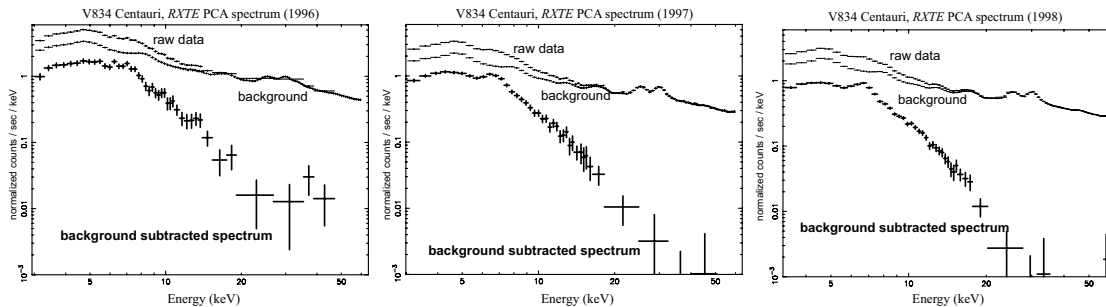


Figure 6.9: X-ray spectra of V834 Cen, obtained with *RXTE* in 1996 (*left*), 1997(*center*), and 1998 (*right*). Raw, background, and background-subtracted spectra are shown in solid, thin, and thick lines, respectively.

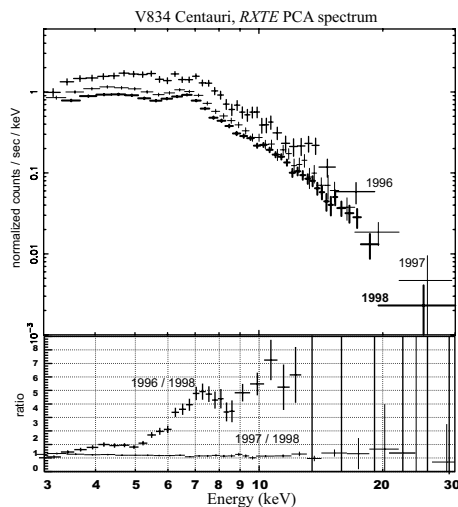


Figure 6.10: The same spectra as presented in figure 6.9 with thick lines, shown together with their ratios (bottom panel).

We first construct a model to quantify the PCA spectra of V834 Cen, using the summed X-ray data from the 1997 and 1998 observations (excluding the 1996 data for a moment). Here and hereafter, we always include 2 % systematic errors to all data bins when analyzing the PCA data. To avoid a complex absorption structure in softer energies, we restrict the energy range to  $> 5.0$  keV. Over the  $5.0 - 20.0$  keV range, but neglecting the iron-line energy band  $5.5 - 7.8$  keV, the simplest model of single bremsstrahlung with a single absorption can reproduce the PCA continuum spectrum, as shown in table 6.4. However, because of the limited soft-energy sensitivity, the PCA data cannot constrain the photoelectric absorption reliably, and the upper limit is one order of magnitude lower than that obtained by *ASCA* (Model 2 in table 6.1). Furthermore, a negative residual remains

near 8 keV as shown in figure 6.11. This must be due to the iron K-edge absorption. We accordingly modified the absorption model in equation (2.69) as

$$N_{\text{H}}\sigma(E) \rightarrow N'_{\text{H}}\sigma'(E) + N_{\text{Fe}}\sigma_{\text{Fe}}(E_{\text{ed}}, \tau_{\text{ed}}; E), \quad (6.3)$$

where  $E_{\text{ed}}$  is the edge energy and  $\tau_{\text{ed}}$  is the depth of edge absorption;

$$Ab(E) = \exp \left[ -\tau_{\text{ed}} (E/E_{\text{ed}})^{-1/3} \right], \quad (6.4)$$

for  $E > E_{\text{ed}}$ . This model, hereafter called “edge model”, has provided an acceptable fit (table 6.4) to the line-masked spectrum, and the value  $E_{\text{ed}}$  comes in reasonable range; in between 7.1 keV for neutral iron and 9.3 keV for hydrogen-like iron. The edge model introduced here is essentially a simplified version of the continuum Model 4 used to describe the *ASCA* spectra, since the iron K-edge absorption is the most outstanding feature of the highly absorbed component in Model 4. The Fe-K edge depth obtained with the PCA, 0.1 – 0.2 (table 6.4), is consistent with what is expected from the *ASCA* results ( $\sim 50\%$  of the continuum is absorbed by  $N_{\text{H}2} \sim 1 \times 10^{23} \text{ cm}^{-2}$ ; table 6.1). We hence employ the edge model for the continuum.

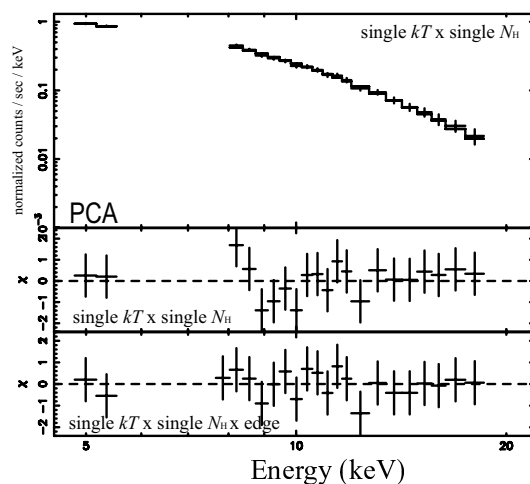


Figure 6.11: Phase averaged X-ray spectrum of V834 Cen (1997 + 1998), fitted with a single bremsstrahlung absorbed by a single column density. The iron K-like band, 5.5 – 7.8 keV, is ignored. Middle and bottom panels show the residuals from a simple absorbed continuum and from that with edge absorption, respectively.

We next fitted the entire spectrum by adding Gaussian(s) to the above continuum model. The fit is acceptable for a narrow Gaussian, and the upper limit on the Gaussian width,  $\sigma$ , is 0.23 keV for a broad one as shown in table 6.4 and figure 6.12. The results by three narrow Gaussian models, as used in the *ASCA* analysis, are also acceptable (table 6.4), in which, however, we cannot determine the center energies of lines because of the insufficient energy resolution of the PCA. We therefore adopt the single broad Gaussian model in evaluating the iron line with the PCA data.

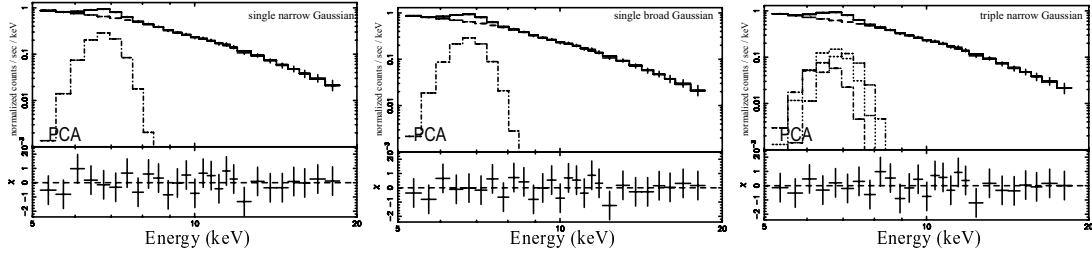


Figure 6.12: The same plot as figure 6.11, but restoring the iron energy band. The histograms show the best fit model with a single narrow Gaussian (*right*), a single broad Gaussian (*center*), and triple narrow Gaussians (*right*). The obtained parameters are summarized in table 6.4.

Table 6.4: The best fit parameters of the iron  $K_{\alpha}$  line for V834 Centauri with the PCA <sup>a</sup>.

model	continuum				iron $K_{\alpha}$ line				statistics
	$kT$ (keV)	$N_{\text{H}}$ $10^{22} \text{ cm}^{-2}$	$E_{\text{eg}}$ (keV)	depth	l.c. 1 <sup>b</sup> (keV)	$\sigma_1$ (keV)	l.c. 2 <sup>b</sup> (keV)	l.c. 3 <sup>b</sup> (keV)	
cont. 1 <sup>c</sup>	$13.1^{+1.6}_{-2.1}$	$< 3.2$	—	—	—	—	—	—	0.64 (18)
cont. 2 <sup>d</sup>	$13.5^{+3.2}_{-4.4}$	$< 9.5$	$8.6^{+0.5}_{-0.5}$	$0.14^{+0.17}_{-0.11}$	—	—	—	—	0.41 (16)
narrow Ga.	$12.7^{+3.5}_{-2.5}$	$< 8.6$	$8.6^{+0.4}_{-0.4}$	$0.17^{+0.08}_{-0.11}$	$6.72^{+0.06}_{-0.04}$	$0.0001^e$	—	—	0.42 (21)
broad Ga.	$12.8^{+2.0}_{-1.4}$	$2.6^{+0.5}_{-0.7}$	$8.6^{+0.4}_{-0.5}$	$0.13^{+0.10}_{-0.09}$	$6.72^{+0.05}_{-0.06}$	$< 0.23$	—	—	0.41 (20)
triple Ga.	$14.8^{+1.9}_{-1.0}$	$< 1.4$	$8.7^{+0.4}_{-0.5}$	$0.11^{+0.04}_{-0.04}$	$> 4.6$	$0.0001^e$	$6.7^{+19.4}_{-3.8}$	$7.0^{+0.1}_{-0.3}$	0.46 (17)

<sup>a</sup> The phase averaged spectrum of *RXTE* PCA in 5.0–20.0 keV band, where the systematic error is set to 2 %.

<sup>b</sup> Line center energy.

<sup>c</sup> Fitting without 5.5 – 7.8 keV band to avoid iron line. Single bremsstrahlung with a single absorption model.

<sup>d</sup> Same as c, but with Fe-K edge included (see text).

<sup>e</sup> Fixed.

### 6.1.5 Phase resolved *RXTE* spectra

In order to examine the iron-line equivalent width for possible phase-dependent modulations as seen in the *ASCA* observation (figure 6.7), we have performed the phase resolved analysis on the PCA data. The background-subtracted light curves acquired with the PCA are modulated at the spin period of V834 Cen, as shown in figure 6.13. Since the data obtained in 1996 are limited in spin phases, we use only the data in 1997 and 1998. We have accumulated the data over the pole-on ( $\phi = 0.73 \pm 0.15$ ) and side-on ( $\phi = 0.23 \pm 0.15$ ) phases separately. We co-added the 1997 and 1998 data based on the common phase ephemeris, and we employ a narrower phase range than in the *ASCA* analysis ( $\pm 0.15$  rather than  $\pm 0.25$ ) utilizing the large-area capability of the PCA.

As presented in figure 6.14, the pole-on phase spectrum indeed exhibits a significantly stronger iron line than the side-on spectrum. Both these spectra have been described successfully by the edge continuum model with a Gaussian model, as established in section 6.1.4. Quantitatively, the iron-line equivalent width in the pole-on phase is  $\zeta_{\text{obs}}(\text{fl} + \text{He} + \text{H}) = 1.4_{-0.5}^{+1.2}$  times that in the side-on phase, as given in table 6.5. To see the results more clearly, we have simultaneously fitted the spectra in both phases by combining the continuum temperature and the line center energy, as was done for the *ASCA* data. As shown in figure 6.15, we can see the iron-line equivalent width is enhanced in pole-on phase, although it is statistically insufficient with the PCA.

To compare this with the *ASCA* results, we calculated the EW-weighted-mean value of  $\zeta_{\text{obs}}$  among the fluorescent, He-like, and H-like lines obtained with what is expected from the *ASCA* measurements (table 6.3). As shown in figure 6.15, the best fit value of  $\zeta_{\text{obs}}(\text{fl} + \text{He} + \text{H})$  with the PCA is consistent with *ASCA*. Therefore, our conclusion on V834 Cen, the first object presenting the resonance scattering effect, has been reinforced by the *RXTE* observations.

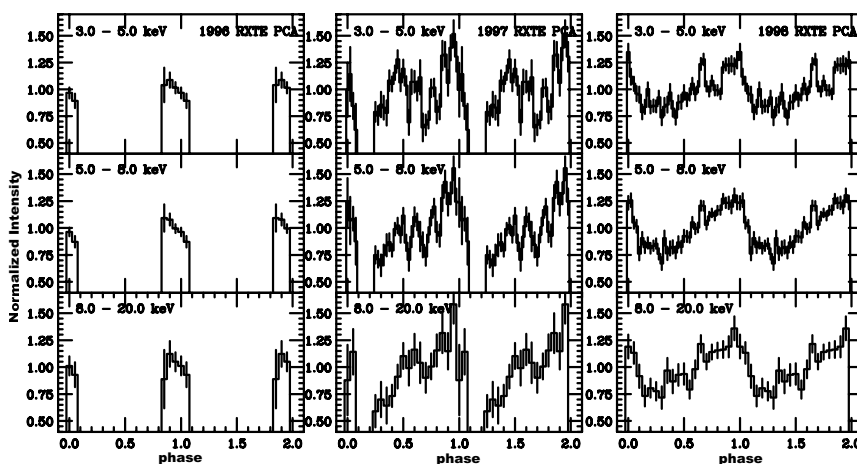


Figure 6.13: Background-subtracted light curves of V834 Cen obtained with the *RXTE* PCA, folded at its spin period, 1.69194 hr. Phase  $\phi = 0$  corresponds to HJD 2445048.9500.

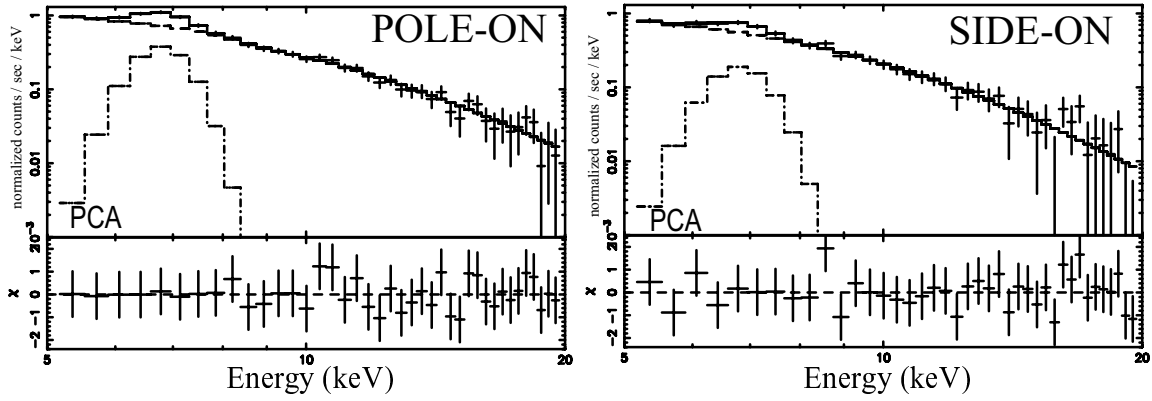


Figure 6.14: Phase resolved spectra of V834 Cen with *RXTE*. The 1997 and 1998 data are co-added. Pole-on corresponds to phase  $\phi = 0.73 \pm 0.15$ , and side-on  $\phi = 0.23 \pm 0.15$  in figure 6.13. The best-fit parameters are shown in table 6.5.

Table 6.5: The best fit parameters of the phase-resolved V834 Cen spectra with *RXTE* PCA<sup>a</sup>.

Phase <sup>b</sup>	continuum				iron $K_{\alpha}$ line			statistics
	kT (keV)	$N_{\text{H}}$ ( $\times 10^{22}$ cm <sup>-2</sup> )	$E_{\text{eg}}$ (keV)	depth	l.c. <sup>c</sup> (keV)	$\sigma_1$ (keV)	$EW$ (eV)	
Average <sup>d</sup>	$12.8^{+2.0}_{-1.4}$	$2.6^{+0.5}_{-0.7}$	$8.6^{+0.4}_{-0.5}$	$0.13^{+0.10}_{-0.09}$	$6.72^{+0.05}_{-0.06}$	$< 0.23$	$526^{+83}_{-77}$	0.41 (20)
Pole-on	$13.6^{+6.0}_{-3.3}$	$4.1^{+5.1}_{-3.1}$	$8.2^{+0.7}_{-2.6}$	$0.17^{+0.16}_{-0.15}$	$6.72^{+0.16}_{-0.07}$	$< 0.43$	$624^{+93}_{-107}$	0.42 (34)
Side-on	$9.4^{+6.6}_{-2.7}$	$< 15$	any	$< 0.37$	$6.75^{+0.22}_{-0.17}$	$< 0.53$	$427^{+217}_{-148}$	0.63 (33)

<sup>a</sup> Fitted in the range of 5.0 – 20.0 keV with the edge continuum model and a single Gaussian model.

<sup>b</sup> Pole-on is  $\phi = 0.73 \pm 0.15$  and side-on  $\phi = 0.23 \pm 0.15$ .

<sup>c</sup> The line center (keV).

<sup>d</sup> Same as **narrow Ga.** in table 6.4.

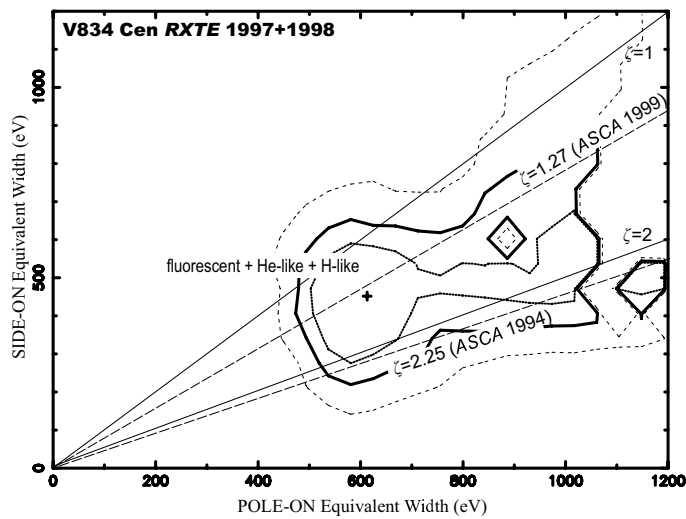


Figure 6.15: The same plot as figure 6.8, but for the dataset of the *RXTE* PCA.

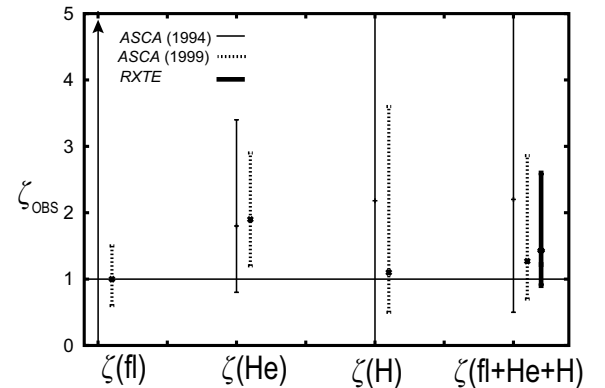


Figure 6.16: Comparison of  $\zeta_{\text{OBS}}$  obtained with *ASCA* and *RXTE*, for the three Fe-K line components and their weighted mean.

## 6.2 AM Herculis

### 6.2.1 *ASCA* observations

The *ASCA* observations of AM Herculis were performed once on September 1993, and twice on March 1995, as shown in table 5.1. Figure 6.17 shows the energy-resolved and background-subtracted light curves obtained with the *ASCA* SIS+GIS, folded by its rotational period, 3.0942 hr (Heise *et al.* 1988). The pole-on phase corresponds to  $\phi \sim 0.84$ . Figure 6.18 shows the background-subtracted X-ray spectra of AM Her obtained with the *ASCA* GIS and SIS. Although the X-ray flux changed between 1993 and 1995, the spectral shape and the folded light curves remained very similar among the three observations. Therefore, we sum up all the observations of AM Herculis for our spectral analysis.

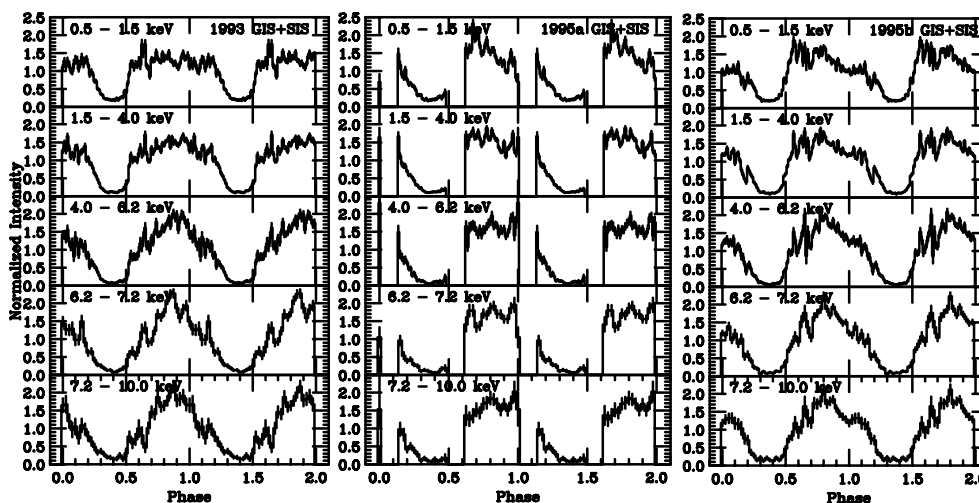


Figure 6.17: Background-subtracted light curves of AM Her obtained with *ASCA*, folded at its spin period of 3.0942 hr. The X-ray arrival times are corrected to the solar barycentric values. Phase 0.0 corresponds to HJD 2443014.76614 (Heise and Verbunt 1988).

Figure 6.19 shows the phase-averaged spectra of the SIS and GIS, summed up over the three observations. We can see similar continuum emission as V834 Cen with iron  $K_{\alpha}$  lines, which are clearly resolved in the SIS data. To model the continuum spectrum, we fitted them in the same way as V834 Cen (section 6.1.1), and obtained essentially the same results, which are presented in table 6.6. However, for AM Herculis, a fit with the double absorption model (Model 4) is unacceptable, and a third absorption (Model 5) is needed. The best fit values of  $kT$  obtained with Model 2 and Model 5 are consistent with that from *Ginga*,  $18.1 \pm 0.4$  keV (Ishida 1991), and hence, we utilize them in fitting the continuum spectra in the 4.5 – 10.0 keV and the 1.0 – 10.0 keV bands, respectively. As for the line model, we adopt the three narrow Gaussian model, as employed in the case of V834 Cen (section 6.1.1). The best fit model is also plotted in figure 6.19. In the SIS data (figure 6.19 left top), we can also see lines from lighter elements, such as He-like Si at 1.8 keV, H-like Si at 2.0 keV, He-like and H-like S lines at 2.4 – 2.6 keV, and Ar lines near 3.1 – 3.3 keV.

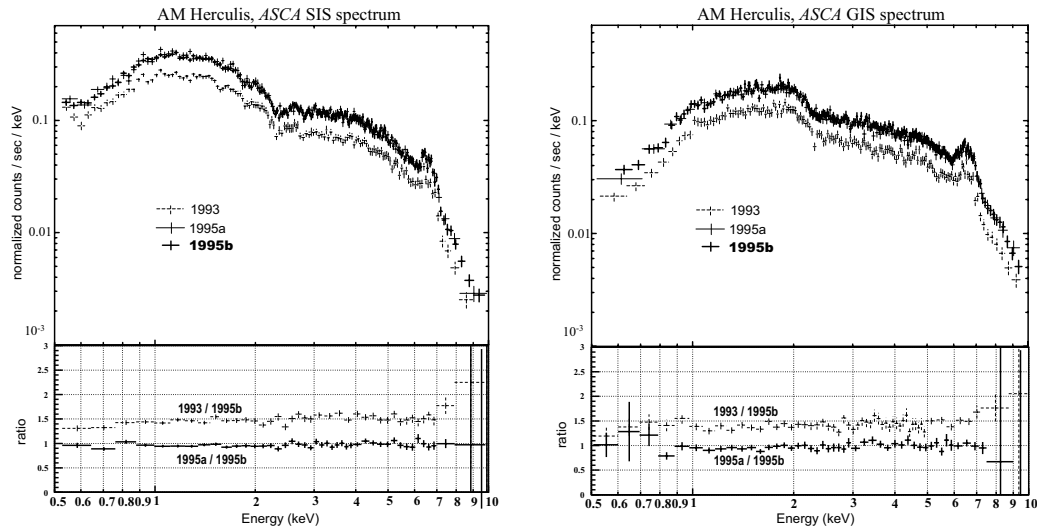


Figure 6.18: X-ray spectra of AM Her obtained with the *ASCA* SIS and GIS on 1993 September 27, 1995 March 6 (1995a), and 1995 March 9 (1995b). The bottom panel shows spectral ratios between the different epochs.

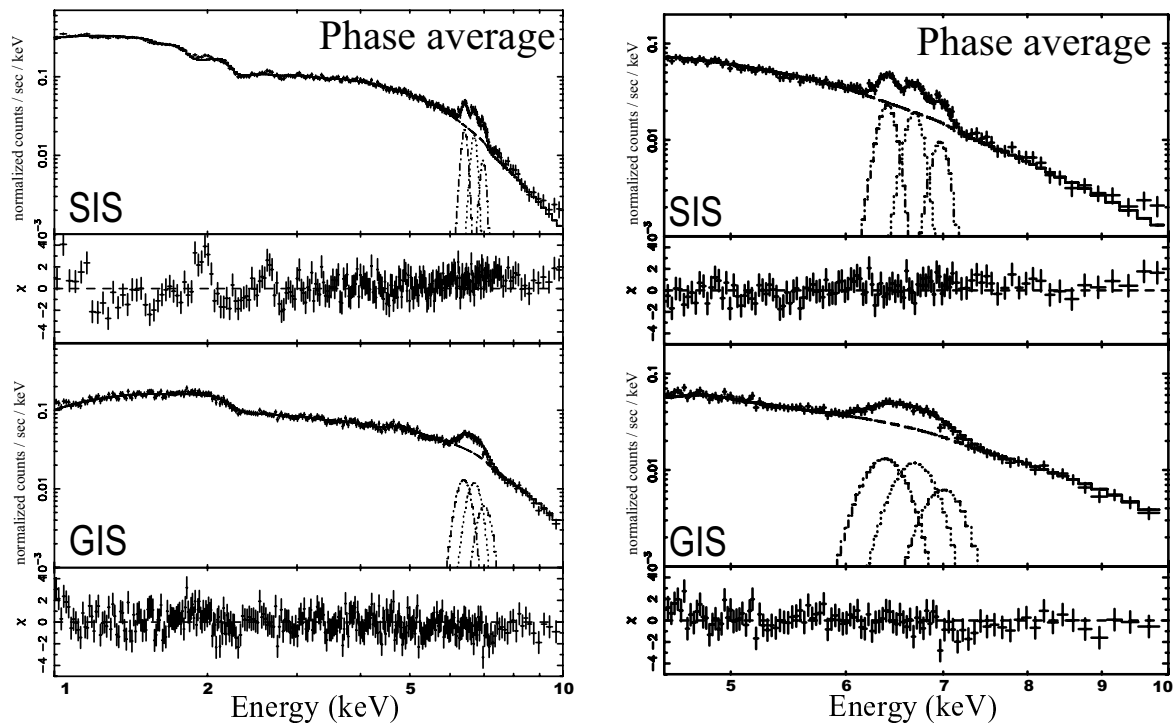


Figure 6.19: Phase averaged spectra of AM Her obtained with *ASCA*. Data from the three observations are co-added. The best-fit Model 5 in table 6.6 with three narrow Gaussians (*left*), and Model 2 with three Gaussians (*right*) are plotted with dashed curves. The GIS and SIS spectra are simultaneously fitted, and the obtained parameters are summarized in tables 6.6 and 6.7.

Table 6.6: The best fit continuum parameters for the ASCA GIS and SIS spectra of AM Herculis<sup>a</sup>.

Model	band <sup>b</sup>	$kT_1$ keV	$N_{H1}$ $\times 10^{22} \text{ cm}^{-2}$	$N_{H2}$ $\times 10^{22} \text{ cm}^{-2}$	$N_{H3}$ $\times 10^{22} \text{ cm}^{-2}$	cov. frac 1 <sup>c</sup> %	cov. frac 2 <sup>c</sup> %	bol. lum. <sup>d</sup> ( $10^{31} \text{ erg s}^{-1}$ )	$\chi^2_r$ (dof)
<b>Phase average</b>									
Model 1 (1 $N_H$ , 1 $kT$ )	W	> 198	$0.22^{+0.01}_{-0.01}$	—	—	—	—	(44.9)	4.62 (450)
Model 2 (1 $N_H$ , 1 $kT$ )	N	$19.5^{+10.3}_{-5.3}$	$9.3^{+2.4}_{-2.4}$	—	—	—	—	16.7	0.73 (129)
Model 4 (PCF, 1 $kT$ )	W	> 91.8	< 0.02	$5.9^{+0.8}_{-0.4}$	—	$40.0^{+0.9}_{-0.9}$	—	(33.2)	1.45 (450)
Model 4		18.1 <sup>e</sup>	< 0.09	$9.0^{+0.7}_{-0.8}$	—	$53.3^{+0.9}_{-0.9}$	—	13.3	1.78 (451)
Model 5 (2 PCF, 1 $kT$ )	W	$15.9^{+5.4}_{-3.0}$	< 0.01	$3.4^{+0.3}_{-0.3}$	$33.8^{+5.5}_{-5.4}$	$45.1^{+2.8}_{-4.0}$	$49.0^{+4.7}_{-6.1}$	17.6	1.18 (448)
Model 5		18.1 <sup>e</sup>	< 0.01	$3.4^{+0.3}_{-0.3}$	$32.9^{+5.7}_{-5.1}$	$43.4^{+1.6}_{-0.2}$	$46.5^{+3.0}_{-2.9}$	18.0	1.18 (449)
<b>POLE_ON phase<sup>f</sup></b>									
Model 5 (2 PCF, 1 $kT$ )	W	$16.6^{+8.1}_{-3.8}$	< 0.01	$3.3^{+0.3}_{-0.3}$	$30.4^{+5.8}_{-5.2}$	$50.6^{+3.2}_{-4.2}$	$50.6^{+5.2}_{-6.8}$	30.8	1.05 (437)
<b>SIDE_ON phase<sup>f</sup></b>									
Model 5 (2 PCF, 1 $kT$ )	W	$15.9^{+38.6}_{-7.3}$	< 0.02	$2.9^{+0.7}_{-0.7}$	$37.5^{+31.9}_{-15.2}$	$38.4^{+9.9}_{-12.3}$	$43.6^{+16.8}_{-20.8}$	17.6	0.73 (256)

<sup>a</sup> Excluding the Fe  $K_\alpha$  line band (6.0 – 7.5 keV). The GIS and SIS spectra are fitted simultaneously.

<sup>b</sup> Energy bandpass for fitting. “W” means 1.0 – 10.0 keV, and “N” 4.5 – 10.0 keV.

<sup>c</sup> The covering fraction (%) of  $N_{H1}$  and  $N_{H2}$ .

<sup>d</sup> Bolometric luminosity. The distance is assumed to be 100 pc.

<sup>e</sup> Continuum temperature fixed at the value measured with Ginga (Ishida 1991).

<sup>f</sup> Pole-on corresponds to  $\phi = 0.68 - 1.00$ , and side-on to  $\phi = 0.00 - 0.23, 0.50 - 0.68$ .

### 6.2.2 Phase resolved *ASCA* spectra

To examine the iron-line equivalent width for the expected rotational modulation, we have accumulated the GIS and SIS data over the pole-on ( $\phi = 0.68 - 1.00$ ) and side-on phases ( $\phi = 0.00 - 0.23, 0.50 - 0.68$ ), separately. We discarded the data during the phase  $\phi = 0.23 - 0.50$ , since the viewing angle  $\theta$  to the accretion column is expected to exceed  $90^\circ$  (i.e., the accretion column is eclipsed; figure 5.2). We, again, co-added all the three observations, by referring to the rotational phase ephemeris that is considered accurate enough to cover the 2-year time span.

Figure 6.20 shows the phase-resolved spectra, together with the best fit continuum of Model 2 and three narrow Gaussians. For the second Gaussian (He-like line) in this figure, we can see that the line intensity to the continuum level (i.e., equivalent width) is enhanced at pole-on phase, whereas those of the first and third Gaussians (fluorescence and H-like line, respectively) are similar between the two phases. Quantitatively, we have obtained the fitting results as given in table 6.7; the equivalent widths of fluorescent and hydrogenic iron  $K_\alpha$  lines are statistically consistent with being unmodulated, whereas that of the He-like component tends to be enhanced by a factor of  $\zeta_{\text{obs}}(\text{He}) = 1.5^{+2.0}_{-0.6}$ . This result does not change when we adopt Model 5 for the continuum [ $\zeta_{\text{obs}}(\text{He}) = 1.5^{+0.2}_{-0.5}$ ; see table A.4].

To see the result more clearly, we performed the same simultaneous fitting of the two phases as for V834 Cen (figure 6.8). As demonstrated in figure 6.21, the equivalent width of fluorescent and H-like lines stay constant (on “ $\zeta = 1$ ” curve), whereas that of He-like line is enhanced at the pole-on phase within 68 % confidence level. Although statistical significance is smaller than that of V834 Cen, this result supports our beaming mechanism.

Table 6.7: The best fit parameters of the iron  $K_\alpha$  lines of AM Her with *ASCA*<sup>a</sup>.

Phase <sup>b</sup>	continuum		Fluo.	He-like $K_\alpha$		H-like $K_\alpha$		$\chi^2_\nu$ (dof)
	kT	$N_{\text{H}}$	EW	l. c. <sup>c</sup>	EW	l. c. <sup>c</sup>	EW	
	(keV)	$\times 10^{22} \text{ cm}^{-2}$	(eV)	(keV)	(eV)	(keV)	(eV)	
Average	$18.9^{+5.1}_{-4.4}$	$9.8^{+2.0}_{-3.2}$	$215^{+17}_{-17}$	$6.68^{+0.03}_{-0.02}$	$232^{+19}_{-20}$	6.97	$148^{+19}_{-24}$	0.80 (208)
Pole-on	$18.7^{+12.4}_{-4.3}$	$10.6^{+3.3}_{-3.9}$	$215^{+16}_{-24}$	$6.67^{+0.04}_{-0.02}$	$241^{+40}_{-47}$	6.95	$154^{+17}_{-38}$	0.76 (198)
Side-on	$21.0^{+21.5}_{-8.4}$	$6.8^{+1.9}_{-3.1}$	$205^{+41}_{-48}$	$6.67^{+0.07}_{-0.03}$	$160^{+93}_{-80}$	6.95	$161^{+91}_{-38}$	0.47 (73)

<sup>a</sup> The determination of continuum spectrum is performed in 4.5 keV – 10.0 keV with Model 2 in table 6.6.

<sup>b</sup> Pole-on is  $\phi = 0.68 - 1.00$  and Side-on  $\phi = 0.00 - 0.23, 0.50 - 0.68$ .

<sup>c</sup> The line center (keV). That of the fluorescent component is fixed at 6.40 keV, and the ratio of H-like and He-like line is fixed to 1.042.

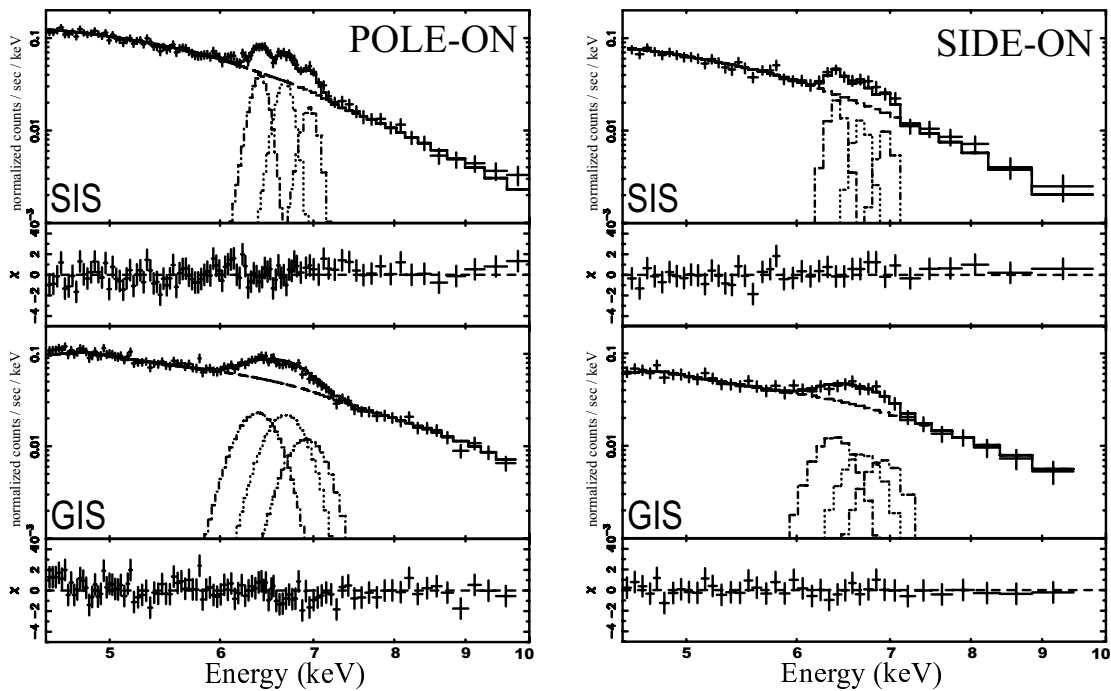


Figure 6.20: Phase resolved spectra of AM Her over the Fe-K line energies shown together with best fit model. The GIS and SIS data are simultaneously fitted, and the divided parameters are given in tables 6.7.

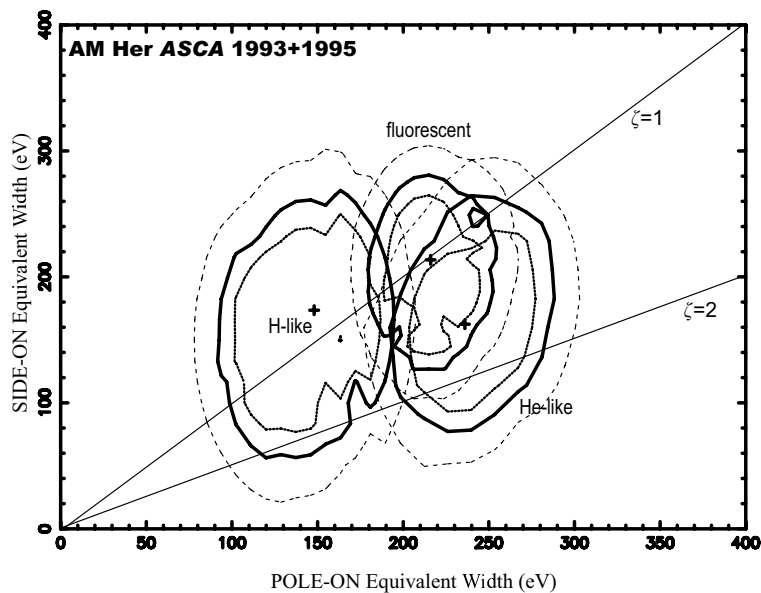


Figure 6.21: The same plot as figure 6.8, but for the dataset of AM Herculis with ASCA.

### 6.2.3 *BeppoSAX* observations

To reconfirm the *ASCA* results, we analyzed the *BeppoSAX* data of AM Hercuris, acquired on two occasions in 1998 (table 5.3). As shown in figure 6.22, the background-subtracted X-ray light curves are similar to those by *ASCA* (figure 6.17). The X-ray spectrum obtained with the *BeppoSAX* MECS is shown in figure 6.23, which was summed up over the two epochs. We can see the X-ray continuum emission and iron line as has been seen in the *ASCA* spectra.

We fitted the spectral continuum in the same way as the *ASCA* analysis (section 6.2.1), and obtained essentially the same results as summarized in table 6.8. For the MECS data, however, a third absorption (Model 5) is not needed, because of the limited sensitivity in the softer energy range (figure 4.1). We hence utilize Model 4 or Model 2 to reproduce the continuum spectra in the 1.6 – 10.0 keV (the entire range for the MECS) and 5.0 – 10.0 keV bands, respectively. Since the same line model (three narrow Gaussians) as used in the *ASCA* analysis can produce the iron line profile as shown in table 6.9, we apply this model to the MECS spectra.

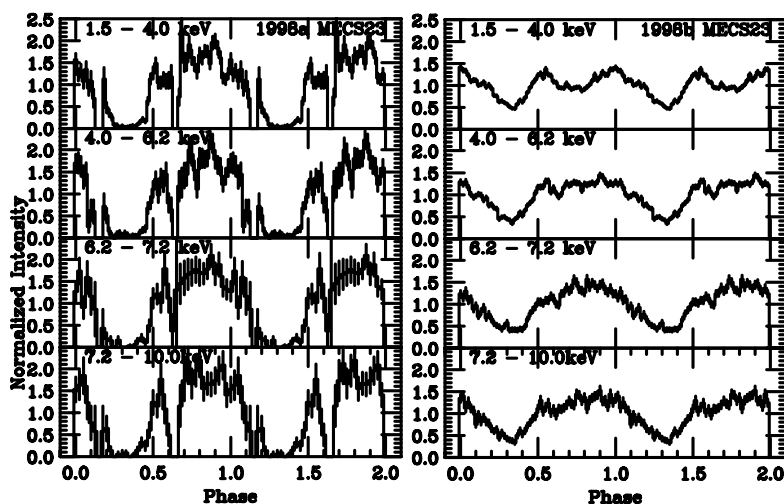


Figure 6.22: Background-subtracted light curves of AM Her obtained with *BeppoSAX*, folded at its spin period of 3.0942 hr. The X-ray arrival times are corrected to the solar barycentric values. Phase 0.0 corresponds to HJD 2443014.76614 (Heise and Verbunt 1988).

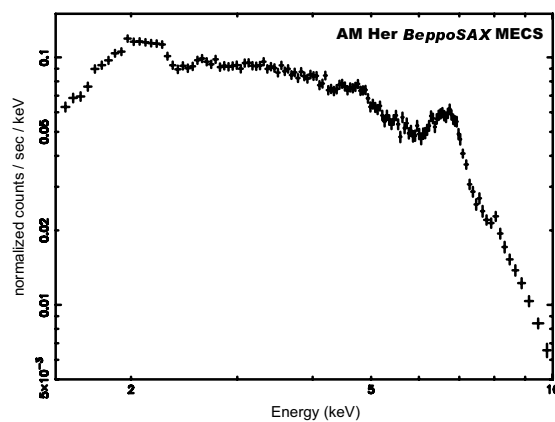


Figure 6.23: Phase averaged spectrum of AM Her obtained with the *BeppoSAX* MECS.

Table 6.8: The best fit continuum parameters for the *BeppoSAX* MECS spectra of AM Herculis<sup>a</sup>.

Model	band <sup>b</sup>	$kT_1$ keV	$N_{\text{H1}}$ $\times 10^{22} \text{ cm}^{-2}$	$N_{\text{H2}}$ $\times 10^{22} \text{ cm}^{-2}$	$N_{\text{H3}}$ $\times 10^{22} \text{ cm}^{-2}$	cov. frac 1 <sup>c</sup> %	cov. frac 2 <sup>c</sup> %	bol. lum. <sup>d</sup> ( $10^{31} \text{ erg s}^{-1}$ )	$\chi^2_{\nu}$ (dof)
<b>Phase average</b>									
Model 1	(1 $N_{\text{H}}$ , 1 $kT$ )	$84.0^{+26.0}_{-17.6}$	$0.21^{+0.06}_{-0.06}$	–	–	–	–	(56.4)	1.18 (110)
Model 2	(1 $N_{\text{H}}$ , 1 $kT$ )	$23.6^{+10.9}_{-6.0}$	$4.8^{+2.5}_{-2.4}$	–	–	–	–	30.5	1.12 (47)
Model 4	(PCF, 1 $kT$ )	$35.8^{+15.8}_{-9.3}$	$< 0.26$	$12.2^{+10.9}_{-6.6}$	–	$17.8^{+5.4}_{-5.9}$	–	(35.0)	1.00 (108)
Model 4		$18.1^e$	$0.34^{+0.02}_{-0.04}$	$27.9^{+8.9}_{-6.9}$	–	$33.2^{+3.6}_{-2.9}$	–	30.1	1.14 (109)
Model 5	(2 PCF, 1 $kT$ )	$22.4^{+22.8}_{-3.2}$	$< 0.23$	$5.6^{+10.7}_{-2.2}$	$59.9^{+53.1}_{-41.0}$	$24.2^{+7.7}_{-10.8}$	$27.4^{+0.7}_{-26.0}$	35.5	1.02 (106)
Model 5		$18.1^e$	$< 0.27$	$6.1^{+7.3}_{-2.5}$	$65.1^{+34.9}_{-22.0}$	$26.4^{+7.2}_{-9.1}$	$35.2^{+9.4}_{-27.3}$	36.7	1.03 (107)
<b>POLE_ON phase<sup>f</sup></b>									
Model 4	(PCF, 1 $kT$ )	$30.1^{+38.1}_{-12.8}$	$< 0.38$	$> 5.54$	–	$< 39.0$	–	38.6	0.80 (129)
Model 5	(2 PCF, 1 $kT$ )	$25.9^{+32.6}_{-11.2}$	$< 0.31$	any	$51.7^{+50.3}_{-28.4}$	any	$20.6^{+7.5}_{-5.9}$	37.0	0.81 (127)
<b>SIDE_ON phase<sup>f</sup></b>									
Model 4	(PCF, 1 $kT$ )	$36.2^{+41.3}_{-13.9}$	$< 0.38$	$15.5^{+11.2}_{-8.3}$	–	$25.2^{+9.2}_{-10.3}$	–	35.5	0.82 (126)
Model 5	(2 PCF, 1 $kT$ )	$26.2^{+52.3}_{-4.3}$	$< 0.40$	any	$25.0^{+10.6}_{-23.4}$	any	$< 67.7$	33.7	0.85 (124)

<sup>a</sup> Excluding the Fe  $K_{\alpha}$  line band (6.0 – 7.5 keV).<sup>b</sup> Energy bandpass for fitting. “W” means 1.6 – 10.0 keV, and “N” 5.0 – 10.0 keV.<sup>c</sup> The covering fraction (%) of  $N_{\text{H1}}$  and  $N_{\text{H2}}$ .<sup>d</sup> Bolometric luminosity. The distance is assumed to be 100 pc.<sup>e</sup> Continuum temperature fixed at the value measured with *Ginga* (Ishida 1991).<sup>f</sup> Pole-on corresponds to  $\phi = 0.68 - 1.00$ , and side-on to  $\phi = 0.00 - 0.23$ ,  $0.50 - 0.68$ .

To examine the spin modulation of the iron-line equivalent width, we have accumulated the MECS data over the pole-on ( $\phi = 0.68 - 1.00$ ) and the side-on ( $\phi = 0.00 - 0.23, 0.50 - 0.68$ ) phases separately. This definition is the same as in the *ASCA* analysis. The obtained phase-resolved X-ray spectra are plotted in figure 6.24.

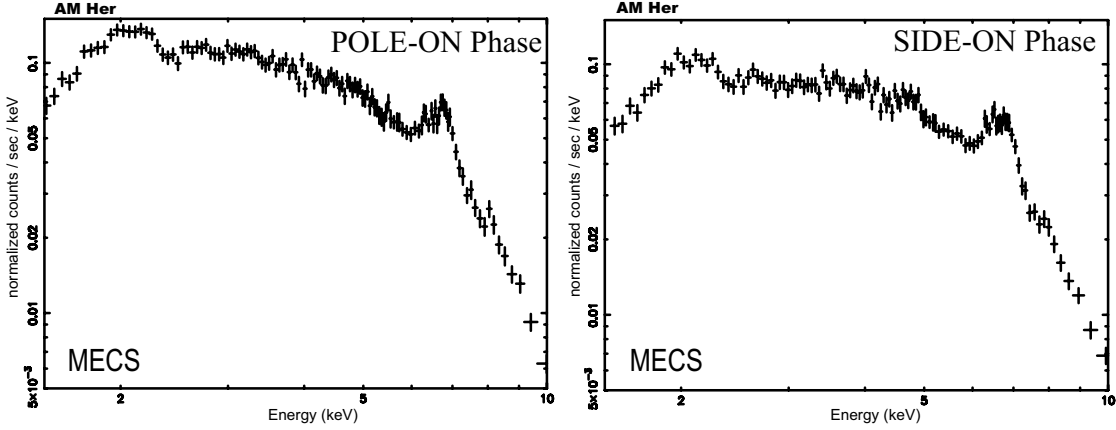


Figure 6.24: Phase resolved spectra of AM Herculis with *BeppoSAX*.

To quantify the equivalent width of iron K lines, we took the same approach as to the *ASCA* data. That is, we independently and simultaneously fitted the two spectra, with Model 2 and three Gaussians whose parameters are constrained in the same way (section 6.1.2). The results obtained from the independent fittings are summarized in figure 6.25 and table 6.9, while those from the simultaneous fittings in figure 6.26. The equivalent widths of He-like and H-like lines are consistent with the *ASCA* result, whereas that of fluorescent line is significantly reduced. This phenomena has been observed in the case of V834 Cen with *ASCA* (section 6.1.2). The modulation pattern is similar that observed with *ASCA* (figure 6.21); the equivalent widths of fluorescent and H-like lines stay constant, and that of He-like line tend to increase at the pole-on phase. Quantitatively, the enhancement of ionized line equivalent width is  $\zeta_{\text{obs}}(\text{H}) = 1.0^{+0.9}_{-0.5}$  and  $\zeta_{\text{obs}}(\text{He}) = 1.5^{+2.0}_{-1.0}$ , for H-like and He-like iron lines, respectively. These values show a nice agreement with the *ASCA* result ( $0.9^{+1.3}_{-0.5}$  and  $1.5^{+1.2}_{-0.9}$ , respectively). Therefore, the rotational modulation of the He-like line observed with *ASCA* must be a real feature of AM Herculis.

Table 6.9: The best fit parameters of the iron  $K_{\alpha}$  lines of AM Her with *BeppoSAX*<sup>a</sup>.

Phase <sup>b</sup>	continuum		Fluo.	He-like $K_{\alpha}$		H-like $K_{\alpha}$		$\chi^2_{\nu}$ (dof)
	kT	$N_{\text{H}}$	EW	l. c. <sup>c</sup>	EW	l. c. <sup>c</sup>	EW	
	(keV)	$\times 10^{22} \text{ cm}^{-2}$	(eV)	(keV)	(eV)	(keV)	(eV)	
Average	$21.3^{+3.7}_{-16.7}$	$6.2^{+1.6}_{-1.6}$	$86^{+21}_{-17}$	$6.71^{+0.01}_{-0.08}$	$171^{+22}_{-21}$	6.99	$180^{+20}_{-25}$	0.98 (65)
Pole-on	$21.7^{+26.7}_{-1.9}$	$< 3.2$	$80^{+18}_{-68}$	$6.70^{+0.13}_{-0.13}$	$232^{+15}_{-137}$	6.98	$226^{+18}_{-139}$	0.92 (87)
Side-on	$22.2^{+61.2}_{-10.1}$	$< 16.9$	$98^{+53}_{-41}$	$6.69^{+0.03}_{-0.04}$	$153^{+95}_{-108}$	6.97	$218^{+91}_{-76}$	0.57 (84)

<sup>a</sup> The determination of continuum spectrum is performed in 5.0 keV – 10.0 keV with Model 2 in table 6.6.

<sup>b</sup> Pole-on is  $\phi = 0.68 - 1.00$  and Side-on  $\phi = 0.00 - 0.23, 0.50 - 0.68$ .

<sup>c</sup> The line center (keV). That of the fluorescent component is fixed at 6.40 keV, and the ratio of H-like and He-like line is fixed to 1.042.

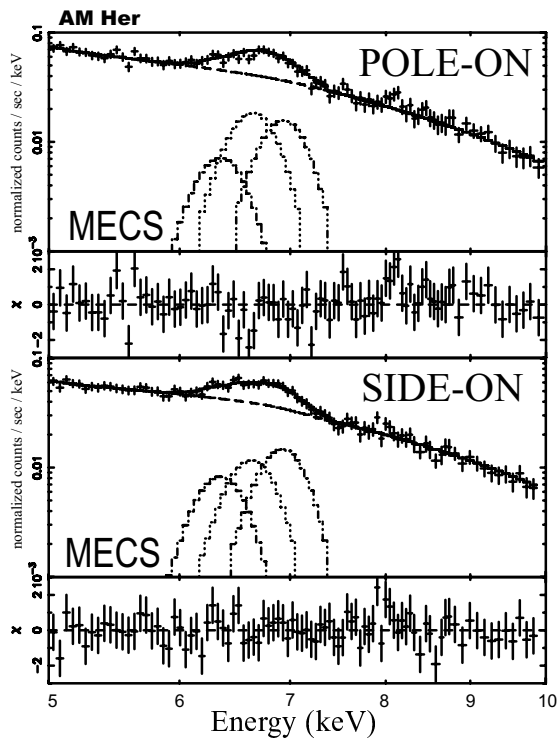


Figure 6.25: Phase resolved spectra of AM Her over the Fe-K line energies with best fit model. The GIS and SIS data are simultaneously fitted, and the divided parameters are shown in tables 6.9.

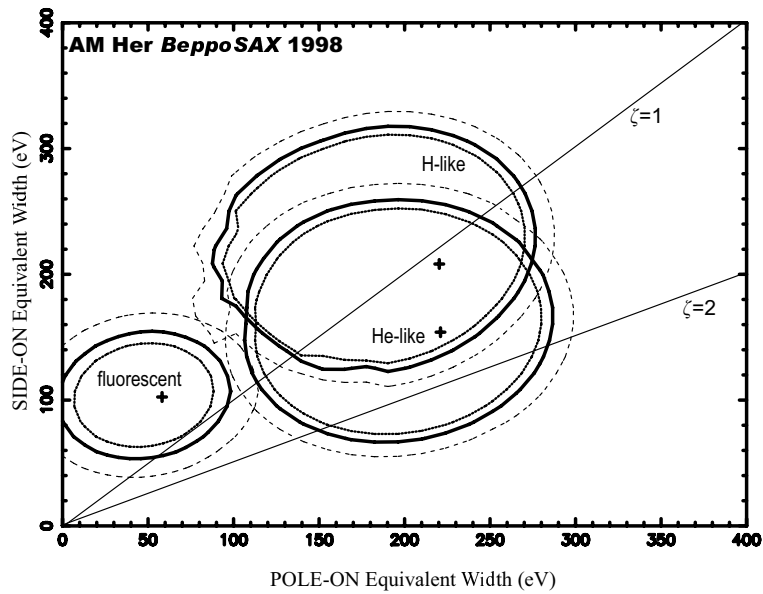


Figure 6.26: The same plot as figure 6.8, but for the dataset of AM Herculis with *BeppoSAX*.

### 6.2.4 *RXTE* observation

The *RXTE* observation of AM Herculis was performed in 1998 (table 5.2). As shown in the background-subtracted spectrum of figure 6.27, the X-ray signal is clearly detected above the background up to  $\sim 25$  keV. We can see bremsstrahlung-like continuum with iron line emission. The edge model, as utilized in V834 Cen (section 6.1.4), can reproduce the spectrum as shown in figure 6.28 and table 6.10; the edge structure is clearly needed as shown in figure 6.29. We therefore adopt the edge model in the spectral analysis.

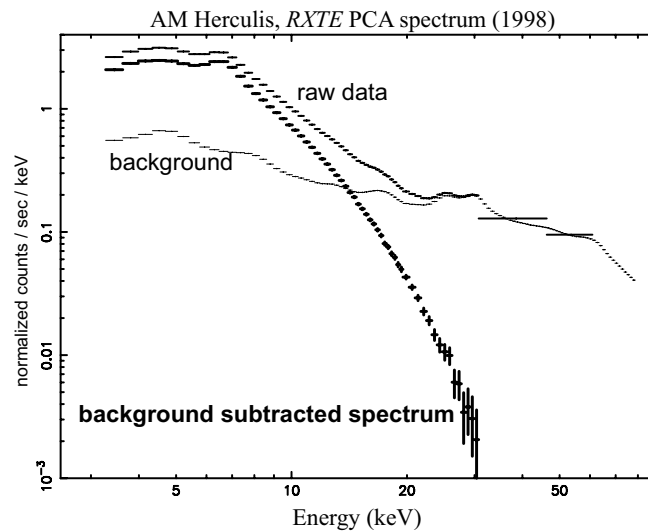


Figure 6.27: The *RXTE* PCA spectra of AM Her. Raw, background and background-subtracted spectra are shown in solid, thin, and thick lines, respectively.

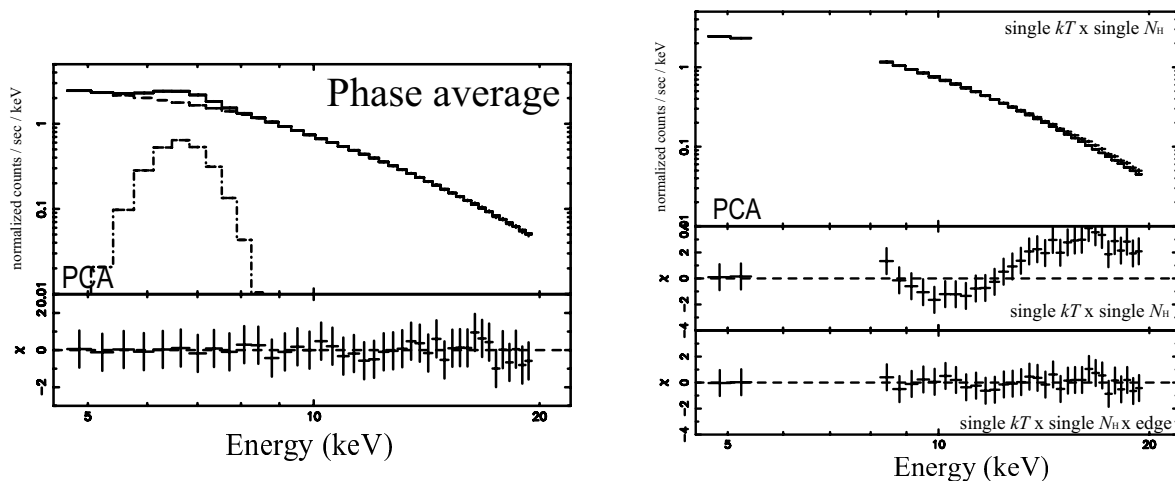


Figure 6.28: The same plot as “background-subtracted spectrum” in figure 6.27, shown together with the best fit edge model (see text) plus a broad Gaussian. Parameters are given in table 6.10.

Figure 6.29: The same plot as in figure 6.28, but for the data of AM Herculis; i.e., the fitting results with and without edge absorption near the 7 – 9 keV band. The obtained parameters are shown in table 6.10.

Table 6.10: The best fit parameters of the AM Herculis spectra with the *RXTE* PCA

phase <sup>a</sup>	continuum				iron K <sub>α</sub> line			statistics
	<i>kT</i> (keV)	<i>N</i> <sub>H</sub> (×10 <sup>22</sup> cm <sup>-2</sup> )	<i>E</i> <sub>eg</sub> (keV)	depth	l.c. <sup>b</sup> (keV)	<i>σ</i> <sub>1</sub> (keV)	<i>EW</i> (eV)	
Average <sup>c</sup>	13.6	3.9	—	—	—	—	—	4.57 (30)
Average <sup>d</sup>	16.0 <sup>+1.4</sup> <sub>-1.0</sub>	3.4 <sup>+1.6</sup> <sub>-1.8</sub>	9.1 <sup>+0.4</sup> <sub>-0.2</sub>	0.23 <sup>+0.06</sup> <sub>-0.05</sub>	—	—	—	0.23 (28)
Average <sup>e</sup>	16.6 <sup>+0.6</sup> <sub>-1.2</sub>	2.9 <sup>+2.0</sup> <sub>-1.5</sub>	9.1 <sup>+0.4</sup> <sub>-0.3</sub>	0.10 <sup>+0.06</sup> <sub>-0.05</sub>	6.64 <sup>+0.05</sup> <sub>-0.05</sub>	0.28 <sup>+0.11</sup> <sub>-0.12</sub>	515 <sup>+60</sup> <sub>-75</sub>	0.19 (33)
Pole-on <sup>e</sup>	17.8 <sup>+2.7</sup> <sub>-1.1</sub>	5.2 <sup>+1.8</sup> <sub>-3.0</sub>	8.9 <sup>+0.3</sup> <sub>-0.1</sub>	0.13 <sup>+0.05</sup> <sub>-0.03</sub>	6.63 <sup>+0.04</sup> <sub>-0.05</sub>	0.23 <sup>+0.09</sup> <sub>-0.22</sub>	545 <sup>+54</sup> <sub>-65</sub>	0.28 (34)
Side-on <sup>e</sup>	15.0 <sup>+1.3</sup> <sub>-1.5</sub>	< 4.2	9.2 <sup>+0.5</sup> <sub>-0.3</sub>	0.10 <sup>+0.05</sup> <sub>-0.06</sub>	6.64 <sup>+0.06</sup> <sub>-0.07</sub>	0.26 <sup>+0.16</sup> <sub>-0.10</sub>	397 <sup>+45</sup> <sub>-41</sub>	0.31 (33)

<sup>a</sup> Pole-on is  $\phi = 0.70 - 1.00$  and side-on  $\phi = 0.1 - 0.2, 0.4 - 0.6$ .

<sup>b</sup> The line center (keV).

<sup>c</sup> 5.5 – 7.8 keV band is excluded. Fitted with a single bremsstrahlung with a photoelectric absorption model.

<sup>d</sup> 5.5 – 7.8 keV band is excluded. Fitted with the same model as *c* plus edge absorption model.

<sup>e</sup> 5.0 – 20.0 keV band. Fitted with the same model as *d* plus a broad Gaussian model.

Having constrained the spectral model, we are ready to study the phase-resolved spectra. The background-subtracted light curves show a clear modulation at the spin period of AM Her, as seen in figure 6.30. Since the modulation is similar to that recorded by *ASCA*, we have accumulated the data over the pole-on ( $\phi = 0.70 - 1.00$ ) and side-on ( $\phi = 0.0 - 0.1, 0.4 - 0.6$ ) phases, separately. In the phase-resolved spectra of figure 6.31, we can see an enhanced iron line emission relative to the continuum in the pole-on phase as expected. As has been performed in the case of V834 Cen, we quantified the spectra by independently or simultaneously fitting with the edge model and a Gaussian. The obtained results are summarized in table 6.10 and figure 6.32, respectively. Thus, the equivalent width of iron line is clearly enhanced by a factor of  $\zeta_{\text{obs}}(\text{fl} + \text{He} + \text{H}) = 1.3^{+0.1}_{-0.2}$  at the pole-on phase compared to the side-on phase, with  $> 99\%$  significance. Considering that the spin enhancement in the pole-on phase is seen only for the He-like line with *ASCA* and *BeppoSAX* observations (figures 6.21 and 6.26), the obtained enhancement of the PCA is thought to be caused mainly by the He-like iron line.

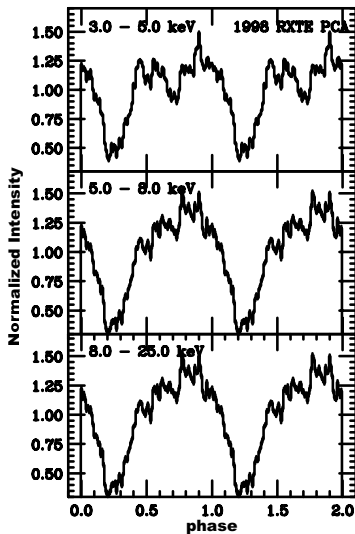


Figure 6.30: The background-subtracted light curves of AM Her with *RXTE*, folded at the spin period of 3.0942 hr. Phase 0.0 corresponds to HJD 2443014.76614 (same as the *ASCA* light curves; figure 6.17).

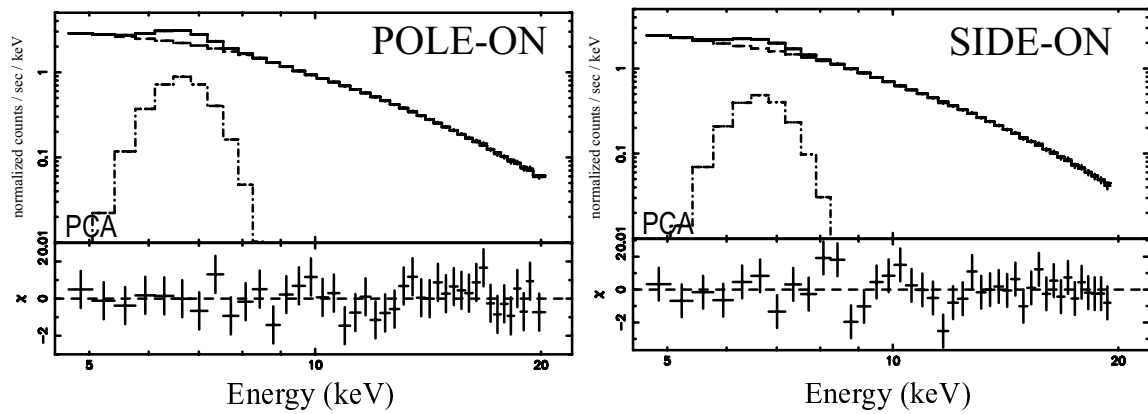


Figure 6.31: The same plot as figure 6.28, but shown separately for the pole-on phase ( $\phi = 0.7 - 1.0$ ) and side-on phase ( $\phi = 0.00 - 0.10, 0.40 - 0.60$ ).

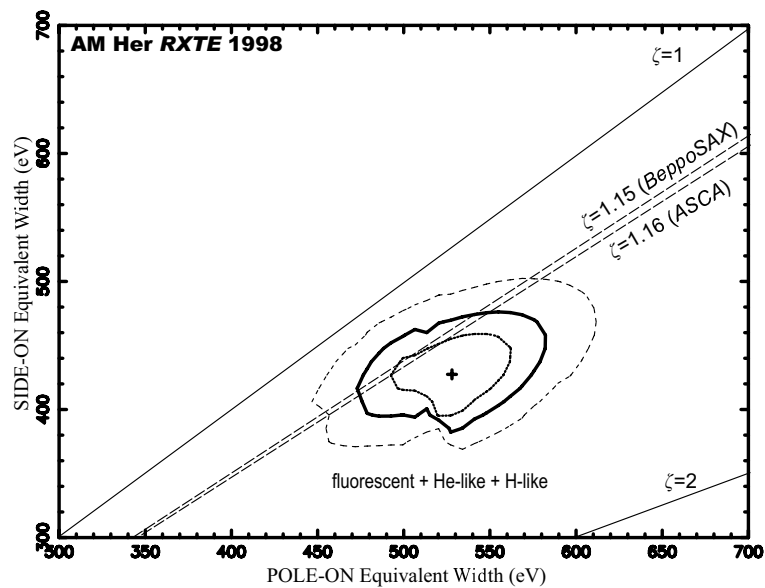


Figure 6.32: A confidence contour of the equivalent width of iron line in two phases. The same plot as figure 6.32, but for the dataset of AM Herculis with the PCA.

### 6.2.5 Comparison of *ASCA*, *BeppoSAX*, and *RXTE* observations

To examine consistency of the result among *ASCA*, *BeppoSAX*, and *RXTE*, we compared  $\zeta_{\text{obs}}(\text{fl} + \text{He} + \text{H})$  obtained by *RXTE* with the weighted-mean  $\zeta_{\text{obs}}$  of three line components calculated by the *ASCA* and *BeppoSAX* results (tables 6.7 and 6.9). Based on the comparison presented in figure 6.33, we conclude that the results from the three satellites are consistent with one another.

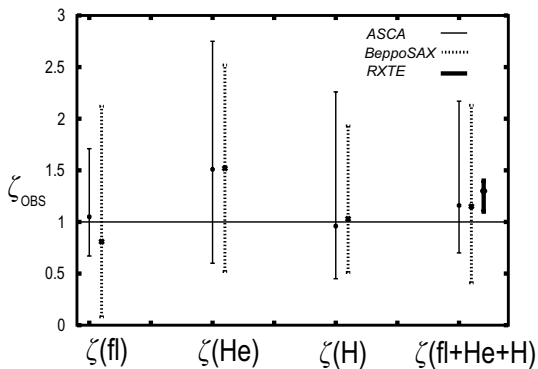


Figure 6.33: Comparison of  $\zeta_{\text{OBS}}$  of iron line equivalent widths obtained by *ASCA*, *BeppoSAX*, and *RXTE*.

Is the clear modulation observed with *RXTE* (figure 6.32) really attributable to the He-like component? Although the PCA cannot resolve the three line components, the line center energy of iron line is determined with  $\sim 1\%$  accuracy (table 6.10), and hence we can estimate the relative contributions of the three line components based on the measured line-center energy. For this purpose, let us assume that the ratio of the equivalent widths of He-like to H-like iron line is that obtained by *ASCA*, 1.56 (table 6.7), or by *BeppoSAX*, 1.0 (table 6.9); the mean line center of the ionized iron lines then comes at 6.80 keV or 6.83 keV, respectively. Under this assumption, the phase-averaged line-center energy,  $6.64 \pm 0.05$  keV measured with the PCA, implies that  $40^{+13}_{-28}\%$  or  $44^{+12}_{-11}\%$  of the observed line EW is contributed by the fluorescent line. In the same way, we can constrain contribution of the neutral component to the phase-resolved PCA spectra, to estimate that the enhancement of equivalent width of ionized iron lines (H-like plus He-like line) as  $\zeta_{\text{obs}}(\text{He} + \text{H}) = 1.3^{+0.8}_{-0.5}$  or  $1.4^{+0.8}_{-0.6}$ . These values are also consistent with the weighted  $\zeta_{\text{obs}}$  by the *ASCA* and *BeppoSAX* results.

If we assume that both H- and He-like lines are unmodulated between the two phases, the fluorescent line must be enhanced at pole-on phase by a factor of  $\zeta_{\text{obs}}(\text{fl}) = 2.0^{+3.8}_{-0.5}$  or  $1.8^{+0.9}_{-0.4}$  to explain the value of  $\zeta_{\text{obs}}(\text{fl} + \text{He} + \text{H})$  with the PCA. The corresponding mean-weighted line-center energy in pole-on phase is consistent with the observed value (table 6.10), whereas that in side-on phase comes higher value than the observation as  $6.71^{+0.04}_{-0.03}$  keV or  $6.74^{+0.03}_{-0.04}$  keV, respectively. Therefore, to explain the iron line enhancement observed with the PCA, we conclude that not only the equivalent width of fluorescent line but also those of ionized lines are enhanced at pole-on phase.

Considering the *ASCA*, *BeppoSAX*, and *RXTE* results altogether, AM Her thus becomes a second object in which the rotational modulation of the resonance Fe-K line has been confirmed.

### 6.3 Other Polars

In order to reinforce the mechanism of anisotropic photon transfer, we also searched the data of the other eight polars for possible evidence of the enhancement of line equivalent width, using *ASCA* and *BeppoSAX*. As described in Chapter 5, these objects are simply selected by their X-ray flux ( $> 0.05$  cnt/s for the GIS or the MECS) and/or by their photon statistics ( $> 20$  ksec exposure) among the polars listed in tables 5.1 and 5.3. The eight objects are given in table 6.11, and the X-ray light curves folded by their spin periods are shown in figure 6.34. Like V834 Cen and AM Her, these objects mostly exhibit single-peaked folded light curves, often with absorption notches at softer energy bands in the pole-on phase caused by the pre-shock stream. These features indicate that we are observing a single pole, and that our line of sight becomes close to the right pole-on to it. Therefore, these polars are suited to our study. We accumulated the spectra over pole-on and side-on phases as defined in table 6.11. In some objects (e.g., RX J1015.5+0904, V1432 Aqr, and V2301 Oph), the folded light curves decreases almost to zero, suggesting that the only one pole is accreting and it is self-eclipsed for a certain phase interval. We exclude these self-eclipse phase from our analysis, just like in the case of AM Her. The phase-resolved spectra are shown in figure 6.35.

To quantify the equivalent widths of iron lines, we adopted Model 2 (section 6.1.1) with three narrow Gaussians; the energy range is shown in appendix A.1, as determined by the way described in §3.2 of Ezuka and Ishida 1994. The results of phase-resolved spectroscopy are summarized in figure 6.36. Although the enhancement of H-like line is unclear mainly due to large errors associated with the individual measurements, the equivalent width of He-like iron line is systematically larger in the pole-on phase. Quantitatively, the enhancement of H-like and He-like iron K line weighted by the absolute values of their equivalent widths are  $\zeta_{\text{OBS}}(\text{H}) = 1.0 \pm 0.4$  and  $\zeta_{\text{OBS}}(\text{H}) = 1.8 \pm 0.7$ . Therefore, we have detected the enhancement of He-like line in a statistical sense, although individual cases were insignificant.

In figure 6.37, we have plotted the enhancement of He-like line  $\zeta$ , as a function of pole angle  $\theta$  measured from the vertical axis (defined in figure 5.1). The observational results are consistent with our Monte Carlo simulation in the nominal case (section 3.4). These results imply that the mechanism proposed in Chapter 3 is universal among polars.

Table 6.11: The definition of the pole-on and side-on phases of polars.

object	phase 0.0	pole-on phase	side-on phase
BL Hyi	HJD 2450379.4725	0.00 – 0.30, 0.95 – 1.0	0.30 – 0.50, 0.80 – 0.95
BY Cam	HJD 2446138.8202	0.35 – 0.90	0.00 – 0.35, 0.90 – 1.00
EF Eri	HJD 2443894.6824	0.25 – 0.60	0.00 – 0.25, 0.60 – 1.00
EK UMa	HJD 2448755.3880	0.00 – 0.35	0.35 – 0.50, 0.85 – 1.00
QQ Vul	HJD 2448446.4711	0.00 – 0.10, 0.60 – 1.00	0.10 – 0.60
RXJ1015+0904	HJD 2451302.500	0.00 – 0.18, 0.83 – 1.00	0.18 – 0.38, 0.68 – 0.83
V1432 Aql	HJD 2450540.500	0.52 – 0.74	0.30 – 0.52, 0.74 – 0.90
V2301 Oph	HJD 2448071.02014	0.04 – 0.10, 0.60 – 0.92	0.10 – 0.20, 0.42 – 0.60

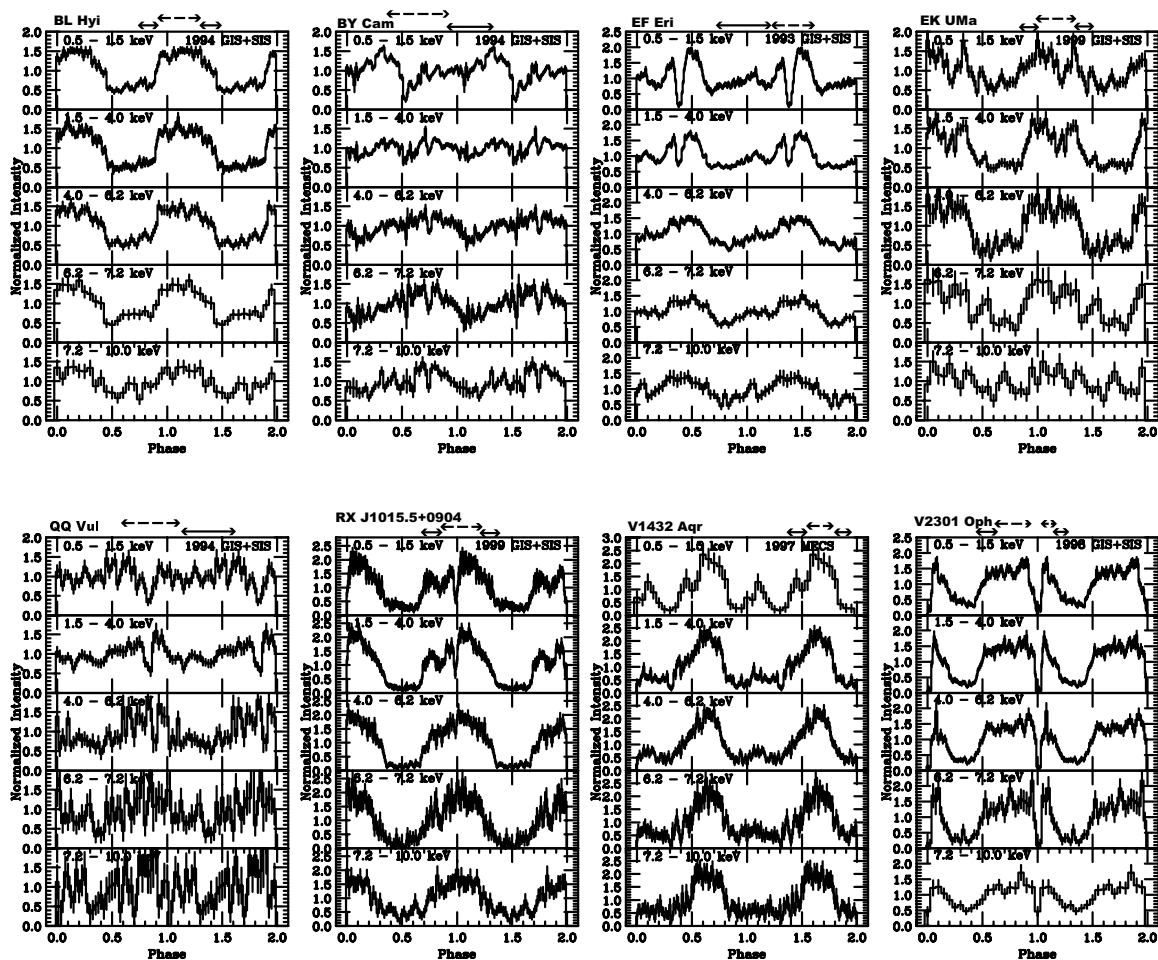


Figure 6.34: X-ray light curves of the other polars observed with *ASCA* or *BeppoSAX*, folded by their spin periods listed in table 2.1. The dashed arrow shows the pole-on phase, and solid arrow the side-on phase. Their definitions and respective phase 0.0 are given in table 6.11.

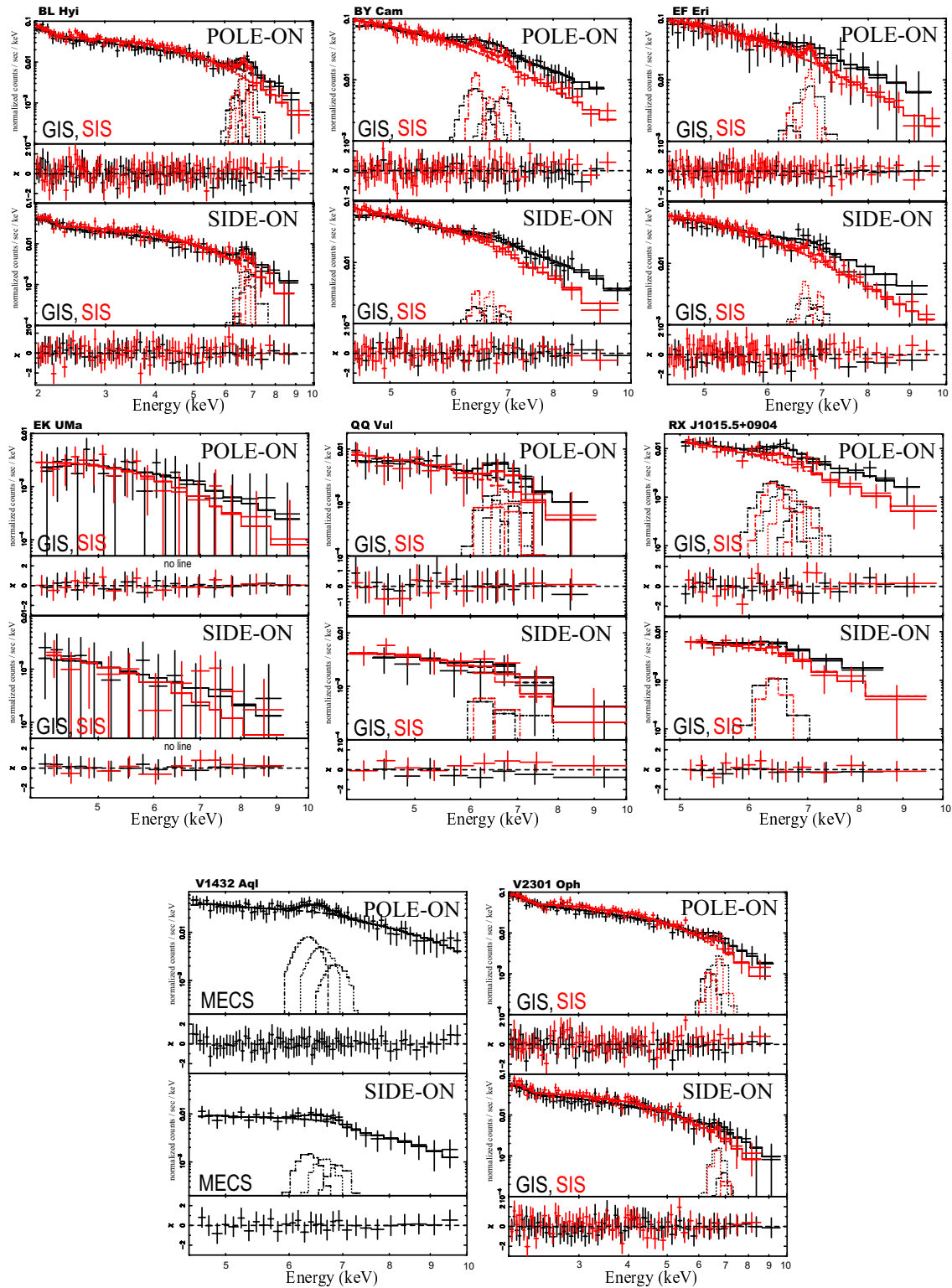


Figure 6.35: Phase resolved spectra near the iron energy band of the sample of polars, acquired with the *ASCA* SIS and GIS, or the *BeppoSAX* MECS. The best fit Model 2 (section 6.1.1) with three narrow Gaussians are also plotted. We discarded EK UMa for the phase-resolved analysis, because of lack of photon statistics

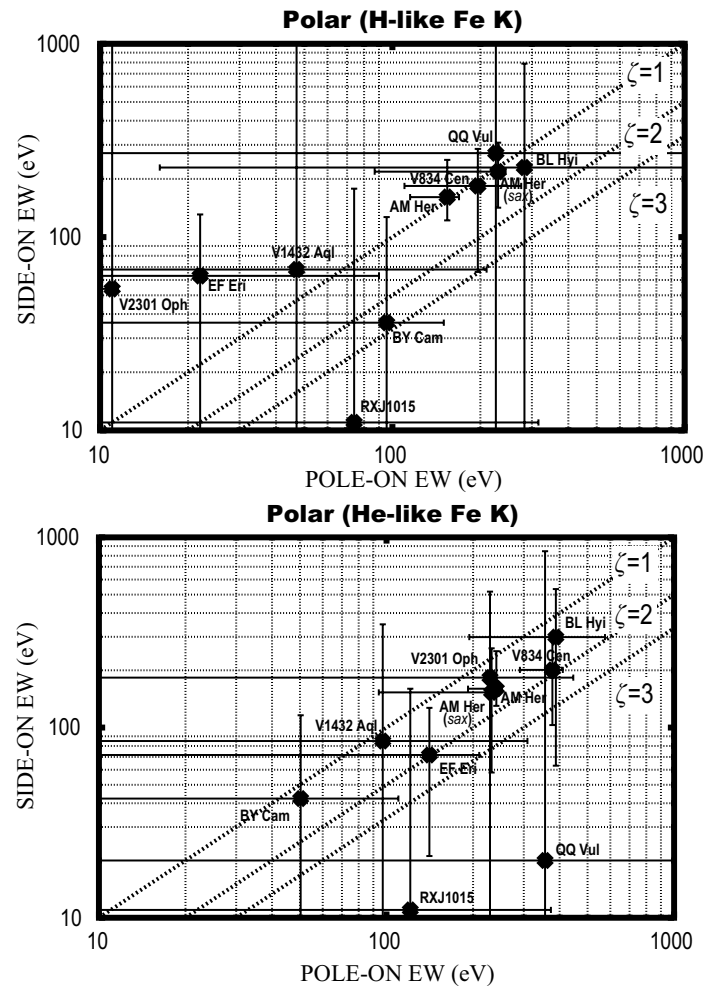


Figure 6.36: Scatter plots of the line equivalent widths of polars in the pole-on phase versus that in the side-on phase, obtained by *ASCA* and/or *BeppoSAX* observations.

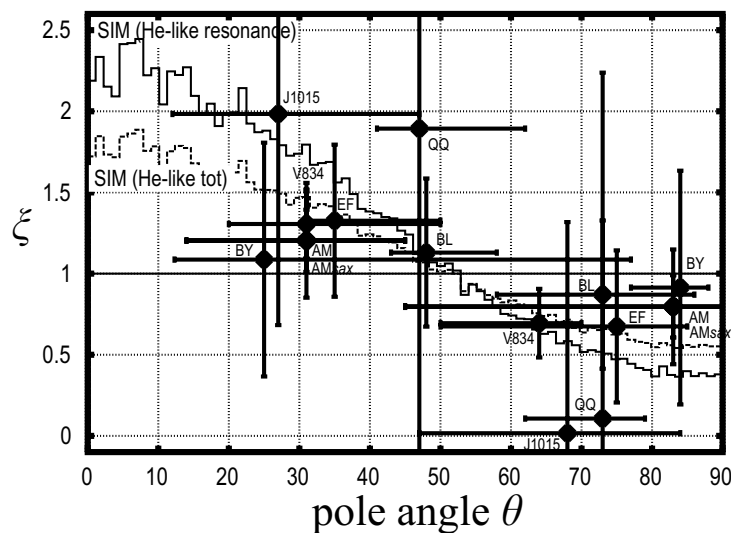


Figure 6.37: The enhancement  $\zeta$  of the helium-like line iron line EW, relative to the phase-averaged EW, of the polars observed with *ASCA* or *BeppoSAX*. It is shown as a function of pole angle  $\theta$ , which is calculated by adopting the nominal values of  $i$  and  $\beta$  in table 2.1. The angular distributions predicted by our Monte Carlo simulation in nominal case (see section 3.4) are also plotted.

# Chapter 7

## DISCUSSION

### 7.1 The Origin of the Observed Line Modulation

#### 7.1.1 Essence of the observation

To confirm the anisotropic radiation transfer of resonance photons, we have observed polars with *ASCA*, *RXTE*, and *BeppoSAX* (Chapters 5 and 6). We have examined the rotational modulation of iron- $K_\alpha$  line intensity in terms of  $\zeta$ ; the ratio of the equivalent width between the pole-on and side-on phases (equation 6.1), which is related to  $\xi$  as equation (6.2).

With the *ASCA* observation of a polar V834 Centauri, we have confirmed that the equivalent width of He-like iron  $K_\alpha$  line is enhanced by a factor of  $\zeta_{\text{OBS}}(\text{He}) = 1.9_{-0.6}^{+0.9}$  at pole-on phase with  $> 90\%$  significance (section 6.1.3). Furthermore, with the observation of another polar AM Herculis by *RXTE*, the EW of iron  $K_\alpha$  line (which is a mixture of the fluorescent, He-like, and H-like line) is clearly enhanced by a factor of  $\zeta_{\text{OBS}}(\text{Fl} + \text{He} + \text{H}) = 1.3_{-0.2}^{+0.1}$  at pole-on phase with  $> 99\%$  significance (section 6.2.4). The rotational modulations in these polars are consistently observed by *ASCA*, *RXTE* and *BeppoSAX* (sections 6.1.4, 6.2.1, and 6.2.3), although all measurements do not necessarily have sufficient significance. Furthermore, through systematic studies with *ASCA* and *BeppoSAX* of other 7 polars (section 6.3), this property has been confirmed to be a common feature of them in the statistical sense, because their average becomes  $\zeta_{\text{OBS}}(\text{He}) = 1.8 \pm 0.7$ , although individual cases are statistically insufficient.

#### 7.1.2 Alternative possibilities of the intensity enhancement

Can we explain the observed rotational modulation of the iron-line EW by some conventional mechanisms without invoking the resonance scattering? Any candidate mechanism must explain the intensity modulation in terms of the equivalent width, which is defined by the line intensity normalized to the continuum emission (section 2.6.3), the latter exhibiting an isotropic radiation from the white-dwarf accretion column.

Is the EW enhancement caused by a possible modulation of plasma parameter(s)?

Density variation, for example, originating from the fluctuation of mass transfer rate  $\dot{M}$ , cannot bring the EW modulation, since the emissivities of line and continuum photons have the same dependence of  $\propto n^2$  (equation 2.63). Another obvious possibility is some temperature variation, because the emissivity of the continuum has different temperature dependence ( $\propto kT^{1/2}$ ; equation 2.65) from that of the iron line (figure 2.27). Actually, the observed continuum temperature tends to become higher in the pole-on phase than in the side-on phase (tables 6.3, 6.5, 6.6, 6.7, 6.7, 6.8, and 6.10). However, they are consistent with being constant within the measurement and modeling uncertainties. Furthermore, since the plasma temperature is determined only by the depth of the gravitational potential of the white dwarf (equation 2.37), there is no reason for the plasma temperature to depend on the spin phase. Even if these marginal variations of the temperature were real, their effect on the iron line EW would be in the opposite sense, since the line EW decreases as the temperature increases in the range of interest, 10 – 20 keV (figure 2.27). Therefore, we can exclude this possibility.

Alternatively, does the EW change due to an eclipse of the accretion column by the white dwarf? Since the accretion column has a multi-temperature structure as described by the Aizu model (section 2.4.6), the line EW has a significant gradient along the accretion column, and hence the line EW will change by a partial eclipse of the emission region. Since the He-like iron  $K_\alpha$  line is mainly produced at the bottom part of the accretion column (figure 2.30), its EW would be reduced by  $\sim 30\%$ , for example, when  $\sim 1/4$  of the column is eclipsed. However, we have carefully discarded the data during the eclipse phase (pole angle  $\theta > 90^\circ$ ) in the analyses of polars, to make the results free from this possibility. The mild X-ray intensity modulation, remaining in the non-eclipse phase, can be explained away in terms of varying contribution from the scattered / reflected component (section 2.6.4; Beardmore *et al.* 1995) rather than by partial eclipse. Since the reflection works equally to the line and continuum photons (except for the formation of absorption edge and fluorescent lines; section 2.6.6), it cannot cause the EW modulation in ionized iron line. Therefore, the observed rotational modulation cannot be accounted for by partial eclipses of the emission region, either.

Having excluded alternative mechanisms to enhance the line equivalent width, we conclude that the observed iron line modulation is caused by the resonance scattering effects.

How about the H-like iron  $K_\alpha$  line, which consists entirely of resonant photons? With *ASCA* and/or *BeppoSAX* observations of polars, including V834 Cen and AM Her, the modulations of H-like line have been statistically insignificant. Presumably, this must be mainly due to technical difficulties in detecting this weak line under the presence of the stronger He-like line adjacent to it; about half objects exhibit H-like line EW of less than 100 eV, whereas most objects have He-like EW of over 100 eV.

### 7.1.3 Quantitative examination of the enhancement

Having confirmed the resonance scattering effect, we examine whether the physical enhancement (section 3.3) is required to explain the observational results in addition to the geometrical effect (section 3.2).

We first estimate the enhancement of pure He-like resonance line,  $\zeta(\text{He}, r)$ , from the observed value,  $\zeta_{\text{OBS}}(\text{He})$ , the latter being a blend of the resonance, intercombination, and forbidden lines. Under a typical temperature of polars (10 – 20 keV), the resonant photons contribute about 65% to the observed He-like iron  $K_\alpha$  line blend, the rest coming from intercombination ( $\sim 20\%$ ) and forbidden ( $\sim 15\%$ ) lines (figure 2.28). After correcting for this reduction, the true value of  $\zeta(\text{He}, r)$  is calculated to be

$$\zeta(\text{He}, r) = \frac{\zeta_{\text{OBS}}(\text{He}) - 0.35}{0.65}, \quad (7.1)$$

which becomes  $2.4_{-1.1}^{+1.5}$  for V834 Cen and  $1.8_{-0.9}^{+3.1}$  for AM Her.

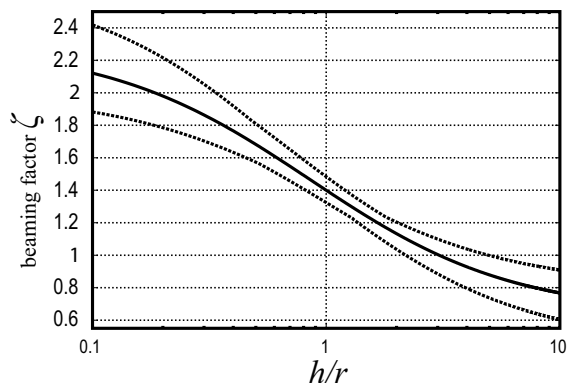


Figure 7.1: An estimation of the geometrical beaming effect on V834 Centauri. The expected beaming factor  $\zeta_{\text{OBS}}$  due to pure geometrical effects, at the limit of large optical depth, is plotted as a function of the ratio of column height to its radius,  $h/r$ . The solid curve corresponds to the most likely system geometry of V834 Cen ( $i = 45^\circ, \beta = 25^\circ$ ; table 2.1), while dashed curves reflect uncertainties in the system geometry.

We next examine whether the obtained  $\zeta(\text{He}, r)$  can be explained by the geometrical effect alone. When the optical depth of resonance scattering is very high and hence the line photons come solely from the surface of the accretion column, the angular distribution of the iron line intensity is given analytically by equation (3.9). By averaging this distribution under the actual system geometry, and taking into account the exposure for the two phases, we have calculated the expected line beaming factor  $\zeta_{\text{OBS}}$  for the *ASCA* data of V834 Cen in 1999, as shown in figure 7.1. Note that  $\zeta$  can take values larger than the maximum factor of geometrical enhancement, that is 2.0 (calculated in section 3.2) in terms of  $\xi$  (normalized to the angular average), since  $\zeta$  is defined as a ratio of the pole-on EW to the side-on EW (equations 6.1 and 6.2). In actual conditions,  $\zeta_{\text{OBS}}$  should be lower by about 30 – 40% than the limiting case shown in figure 7.1, as already demonstrated in figure 3.11. Then, to explain the observed enhancement of He-like line  $\zeta(\text{He}, r) = 2.4$  solely by the geometrical beaming, a very flat coin-shaped column with  $h/r \ll 0.05$  would be required. In order to explain the observed temperature (14.7 keV) and volume emission measure ( $n^2 \times \pi r^2 h \sim 10^{54} \text{ cm}^{-3}$ ), this condition of  $h/r \ll 0.05$

requires a compact accretion column with extremely small shock height,  $h \ll 8 \times 10^4$  cm, and in turn extremely high electron density,  $n_e \gg 2 \times 10^{18}$  cm $^{-3}$ , much exceeding the typical values (section 2.4.5). Then, the plasma would no longer be optically thin even to the continuum photons, especially on the side-on phase. This situation is inconsistent with the thin thermal X-ray spectra observed from V834 Cen. We can arrive at the same inference for AM Herculis and other polars. We hence conclude that the geometrical mechanism alone is insufficient to explain the observed iron line enhancement in polars, and the additional physical collimation due to the velocity gradient, we propose, is needed.

## 7.2 Implications of the Resonance Scattering Effects

### 7.2.1 Impact on the temperature and abundance determinations

When we properly consider the resonance scattering effects, some results from previous iron-line diagnostics of polars (section 2.6) may need revisions. These include estimates of the ionization temperature using the measured ratio of H-like to He-like line intensities, and the iron abundance determinations (section 2.6.5).

To examine how the relative intensities of the H-like and He-like iron  $K_\alpha$  lines are affected by the resonance scattering, we again performed the Monte Carlo simulations under the nominal condition (section 3.4). As shown in figure 7.2 left, the pure He-like resonance line was found to be collimated more strongly than the H-like resonance line (section 3.4.5), and hence their ratio becomes somewhat dependent on the pole angle  $\theta$ . However, in actual observations with limited energy resolution, we use the He-like *line blend* (mixture of resonance, intercombination, and forbidden lines). Then, the line ratio becomes less dependent on the angle as seen in figure 7.2 bottom left. In other words, the resonance scattering affects the He-like iron  $K_\alpha$  blend and the H-like iron  $K_\alpha$  line to a very similar extent, for a wide range of plasma parameters (figure 7.2 right). Therefore, the previous estimates on the ionization temperature must be valid.

In contrast to the temperature determination based on the line flux ratios, the abundance measurements relying on the absolute line EW can be more strongly affected by the anisotropic photon transfer. To examine this, we took abundance measurements of 5 polars with *ASCA* by Ezuka & Ishida (1999), and calculated for each object a phase-averaged enhancement factor,

$$\bar{\xi} \equiv \langle \xi \rangle_{\text{phase}} \quad , \quad (7.2)$$

utilizing  $i$  and  $\beta$  given in table 2.1 and assuming for simplicity that the plasma is in the nominal condition. To correct the published abundance measurements for the anisotropic effects, obviously we must divide them by  $\bar{\xi}$ . Figure 7.3 summarizes these corrections to the iron abundance determinations. Thus, the implied corrections are at most  $\pm 30\%$ , which is generally within the measurement error. Polars with almost side-on or almost

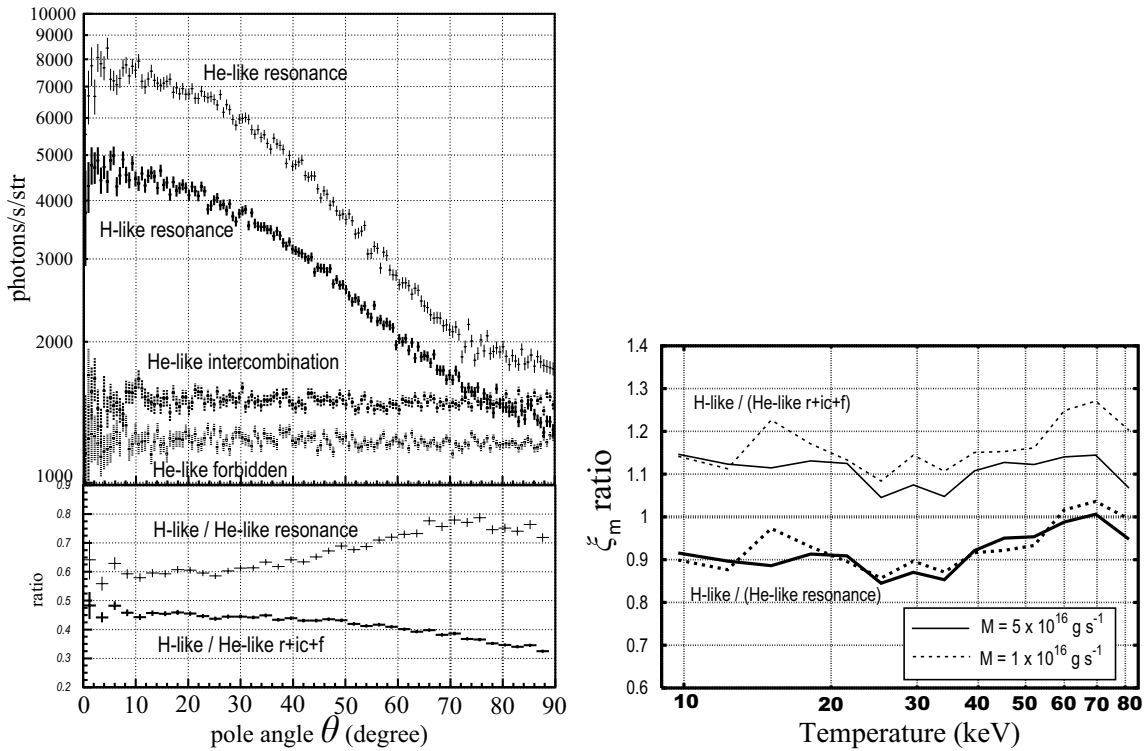


Figure 7.2: Comparison of the anisotropic effects between the H-like and He-like iron  $K_\alpha$  lines, based on the Monte-Carlo simulation. (*left*) Line fluxes of various iron  $K_\alpha$  line components and their ratios, calculated under the nominal condition (section 3.4) and plotted as a function of pole angle  $\theta$ . (*right*) The ratio of the enhancement factor  $\xi_m$  (equation 3.18) between the H-like and He-like lines, displayed as a function of the post-shock plasma temperature. Calculations were done for the same sets of conditions as figure 3.17 .

pole-on geometries, like POLEs, would be subject to relatively large modifications in the abundance estimates, but such a geometry is rare. As a result, the distribution of metal abundances of polars, 0.1 – 0.8 solar obtained by Ezuka & Ishida (1999; figure 7.3 bottom), is considered to remain still valid.

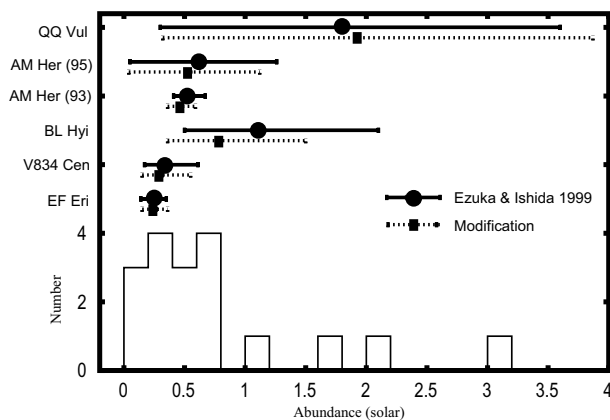


Figure 7.3: Corrections to the iron abundances of 5 polars, by considering the resonance scattering effects. The original abundance measurements are based on the *ASCA* observations by Ezuka and Ishida (1999). The implied abundance distribution among MCVs is shown at the bottom (essentially the same as figure 2.45).

## 7.2.2 Solution to the mystery of POLEs

To solve the mystery of unrealistically strong iron line emission from POLEs (section 2.6.7) has been the first motivation of this thesis. The face-value abundances of POLEs, implied by the *ASCA* spectra, are extremely high;  $\sim 2$  solar for AX J2315-0592,  $3.04 \pm 1.47$  solar for RX J1802.1+1804, and  $3.0_{-0.9}^{+4.3}$  solar for AX J1842-0423. These are in a strong disagreement with those of other MCVs shown in figure 7.3 (or figure 2.45). Then, the remaining issue is whether the abundances of POLEs comes into a reasonable range when they are also corrected by  $\bar{\xi}$ .

Our Monte-Carlo simulations (section 3.4) and the observational study (Chapter 6) consistently indicate that the resonance iron K lines are enhanced by a factor of  $\xi_m = 2 - 3$  in the axial direction of accretion column; we can expect  $\xi_m = 2 - 2.5$  both for the H-like and He-like lines, even if the latter is a blend of the resonance, intercombination, and forbidden lines. Consequently, if a polar with a co-aligned magnetic axis ( $\beta \sim 0$ ) is viewed from nearly the pole-on direction ( $i \sim 0$ ), we expect the iron K line EW to be persistently enhanced by  $\bar{\xi} \simeq \xi_m = 2 - 2.5$  times. By applying a correction with  $\xi_m > 2$ , the extremely high face-value abundance of AX J2315-0592 will be modified to  $\sim 1$  solar, and the corrected abundances of RX J1802.1+1804 and AX J1842-0423 also come into agreement with those of other polars within errors. Therefore, we conclude that the three POLEs are exactly such objects (section 2.6.7).

The number “three” of POLEs, which have the geometrical condition of  $i \sim \beta \sim 0$ , corresponds to  $\sim 6\%$  of the currently-known 50 polars. Does this number agree with statistical expectations? To estimate the enhancement  $\bar{\xi}$  of iron line under various geometrical conditions ( $i$  and  $\beta$ ), we calculated  $\bar{\xi}$  on the  $i - \beta$  plane using the Monte Carlo simulation in the nominal and strong cases (section 3.4.5). The obtained results are presented in figure 7.4. This calculation was performed for the He-like blend iron K line only, but the result for the H-like line is expected to be similar (figure 7.2). Assuming that  $i$  and  $\beta$  are randomly oriented to the line of sight, we have converted the result of figure 7.4 into a cumulative probability distribution of  $\bar{\xi}$ , as shown in figure 7.5. We hence expect  $\bar{\xi} > 2$  with a probability of  $\sim 4.5\%$ , if the condition of strong case holds. Although the expected probability is apparently very low if the nominal case is to be employed, this estimation yields a lower-limit probability because  $\beta$  tend to be distributed over  $< 70^\circ$  (i.e., the magnetic and rotational axes tending to align) as is inferred from figure 7.4. The estimate is therefore in an rough agreement with the observed probability. Thus, we conclude that the mystery of POLEs has been solved by the proposed line-collimation mechanism.

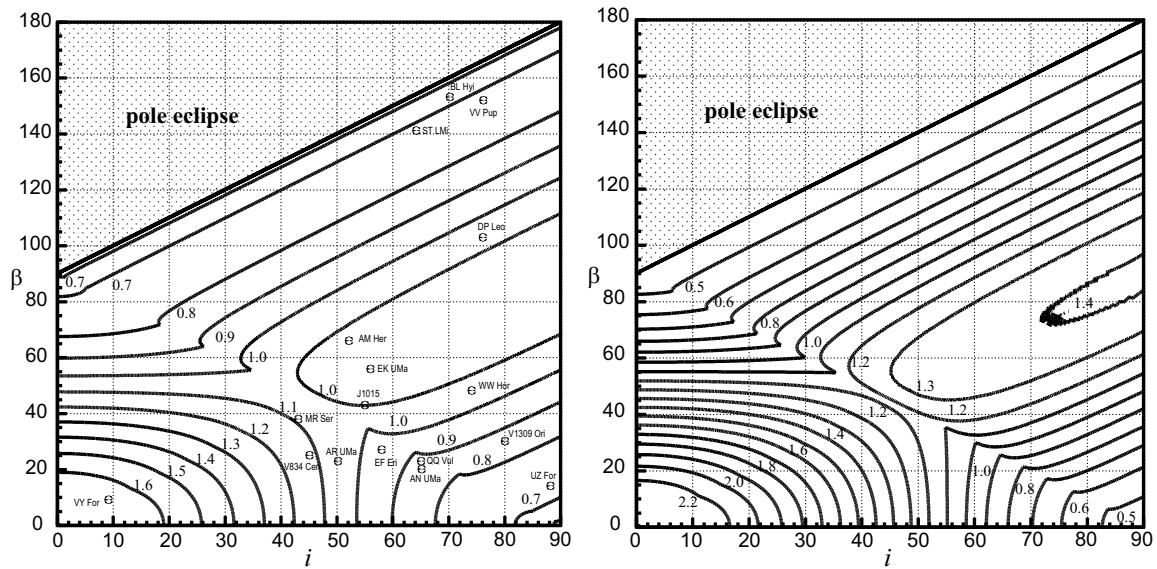


Figure 7.4: Contours of the expected average enhancement  $\bar{\xi}$ , displayed on the plane of  $(i, \beta)$ . A single pole is assumed to be accreting, under the nominal (*left*) or the strong (*right*) conditions (section 3.4.5). The polars with known geometries (table 2.1) are also plotted in the left panel with tick marks.

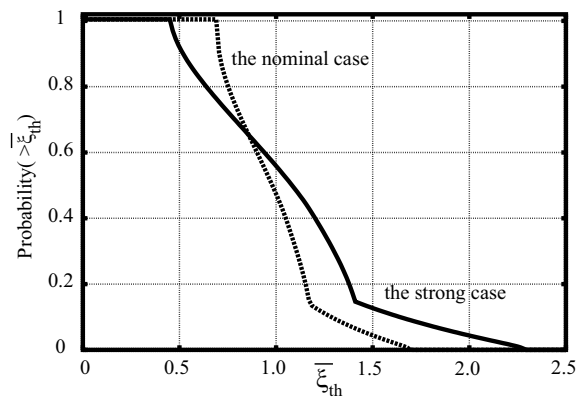


Figure 7.5: The cumulative probability distribution of finding  $\bar{\xi}$  higher than the specified threshold  $\bar{\xi}_{th}$ . Objects are assumed to be randomly distributed in terms of  $i$  and  $\beta$ . The dotted and solid curves represent the nominal case and the strong case, respectively.

### 7.2.3 A new plasma diagnostic method in the accretion column

The line beaming effect we have discovered is expected to provide unique diagnostics of the accretion column of magnetic white dwarfs. If we adopt the Aizu regime (section 2.4.6), the physical condition in the accretion column is described by four parameters:  $kT^{\text{sh}}$ ,  $h$ ,  $r$ , and  $n_e^{\text{sh}}$ . To determine these parameters, four observational or theoretical constraints are required. Usually, observations of continuum spectra provide two independent quantities, the temperature  $kT_{\text{OBS}}$  and the emission measure  $EM$ , which is  $\sim n_e^2 h r^2$  (equation 2.65). Also there is one theoretical constraint, that the shock heated plasma cools only by the free-free cooling, which relates  $kT^{\text{sh}}$ ,  $n_e^{\text{sh}}$ , and  $h$  as in equation (2.44).

With these three constraints, we can express  $h$  and  $r$  in terms of  $n_e^{\text{sh}}$  as

$$h = 1.5 \times 10^7 \text{cm} \left( \frac{kT^{\text{sh}}}{14.7 \text{keV}} \right)^{\frac{1}{2}} \left( \frac{n_e^{\text{sh}}}{10^{16} \text{cm}^{-3}} \right)^{-1} \quad (7.3)$$

$$r = 2.4 \times 10^7 \text{cm} \left( \frac{EM}{1.3 \times 10^{54} \text{cm}^{-3}} \right) \left( \frac{kT^{\text{sh}}}{14.7 \text{keV}} \right)^{-\frac{1}{4}} \left( \frac{n_e^{\text{sh}}}{10^{16} \text{cm}^{-3}} \right)^{-\frac{1}{2}}. \quad (7.4)$$

Here, we normalized the relevant quantities to the values observed from V834 Cen with *ASCA* in 1999 (Model 4 in table 6.1 where the temperature is set to the *Ginga* value), adopting a distance of 86 pc by Warner (1987). When  $n_e^{\text{sh}}$  is low, the solutions to  $h$  and  $r$  imply a long cylinder-like column, while a flat coin-shaped geometry is indicated by high values of  $n_e^{\text{sh}}$ . However, due to the lack of one more piece of information, we have not been able to determine the column geometry.

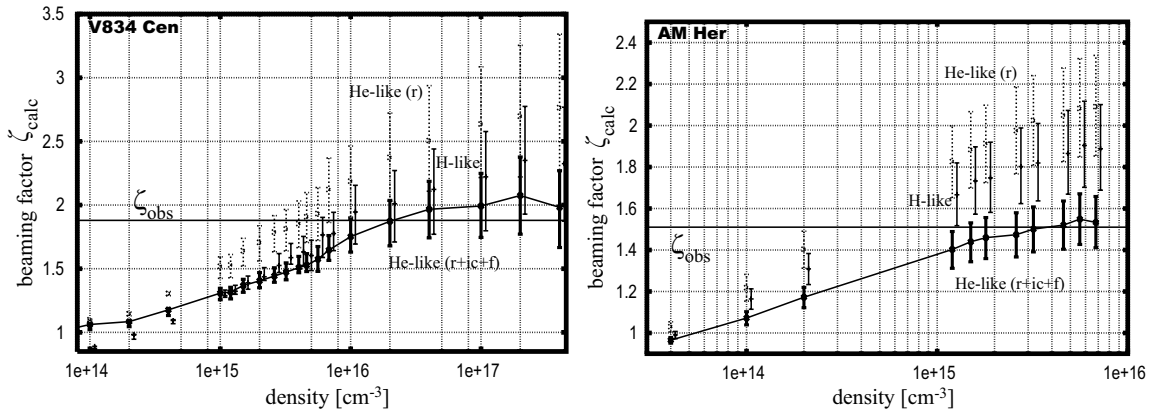


Figure 7.6: The beaming factor  $\zeta_{\text{calc}}$  of V834 Cen (*left*) and AM Her (*right*) calculated by our Monte Carlo simulation, as a function of the assumed post-shock density. It is calculated under the actual observing condition with *ASCA*; i.e., the exposure in each phase is set to be the actual accumulation time, the viewing angle  $\theta$  of each phase is calculated by their  $i$  and  $\beta$  (table 2.1), and the temperature and volume emission measure are set to the observed values. The dashed and thin solid data points indicate  $\zeta$  of He-like and H-like resonance iron  $K_\alpha$  photons, respectively. The thick data points show  $\zeta$  of the blended He-like iron line, which includes intercombination and forbidden lines. The error bars take into account those of the geometrical parameters shown in table 2.1.

Now that we have understood the anisotropic transfer of resonance photons, the phase-resolved iron line spectroscopy provides us with the needed fourth information; the value of  $\zeta$  which reflects the accretion column shape. If we specify a value of  $n_e^{\text{sh}}$ , then  $h$  and  $r$  are determined through equations (7.3) and (7.4), respectively. Using these  $n_e^{\text{sh}}$ ,  $h$  and  $r$  as inputs, we can calculate  $\zeta$  via Monte-Carlo simulations. In this way, we have calculated  $\zeta$  for V834 Cen and AM Her as a function of the assumed  $n_e^{\text{sh}}$ , and obtained the results in figure 7.6. Thus, the observed enhancements of V834 Cen and AM Her can be best explained by  $n_e^{\text{sh}} \sim 2.0 \times 10^{16} \text{ cm}^{-3}$ , and  $\sim 3.8 \times 10^{15} \text{ cm}^{-3}$ , respectively. This in turn fixes the column height and the radius as summarized in table 7.1. These values are considered typical for polars.

Currently, the observational errors are so large that the values obtained above are quite uncertain. However, our new method will provide a powerful tool for next generation instruments with a larger effective area and an improved energy resolution, including *Chandra*, *XMM-Newton*, and *ASTRO-E II* (section 4.1.2).

Table 7.1: The plasma parameters for the accretion column of V834 Cen and AM Her<sup>a</sup>.

Object	$n_e^{\text{sh}}$	$h$	$r$	Note
V834 Cen	$2.0_{-1.0}^{+83} \times 10^{16} \text{ cm}^{-3}$ ( $5 \times 10^{14} - \infty$ )	$0.8_{-0.6}^{+0.8} \times 10^7 \text{ cm}$ ( $0 - 3 \times 10^8$ )	$1.7_{-1.4}^{+0.7} \times 10^7 \text{ cm}$ ( $0 - 1 \times 10^8$ )	<i>b</i>
AM Her	$3.8_{-2.5}^{+18} \times 10^{15} \text{ cm}^{-3}$ ( $0 - \infty$ )	$4.4_{-3.7}^{+8.4} \times 10^7 \text{ cm}$ ( $0 - \infty$ )	$20_{-12}^{+15} \times 10^7 \text{ cm}$ ( $0 - \infty$ )	<i>b</i> <i>c</i>

*a* Based on the *ASCA* observations (In the case of V834 Cen, only for the 1999 data).

*b* The best values estimated by the Monte Carlo simulations (see text).  
The error bar includes only the geometrical uncertainties.

*c* Include the statistical error in the enhancement factor  $\xi_{\text{OBS}}$  in the *ASCA* observations.

### 7.3 Prospects for the Future Studies

The essence of the anisotropic effect of resonance photons proposed in this thesis is that the mass of ion is heavy enough for the thermal Doppler effect compared to the Doppler shift by the bulk motion (equation 3.12). In this prospect, the iron line has been the best target of our study. In the near future, very high energy resolution of  $\sim 10$  eV is available around the iron- $K_\alpha$ -line range for the first time, by the XRS on board *ASTRO-E II*, which is the recovery mission of the lost *ASTRO-E* (section 4.1.2), and is scheduled for launch in early 2005. Since it can resolve the fine structure of iron  $K_\alpha$  lines, we can measure detailed information from the phase-resolved X-ray spectra, as demonstrated in figure 3.14, such as energy width by the thermal broadening, the Doppler energy by the bulk motion, and the enhancement of pure resonance lines and/or others, separately. Since these quantities are strongly related to the anisotropy of the plasma, we can feedback to our Monte Carlo simulation code to improve the knowledge of the radiative transfer of atomic line photons in the plasma of the accretion column.

We can expect the anisotropic effect also in line photons from lighter elements, which are mainly emitted from the bottom part of the accretion column (figure 2.31), although they suffer larger thermal broadening effect. The quantitative estimations for them with the Monte Carlo simulation are shown in figure 7.7. As expected, the collimation effects of the resonance line photons decreases as the atomic number decreases. Nevertheless, we expect significant anisotropy for Si, S, and Mg, which are also abundant in the universe. A further merit of these elements is that their  $K_\alpha$  lines, emitted in the 1.2 – 2.6 keV range, can be studied with a high energy resolution with the grating spectrometers on the currently active missions, *Chandra* and *XMM-Newton*. We plan to make proposals to use these instruments, and analyze their data which are about to be released. Needless to say, these lines are the target for *ASTRO-E II*, which has larger effective area than these instruments keeping the high energy resolution also in the soft X-ray band.

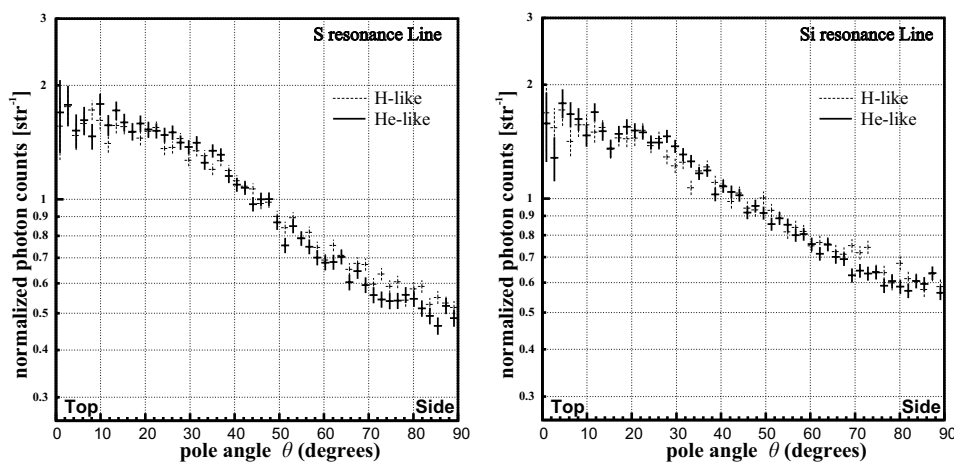


Figure 7.7: The angular distributions of resonance lines from light elements, S, Si, Al, Mg, Na, Ne, and O. They are calculated by the Monte Carlo simulation adopting their emissivities by Mewe et al (1984), and assuming one solar abundances. The plasma parameters are set to the nominal case (see section 3.4).

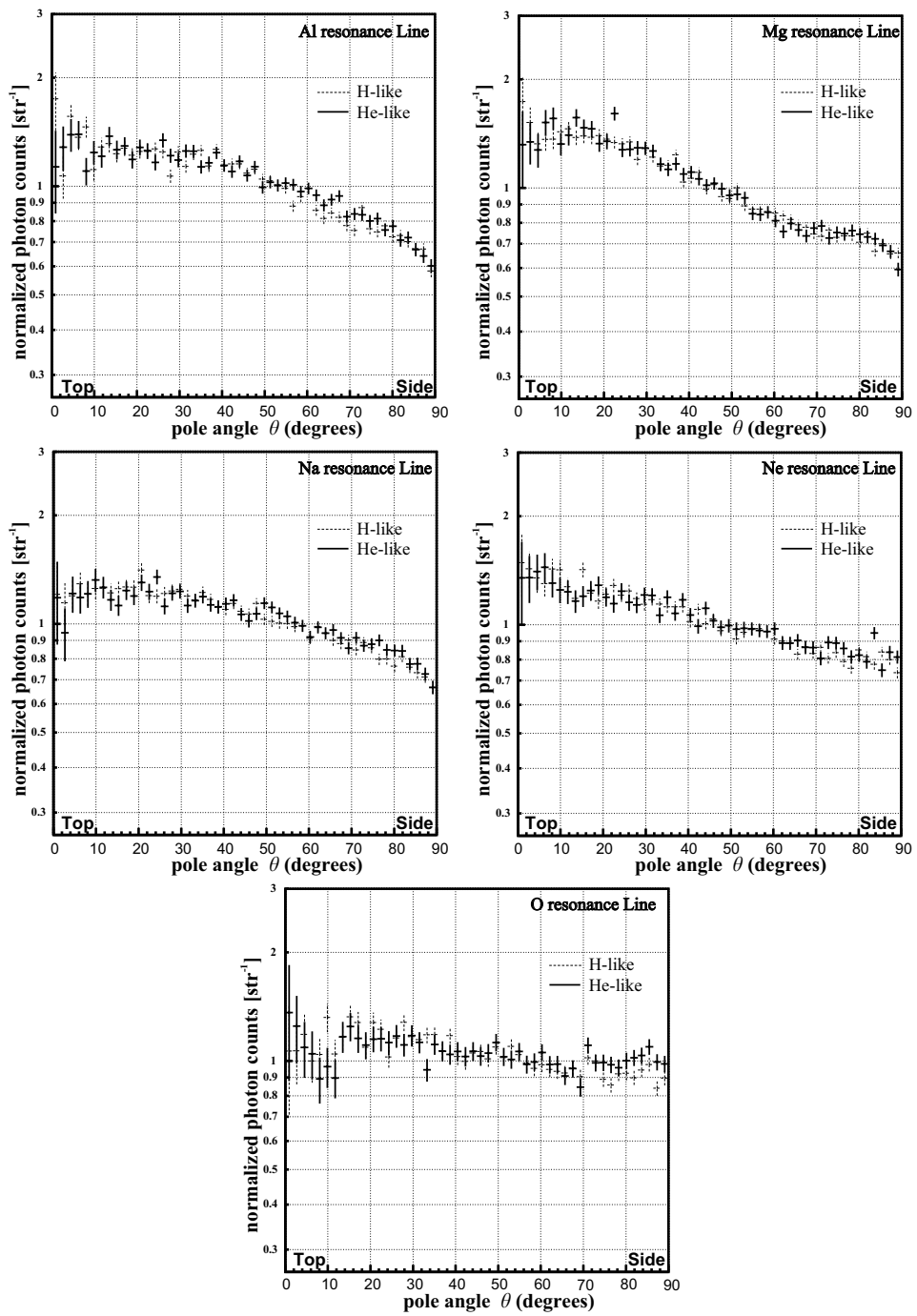


Figure 7.7: Continued.

# Chapter 8

## CONCLUSION

We have observational and numerically studied the X-ray emitting hot plasma in the accretion column on white dwarfs of polars as an ideal example of optically “gray” plasmas; i.e., it is optically thin for Compton scattering, while thick for resonance scattering in atomic photons. Our results are summarized in the following five points.

- We have proposed a new effect of anisotropic radiative transfer for resonance photons in the accretion column of white dwarfs, in order to explain the extremely intense iron  $K_\alpha$  lines observed from several Galactic X-ray sources, called POLEs. The idea consists of two different mechanisms, both of which enhance the resonance photons along the axis of accretion column. One is the geometrical effect, which becomes effective as the accretion column becomes shorter. The other is the physical effect, that the cross section of resonance scattering is reduced when the resonant photons propagate along the magnetic field lines because of the differential Doppler shift in the post-shock flow.
- We have calculated the radiative transfer of resonance photons in the accretion column using our own Monte-Carlo code, and confirmed that the anisotropic effect can enhance the equivalent width of H-like and He-like iron  $K_\alpha$  resonance lines in the vertical direction, up to a factor of 2 – 3 as compared to the angular average. This is higher than the maximum collimation that is available with the geometrical effect alone.
- Combining the *ASCA*, *RXTE*, and *BeppoSAX* observations, we have confirmed that V834 Centauri and AM Herculis show clear enhancement of the equivalent width of iron  $K_\alpha$  line in the pole-on phase relative to the side-on phase. Quantitatively, the former exhibits the enhancement of He-like iron line EW by a factor of  $1.9^{+0.9}_{-0.6}$  in the pole-on phase relative to the side-on phase with  $> 90\%$  significance, and the latter exhibits that of blended iron line EW (i.e, fluorescent, H-like, and He-like) by a factor of  $1.3^{+0.1}_{-0.2}$  with  $> 99\%$  significance. Furthermore, the *ASCA* and *BeppoSAX* data of seven other polars indicate their He-like iron  $K_\alpha$  line EW is systematically

larger in the pole-on phase than in the side-on phase, even though the effect is insignificant for individual sources. Their EWs of H-like iron line are statistically consistent with being unmodulated.

- We conclude that the observed enhancements in the line EW in the pole-on phase are due to the anisotropic mechanism we proposed, since we can exclude other possible mechanisms to increase the line EWs. We have estimated that this effect have a minor impact on the previous measurements of ionization temperature and iron abundance. However, the modification on the abundances of POLEs is expected to be large ( 2 – 2.5 times) because of their extreme geometries,  $i \sim \beta \sim 0$ . After these revisions, the iron abundances of POLEs become normal ( $\sim 1$  solar abundances), thus allowing us to conclude that the large EWs of their iron lines are due to the anisotropic photon transfer.
- We have proposed that the rotational modulation of the iron-line EW can be used as a new method of plasma diagnostics for accretion column, to uniquely determine the physical condition, such as temperature, density, and the plasma shape. This must be a powerful tool for the next generation instruments, like the *Chandra* grating optics and the *ASTRO-E II* X-ray calorimeter.



# Appendix A

## Analysis

### A.1 Energy range in *ASCA* and *BeppoSAX* analyses

In *ASCA* and *BeppoSAX* analyses, we used the energy range of  $E_{\min} - 10.0$  keV band for fitting with the continuum Model 2 with three Gaussians (see section 6.1). The lower limit,  $E_{\min}$ , was determined to optimize the determination of model parameters (the temperature of the bremsstrahlung model), as described in § 3.2 of Ezuka and Ishida (1994). The  $E_{\min}$  that we have used in this thesis are listed in table A.1.

Table A.1: The lower energy range  $E_{\min}$  for the continuum modeling of MCVs.

object <sup>a</sup>	$E_{\min}$ keV	object <sup>b</sup>	$E_{\min}$ keV
V834 Cen	4.5	AE Aqr	No <sup>c</sup>
AM Her	4.5	AO Psc	4.0
BL Hyi	2.0	BG CMi	4.0
BY Cam	4.5	EX Hya	2.0
EF Eri	4.5	FO Aqr	4.0
EK UMa	No <sup>c</sup>	PQ Gem	5.0
QQ Vul	4.0	RXJ1712-2414	5.0
RXJ1015+0904	5.0	TV Col	4.5
V1432 Aql	4.5	TX Col	4.5
V2301 Oph	2.0	V1062 Tau	4.5
		V1223 Sgr	5.0
		V405 Aur	5.0
		XY Ari	5.0

<sup>a</sup> Polars

<sup>b</sup> Intermediate polars

<sup>c</sup> Discarded for phase-resolved analyses of iron K line.

### A.2 Fitting results for V834 Cen and AM Herculis

Table A.2: Best Fit continuum parameters for the ASCA GIS and SIS spectra of V834 Cen<sup>a</sup>.

Model	band <sup>b</sup>	$kT_1$ keV	$kT_2$ keV	$N_{H1}$ $\times 10^{22}$ cm <sup>-2</sup>	$N_{H2}$ $\times 10^{22}$ cm <sup>-2</sup>	Cov. Frac <sup>c</sup> %	Bol. lum. <sup>d</sup> ( $10^{31}$ erg s <sup>-1</sup> )	$\chi^2$ (dof)
<b>POLE_ON phase (1994)</b>								
Model 1	(single $n_H$ , single $kT$ )	> 25.5	–	< 0.10	–	–	6.8	0.41 (122)
Model 2	(single $n_H$ , single $kT$ )	> 0.5	–	< 25.2	–	–	2.5	0.23 (16)
Model 3	(single $n_H$ , double $kT$ )	> 10.0	< 10.3	< 1.1	–	–	6.2	0.40 (120)
Model 3		14.7 <sup>e</sup>	0.16 <sup>+0.13</sup> <sub>-0.15</sub>	0.35 <sup>+0.78</sup> <sub>-0.10</sub>	–	–	2.1	0.41 (121)
Model 4	(multi $n_H$ , single $kT$ )	> 4.7	–	< 0.01	any	< 60	2.5	0.41 (120)
Model 4		14.7 <sup>e</sup>	–	< 0.01	3.1 <sup>+10.2</sup> <sub>-2.0</sub>	32.0 <sup>+8.3</sup> <sub>-8.4</sub>	2.3	0.40 (121)
<b>SIDE_ON phase (1994)</b>								
Model 1	(single $n_H$ , single $kT$ )	44.1 <sup>+32.0</sup> <sub>-20.5</sub>	–	< 0.03	–	–	3.5	0.67 (135)
Model 2	(single $n_H$ , single $kT$ )	> 2.6	–	< 24.5	–	–	2.1	0.60 (23)
Model 3	(single $n_H$ , double $kT$ )	> 12.4	0.17 <sup>+0.13</sup> <sub>-0.12</sub>	0.20 <sup>+0.37</sup> <sub>-0.19</sub>	–	–	2.4	0.65 (133)
Model 3		14.7 <sup>e</sup>	0.16 <sup>+0.10</sup> <sub>-0.05</sub>	0.25 <sup>+0.35</sup> <sub>-0.06</sub>	–	–	1.9	0.66 (134)
Model 4	(multi $n_H$ , single $kT$ )	44.7 <sup>+32.0</sup> <sub>-21.1</sub>	–	< 0.01	any	< 77.5	3.6	0.68 (133)
Model 4		14.7 <sup>e</sup>	–	0.11 <sup>+0.02</sup> <sub>-0.04</sub>	any	< 10.0	1.8	0.77 (134)
<b>POLE_ON phase (1999)</b>								
Model 1	(single $n_H$ , single $kT$ )	> 200	–	0.22 <sup>+0.03</sup> <sub>-0.03</sub>	–	–	(14)	2.01 (174)
Model 2	(single $n_H$ , single $kT$ )	14.5 <sup>+144</sup> <sub>-7.9</sub>	–	12.5 <sup>+8.2</sup> <sub>-4.1</sub>	–	–	5.6	0.50 (40)
Model 3	(single $n_H$ , double $kT$ )	> 80	0.16 <sup>+0.06</sup> <sub>-0.01</sub>	0.67 <sup>+0.18</sup> <sub>-0.03</sub>	–	–	(11)	1.09 (172)
Model 3		14.7 <sup>e</sup>	0.17 <sup>+0.01</sup> <sub>-0.01</sub>	1.5 <sup>+0.1</sup> <sub>-0.1</sub>	–	–	3.2	1.55 (173)
Model 4	(multi $n_H$ , single $kT$ )	> 39	–	< 0.03	7.3 <sup>+2.7</sup> <sub>-1.7</sub>	47.6 <sup>+0.1</sup> <sub>-8.7</sub>	(8.6)	0.85 (172)
Model 4		14.7 <sup>e</sup>	–	< 0.10	8.9 <sup>+2.2</sup> <sub>-1.8</sub>	60.2 <sup>+2.4</sup> <sub>-2.6</sub>	4.2	0.95 (173)
<b>SIDE_ON phase (1999)</b>								
Model 1	(single $n_H$ , single $kT$ )	> 164	–	0.05 <sup>+0.03</sup> <sub>-0.02</sub>	–	–	(11)	0.97 (162)
Model 2	(single $n_H$ , single $kT$ )	7.9 <sup>+72.7</sup> <sub>-4.4</sub>	–	16.1 <sup>+12.7</sup> <sub>-10.2</sub>	–	–	3.9	0.58 (26)
Model 3	(single $n_H$ , double $kT$ )	> 55	0.13 <sup>+0.15</sup> <sub>-0.04</sub>	0.21 <sup>+0.11</sup> <sub>-0.05</sub>	–	–	(5.0)	0.91 (160)
Model 3		14.7 <sup>e</sup>	0.20 <sup>+0.02</sup> <sub>-0.03</sub>	0.89 <sup>+0.24</sup> <sub>-0.13</sub>	–	–	2.3	1.07 (161)
Model 4	(multi $n_H$ , single $kT$ )	> 19	–	< 0.05	9.5 <sup>+12.5</sup> <sub>-3.0</sub>	30.0 <sup>+17.2</sup> <sub>-10.2</sub>	(6.0)	0.78 (160)
Model 4		14.7 <sup>e</sup>	–	< 0.09	11.1 <sup>+5.0</sup> <sub>-3.7</sub>	49.1 <sup>+5.2</sup> <sub>-5.0</sub>	3.1	0.81 (161)

<sup>a</sup> Excluding the Fe K $\alpha$  line band (6.0 – 7.5 keV).<sup>b</sup> Energy bandpass for fitting. “W” means 1.0 – 10.0 keV, and “N” 4.5 – 10.0 keV.<sup>c</sup> The covering fraction (%) of  $N_{H1}$ .<sup>d</sup> Bolometric luminosity. The distance is assumed to be 100 pc.<sup>e</sup> Continuum temperature fixed at the value measured with Ginga (Ishida 1991).<sup>f</sup> Pole-on corresponds to  $\phi = 0.73 \pm 0.25$ , and Side-on to  $\phi = 0.23 \pm 0.25$ .

To examine the observational results of V834 Cen and AM Herculis with *ASCA* and/or *BeppoSAX*, we have fitted the spectra with the other continuum model. Since Model 4 (section 6.1.1) can also reproduce the phase-resolved spectra of V834 Cen as shown in table A.2, we fitted the spectra of both phases with fixing their best-fit continuum Model 4, and obtained the equivalent widths of iron lines as listed in table A.3. This result is consistent with that by narrow band fitting (table 6.3). Similarly, we obtained the results of AM Herculis with *ASCA* and *BeppoSAX* as in tables A.4 and A.5, respectively. These are consistent with those by the narrow band fitting (tables 6.7 and 6.9, respectively).

Table A.3: Best Fit parameters of the iron  $K_\alpha$  line for V834 Centauri with *ASCA*<sup>a</sup>.

Phase <sup>b</sup>	Fluo. EW (eV)	He-like $K_\alpha$		H-like $K_\alpha$		$\chi_\nu^2$ (dof)
		l. c. <sup>c</sup> (keV)	EW (eV)	l. c. <sup>c</sup> (keV)	EW (eV)	
<b>In 1994</b>						
Average	178 <sup>+153</sup> <sub>-160</sub>	6.69 <sup>+0.08</sup> <sub>-0.06</sub>	358 <sup>+165</sup> <sub>-161</sub>	6.97	< 287	0.62 (110)
Pole-on	< 593	6.68 <sup>+0.12</sup> <sub>-0.25</sub>	665 <sup>+516</sup> <sub>-497</sub>	6.96	< 822	0.36 (136)
Side-on	< 353	6.71 <sup>+0.09</sup> <sub>-0.39</sub>	359 <sup>+225</sup> <sub>-144</sub>	6.99	< 321	0.71 (147)
<b>In 1999</b>						
Average	406 <sup>+56</sup> <sub>-53</sub>	6.70 <sup>+0.05</sup> <sub>-0.06</sub>	365 <sup>+60</sup> <sub>-68</sub>	6.98	296 <sup>+72</sup> <sub>-68</sub>	1.07 (245)
Pole-on	400 <sup>+75</sup> <sub>-73</sub>	6.70 <sup>+0.07</sup> <sub>-0.10</sub>	465 <sup>+84</sup> <sub>-94</sub>	6.98	302 <sup>+106</sup> <sub>-91</sub>	0.86 (234)
Side-on	416 <sup>+100</sup> <sub>-98</sub>	6.69 <sup>+0.62</sup> <sub>-0.13</sub>	247 <sup>+124</sup> <sub>-107</sub>	6.97	302 <sup>+118</sup> <sub>-143</sub>	0.75 (192)

<sup>a</sup> The determination of continuum spectrum is performed in 1.0 keV – 10.0 keV with Model 4 in table 6.1.

The temperature is fixed to the Ginga value, 14.7 keV, and continuum parameters are fixed.

<sup>b</sup> Pole-on is  $\phi = 0.73 \pm 0.25$  and Side-on  $\phi = 0.23 \pm 0.25$ .

<sup>c</sup> The line center (keV). That of the fluorescent component is fixed at 6.40 keV, and the ratio of H-like and He-like line is fixed to 1.042.

Table A.4: Best Fit parameters of the iron  $K_\alpha$  line for AM Herculis with *ASCA*<sup>a</sup>.

Phase <sup>b</sup>	Fluo. EW (eV)	He-like $K_\alpha$		H-like $K_\alpha$		$\chi_\nu^2$ (dof)
		l. c. <sup>c</sup> (keV)	EW (eV)	l. c. <sup>c</sup> (keV)	EW (eV)	
Average	202 <sup>+19</sup> <sub>-15</sub>	6.68 <sup>+0.04</sup> <sub>-0.02</sub>	220 <sup>+18</sup> <sub>-20</sub>	6.96	136 <sup>+18</sup> <sub>-24</sub>	1.19 (535)
Pole-on	205 <sup>+22</sup> <sub>-18</sub>	6.68 <sup>+0.03</sup> <sub>-0.01</sub>	227 <sup>+20</sup> <sub>-26</sub>	6.96	129 <sup>+26</sup> <sub>-23</sub>	1.05 (519)
Side-on	205 <sup>+27</sup> <sub>-69</sub>	6.67 <sup>+0.07</sup> <sub>-0.08</sub>	147 <sup>+82</sup> <sub>-30</sub>	6.95	150 <sup>+76</sup> <sub>-43</sub>	0.70 (291)

<sup>a</sup> The determination of continuum spectrum is performed in 1.0 keV – 10.0 keV with Model 5 in table 6.6.

<sup>b</sup> Pole-on is  $\phi = 0.68 - 1.00$  and Side-on  $\phi = 0.00 - 0.23, 0.50 - 0.68$ .

<sup>c</sup> The line center (keV). That of the fluorescent component is fixed at 6.40 keV, and the ratio of H-like and He-like line is fixed to 1.042.

Table A.5: Best Fit parameters of the iron  $K_\alpha$  line for AM Herculis with *BeppoSAX*<sup>a</sup>.

Phase <sup>b</sup>	Fluo. EW (eV)	He-like $K_\alpha$		H-like $K_\alpha$		$\chi_\nu^2$ (dof)
		l. c. <sup>c</sup> (keV)	EW (eV)	l. c. <sup>c</sup> (keV)	EW (eV)	
Average	81 <sup>+19</sup> <sub>-20</sub>	6.70 <sup>+0.10</sup> <sub>-0.07</sub>	170 <sup>+136</sup> <sub>-215</sub>	6.98	175 <sup>+27</sup> <sub>-26</sub>	1.00 (141)
Pole-on	59 <sup>+44</sup> <sub>-31</sub>	6.71 <sup>+0.09</sup> <sub>-0.18</sub>	214 <sup>+33</sup> <sub>-85</sub>	6.99	144 <sup>+61</sup> <sub>-67</sub>	0.79 (163)
Side-on	154 <sup>+20</sup> <sub>-52</sub>	6.72 <sup>+0.10</sup> <sub>-0.14</sub>	155 <sup>+120</sup> <sub>-60</sub>	7.00	220 <sup>+17</sup> <sub>-131</sub>	0.75 (160)

<sup>a</sup> The determination of continuum spectrum is performed in 1.6 keV – 10.0 keV with Model 4 in table 6.8.

<sup>b</sup> Pole-on is  $\phi = 0.68 - 1.00$  and Side-on  $\phi = 0.00 - 0.23, 0.50 - 0.68$ .

<sup>c</sup> The line center (keV). That of the fluorescent component is fixed at 6.40 keV, and the ratio of H-like and He-like line is fixed to 1.042.

### A.3 Intermediate Polars

We have searched the *ASCA* data of intermediate polars for possible evidence of the enhancement of line equivalent width, in the same way of section 6.3. We have analyzed all the intermediate polars listed in table 5.1. The light curves folded by their orbital and spin periods are shown in figure A.1. It is difficult to determine the pole-on phase, because the geometries of the accretion column can not be measured in the optical band (section 2.4). We defined the pole-on (MIN) and side-on (MAX) phases as in table A.6, based on the observed X-ray spin modulation; X-ray faint phase corresponds to the pole-on as described in section 2.6.4. The phase resolved spectra are shown in figure A.2.

To quantify the equivalent width of iron lines, we adopted Model 2 (section 6.1.1) with three narrow Gaussians. As summarized in figure A.3, the spin modulations of the equivalent width are insufficient both for H-like and He-like iron  $K_{\alpha}$  lines. Quantitatively, the mean-weighted enhancement is  $\bar{\xi}_{\text{OBS}}(\text{H}) = 1.0 \pm 0.5$  and  $\bar{\xi}_{\text{OBS}}(\text{He}) = 1.1 \pm 0.4$ , for H-like and He-like lines, respectively.

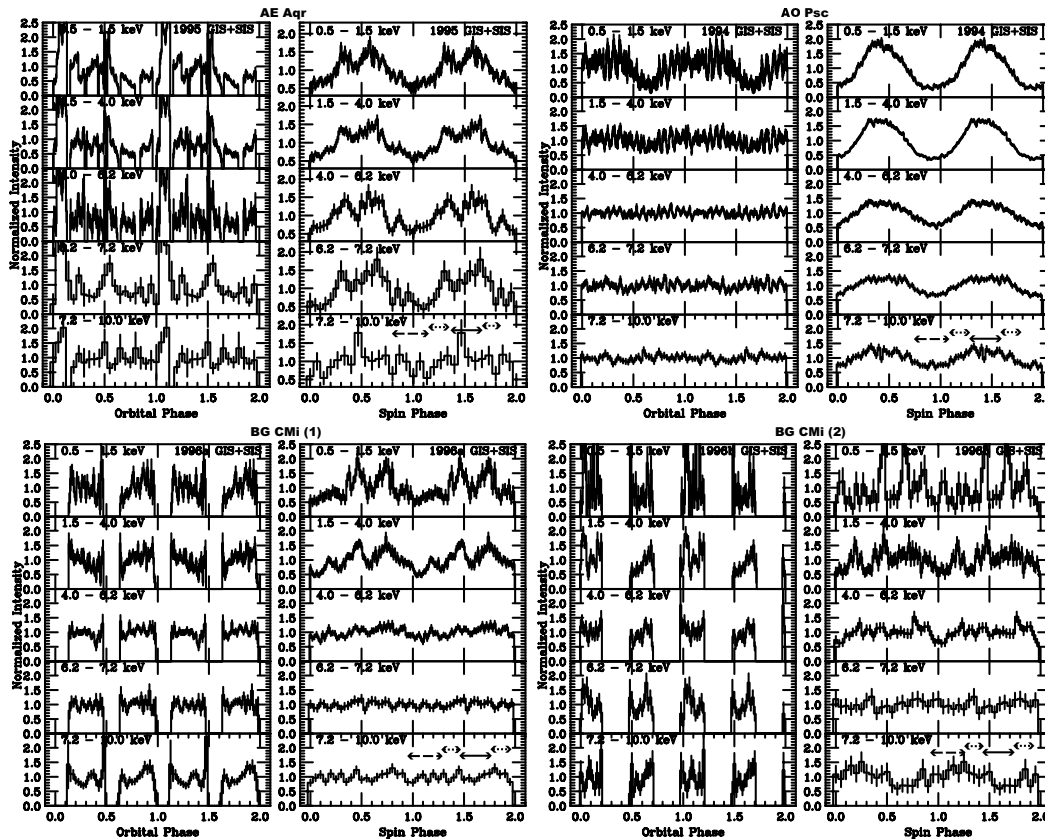


Figure A.1: X-ray light curves of intermediate polars with *ASCA* and *BeppoSAX*, folded by their spin period listed in table 2.2. Dashed arrow shows the MIN phase, solid arrow shows MAX phase, and dotted arrow the TRN phase. The corresponding phase 0.0 and the definition of phases are summarized in table A.6.

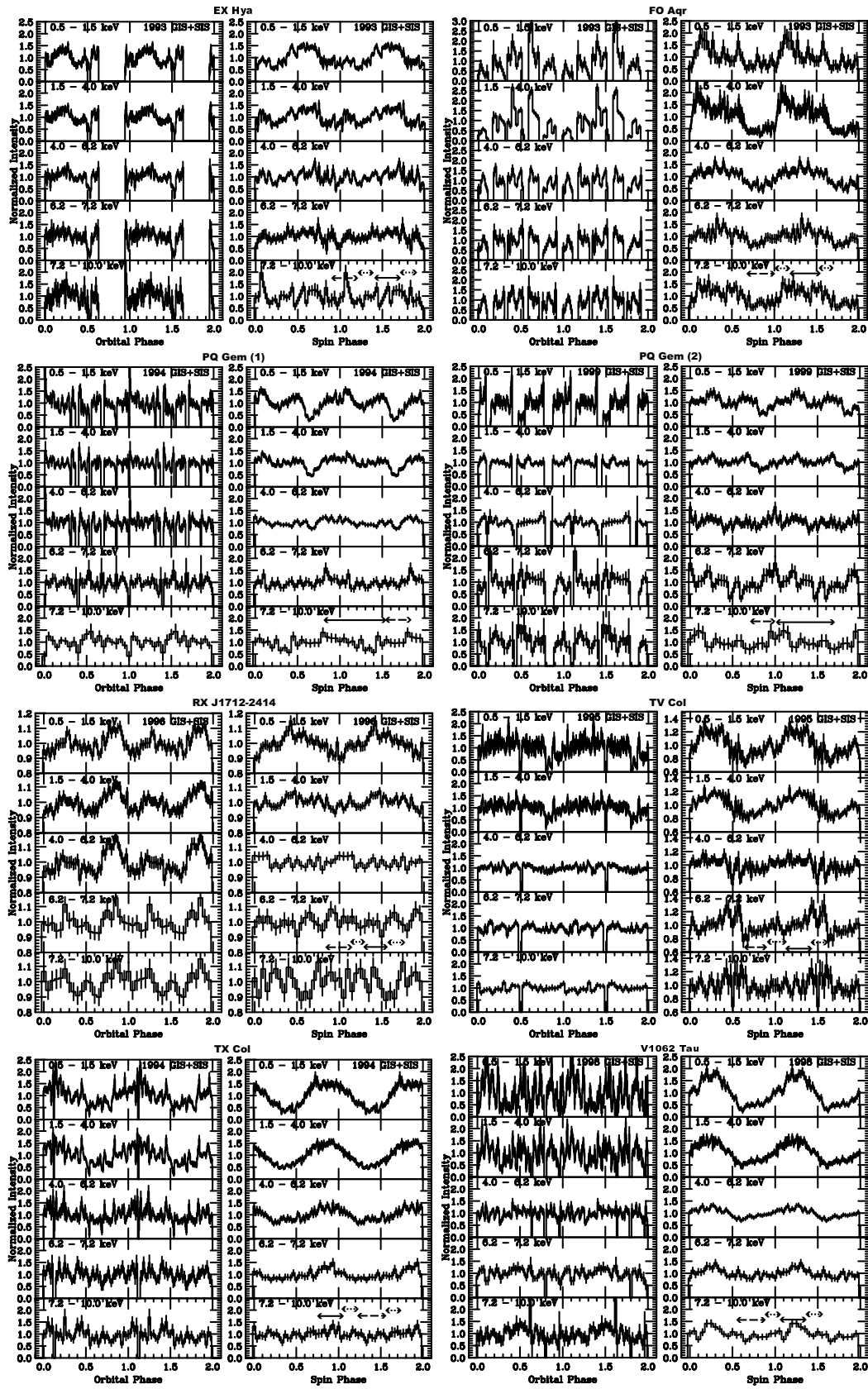


Figure A.1: Continued.

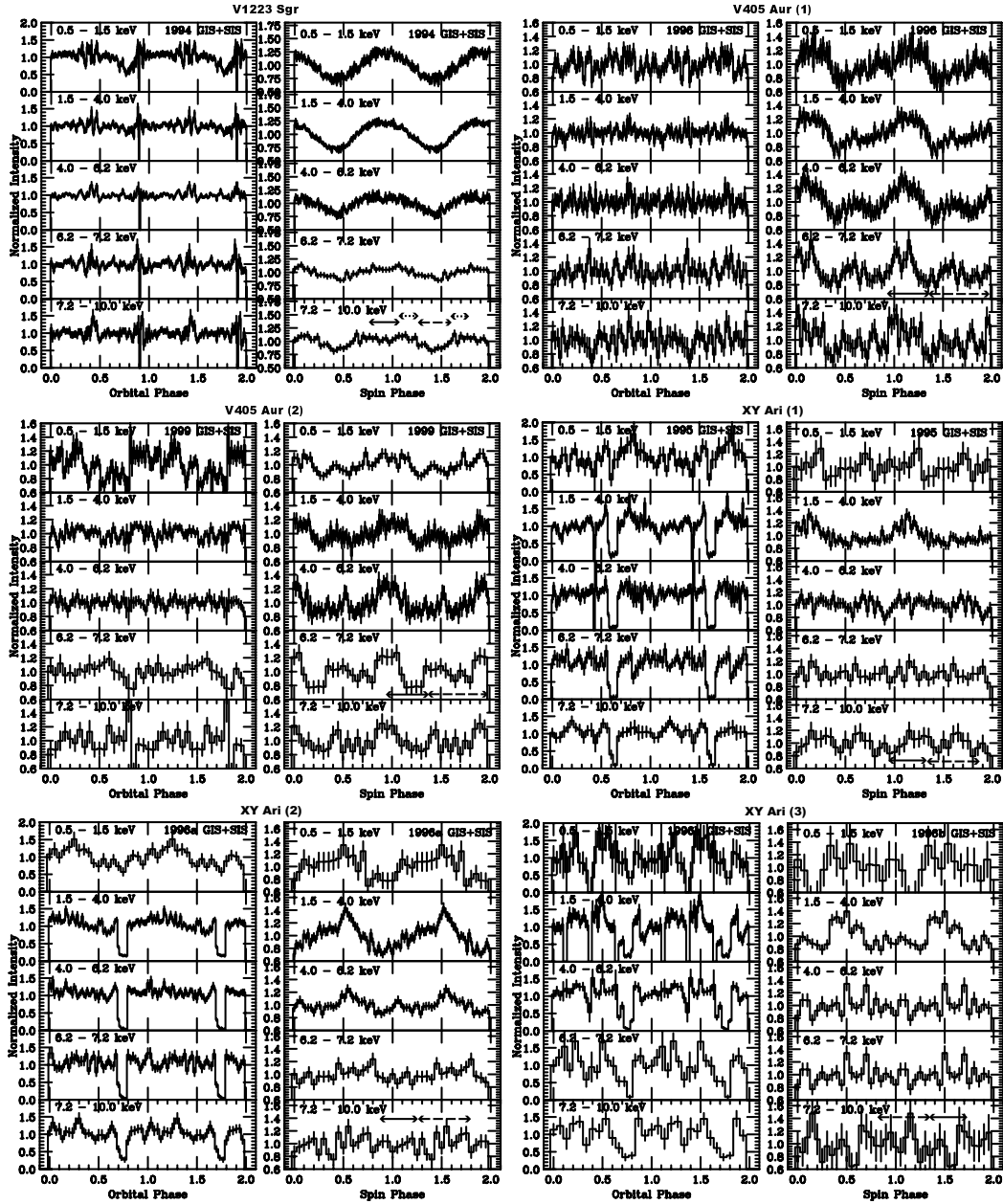


Figure A.1: Continued.

Table A.6: The phase definition of intermediate polars.

object	phase 0.0	MIN phase	TRN phase	MAX phase
AE Aqr	HJD 2450002.5	0.00 - 0.17, 0.83 - 1.00	0.17 - 0.33, 0.67 - 0.83	0.33 - 0.67
AO Psc	HJD 2444883.92074	0.00 - 0.08, 0.74 - 1.00	0.08 - 0.24, 0.58 - 0.74	0.24 - 0.58
BG CMi	HJD 2450186.5	0.00 - 0.27, 0.93 - 1.00	0.27 - 0.43, 0.77 - 0.93	0.43 - 0.77
EX Hya	HJD 2437699.8914	0.00 - 0.20, 0.90 - 1.00	0.20 - 0.40, 0.70 - 0.90	0.40 - 0.70
FO Aqr	HJD 2446097.243668	0.68 - 1.00	0.00 - 0.15, 0.55 - 0.68	0.15 - 0.55
PQ Gem (1)	HJD 2449297.9730	0.52 - 0.80	-	0.00 - 0.52, 0.80 - 1.00
PQ Gem (2)	HJD 2449297.9730	0.70 - 0.98	-	0.00 - 0.70, 0.98 - 1.00
RXJ1712-2414	HJD 2450159.5	0.00 - 0.12, 0.87 - 1.00	0.12 - 0.28, 0.62 - 0.78	0.28 - 0.62
TV Col	HJD 2447139.524	0.56 - 0.86	0.00 - 0.10, 0.40 - 0.56, 0.86 - 1.00	0.10 - 0.40
TX Col	HJD 2449627.5	0.21 - 0.55	0.05 - 0.21, 0.55 - 0.71	0.00 - 0.05, 0.71 - 1.00
V1062 Tau	HJD 2450859.5	0.53 - 0.87	0.00 - 0.03, 0.37 - 0.53, 0.87 - 1.00	0.03 - 0.37
V1223 Sgr	HJD 2445626.13067	0.23 - 0.57	0.07 - 0.23, 0.57 - 0.73	0.00 - 0.07, 0.73 - 1.00
V405 Aur	HJD 2449689.573466	0.32 - 0.96	-	0.00 - 0.32, 0.96 - 1.00
XY Ari	HJD 2449935.5	0.38 - 0.88	-	0.00 - 0.38, 0.88 - 1.00

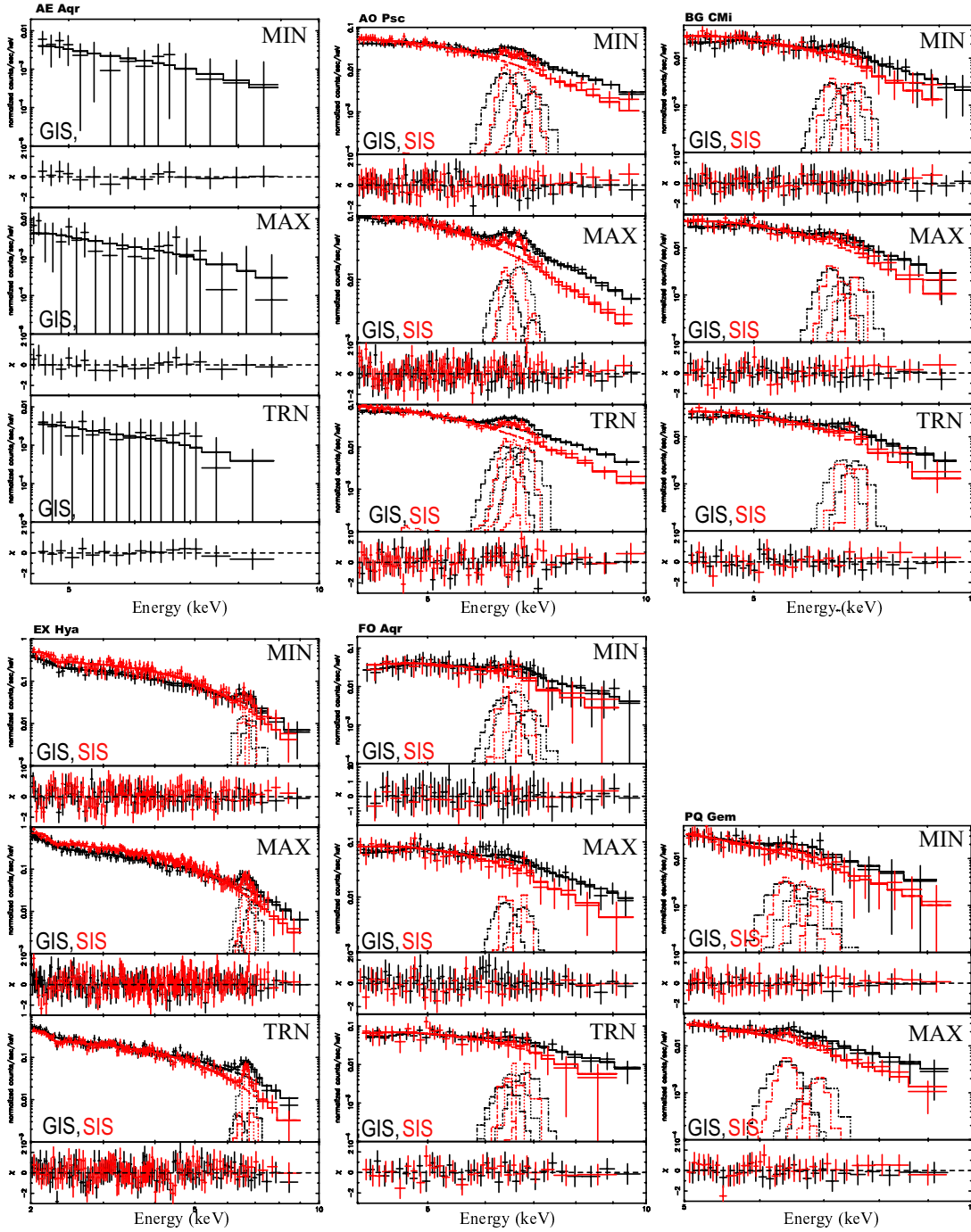


Figure A.2: Phase resolved X-ray spectra of intermediate polars with *ASCA*. The definition of the phases are listed in table A.6. We discarded the SIS data of AE Aqr for phase-resolved analysis, because of insufficient timing resolution of the SIS.

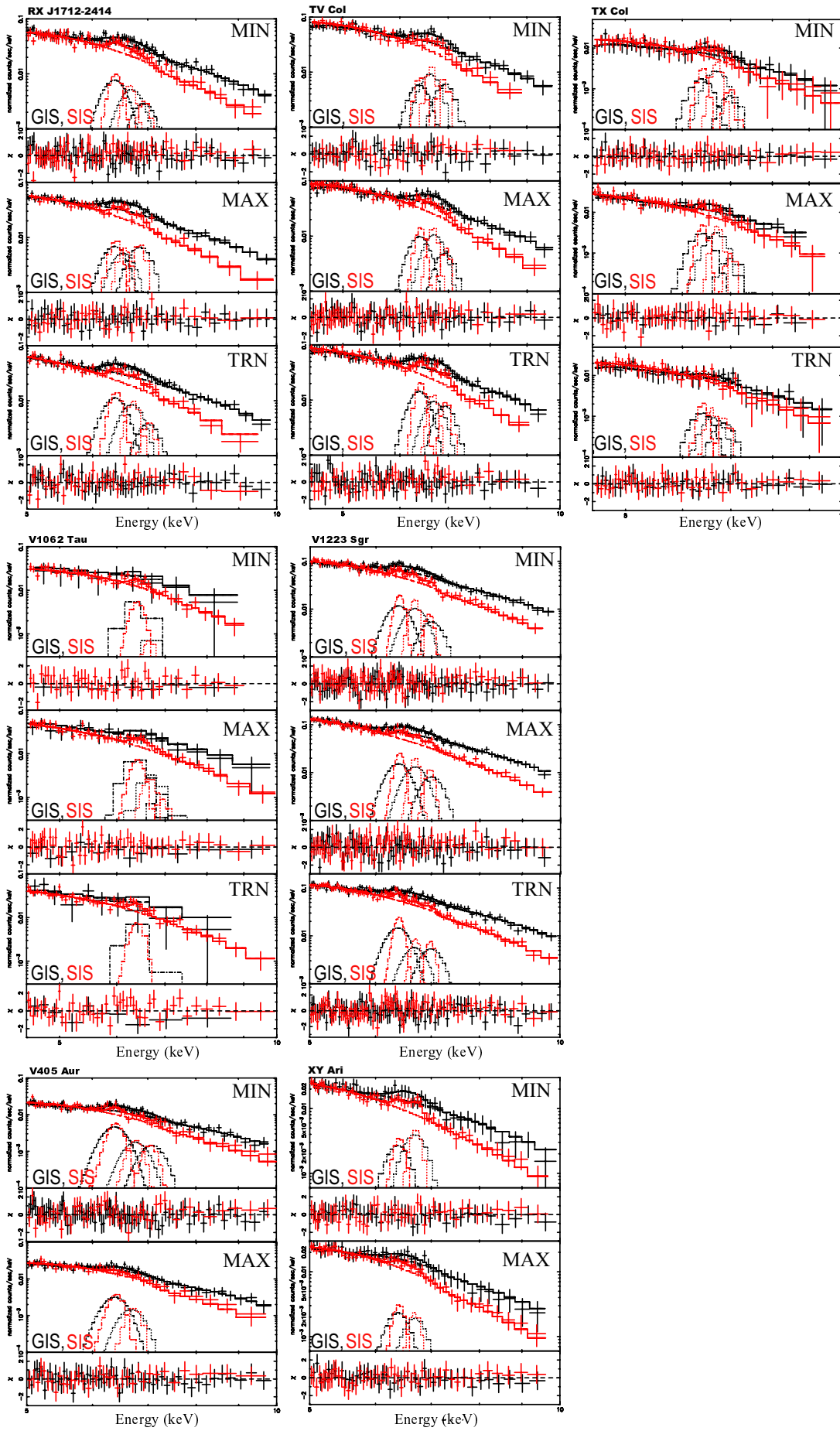


Figure A.2: Continued.

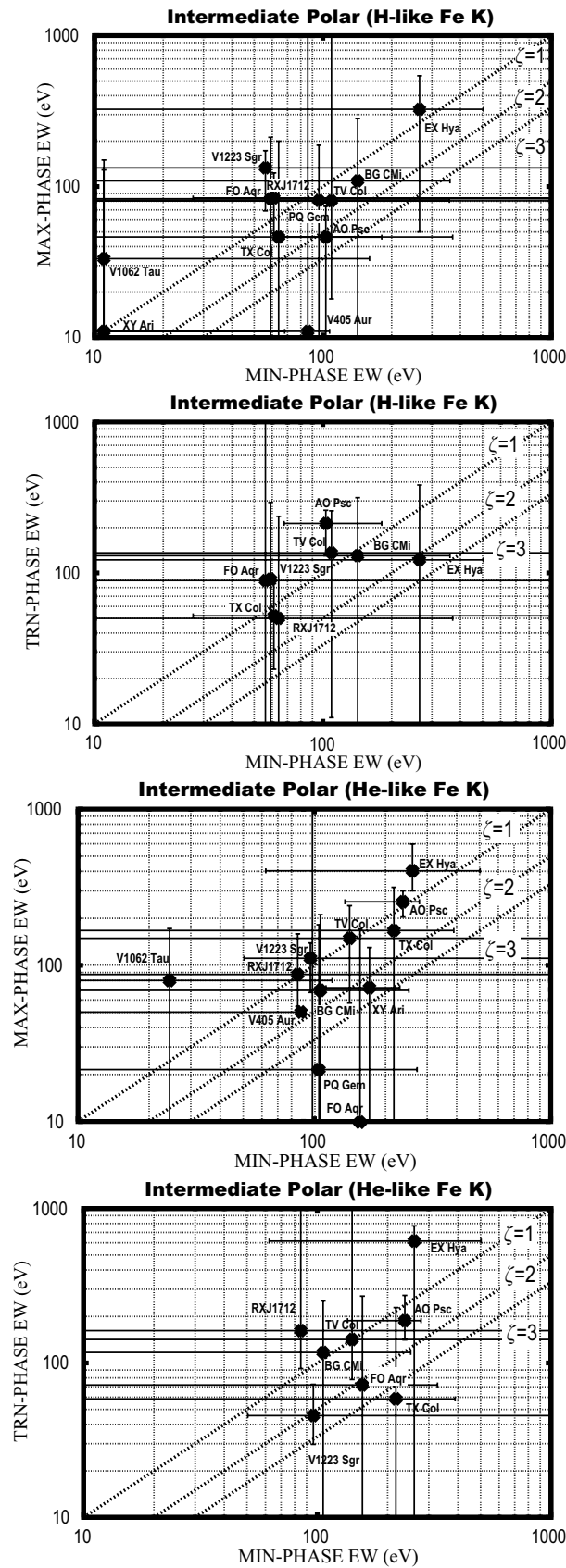


Figure A.3: Scatter plots of line equivalent widths among pole-on (min-phase), side-on (max-phase), and medium (transition) phases.



# Bibliography

- [1] Achilleos N., Wickramasinghe D. T., and Wu K. 1992, MNRAS 256, 80
- [2] Aizu K. 1973, Progress of Theoretical Physics 49, 1184
- [3] Allan A., Horne K., Hellier C., Mukai K., Barwig H., Bennie P. J., Hilditch R. W. 1996 MNRAS 279, 1345
- [4] Angel J. R., Borra E. F., Landstreet J. D. 1981, ApJS 45, 457
- [5] Angel J. R. P., Liebert J. Stockman H. S. 1985, ApJ 175, L85
- [6] Arnaud M. and Rothenflug R. 1985, A&AS 60, 425
- [7] Arnaud M. and Rothenflug R. 1992, A&AS 398, 394
- [8] Augusteijn T., Heemskerk M. H. M., Zwarthoed G. A. A., van Paradijs J. 1994, A&AS 107, 219
- [9] Bailey J. A. 1981, MNRAS 197, 31
- [10] Bailey, J., Axon, D. J., Hough, J. H., Watts, D. J., Giles, A. B., Greenhill, J. G. 1983, MNRAS, 205, 1
- [11] Bailey J. A., Wickramasinghe D. T., Hough J. H., and Cropper M. S. 1988, MNRAS 234, 19
- [12] Bailey J., Ferrario L. and Wickramasinghe D. T. 1991, MNRAS 251, 37
- [13] Barrett P. E. and Chanmugam G. 1985, ApJ 298, 743
- [14] Beardmore A. P., Done C., Osborne J. P., and Ishida M. 1995, MNRAS 272, 749
- [15] Bekefei G. 1966, Radiation Processes in Plasmas (New York; Wiley)
- [16] Bergeron P., Saffer R. A. and Liebert J. 1992, ApJ 394, 228
- [17] Bergeron P., Saffer R. A., Liebert J. 1992, ApJ 394, 228
- [18] Beuermann K., Thomas H. -C. , Giommi P. and Tagliaferri G. 1986 IAUC, 4289

- [19] Beuermann K., Thomas H. -C. , Giommi P. and Tagliaferri G. 1988 IAUC, 4671
- [20] Beuermann K., Thomas H. -C. , and Schwope A. 1989b, IAUC, 4775
- [21] Biermann P., Kühr H., Liebert J., Stockman H. S., Strittmatter P. A., and Tapia S. 1982, IAUC 3680
- [22] Biermann P. S. 1985, ApJ 293, 303
- [23] Biermann P., Schmidt G. D., Liebert J., Stockman H. S., Tapia S., Kühr H., Strittmatter P. A., West S. and Lamb D. Q. 1985, ApJ 293, 303
- [24] Blanford R. D., Applegate J. H. and Hernquist L. 1983, MNRAS 204, 1025
- [25] Boella G., Chiappetti L., Conti G., Molendi S., Cusumano G., Del S. S. La Rosa G., Maccarone M. C., Re S., Sacco B., Tripiciano M. ; Braeuninger H. W., Burkert W. 1995, SPIE 2517, 223
- [26] Boella G., Butler R. C., Perola G. C., Piro L., Scarsi L., and Bleeker J. 1997 A&AS 122, 299
- [27] Boley, private communication in Griffiths et al (1979)
- [28] Bond I. A., and Freeth R. V. 1988, MNRAS 232, 753
- [29] Bradt H. V., Remillard R. A., Tuohy I. R., Buckley D. A., Brissenden R., Schwartz D. A., and Roberts W. 1988, Proc. of the symposium on the Physics of Neutron Star and Black Holes, Tokyo, ed. Tanaka Y., Univ. Academic Press Inc. Tokyo
- [30] Buckley D. A. H., and Tuohy I. R. 1989, A&A 344, 376
- [31] Buckley D.A.H., Sekiguchi K., Motch C., O'Donoghue D., Chen An-Le, Schwarzenberg-Czerny A., Pietsch W., Harrop-Allin M. K. 1995, MNRAS 275, 1028
- [32] Buckley D.A.H., Haberl F., Motch C., Pollard K., Schwarzenberg-Czerny A., Sekiguchi K. 1997, MNRAS 287, 117
- [33] Burke B.E., Mountain R.W., Harrison D. C., Bautz M. W., Doty J. P., Ricker G. R., and Daniels, P.J. 1991, IEEE Trans. Nucl. Sci., ED-38, 1069
- [34] Burke B.E., Mountain R.W., Daniels P.J., Cooper M.J., Dolat V.S. 1994, IEEE Trans. Nucl. Sci., NS-41, 375
- [35] Burwitz V., Reinsch K., Schwope A. D., Hakala P. J., Beuermann K., Rousseau Th., Thomas H.-C., Gansicke B. T., Pirola V., Vilhu O. 1998, A&A 331, 262
- [36] Catalan M. S., Schwope A. D., Smith R. C. 1999, MNRAS 310, 123

- [37] Chandrasekhar S. 1931, MNRAS 91, 456
- [38] Chandrasekhar S. 1939, An Introduction to the Study of Stellar Structure (Univ. of Chicago Press, Chicago)
- [39] Chanmugam G. and Gabriel M. 1972, A & A 16, 149
- [40] Chanmugam G. 1992, Annu. Rev. Astron. Astrophys 30, 143
- [41] Citterio O et al. 1985, SPIE Proc. 597, 102
- [42] Conti G. et al. 1994, SPIE Proc. 2279, 101
- [43] Cropper M. 1982, IBVS, 2096
- [44] Cropper M. 1988a, AdSpR 8, 273
- [45] Cropper M. 1988b, MNRAS 231, 597
- [46] Cropper M., Mason K. O., Allington-Smith J. R., Branduardi-Raymont G., Charles P. A., Mittaz J. P. D., Mukai K., Murdin P. G., Smale A. P. 1989, MNRAS 236, 29
- [47] Cropper M. 1990, Space Sci. Rev. 54, 195
- [48] Cropper M. and Wickramasinghe D. T. 1993, MNRAS 260, 696
- [49] Cropper M., Ramsay G., and Wu K. 1998, MNRAS 293, 222
- [50] Cropper M., Ramsay G., and Whu K. 1998, MNRAS 293, 222
- [51] Dotani T., Yamashita A., Rasmussen A., and the SIS team 1995, NASA ASCA News 3, 25  
(see [http://asca.gsfc.nasa.gov/docs/asca/newsletters/rad\\_dam\\_sis3.html](http://asca.gsfc.nasa.gov/docs/asca/newsletters/rad_dam_sis3.html))
- [52] Drilling J. S. and Schonberner D. 1985, A & A 146, L23
- [53] Ezuka H. and Ishida M. 1999, ApJS 120, 277
- [54] Ferrario L., Wickramasinghe D. T., Tuohy I. R., Bailey J. 1988 IAUC, 4523
- [55] Ferrario L., Wickramasinghe D. T., Bailey J., Tuohy I. R., Hough J. H. 1989, ApJ 337, 832
- [56] Ferrario L., Whchramasinghe D. T., Bailey J. A., Hough J. H. and Tuohy I. R. 1992, MNRAS 256, 252
- [57] Ferrario L., Wickramasinghe D. T., Bailey J., Hough J. H., Tuohy I. R. 1992, MNRAS 256, 252

- [58] Ferrario L., Bailey J., Wickramasinghe D. T. 1993, MNRAS 262, 285
- [59] Ferrario L., Wickramasinghe D. T., Bailey J. A., Buckley D. A. H. 1994, MNRAS 268, 128
- [60] Ferrario L., Wickramasinghe D., Bailey J., Buckley D. 1995a, MNRAS 273, 17
- [61] Ferrario L., Wickramasinghe D. T., Bailey J. 1995c, PASA 12, 81
- [62] Ferrario L., Bailey J., Wickramasinghe D. T. 1996, MNRAS 282, 218
- [63] Fontaine G., Thomas J. H., and van Horn H. M. 1973 ApJ 184, 911
- [64] Frank J., King A. R. and Raine D. J. 1985, *Accretion Power in Astrophysics*, Cambridge University Press.
- [65] Frontera F., Costa E., Dal Fiume D., Feroci M., Nicastro L., Orlandini M., Palazzi E., and Zavattini G. 1997, A&AS 122, 357
- [66] Fujimoto R. and Ishida M. 1996, ApJ 474, 774
- [67] Fujimoto R. and Ishida M. 1997, ApJ 474, 774
- [68] Fujimoto R. 1998, Ph.D thesis, University of Tokyo
- [69] Gehrels N. and Williams E. D. 1993, ApJL 418, 25
- [70] Gendreau K. C. 1994, NASA ASCA News 2, 5  
(see [http://asca.gsfc.nasa.gov/docs/asca/newsletters/sis\\_back2.html](http://asca.gsfc.nasa.gov/docs/asca/newsletters/sis_back2.html))
- [71] Gendreau K. C., Mushotzky R., Fabian A. C., Holt S. S., Kii T., Serlemitsos P. J., Ogasaka Y., Tanaka Y., Bautz M. W., Fukazawa Y., Ishisaki Y., Kohmura Y., Makishima K., Tashiro M., Tsusaka Y., Kunieda H., Ricker, G. R., Vanderspek R. K. 1995, PASJ 47, 5
- [72] Giommi P., Angelini L., Osborne J., Stella L., Tagliaferri G., Beuermann K., Thomas H.-C. 1987, IAUC 4486
- [73] Greiner, J., Remillard, R. A., Motch, C. 1998, A&A, 336, 191
- [74] Haberl F., Throsten J. R., Motch C., Schwarzenberg-Czerny A., Pakull M., Shambrook A., Pietsch W. 1994, A&A 291, 171
- [75] Hamada T. and Salpeter E. E. 1961, ApJ, 134, 683
- [76] Hameury J. M., King A. R., Lasota J. P. and Ritter H. 1988, MNRAS 231, 535
- [77] Harrop-Allin M. K., Cropper M., Potter S. B., Dhillon V. S., Howell Steve B. 1997, MNRAS 288 1033

- [78] Hayashida K., Inoue H., Koyama K., Awaki H., Takano S. 1989, PASJ 41, 373
- [79] Heise J. and Verbunt F. 1988, A&A, 189, 122
- [80] Hellier C. Mason K. O., Rosen S. R., Cordova F. A. 1987 MNRAS 228, 463
- [81] Hellier C. Mason K. O. and Cropper M. 1990, MNRAS 242, 250
- [82] Hellier C., Mason K. O., Mittaz J. P. D. 1991, MNRAS 248, 5
- [83] Hellier C. and Spoats L. N. 1992, IBVS 3724, 1
- [84] Hellier C. 1996, in Proc. of IAU Colloq. 158, Cataclysmic variables and related objects, ed. N. Evans and J. Wood
- [85] Hellier C., Mukai K., Ishida M., Fujimoto R. 1996, MNRAS 280, 877
- [86] Hellier C. 1997, MNRAS 288, 817
- [87] Herber U., Napiwotzki R., and Reid I. N. 1997, A&A 323, 819
- [88] Hilditch R. W. 2001, Close Binary Stars, (Cambridge University Press)
- [89] Hoshi R. 1973, Progress of Theoretical Physics 49, 776
- [90] Howell S. B., Nelson L. A. and Rappaport S. 2001, ApJ 550, 897
- [91] Ichimaru S. 1997, Phys. Let. A 235, 83
- [92] Ishida M. 1991, Ph.D thesis, University of Tokyo
- [93] Ishida, M., Greiner, J., Remillard, R. A., Motch, C., 1998, A&A, 336, 200
- [94] Ishisaki Y. 1998, Ph.D thesis, University of Tokyo
- [95] Ishisaki Y., Kagei T., Ohashi T., and Kikuchi K. 2000, 日本天文学会 秋期, W23b (in Japanese)
- [96] Jablonski F. and Steiner J. E. 1987, ApJ 323, 672
- [97] Jahoda K., Strohmayer T. E., Smith D. A., Stark M. J. 1999, HEAD 31 2607
- [98] Kaluzny J. and Semeniuk I. 1988, IBVS 3145
- [99] Kamata Y., Tawara Y., and Koyama K. 1991, ApJ 379, L65
- [100] Kittel C, 1996, Introduction to Solid State Physics, 7th Edition, (Wiley New York)
- [101] Koester D. and Weidemann V. 1980, A&A 81, 145

- [102] Koyama K., Ikegami T., Inoue H., Kawai N., Makishima K., Matsuoka M., Mitsuda K., Murakami T., Ogawara Y., Ohashi T., Suzuki K., Tanaka Y., Waki I. 1984, PASJ 36, 659
- [103] Kruszewski A. and Semeniuk I. 1993, AcA 43, 127
- [104] Kubiak M. 1984, AcA 34, p397
- [105] Lamb D. Q. and Masters A. R. 1979, ApJ 234, L117
- [106] Lamb D. Q. 1988, in Polarized Radiation of Circumstellar Origin, ed. G. V. Coyne et al. (Vatican, Vatican Observatory), 153
- [107] Lance C. M., McCall M. L., Uomoto A. K. 1988, ApJS 66, 151
- [108] Latham D. W., Liebert J., Steiner J. E. 1981, ApJ 246, 919
- [109] Liebert J. 1988, PASP 100, 1302
- [110] Liebert J., Dahn C. C., and Monet D. G. 1988, ApJ 332, 891
- [111] Makishima K. 1986, Lect. Note Phys. 266, 249
- [112] Makishima K., Tashiro M., Ebisawa K., Ezawa H., Fukazawa Y., Gunji S., Hirayama M., Idesawa E., Ikebe Y., Ishida M., Ishisaki Y., Iyomoto N., Kamae T., Kaneda H., Kikuchi K., Kohmura Y., Kubo H., Matsushita K., Matsuzaki K., Mihara T., Nakagawa K., Ohashi T., Saito Y., Sekimoto Y., Takahashi T., Tamura T., Tsuru T., Ueda Y., Yamasaki N. Y. 1996, PASJ, 48, 171
- [113] Masai K. 1984, Astrophys. Space Sci. 98, 367
- [114] Mason K., Middleditch J., Cordova F., Jensen K., Reichert G., Bowyer S., Murdin P., Clark, D. 1982 IAUC 3684
- [115] Mason K. O. 1985, Sp. Sci. Rev. 40, 99
- [116] Mason K. O. 1997, MNRAS 285, 493
- [117] Mastel L. 1961, MNRAS 122, 473
- [118] Masters A. R. 1978, Ph.D. Thesis, University of Illinois
- [119] McCook G. P. and Sion E. M. 1987, ApJS 65, 603
- [120] McCook G. P. and Sion E. M. 1999, ApJS 121, 1
- [121] Mestel L. 1961, ApJ 122, 473
- [122] Mewe, R., Gronenschild, E. H. B. M., van den Oord, G. H. J. 1985, A&AS, 62, 197

- [123] Mihara T., Makishima K., Kamijo S., Ohashi T., Nagase F. 1991, *ApJL* 379, L61
- [124] Misaki, K., Terashima, Y., Kamata, Y., Ishida, M., Kunieda, H., Tawara, Y. 1996, *ApJ*, 470, 53
- [125] Morris S. L., Schmidt G. D., Liebert J., Stocke, J., Gioia I. M., Maccacaro T. 1987 *ApJ* 314, 641
- [126] Morrison R. M., and McCammon D. 1983, *ApJ* 270, 119
- [127] Moss D. 1986, *Phys. Reports* 140, 1
- [128] Mukai K., and Charles P. A. 1986, *MNRAS* 222, 1
- [129] Mukai K. and Charles P. 1987, *MNRAS* 226, 209
- [130] Mukai K., Charles P. A., Smale A. P. 1988, *A&A* 194, 153
- [131] Mumford G. S. 1976, *BAAS* 8, 346
- [132] Nauenberg M. 1972, *ApJ* 175, 417
- [133] Norton A. J., Hellier C., Beardmore A. P., Wheatley P. J., Osborne J. P., Taylor P. 1997, *MNRAS* 289, 362
- [134] Nousek J., Luppino G., Gajar S., Bond H. E., Grauer A. D., Schmidt G., Hill G., Tapia S. 1982 *IAUC* 3733
- [135] Oda M. 1972, 宇宙の探求、中央公論社 (in Japanese)
- [136] Ohashi T., Ebisawa K., Fukazawa Y., Hiyoshi K., Horii M., Ikebe Y., Ikeda H., Inoue H., Ishida M., Ishisaki Y., Ishizuka T., Kamijo S., Kaneda H., Kohmura Y., Makishima K., Mihara T., Tashiro M., Murakami T., Shoumura R., Tanaka Y., Ueda Y., Taguchi K., Tsuru T., Takeshima T. 1996, *PASJ*, 4 NS-41, 3758, 1570
- [137] Otani C. and Dotani T. 1994, *NASA ASCA News* 2, 25  
(see [http://asca.gsfc.nasa.gov/docs/asca/newsletters/sis\\_echo2.html](http://asca.gsfc.nasa.gov/docs/asca/newsletters/sis_echo2.html))
- [138] Paczyński B. 1971, *ARA&A* 9, 183
- [139] Parmar A.N., Martin D.D.E., Bavdaz M., Favata F., Kuulkers E., Vacanti G., Lammers U., Peacock A., and Taylor B.G. 1997, *A&AS* 122, 309
- [140] Patterson J. 1979, *ApJ* 231 789
- [141] Patterson J. P. 1984, *ApJS* 54, 443
- [142] Patterson J. 1988, *IBVS* 3264

- [143] Patterson J. P. 1994, PASP 106, 209
- [144] Potter S.B., Cropper M., Mason K. O., Hough J. H., Bailey J. A. 1997, MNRAS 285, 82
- [145] Provencal J. L., Shipman H. L., Hog E., and Thejll P. 1998, ApJ 494 759
- [146] Rappaport S., Joss P. C. and Webbink R. F. 1982, ApJ 254, 616
- [147] Ritter H. 1987, A&AS 70, 335
- [148] Ritter H. and Kolb U. 1998, A&AS 129, 83
- [149] Ritter H. and Kolb U. 1998, A&AS 129, 83
- [150] Ronsen S. R. 1992, MNRAS 254, 493
- [151] Rothschild R. E., Gruber D. E., Knight F. K., Matteson J. L., Swank J. H., Holt S. S., Serlemitsos P. J., Mason K. O., and Tuohy I. R. 1981, ApJ 250, 723
- [152] Rothschild R. E., Blanco P. R., Gruber D. E., Heindl W. A., MacDonald D. R., Marsden D. C., Pelling M. R., Wayne L. R., Hink P. L. 1998, ApJ 496, 538
- [153] Rybicki G. B. and Lightman A. P. 1979, Radiative Processes in Astrophysics (Wiley, New York)
- [154] Schmidt G. D., Stockman H. S., Margon B. 1981, ApJ 243, 157
- [155] Schmidt G. D., Stockman H. S., Grandi S. A. 1983, ApJ 271, 735
- [156] Schmidt G. D. and Smith P. S. 1994, ApJ 423, L63
- [157] Schmidt Gary D. and Stockman H. S. 2001, ApJ 548, 410
- [158] Schwope A. D. and Beuermann K. 1990 A & A 238, 173
- [159] Schwope A. D., Beuermann K., Thomas H.-C. 1990, A&A 230, 120
- [160] Schwope A. D., Beuermann K. 1990, A&A 238, 173
- [161] Schwope, A. D., Thomas, H. -, Beuermann, K., Reinsch, K. 1993, A&A, 267, 103
- [162] Schwope A. D., Thomas H. C., Beuermann K. 1993, A&A 271, 25
- [163] Schwope A. D., Beuermann K., Jordan S., Thomas H.-C. 1993, A&A 278, 487
- [164] Schwope A. D. Schwarz R. , and Greiner J. 1999, A & A 348, 861
- [165] Schwope A. D., Cataln M. S., Beuermann K., Metzner A., Smith R. C., Steeghs D. 2000, MNRAS 313, 533

- [166] Semeniuk I. and Kałuży J. 1988, *AcA* 38, 49
- [167] Serlemitsos P. J., Jalota L., Soong Y., Kunieda H., Tawara Y., Tsusaka Y., Suzuki H., Sakima Y., Yamazaki T., Yoshioka H., Furuzawa A., Yamashita K. Awaki H., Itoh M., Ogasaka Y., Honda H., Uchibori Y. 1995, *PASJ*, 47, 105
- [168] Shafter A. W. and Macry J. D. 1987, *MNRAS* 228, 193
- [169] Shapiro S. and Teukolsky 1983, *Black Holes, White Dwarfs, and Neutron Stars* (Wiley New York)
- [170] Shull J. M. and van Steenberg M. 1982, *ApJS* 48, 95 (*ApJS* 49, 351)
- [171] Sion E. M., Fritz M. L., McMullin J. P., Lallo M. D. 1988, *AJ* 96, 251
- [172] Skillman D. 1996, *PASP* 108, 130
- [173] Spitzer L. 1962, *Physics of Fully Ionized Gases* (Wiley, New York)
- [174] Spruit H. C., Ritter H. 1983, *A & A* 124, 267
- [175] Steiner J. E., Schwartz D. A., Jablonski F. J., Busko I. C., Watson M. G., Pye J. P., McHardy I. M. 1981, *ApJ* 249, L21
- [176] Stockman H. S., Liebert J., Tapia S., Green R. F., Williams R. E., Ferguson D. H., and Szkody P. 1981, *IAUC* 3616
- [177] Stockman H., Liebert J., Tapia S., Green R., Williams R., Ferguson D., Szkody P. 1981, *IAUC* 3616
- [178] Stockman H., Foltz C., Tapia S., Schmidt G., Grandi S. 1982, *IAUC* 3696
- [179] Szkody P., Vennes S., Schmidt G. D., Wagner R. M., Fried R., Shafter A. W., Fierce E. 1999, *ApJ* 520, 841
- [180] Takano S., Koyama K., Tawara Y., Matsumoto T., Noguchi K., Iwata T., Takahashi N., Umemoto T., Tatematsu K., Ohashi N., Fukui Y. Makishima K. 1989, *IAUC*. 4745, 1
- [181] Tanaka Y., Fujii M., Inoue H., Kawai N., Koyama K., Maejima Y., Makino F., Makishima K., Matsuoka M., Mitsuda K. 1984, *PASJ* 36, 641
- [182] Tanaka Y., Inoue H., Holt S. S. 1994, *PASJ* 46, L37
- [183] Tapia S. 1976, *IAUC* 2987
- [184] Tapia S. 1977, *ApJ* 212, L125

- [185] Tashiro M., Makishima K., Ezawa H., Fukazawa Y., Idesawa E., Ishisaki Y., Iyomoto N., Kamae T., Kaneda H., Matsushita K., Matsuzaki K., Saito Y., Sekimoto Y., Tamura T., Hirayama M., Ishida M., Kubo H., Okada K., Takahashi T., Ueda Y., Kikuchi K., Ohashi T., Yamasaki N., Kohmura Y., Ikebe Y., Mihara T., Tsuru T., Ebisawa K., Gunji S. 1995, SPIE 2518, 2
- [186] Terada Y., Kaneda H., Makishima K., Ishida M., Matsuzaki K., Nagase F. Kotani T. 1999, PASJ, 51, 39
- [187] Terada Y., Ishida M., Makishima K., Imanari T., Fujimoto R., Matstuzaki K., Kaneda H. 2001, MNRAS 328, 112
- [188] Thomas, H. -C., Reinsch, K. 1996, A&A, 315, L1
- [189] Tsusaka Y., Suzuki H., Yamashita K., Kunieda H., Tawara Y., Ogasaka Y., Uchibori Y., Honda H. et al. 1995, Appl. Opt. 34, 4848
- [190] Tuohy I. R., Ferrario L., Wickramasinghe D. T., Hawkins M. R. S. 1987, PASAu 7, 60
- [191] van Amerongen S., Augusteijn T., and van Paradijs 1987, MNRAS 228, 377
- [192] van Gent H. 1931 Bull. astr. Neth. 6 93
- [193] Vaeth H. 1997, A&A 317, 476
- [194] Vennes S. 1999, ApJ 525, 995
- [195] Visvanathan N. V., and Wickramasinghe D. T. 1979, Nature 281, 47
- [196] Warner B. and Cropper M. 1984, MNRAS 206, 261
- [197] Warner B. 1987 MNRAS 227, 23
- [198] Webbink R. F. 1990, in Mauche C. W., ed. Accretion Powered Compact Binaries, (Cambridge Univ. Press, Cambridge), 177
- [199] Weidemann V. 1977, A & A 61, L27
- [200] Welsh W. F., Horne K., and Gomer R. 1994, MNRAS 257, 649
- [201] Wendell C. E., van Horn H. M. and Sargent D. 1987, ApJ 313, 284
- [202] White N. E. 1981, ApJ 244, L85
- [203] Wickramasinghe D. T. and Meggitt S. M. A. 1982, MNRAS 198, 975
- [204] Wickramasinghe D. T., Visvanathan N., Tuohy I. R. 1984, ApJ 286, 328

- [205] Wickramasinghe D. T. and Martin B. 1985, MNRAS 212, 353
- [206] Wickramasinghe D. T., Tuohy I. R. and Visvanathan N. 1987, ApJ 318, 326
- [207] Wickramasinghe D. T., Ferrario L., Bailey J. 1989, ApJ 342, 35
- [208] Wickramasinghe D. T., Cropper M., Mason K. O., Garlick M. 1991, MNRAS 250, 692
- [209] Wickramasinghe D. T. and Ferrario L. 2000, PASP 112, 873
- [210] Woerd H., de Cool M., Paradijs 1984, A&A 131, 137
- [211] Wood M. A. 1990, Ph.D thesis, University of Texas at Austin
- [212] Wood M. A. 1995, in Proc. 9th European Workshop on White Dwarfs, ed. D. Koester & K. Werner (Berlin: Springer), 41
- [213] Wu K., Chanmugam G., and Shaviv G. 1995, ApJ 455, 260
- [214] Wunner G. 1990, in AIP Conf. Proc. 216, Spectral Line Shapes, ed. L. Frommhold and E. Keto (New York: AIP), 563
- [215] Yamashita A. 1995, Master thesis, University of Tokyo (in Japanese)
- [216] Yamashita A., Dotani T., Bautz M., Crew G., Ezuka H., Gendreau K., Kotani T., Mitsuda K., Otani C., Rasmussen A., Ricker G., Tsunemi H. 1997, IEEE Trans. Nucl. Sci., NS-44, 847
- [217] Zhang E. and Robinson E. L. 1994, IBSconf, 358

# Acknowledgement

First of all, I would like to greatly appreciate very much to Prof. K. Makishima for his continuous support on this thesis (giving me the motivation of this study), as well as on various situations during my graduated school period, including the day when *ASTRO-E* satellite was lost after very hard work on the development of our detector, Hard X-ray Detector (HXD). He always lead me with a deep scientific view on various issues, and taught me the pleasure of finding out “physics” on them.

I deeply wish to thank Prof. M. Ishida for guiding me on the plasma in magnetic white dwarfs. He gave me useful advice and comments on this study, since the discovery of strong line emission from POLEs.

I also express my thanks to Dr. Kaneda, who gave me a first motivation and taught me the way to analyze *ASCA* data, and Dr. Matsuzaki, who showed me a policy in programming a large numerical code. I thank Prof. Chris. Mauche for his useful comments on this study.

I owe a great deal to all the scientists and engineers who work on *ASCA*, and I would like to acknowledge all the member of *ASCA* team.

I am grateful to Mr. N. Isobe, Ms. Y. Matsumoto, and Ms. C. Tanihata, who shared all the five years during my graduated school. We had a hot discussions on scientific issues, instrumental experiments, and other things; we sometimes came in the resonance condition to share our time all night long. I thank all the graduated students and stuffs in Makishima laboratory.

Finally, I wish to thank all the members of X-ray astrophysical group in the University of Tokyo, ISAS, RIKEN, and Saitama University, and the best family in the *ASTRO-E* HXD team, including Prof. T. Kamae, Prof. T. Takahashi, Prof. M. Tashiro, Prof. Y. Fukazawa, and Prof. T. Murakami, hoping a successful achievement of the recovery mission of *ASTRO-E II*.